



Direct Numerical Simulation of Turbulent Flames On Parallel Computers

Dissertation

zur Erlangung des akademischen Grades

**Doktoringenieur
(Dr.-Ing.)**

von **M.Sc. Gordon Fru Atanga**

geb. am 06. April 1977 in Mbatu, Kamerun

genehmigt durch die Fakultät für Verfahrens- und Systemtechnik
der Otto-von-Guericke-Universität Magdeburg

Gutachter:

Prof. Dr. Ing. Dominique Thévenin
Prof. Dr. rer. nat. habil. Ulrich Maas
Prof. Dr. Vincent Giovangigli

Promotionskolloquium am: 02.02.2012

To my King

To my Queen

To my Princess

Acknowledgements

The road has been rather long yet wonderful, somewhat winding and often paved with overwhelming experiences. Nevertheless, it has been my good fortune to encounter many people who have given me patiently more of their time, companionship, professional and personal help more than was perhaps warranted.

I would first of all like to thank my most competent, intuitive and smart advisor, Prof. D. Thévenin. He not only gave me the scientific support and supervision that a graduate student can expect from his professor, but has also been extremely encouraging, with a fatherly ear. Thanks to him, I have grown to find my pleasure and lot within this exciting field of numerical combustion. His ideas and especially his unique brand of enthusiasm, optimism and confidence in me form the bedrock on which most of this thesis has been built. Without such backing, I would never have made it this far. Thank you!

There are several fellow researchers and countless individuals whom I would specifically like to thank for the support they have given me throughout my time as a graduate student: Dr. G. Janiga was basically my second supervisor. I could not have wished for a more thorough discussion partner and sounding board (on *almost any* subject under the sun) associated to his excellent computer science background. He has been instrumental in helping the numerical developments and software extensions described in this thesis come to life. Dr. H. Shalaby helped in introducing me to the flame solvers and the basics of the FPI tabulation technique shortly after my arrival at the Lab. Thank you. Finally, I am grateful to Dr. A. Laverdant at the French Aerospace Laboratory (ONERA, Paris) for interesting discussions and support regarding the employed detailed chemistry flame solver, under whose supervision it was extended with the third dimension. Dr. B. Witter at the IMPRS has been of enormous help with local administration huddle. It gave me more time to concentrate on the research.

A list that, alas, has far too many names on it to mention separately is that of all the co-workers, group members, and mates that I have worked, talked, and rubbed shoulders with over the years. My gratitude goes out to all these colleagues and former colleagues at the Institute of Fluid Dynamics and Thermodynamics at the University of Magdeburg (Germany) and the CFD team at the European Center for Research and Advanced Training in Scientific Computing (CERFACS) in Toulouse (France). Many thanks to Prof. B. Cuenot who welcomed me in CERFACS and generously guided me for the three months spend there. Together with Dr. E. Riber and many others, we had stimulating and exciting times of scientific exchange, and I treasure the memories.

Moving towards more personal acknowledgements, I would like to execute a big *blocksend()* of aggregated thanks towards all my family and friends (you definitely know who you are) — with a special shout-out to my father (J. Gado) and sisters (M. Esther, T. Sarah and T. Pamela) and their respective families. Your unfeigned and unprecedented moral, spiritual and financial support at various stages of my life thus far have been foundational.

I am, of course, particularly indebted to my Lord and *King* (Jesus), my angelic wife and *queen* (Rophine) and our precious daughter and *princess* (Amy) for their monumental, unwavering support and encouragement on all fronts. They have truly always been there for me and without them none of this would have been even remotely possible.

Last but not the least, I appreciate and count it a privilege being part of the CMFI Germany Christian community. You have been exceedingly encouraging. Thank you.

The financial support from the federal state of Saxony-Anhalt (Sachsen-Anhalt, Germany) for the greater bulk of the work, and from the Marie-Curie Action on Efficient and Clean Combustion Experts Training program is gratefully acknowledged. Part of the work was carried out within the frame of the Distributed European Infrastructure for Supercomputing Application (DEISA) Extreme Computing Initiative (DECI), as part of the 7th framework program financed by the EU. They also provided most of the computing resources under the *DNS-HiRe* project. A special word of gratitude to the DEISA help desk at LRZ (Germany), IDRIS (France) and EPCC (Scotland). My gratitude also goes to all the members of the *DNS-HiRe* project for their support and its various follow-up efforts and spin-offs.

*Magdeburg,
February 24, 2012*

Gordon Fru Atanga

Declaration

I hereby declare that I prepared the submitted work without inadmissible assistance and without the use of any aids other than those indicated. Facts or ideas taken from other sources, either directly or indirectly have been marked as such.

In particular, I did not use the services of a commercial graduation consultation. Further more, I have not made payments to third parties either directly or indirectly for any work connected with the content of the submitted dissertation.

This work has so far not been submitted either in Germany or abroad in same or similar form as a dissertation and has also not yet been published as a whole.

Magdeburg, February 24, 2012

Gordon Fru Atanga

Abstract

The availability of electrical energy and all transportation systems rely largely on turbulent combustion processes, such as in gas turbines and Internal Combustion engines, burning either fossil or renewable fuels. Detailed fundamental studies of the underlying processes are necessary towards the design, construction and optimization of efficient low emission burners. A number of issues that play a major role for such predictive numerical studies of turbulent combustion are addressed in this work. Computations of turbulent premixed and diffusion flames using Direct Numerical Simulations (DNS) on massively parallel computers are carried out for this purpose.

Data Input/Output strategies and pseudo-turbulence generation techniques, which limit fine-grain parallelism of usual flame solvers are first addressed. In tandem with other optimized modules, quantitative parametric studies of turbulent flames burning hydrogen (H_2), syngas (CO/H_2) and methane (CH_4) as fuel are realized at very high values of the turbulent Reynolds numbers (Re_t). Complex physicochemical models including volume viscosity (κ) are employed. In conjunction with ensemble averaging, the individual and combined effect of increasing turbulence intensities (u') and of κ on the flame structure are extensively investigated and quantified.

Stepping up for instance u' from 3 to 12 m/s leads to an increase in the scaled integrated heat release rate from 2 to 16. This illustrates the interest of combustion in a highly turbulent medium in order to obtain high volumetric heat release rates in compact burners. Flame thickening is observed to be predominant at high Re_t . Peak probability density functions of the mean flame curvature and tangential strain rates extracted along the flame front are highly flattened when increasing Re_t and reveal structural changes associated with κ . The fuel consumption speed, which is an interesting measure of the turbulent flame speed shows increasing local quenching events for highly turbulent conditions, particularly for lean mixtures.

It is shown that laminar flames are not modified by κ , while the local structure of turbulent flames may differ considerably when taking it into account. This is attributed to the chaotic nature of turbulence. Noticeable modifications induced by κ are found for CO/H_2 as well as for H_2 flames. For such H_2 -containing fuels, the differences appear to remain unchanged when increasing Re_t . On the other hand, turbulent flames burning CH_4 show no significant impact due to κ . Thus, whenever possible, κ should be taken into account for detailed studies of turbulent flames burning H_2 -containing fuels, in particular for DNS, while this term can be safely neglected for higher hydrocarbon flames.

The associated cost for such high-fidelity computations in terms of computing time and required memory remain tremendous and sometimes prohibitive. To solve this issue, the Flame Prolongation of ILDM (FPI) technique is reconsidered as a practical alternative to complete reaction mechanisms. With two major modifications to include realistic transport phenomena, corresponding DNS results show clear improvements relative to the classical FPI tables.

There is still a lot to be done regarding the thorough understanding of turbulent combustion and its associated challenges at different levels. In particular, the present study demonstrates that, (1) repeating DNS realizations towards statistically significant results is very important, and (2) analyzing DNS results computed with detailed models at high Re_t values is essential to obtain reliable information for modeling purposes. Since experiments are often costly and time-consuming, extreme scale computing appears to be a key to accelerate corresponding studies regarding high energy efficiency and clean combustion in a world increasingly constrained by crude oil depletion.

Keywords: Turbulent combustion, Direct Numerical Simulation, High Performance Computing, detailed physicochemical models, chemistry tabulation, volume viscosity, high Reynolds number

Zusammenfassung

Die Verfügbarkeit von elektrischer Energie und allen Transportsystemen basiert zu großen Teilen auf turbulenten Verbrennungsprozessen. Als Beispiele seien die Verbrennung von fossilen oder erneuerbaren Brennstoffen in Gasturbinen oder Verbrennungsmotoren genannt. Für die Auslegung, Konstruktion und Optimierung von effizienten, emissionsarmen Brennern sind detaillierte grundlegende Studien der zugrundeliegenden Prozesse notwendig. Aus diesem Grund wird in dieser Arbeit eine Reihe von Aspekten behandelt, die eine größere Rolle für solche voraussagenden numerischen Studien von turbulenten Verbrennungsprozessen spielen. Es werden zu diesem Zweck Berechnungen von turbulenten vorgemischten und Diffusionsflammen mit Hilfe von Direkten Numerischen Simulationen (DNS) auf massiv parallelen Rechnern durchgeführt.

Zuerst werden Datenein- und Ausgabe-Strategien (I/O) und Techniken zur Erzeugung von Pseudo-Turbulenz behandelt, welche die feinkörnige Parallelisierung von üblichen Lösern begrenzen. Zusammen mit anderen optimierten Modulen wurden quantitative Parameterstudien von turbulenten Flammen bei der Verbrennung von Wasserstoff (H_2), Synthesegas (CO/H_2) und Methan (CH_4) als Brennstoff durchgeführt. Dabei wurden sehr hohe Werte für die turbulente Reynoldszahl betrachtet (Re_t). Es wurden komplexe physikalisch-chemische Modelle einschließlich der Volumenviskosität κ verwendet. In Verknüpfung mit ensemble averaging wurde der einzelne sowie der kombinierte Effekt von sukzessive erhöhten Turbulenzintensitäten (u') und von κ auf die Flammenstruktur ausführlich untersucht und quantifiziert.

Wenn beispielsweise u' von 3 auf 12 m/s erhöht wird, führt dies zu einer Erhöhung der skalierten integrierten Wärmeabgaberate von 2 auf 16. Dies verdeutlicht die Bedeutung der Verbrennung in einem hochturbulenten Medium, um hohe volumetrische Wärmeabgaberraten in kompakten Brennern zu erhalten. Bei hohem Re_t ist vorwiegend ein Verdicken der Flamme zu beobachten. Die sogenannten Peak probability density functions (PDF) der mittleren Flammenkrümmung und tangentialen Dehnungsgeschwindigkeiten, die entlang der Flammenspitze ausgewählt werden, flachen stark ab, wenn Re_t erhöht wird, und zeigen Strukturveränderungen, die mit κ zusammenhängen. Die Geschwindigkeit, mit der der Brennstoff verbraucht wird, die ein bedeutsames Maß für die Geschwindigkeit der turbulenten Flamme ist, zeigt unter hochturbulenten Bedingungen zunehmende lokale Verlöschungen, speziell für dünne Mischungen.

Es wird gezeigt, dass laminare Flammen nicht durch κ verändert werden, während sich die lokale Struktur von turbulenten Flammen erheblich unterscheiden kann, wenn man κ berücksichtigt. Dies wird der chaotischen Natur der Turbulenz zugeschrieben. Erkennbare Veränderungen, die von κ erzeugt werden, treten bei CO/H_2 sowie bei H_2 Flammen auf. Für solche H_2 – enthaltenden Brennstoffe bleiben die Unterschiede bestehen, wenn Re_t erhöht wird. Turbulente, CH_4 verbrennende Flammen zeigen dagegen keinen nennenswerten Einfluß von κ . Aus diesem Grund sollte κ bei detaillierten Studien von turbulenten Flammen bei der Verbrennung von H_2 –haltigen Brennstoffen, speziell für DNS, berücksichtigt werden. Bei höheren Kohlenwasserstoffen dagegen kann dieser Term vernachlässigt werden.

Die mit solchen Berechnungen einhergehenden Kosten in Bezug auf Rechenzeit und benötigten Speicher bleiben enorm und manchmal unerschwinglich. Um dieses Problem zu lösen, wurde die Flame Prolongation of ILDM (FPI)-Technik als eine praktische Alternative zu kompletten Reaktionsmechanismen neu betrachtet. Mit zwei wesentlichen Modifikationen zur Berücksichtigung realistischer Transport-Phänomene zeigen die entsprechenden DNS-Ergebnisse deutliche Verbesserungen im Vergleich zu klassischen FPI-Tabellen.

Es bleibt auf verschiedenen Ebenen immer noch vieles in Bezug auf das gründliche Verständnis der turbulenten Verbrennung und der dazugehörigen Herausforderungen zu tun. Die vorliegende Arbeit zeigt insbesondere, dass (1) die Wiederholung von DNS-Realisierungen zur Erzeugung statistisch signifikanter Resultate sehr wichtig ist, und (2) die Analyse von DNS-Ergebnissen, die mittels detaillierter

modelle und hohen Re_t – Werten berechnet wurden, essentiell ist, um verlässliche Informationen für Modellierungszwecke zu erhalten. Da Experimente oft teuer und zeitaufwändig sind, erscheint die Simulation von extremen Skalen ein Schlüssel zur Beschleunigung von Studien bezüglich hoher Energieeffizienz und sauberer Verbrennung zu sein, in einer Welt, die zunehmend von der Endlichkeit der Rohölreserven eingeschränkt wird.

Keywords: turbulente Verbrennung, Direkte Numerische Simulation, Hochleistungsrechnen, detaillierte physikalisch-chemische Modelle, Chemie Tabellierung, hohe Reynoldszahl, Volumenviskosität

CONTENTS

Index	xii
Nomenclature	xv
1 Introduction	1
1.1 Turbulent combustion: A grand challenge!	1
1.2 Thesis outline	3
2 Mathematical formulations	7
2.1 General governing equations	7
2.1.1 Mass conservation	7
2.1.2 Momentum conservation	7
2.1.3 Species conservation	7
2.1.4 Energy conservation	8
2.2 Thermodynamic relations	8
2.2.1 Ideal gas law	8
2.2.2 Specific enthalpy and heat	9
2.3 Transport models	9
2.3.1 Viscous stress tensor	9
2.3.2 Diffusion velocities	12
2.3.2.1 General expression	12
2.3.2.2 First-order approximation	13
2.3.2.3 Hirschfelder-Curtiss approximation	13
2.3.2.4 Fick's law approximation	13
2.3.2.5 Lewis number approximation	14
2.3.2.6 Unity Lewis number approximation	14
2.3.3 Heat flux	14
2.4 Chemistry models	14
2.4.1 Single-step mechanism	15
2.4.2 Complete mechanism	15
2.4.3 Reduced chemical kinetics schemes	16
2.4.4 Tabulated chemistry	17
2.5 Summary	17
3 Model reduction	19
3.1 Introduction	19
3.2 Brief overview of chemistry tabulation techniques	20
3.2.1 Computational Singularity Perturbation (CSP)	20
3.2.2 In-Situ Adaptive Tabulation (ISAT)	20
3.2.3 Intrinsic Low-Dimensional manifold (ILDm)	20

3.2.4	Flame(let) Prolongated ILDM (FPI)	21
3.2.5	Flamelet Generated manifold (FGM)	21
3.3	Attributes of a good chemical look-up table	21
3.4	FPI complex chemistry tabulation	22
3.4.1	One-dimensional premixed flame computations	22
3.4.2	Database implementation	23
3.4.2.1	Choice of table coordinates	23
3.4.2.2	Choice of data structure	25
3.4.2.3	Information tabulation	27
3.4.2.4	Storage constraints	28
3.4.3	Advanced FPI	30
3.4.3.1	Motivation and challenges	30
3.4.3.2	Proposed modifications	30
3.4.4	Data base functionality	34
3.4.4.1	Information location and retrieval	34
3.4.4.2	Out-of-bound approximation	36
3.4.4.3	Stand-alone verifications	36
3.4.5	Advantages of new FPI formulation	37
3.4.6	FPI at work	38
3.5	Low Mach number approximation	39
3.6	Summary	40
4	Numerical combustion	41
4.1	Introduction	41
4.2	Combustion modes and configurations	42
4.2.1	Premixed combustion	42
4.2.2	Non-premixed combustion	44
4.3	Numerical combustion approaches	45
4.3.1	Reynolds-Averaged Navier-Stokes (RANS)	46
4.3.2	Large Eddy Simulation (LES)	46
4.3.3	Direct Numerical Simulations	47
4.4	Employed research tools	48
4.4.1	Compressible DNS solver: <i>parcomb</i>	48
4.4.1.1	Numerical method	49
4.4.1.2	Data Input/Output enhancement	50
4.4.1.3	Parallel performance and optimization	51
4.4.2	Incompressible DNS solver: π^3	54
4.4.2.1	Numerical method	55
4.4.2.2	Poisson solver	56
4.4.2.3	Parallelization	56
4.4.2.4	Parallel performance	58
4.4.3	Compressible LES/DNS solver: <i>AVBP</i>	59
4.5	Novel turbulence generation strategies	60
4.5.1	Digital Filtering (DF) technique	60
4.5.1.1	Brief theory	60
4.5.1.2	Algorithm	61
4.5.2	Random Noise Diffusion (RND) technique	63
4.5.2.1	Brief theory	63
4.5.2.2	Algorithm	63
4.5.3	<i>A posteriori</i> investigation of generated fluctuating fields	64
4.5.3.1	General flow field	64

4.5.3.2	Energy spectrum and length scales	65
4.5.3.3	Incompressibility	68
4.6	Numerical combustion solution strategy	71
4.7	Summary	73
5	Results and discussions	75
5.1	Introduction	75
5.2	Non-premixed combustion	76
5.2.1	Problem setup and initialization	76
5.2.2	General turbulent flame structure	78
5.2.3	Impact on presumed PDF-based turbulent flame models	79
5.2.4	PDF of scalar dissipation rate	82
5.2.5	Impact of volume viscosity	83
5.2.5.1	Laminar flame structure	83
5.2.5.2	Temporal evolution of turbulent flame	84
5.2.5.3	Normal profiles through the turbulent flame	84
5.2.5.4	Global turbulent flame properties	86
5.2.5.5	Conditional and PDF analysis	89
5.2.5.6	Influence of turbulent intensity	90
5.2.6	Summary	91
5.3	Premixed combustion	92
5.3.1	Problem setup and initialization	93
5.3.2	Highly turbulent planar methane flames	100
5.3.2.1	General turbulent flame structure	100
5.3.2.2	Effect on flame thickness	102
5.3.2.3	Conditional and PDF analysis	103
5.3.3	Highly turbulent spherical methane flames	104
5.3.3.1	Laminar flame structure	104
5.3.3.2	General turbulent flame structure	106
5.3.3.3	Global turbulent flame properties	109
5.3.3.4	Conditional analysis	111
5.3.3.5	Effect of equivalence ratio	111
5.3.3.6	Turbulent burning velocity	114
5.3.4	Impact of volume viscosity	117
5.3.4.1	Laminar flame structure	117
5.3.4.2	Turbulent flame structure	120
5.3.4.3	Turbulent flame properties	123
5.3.4.4	Influence of turbulent intensity	125
5.3.4.5	Statistical significance	126
5.3.5	Summary	129
5.4	Conclusions	130
6	Present challenges	131
6.1	Introduction	131
6.2	Tabulated chemistry results	131
6.2.1	Problem and initialization	131
6.2.2	Laminar flame structure	132
6.2.3	Turbulent flame structure	133
6.2.4	Advanced versus classical FPI tables	133
6.2.4.1	Time evolution profiles	134
6.2.4.2	Flame propagation speed	134

6.2.5	Trade-off in computing time	136
6.2.6	Summary	138
6.3	Towards realistic geometries in DNS	139
6.3.1	Problem and initialization	140
6.3.2	Laminar flame structure	141
6.3.3	Turbulent flame structure	142
6.3.4	Summary	143
7	Conclusions and outlook	145
A	Reaction mechanisms	149
A.1	Hydrogen oxidation mechanism	149
A.2	Syngas oxidation mechanism	150
A.3	Methane oxidation mechanism	152
	References	153
	Curriculum Vitae	163

NOMENCLATURE

Roman Symbols

A	Arrhenius law pre-exponential factor ... [s ⁻¹]	l_{33}	turbulence length scale [m]
A	section surface area of a flow tube [m ²]	\dot{m}	mass flow rate [kg/s]
b_k	digital filter coefficient [-]	M	Mach number [-]
b_{ijk}	three-dimensional digital filter coefficient . [-]	N	number of grid points along one axis [-]
C	reaction progress variable [-]	N	number of tabulated flame quantities [-]
c^{int}	internal heat capacity [J kg ⁻¹ K ⁻¹]	N_c	number of species used for Y_c reconstruction [-]
C_p	mixture specific heat capacities at constant pressure [J kg ⁻¹ K ⁻¹]	N_f	number of 1D premixed flames in a FPI look-up table [-]
C_v	mixture specific heat capacities at constant volume [J kg ⁻¹ K ⁻¹]	n_i	molar concentration of species i [-]
d_i	distance between a point and node N_i in an FPI rectangular grid [-]	N_p	number of flame data points along Y_c [-]
D_{ik}	multicomponent diffusion coefficient for the species i into species k [m ² /s]	N_r	number of elementary reactions [-]
D_{ik}	binary diffusion coefficient for the species i [m ² /s]	N_s	total number of species [-]
Da	Damköhler number [-]	N_t	number of diffusion time steps in the RND turbulence technique [-]
D_i^*	mixture averaged diffusion coefficient for the species i [m ² /s]	N_t	number of triangles in an FPI triangulation [-]
D_i^T	thermal diffusion coefficient of species i [m ² /s]	N_x	half width of a digital filter kernel [-]
E_a	Arrhenius law activation energy [calories/mole]	N_x	number of grid points along x -axis [-]
e_t	total energy per unit volume [J/kg]	N_y	number of grid points along y -axis [-]
erfc	error function [-]	N_z	number of grid points along z -axis [-]
f	source term in Poisson equation [-]	N_z	number of species used for Y_z reconstruction [-]
f_i	component of the external force [N]	\tilde{p}	dynamically perturbed pressure [Pa]
h	total enthalpy (sensitive and chemical) [J/kg]	p	hydrodynamic pressure [Pa]
h_k	specific enthalpy of species k [J kg ⁻¹]	p_0	spatially uniform pressure [Pa]
H_r	integrated heat release rate [kg/m ³ /s]	P_e	parallel efficiency [%]
$h_{f,k}^0$	specific enthalpy of formation of species k at T_0 [J kg ⁻¹]	Q	number of grid points across a flame front [-]
k_{bj}	backward reaction coefficient of reaction j [-]	\mathbf{q}_j	j^{th} component of the heat flux vector ... [kg s ⁻³]
k_{fj}	forward reaction coefficient of reaction j . [-]	\mathbf{q}_r	gas radiative heat flux [-]
L	length of computational domain [m]	q_s	heat source term [-]
L_c	length of the FPI table Y_c -axis [-]	R	ideal gas constant [kg mol ⁻¹ K ⁻¹]
L_z	length of the FPI table Y_z -axis [-]	Re_t	turbulent Reynolds number [-]
Le_k	Lewis number of species k [-]	Re_{jet}	jet Reynolds number [-]
l_t	integral length scale of turbulence [m]	r_j	reaction rate of progress for reaction j ... [-]
l_x	characteristic turbulence length scale ... [m]	S_c	consumption speed [m/s]
		S_f	flame surface area [m ²]
		S_L	laminar flame speed [m/s]

S_T	turbulent flame speed [m/s]
T	absolute temperature [K]
T_1	parallel speedup factor [-]
T_b	burnt gas temperature [K]
T_u	fresh gas temperature [K]
u'	turbulent (or root-mean-square) velocity [m/s]
u_j	components of the hydrodynamic velocity [m/s]
\tilde{U}	turbulent jet velocity [m/s]
U_{m_x}	series of random data [-]
U_{rms}	rms value of a random field [m/s]
\mathcal{V}_i	stored value at node N_i in the FPI rectangular grid [-]
\mathbf{V}_i^*	diffusion velocity predictor term [m/s]
\mathbf{V}_c	diffusion velocity corrector term [m/s]
V_{kj}	diffusion velocity of species k along j .. [m/s]
\dot{w}_k	chemical mass production rate of species k [kg m ⁻³ s ⁻¹]
W_k	molar mass of species k [kg mol ⁻¹]
X_k	mole fraction of species k [-]
Y_c	FPI table progress variable coordinate ... [-]
Y_F	fuel mass fraction [-]
Y_i	mass fraction of species i [-]
Y_O	oxidizer mass fraction [-]
Y_z	FPI table mixture coordinate [-]
$Y_{c,max}$	maximum value of the Y_c values [-]
$Y_{c,min}$	minimum value of the Y_c values [-]
Z	mixture fraction [-]
Z_j^∞	Z_j value in initial composition [-]
Z_j	mass fraction of elements j in the mixture [-]
Z_s	stoichiometric mixture fraction [-]
\widetilde{Z}''^2	Favre-averaged variance [-]
\tilde{Z}	Favre-averaged mean [-]

Greek Symbols

α	scaling constant for Y_c expressions [-]
β	Arrhenius law temperature dependent coefficient [-]
Γ	γ -function [-]
δ	Kronecker symbol [-]
δ_H	full-width at half-maximum of heat release rate [m]
δ_L	thermal thickness based on maximum temperature gradient [m]
δ_{th}	laminar flame thickness [m]
Δt	typical size of time step [s]
Δx	typical cell size along x -axis [m]

ΔY_c	grid size on the FPI Y_c axis [-]
ΔY_z	grid size on the FPI Y_z axis [-]
η_k	Kolmogorov length scale [m]
θ	velocity divergence (dilatation) [s ⁻¹]
θ_i	wave numbers in the i -direction [-]
κ	volume viscosity [kg m ⁻¹ s ⁻¹]
λ'	partial thermal conductivity .. [W K ⁻¹ m ⁻¹]
λ	mixture-averaged thermal conductivity .. [W K ⁻¹ m ⁻¹]
μ	mixture viscosity [kg m ⁻¹ s ⁻¹]
μ_k	shear viscosity of species k [kg m ⁻¹ s ⁻¹]
ν	kinematic viscosity [m ² /s]
ν_F	stoichiometric coefficient of fuel [-]
ν_O	stoichiometric coefficient of oxidizer [-]
ν_P	stoichiometric coefficient of combustion product [-]
ν_{ij}	number of molecules of type i that are consumed with the elementary reaction j ... [-]
ξ	flame index [-]
ρ	mixture mass density [kg/m ³]
σ_{ij}	stress tensor [Pa]
τ_c	chemical time scale [s]
τ_f	flame time-scale [s]
τ_t	mechanical time scale [s]
τ_k^m	average relaxation time of internal energy in mode m for species k [s]
τ_{ij}	viscous shear tensor components [Pa]
Φ	equivalence ratio [-]
χ	scalar dissipation rate [1/s]
$\tilde{\chi}_s$	conditional mean scalar dissipation rate [1/s]
ω	vorticity [s ⁻¹]
$\dot{\omega}_k$	chemical molar production rate of species k [mol m ⁻³ s ⁻¹]
Ω_i	symbol for species i [-]

Miscellaneous Symbols

\aleph	internal energy mode indexing set [-]
\wp	polyatomic species indexing set [-]
!=	figure legend symbol representing \neq [-]

Abbreviations

CFD	Computational Fluid Dynamics
CFL	Courant-Friedrichs-Lewy number
CPU	computational time
CSP	Computational Singularity Perturbation
DECI	DEISA Extreme Computing Initiative
DEISA	Distributed European Infrastructure for Supercomputing Applications
DF	Digital Filtering
DNS	Direct Numerical Simulation

FFT	Fast Fourier transform
FGM	Flamelet Generated Manifold
FPI	Flame Prolongation of ILDM
FWHM	Full-Width at Half-Maximum
HPC	High Performance Computing
I/O	Input/Output
ILDm	Intrinsic Low Dimensional Manifold
ISAT	In-Situ Adaptive Tabulation
LES	Large-Eddy Simulation
MPI	Message Passing Interface
PDF	Probability Density Function

RANS	Reynolds-Averaged Navier-Stokes Simulation
RCCE	Rate-Controlled Constraint Equilibrium
RND	Random Noise Diffusion
SGS	SubGrid Scale
TKE	Turbulent Kinetic Energy
TRZ	Thin Reaction Zone
WCT	World Clock Time

Operators

$\hat{\cdot}$	Fourier transform
---------------	-------------------

CHAPTER

1

Introduction

1.1 Turbulent combustion: A grand challenge!

The last century has witnessed soaring gas prices, deteriorating air quality and alarming global climate changes. In recent years, increasing concerns have been raised with respect to the environmental impacts of energy consumption via the combustion of fossil fuels, for instance in stationary power generation and transportation, emitting greenhouse gases and air pollutants. As a result, governments now set more and more stringent standards. Hence, it is essential to understand and improve combustion processes, in order to reduce fuel consumption and pollutant emissions as much as possible.

This is indeed a formidable task due to the fact that combustion phenomena, which often are turbulent by nature, involve many individual and physical processes of high complexity, such as chemical kinetics, differential molecular diffusion, radiative heat transfer, phase transition, flame/acoustics interactions, and of course the turbulent flow itself, which is indeed one of the last unsolved issues in fluid dynamics. The nonlinear coupling between all these phenomena completely determines the behavior of a wealth of practical systems. For instance, automobile engines, aircraft turbines, domestic boilers, nano-particle reactors, electricity generation by a power plant burning coal or oil, etc. are relevant systems for which turbulent reacting flows are critically essential.

As an additional source of information combined with experimental and theoretical studies, numerical simulation provides an efficient way of analyzing combustion phenomena of gaseous mixtures. Beside the Reynolds-Averaged Navier-Stokes formulation (RANS, where all turbulent scales are modeled) [1] and Large-Eddy Simulations (LES, where small scales are modeled while large ones are solved exactly) [2–4], Direct Numerical Simulations (DNS) [2] offer the most accurate description of turbulent reacting flows when applicable [5].

RANS require simplified turbulent combustion models and thus cannot be used for *a priori* analysis of the coupling process. LES need a sub-grid model to describe all physical processes taking place below grid resolution. Both, though highly interesting in particular for solving large scale problems with a complex geometry, are thus associated with many unsolved issues and challenges [5–9]. This may lead to insufficient accuracy and prevent generalization of the associated observations. In order to improve the predictive accuracy of numerical simulations, further studies are needed to refine the models required for RANS and LES, or to develop alternatives. These studies can rely either on detailed, quantitative experimental measurements or on DNS computations (sometimes also called "numerical experiments"). The latter will be used in the present thesis work.

The DNS method consists of solving directly and as far as possible exactly the complete, unsteady Navier-Stokes equations. All physical, spatial and time scales are resolved accurately

by using a suitable discretization in space and time, so that a turbulence model is not necessary any more. DNS is the best method with the highest level of accuracy when applicable and its results contain all physical information about the turbulent flow as well as all other variables of interest (species concentrations, temperature, density, etc.).

Numerical combustion is very attractive because it is – usually – affordable and – always – informative, even though the high level of complexity and coupling associated with the representative system of equations makes it extremely difficult at present to come up with truly predictive numerical models for realistic installations. Such models are of course necessary to improve existing devices and develop new configurations.

Irrespective of the solution strategy we adopt for a closer investigation of turbulent burning, the highly complex physical phenomena constitute a grand modeling challenge for which a range of coupled problems need to be addressed simultaneously:

- *Numerical complexity*: It is computationally expensive to directly solve for all the wide range of length and time scales embedded in a turbulent flow, which introduces the traditional closure problem of turbulence modeling. Typical spatial scales range from 1 – 10 nm (at the molecular interactions and chemical reaction level) to 10–100 cm (at the combustor level). All these scales must be adequately resolved or modeled.
- *Chemical complexity*: It is important to use detailed chemical kinetics to describe combustion processes, especially in the study of ignition, extinction and pollutant formation. Such mechanisms often involve a large number of species and elementary reactions that spans a wide range of chemical time scales. For instance, a gasoline oxidation requires hundreds of species and thousands of reactions. Such large system usually lead to additional stiffness.
- *Transport complexity*: Differential diffusion at molecular scale as well as turbulent transport of heat and species control mixing and heat transfer. Appropriate and often expensive approximations are mandatory for predictability. For instance, the traditionally neglected volume viscosity transport term may be vital (for instance in computations involving hydrogen-containing fuels) yet expensive (almost doubling the computational time).
- *Multi-physics complexity*: In some cases, two or three phases of mixture (such as in spray combustion, soot emission, etc.) might exist in the system, which requires modeling of complicated interactions between different phases. For example, accurate calculation of radiation effects which influence the flame structure, soot and NO_x formation might be necessary especially in luminous flames. Another area is that of combustion noise applications for which models are required to incorporate flame-acoustic interactions in the flow.
- *Coupled processes*: For the problems listed above, the spatial and temporal dynamics are inherently coupled due to the interactions between turbulence, flame and other mechanisms. Yet all these scales are relevant and must be resolved or appropriately modeled. For example, turbulence/chemistry and turbulence/radiation interactions lead to typical closure problems in turbulent combustion modeling.
- *Post-processing complexity*: DNS lead nowadays to tens of terabytes of raw data, from which useful information must be extracted and analyzed as efficiently as possible. For example, the DNS of a 3D syngas/air flame presented later produces typically around 14 GB of raw data per solution file per saving time. It is obvious that these data have to be post processed efficiently in order to extract all the available useful information. Fast, accurate and flexible post processing tools are needed in order to maximize the scientific output from such investigations and thus lead to improved models.

Sandwiched between the dire need to compute realistic industrial configurations using predictive models and the associated challenges as outlined above, two common pathways are often open towards keeping the user waiting times at acceptable levels.

The first efforts are channeled towards numerical and physical model reduction. It is then important to identify models that will simplify the numerical description of the reacting process, while preserving the coupling between chemistry, heat transfer and fluid dynamics in a quantitative manner. For instance, the effects of complex chemistry can be incorporated into the flow via a tabulated complex chemistry database [10]. On the other hand, accurate and low cost numerical approximations such as the low-Mach number formulation could be adopted instead of the full compressible system of Navier-Stokes equations [11]. Further more, a combination of such techniques will definitely lead to a stronger reduction in computing time (as will be demonstrated).

In the second instance, High Performance Computing (HPC) is readily exploited both in situations when the most accurate numerical algorithms and physical models are required, as well as when reasonable reductions (as those mentioned above) are used. Indeed, the rapid growth of computer technology and HPC in particular, offer formidable platforms to tackle most of the challenges outlined above. Nevertheless, optimized scalable algorithms and software must be provided for such computationally intensive calculations. For instance, in homogeneous isotropic time decaying turbulence in a box, the usual serial turbulence generation methods such as the inverse Fast Fourier Transform (FFT) based techniques become impracticable due to the difficulty of parallelizing it efficiently. In the same manner, sequential Input/Output (I/O) would limit code scalability. Efficient and enhanced collective parallel I/O is often necessary for improving code performance. These algorithmic issues need to be fully addressed and the absence of standards constitutes an additional challenge. All the same, HPC has enabled high-fidelity computations of complex flames, thereby increasing our understanding of the physical processes as well as providing further detailed information on the turbulent flame structure vital for developing efficient burners.

To summarize, any ambitious numerical combustion tool should possess the potentials of handling hundreds of variables on a few hundreds of millions of grid points with a step in time of the order of 10^{-8} seconds. It should be capable of transporting up to 10^8 unknowns for over 10^4 iterations, necessary for a proper statistical backing of the resulting observations [12]. At the same time, such a tool should scaled intelligibly on several thousand computing cores. Today's Tera-scale computing can handle approximately four decades of scales for a cold flow. Clearly, we see that numerical turbulent combustion modeling is a complicated, complex and broad subject – yet an exciting grand challenge!

1.2 Thesis outline

This thesis describes some contributions in tackling several of the above challenges. The research was initially performed in the context of developing a functional complex chemical database, its implementation into an existing incompressible low-Mach number DNS solver and the subsequent parallelization of the solver for fine grain super computers, in the Laboratory of Fluid Dynamics and Technical Flows (LSS), at the University of Magdeburg. The work was continued as part of the activities of the DEISA Extreme Computing Initiative (DECI) under project *DNS-HiRe* (DNS of turbulent combustion at high Reynolds numbers), as part of the 7th framework program financed by the European Union. Part (three months) of the thesis work was carried out within the CFD team at the European Center for Research and Advanced Training in Scientific Computing (CERFACS) in Toulouse, under the Marie-Curie Action (MCA) on Efficient and Clean COMbustion Experts Training program (ECCOMET). In addition to this *Introduction* (**Chapter 1**), the thesis is structured as follows:

Chapter 2 (*Mathematical formulations*) outlines a comprehensive overview of the various numerical and mathematical formulations associated with combustion phenomena relevant to the thesis work. After a brief introduction, the system of governing equations describing a general reacting flow process is presented, together with the underlying thermodynamical closure relations. The transport models are then introduced, followed with a short review of the many different ways by which reduced or complex chemical kinetics effects can be included into turbulent reacting flow simulations. Most of the established chemistry reduction techniques, starting from the simple one-step chemistry strategy to the most complex one – the complete reaction mechanism – are briefly discussed. Two principal approaches of simplifying the chemical kinetics encountered in reacting flows are identified. A third approach, chemistry tabulation is also briefly introduced just before summarizing the chapter.

Chapter 3 (*Model reduction*) isolates and presents two model reduction approaches well suited to most turbulent flame configurations, which when combined in a flame solver, lead to a strong reduction in computing times. Indeed, much progress in computer technology now sometimes allow direct simulations of turbulent flames relying on complete reaction schemes and realistic multi-component transport models. However, the associated price in terms of computing time and memory requirements remain tremendous, often expressed at best in months, usually in years! Concerning pressure-velocity coupling, one suitable model reduction for turbulent flames is the low-Mach number formalism, leading to a strong reduction in terms of computing time. For this reason, the application and validity of tabulated chemistry techniques, in particular the proposed advanced FPI methodology and its implementation in a low-Mach number turbulent flame solver have been considered in this thesis and will be fully discussed in this chapter, together with a description of the low-Mach number formulation.

Chapter 4 (*Numerical combustion*) aims to identify the most suitable numerical methods and algorithms towards an upgrade of current DNS tools. This in turn will harness the available cutting-edge HPC capabilities to efficiently simulate turbulent flames at realistic (i.e., high) turbulent Reynolds number (Re_t). Issues associated to transport models and detailed physicochemical schemes are considered. In the first instance, the exploited flame configurations are specified, together with numerical and computational configurations relevant to the thesis. The three basic numerical combustion approaches (i.e., RANS, LES and DNS) are then described, with emphasis placed on the DNS method, which is the simulation technique used in this thesis. As mentioned earlier, when accurate models are also employed for all other physical processes, DNS qualify indeed as a *numerical experiment*, but lead to very high requirements in computing time and memory. Even when reduced models are employed, the remaining computing time is still impressive. Therefore, it is essential to employ parallel supercomputers to keep acceptable user waiting times. Among other issues, recently added and upgraded modules, scalable I/O strategies, parallel, single- and multi-processor optimizations are discussed for the various flame solvers. Details of the successful derivation, implementation, parallelization on massively parallel computers and associated issues of two novel turbulence generators, based respectively on digital filtering and on random noise diffusion are presented. A general numerical combustion solution strategy is stated just before summarizing the chapter.

Chapter 5 (*Results and discussions*) presents the main results and mile-stones arrived at during this thesis work for the detailed model computations. After the introduction, DNS results of mild and highly turbulent flames burning various fuels with detailed chemical and transport models are presented, analyzed and discussed. The impact of the traditionally neglected volume viscosity transport term on the turbulent flame structure is quantified.

Chapter 6 (*Present challenges*) presents first DNS test results from the implementation of reduced models (low-Mach number, tabulated chemistry), as well as a first attempt of DNS involving a more realistic geometry. The impact of turbulence on a premixed methane-air flame structure is used to validate the chemistry reduction strategy and its proper implementation.

The trade-off in computing time associated to these reduced models is briefly discussed.

Chapter 7 (*Conclusions and outlook*) closes the thesis with a summary and discussion of the presented research topics and results. Some perspectives regarding future numerical combustion research are stated. In particular, we discuss the possibility of using combustion DNS to check recent theoretical developments suggesting an extension/modification of the Navier-Stokes equations, and to confirm if these extensions lead to realistic results. Ways to map computational methods onto emerging computing platforms are finally discussed.

Appendix A (*Reaction mechanisms*) is included for completeness. It contains the various detailed chemical kinetic schemes used in the computations.

CHAPTER

2

Mathematical formulations

2.1 General governing equations

Numerically, a reacting flow system is generally described by the classical Navier-Stokes equations, with additional balance equations for chemical species and for energy. These are further supplemented with expressions for the production/destruction of chemical species, for the molecular diffusion fluxes and for heat transfer. Using the summation convention for the spatial coordinates, we obtain the following system of equations for [13–15]:

2.1.1 Mass conservation

The conservation of mass is expressed by the general continuity equation,

$$\frac{\partial \rho}{\partial t} + \frac{\partial(\rho u_j)}{\partial x_j} = 0 \quad (2.1)$$

where ρ denotes the mixture mass density, u_j the components of the hydrodynamic velocity and t is the time.

2.1.2 Momentum conservation

The conservation of momentum is expressed as

$$\frac{\partial(\rho u_i)}{\partial t} + \frac{\partial(\rho u_j u_i)}{\partial x_j} = -\frac{\partial p}{\partial x_i} + \frac{\partial \tau_{ij}}{\partial x_j} + \rho f_i, \quad i = 1, 2, 3 \quad (2.2)$$

where p is the pressure, τ_{ij} the viscous shear tensor components and f_i is the i^{th} component of the external force. In most practical applications, all other external forces are neglected except the gravity. In other words, $f_i = g_i$. A general stress tensor is often defined, consisting of a hydrodynamic (pressure) and viscous part: $\sigma_{ij} = \tau_{ij} - p\delta_{ij}$ (see Sect. 2.3 for the complete expression)

2.1.3 Species conservation

When chemical reactions are to be considered, conservation equations for species mass fractions Y_i in the mixture are required. When these are not given by simpler approximate models, we have that

$$\frac{\partial(\rho Y_k)}{\partial t} + \frac{\partial(\rho u_j Y_k)}{\partial x_j} = -\frac{\partial(\rho Y_k V_{kj})}{\partial x_j} + \dot{w}_k; \quad k = 1, 2, \dots, N_s \quad (2.3)$$

where N_s is the total number of species, V_{kj} is the component of the diffusion velocity of species k in the direction j and \dot{w}_k is the chemical mass production rate of species k per unit time and volume. It is characteristic for the reactive nature of the flow under consideration. It is worth noting that eq. (2.1) and (2.3) together give an over-complete system such that solving only $N_s - 1$ equations of (2.3) is sufficient. The mass fraction of the remaining species, usually an abundant species such as nitrogen can then be computed using the constraint that

$$\sum_{i=1}^{N_s} Y_i = 1 \quad (2.4)$$

2.1.4 Energy conservation

Many forms of the energy balance equation can be formulated [5]. Here we use the specific total energy with conservation equation given as

$$\frac{\partial(\rho e_t)}{\partial t} + \frac{\partial(\rho u_j e_t)}{\partial x_j} = -\frac{\partial q_j}{\partial x_j} + \frac{\partial(\sigma_{ij} u_i)}{\partial x_j} + q_s + \rho \sum_{k=1}^{N_s} [Y_k f_{kj} (u_j + V_{kj})] \quad (2.5)$$

where q_j is the j^{th} component of the heat flux vector given by eq. (2.26), q_s is a heat source term corresponding to an external energy source such as in spark ignition modeling. The total energy e_t per unit volume is defined as

$$e_t = \frac{1}{2} |\mathbf{u}|^2 - \frac{p}{\rho} + h \quad (2.6)$$

where h is the total enthalpy (sensitive and chemical).

The solution of the above system of partial differential equations (2.1)–(2.5) yields the mixture density ρ , the velocity components u_j , the mass fractions Y_k of the N_s chemical species and a variable describing the energy. In addition, explicit expressions (in the form of realistic models) are required, for example, to evaluate the chemical source term \dot{w}_k , the diffusion velocities V_{ik} , the heat flux, etc. appearing in the above set of equations. Below is a list of some of the frequently used thermodynamic, chemistry and transport closure relations and/or models.

2.2 Thermodynamic relations

2.2.1 Ideal gas law

Most gases considered in numerical combustion obey the perfect gas law, establishing a relationship between pressure, temperature and the local mixture composition:

$$p = \rho \frac{R}{\bar{W}} T \quad (2.7)$$

where T is the absolute temperature, $R = 8.314 \text{ kg/mol.K}$ is the universal gas constant and \bar{W} is the mixture-averaged molar mass, expressed as

$$\bar{W} = \left(\sum_{k=1}^{N_s} \frac{Y_k}{W_k} \right)^{-1} = \sum_{k=1}^{N_s} X_k W_k; \quad \frac{Y_k}{X_k} = \frac{W_k}{\bar{W}} \quad (2.8)$$

where W_k and X_k are the molar mass and mole fraction of species k , respectively.

2.2.2 Specific enthalpy and heat

The second state equation introduces the enthalpy h as a function of temperature:

$$h = \sum_{k=1}^{N_s} Y_k h_k; \quad h_k(T) = h_{f,k}^0 + \int_{T_0}^T C_{p,k}(T) dT \quad (2.9)$$

$$C_p = \sum_{k=1}^{N_s} C_{p,k} Y_k; \quad C_p - C_v = R/\bar{W} \quad (2.10)$$

where h_k is the specific enthalpy of species k and $h_{f,k}^0$ denotes the specific enthalpy of formation of species k at the reference temperature T_0 . C_p and C_v are the mixture specific heat capacities at constant pressure and volume, respectively. Assuming that all the $C_{p,k}$ and $C_{v,k}$ are equal, simpler approximations for the heat capacity dependency on temperature are easily derived for theoretical studies [5], though such simplifications are not true for flames. Often, both the species specific heat capacity and enthalpy of formation are classically tabulated in polynomial forms [16, 17].

2.3 Transport models

To characterize the molecular transport of species, momentum and energy in a multi-component gaseous mixture, the evaluation of the diffusion coefficients, viscosities, thermal conductivities and thermal diffusion coefficients are required. Large linear system of equations [18] have to be solved first in order to obtain these coefficients, since the kinetic theory does not provide explicit expressions [19]. The viscous tensor, heat flux and diffusion velocities also need explicit expressions. Below are some of the usual expressions for these constitutive relationships.

2.3.1 Viscous stress tensor

In terms of fluid properties, viscosity plays a major role for combustion applications due to the fact that it directly controls dissipation processes, and since temperature and composition variations lead to large spatial and temporal changes in viscosity. As a consequence, viscosity is one of the most important terms coupling turbulence and combustion. Both the shear viscosity μ and volume viscosity κ are introduced in the above system of equations via the stress tensor. Assuming a Newtonian fluid and neglecting all body forces other than gravity, it is expressed as

$$\sigma_{ij} = \tau_{ij} - p\delta_{ij} = \mu \left[\frac{\partial u_i}{\partial x_j} + \frac{\partial u_j}{\partial x_i} \right] + \delta_{ij} \left[\left(\kappa - \frac{2}{3}\mu \right) \frac{\partial u_k}{\partial x_k} - p \right] \quad (2.11)$$

where δ is the Kronecker symbol. It should be noted however, that using such a formulation is more expensive compared to using the viscosity given from the kinetic theory obtained by solving a linear system [20]. The volume viscosity is a function of the fluid local properties. Sometimes, the kinematic viscosity $\nu = \mu/\rho$ is used instead of μ .

If the pure species values of μ_k are known, the mixture-averaged value for a given composition could be computed using for instance Wilke's semi-empirical formula [21], possibly with the modification in [22]:

$$\mu = \frac{\sum_{k=1}^{N_s} X_k \mu_k}{\sum_{j=1}^{N_s} X_j \Phi_{kj}}; \quad \Phi_{kj} = \frac{1}{\sqrt{8}} \left(1 + \frac{W_k}{W_j} \right)^{-1/2} \left(1 + \left(\frac{\mu_k}{\mu_j} \right)^{1/2} \left(\frac{\mu_k}{\mu_j} \right)^{1/4} \right)^2 \quad (2.12)$$

Note however that, using this formula is more expensive than using the viscosity given from the kinetic theory obtained by solving a linear system [20]. In some practical combustion systems,

Species	Temperature (K)	κ_i ($\mu\text{Pa}\cdot\text{s}$)	η_i ($\mu\text{Pa}\cdot\text{s}$)	κ_i/η_i
CH ₄	300	14.5	11.4	1.3
	1000	81.3	28.0	2.9
CO	300	9.8	17.9	0.5
	1000	45.0	41.2	1.1
H ₂	300	296	9.1	32.5
	1000	1029	19.8	52.1
O ₂	300	9.9	20.7	0.5
	1000	48.8	48.4	1.0
N ₂	300	12.8	18.2	0.7
	1000	60.4	41.9	1.4

Table 2.1: Volume viscosity κ_i , shear viscosity η_i and ratio κ_i/η_i for species CH₄, CO, H₂, O₂ and N₂ at temperature 300 and 1000 K [26]

the mixture dynamic viscosity is also evaluated using high order polynomial fits of experimental measurements [8].

Unlike the dynamic (or shear) viscosity μ (also written η in what follows), the volume viscosity transport coefficient κ has been traditionally neglected in almost all (numerical) studies for both cold and reactive flows. Volume viscosity is produced by viscous forces that arise when a volume of fluid is compressed or dilated without change in shape. The kinetic theory, as supported by relevant experiments, predicts that volume viscosity effects are negligible in dilute monoatomic gases – a result widely accepted irrespective of the nature and internal structure of the fluid. Neglecting κ in low Mach number and/or classical boundary layer flows is justified by the fact that, even though the contribution of the dilatation term involving the velocity divergence $\nabla \cdot \mathbf{u}$ (last term in Eq. 2.11) and the volume-to-shear viscosity ratio κ/η might not be necessarily small, the term $\nabla \cdot (\kappa(\nabla \cdot \mathbf{u})\mathbf{I})$ is still negligible due solely to its structure as demonstrated in [23]. When high speed flows are considered, such an approximation is irrational since from an experimental point of view, this ratio is non-zero for a good number of fuels employed for combustion. Approximate values of the ratio κ/η for CH₄, CO, H₂, O₂ and N₂ at temperatures of 300 and 1000 K are given in table 2.1 [24–26], together with their species volume (κ) and shear (η) viscosities. Even larger values have been reported for CO₂ and N₂O (see for instance [27] and references therein). From table 2.1 it is clear that volume viscosity is at least of the same order of magnitude as the shear viscosity at 300 K and even larger at 1000 K, with the ratio κ/η for pure hydrogen as high as 52 at a temperature of 1000 K [26].

The temporal evolution of the maximum value of κ and the ratio κ/η are shown in Fig. 2.1 as obtained from the later (Sect. 5.3.4) described Direct Numerical Simulation of a turbulent premixed hydrogen-air (H₂/N₂-air) flame with global mixture ratio $\Phi = 1.0$, using detailed chemistry and transport models at four different turbulent intensities ($u' = 2.0, 4.0, 6.0$ and 8.0 m/s). For all presented cases, the values of κ and κ/η are clearly non-negligible, and tend to increase with increasing turbulence intensity but show saturation around $u' = 6$ m/s. Considering the vertical scale in Fig. 2.1(b), the peak value for κ/η remains almost constant. The observations presented here for a hydrogen flame hold as well for syngas-air (CO/H₂-air) flames, the second fuel considered in this study, as discussed later. The profiles (not shown) for the combustion of the third fuel in this thesis – methane – on the other hand show a negligible influence of volume viscosity, both in space and time [28].

These preliminary observations, in conjunction with the above mentioned experimental measurements all point to the fact that any suggestion towards an a priori elimination of the volume viscosity may not be an explainable choice. This is especially the case in situations where compressibility effects (and hence dilatation $\nabla \cdot \mathbf{u}$) become essential. Furthermore, there is no

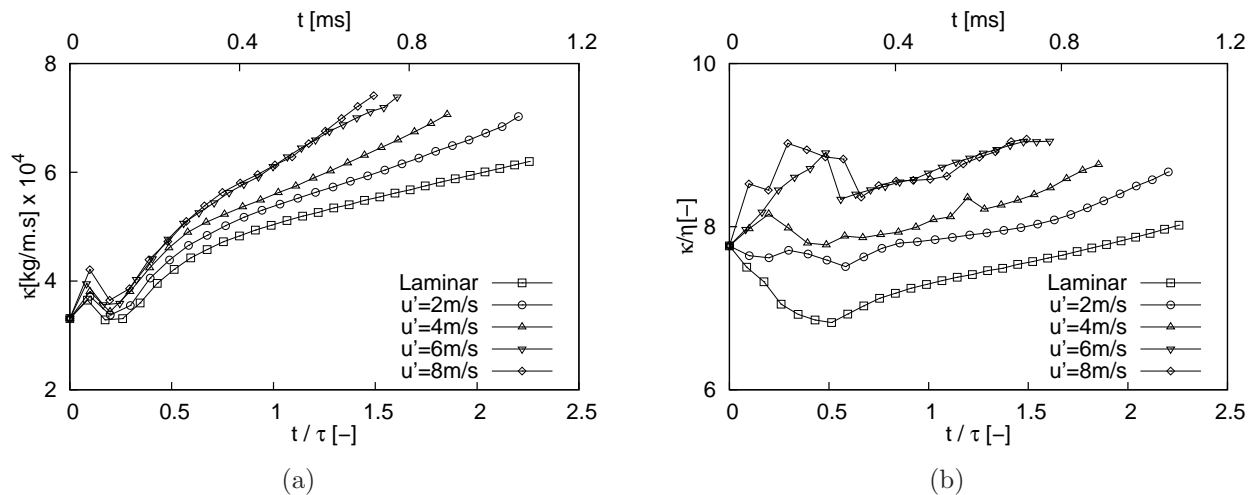


Figure 2.1: Temporal variation of the maximum value of the (a) volume viscosity κ and (b) volume-to-shear viscosity ratio κ/η from the direct simulation of a turbulent stoichiometric premixed hydrogen-air flame using detailed models for various turbulent intensities (lower x -axis), together with the laminar case (upper x -axis)

convincing justification to the claim that $\kappa/\mu \ll 1$ as explained in many introductory fluid dynamics textbooks. This contradiction is discussed further in [23], where the authors investigated the influence of volume viscosity on a laminar planar shock/hydrogen bubble interaction. They demonstrated that κ modifies the whole flow structure and thus recommended its systematic inclusion in reacting flow simulations with compressibility effects.

The main reasons why researchers seldom include the volume viscosity term in computational models may stem from the assumed weak impact of the latter in low Mach number and boundary layer flows. To a larger degree, it is probably a result of the additional computational cost associated with the evaluation of volume viscosity in multi-component mixtures. Finally, an overconfidence in the misleading suggestion of Stokes [23] may have contributed to this systematic evasion. Indeed, the absence of volume viscosity effects in dilute monatomic gases such as Ne [24] is an exception and not a rule [29], since κ also arises noticeably in most dense gases and liquids.

More generally, the need for accurate physical models in practical combustion computations has been demonstrated clearly for various flame configurations (see for example [30, 31] and references therein). The advent of advanced computer technology and the development of efficient computational algorithms have now made it possible to employ such detailed models in the numerical investigation of multi-component, multi-dimensional reactive flows in affordable computing times. Taking into account volume viscosity is therefore possible if necessary. Nevertheless, the influence of volume viscosity is still controversial in the literature [15, 32], since it has been traditionally neglected in almost all turbulent combustion studies up to now. Moreover, studies of the impact of κ on the flame structure while considering only laminar or mild turbulent conditions might lead to biased conclusions since more realistic, higher values of Re_t have seldom been assessed. A systematic quantitative analysis of the influence of κ on the turbulent flame structure burning different fuels and at realistic turbulent values would be of great scientific interest, especially to the combustion DNS and modeling community.

In this thesis, we have therefore considered volume viscosity effects in several DNS computations to further investigate its impact on both laminar and turbulent, premixed and non-premixed flame configurations burning three different fuels. The results are contained in chapter 5. In these computations, the volume viscosity is estimated as follows.

When considering a pure polyatomic gas with a single internal energy mode close to equilib-

rium, the internal energy relaxation time τ^{int} is related to the volume viscosity κ by [33]

$$\kappa = \frac{pR}{c_v^2} c^{int} \tau^{int}, \quad (2.13)$$

where c^{int} is the internal heat capacity. When there are several modes for internal energy and/or several species present in the mixture, the above simple expression is replaced by the solution of a linear system leading finally to the volume viscosity [18]. Within the approximation of Monchick and Mason, neglecting complex collisions with more than one quantum jump, the reduced system is diagonal and typically yields κ by [23]

$$\kappa = \frac{pR}{c_v^2} \sum_{k \in \wp} X_k c_k^{int} \tau_k^{int}, \quad (2.14)$$

where $\wp = 1, \dots, n^p$ is the polyatomic species indexing set. The average relaxation time for internal energy of the k^{th} species τ_k^{int} is expressed as

$$\frac{c_k^{int}}{\tau_k^{int}} = \sum_{m \in \aleph} \frac{c_k^m}{\tau_k^m}, \quad (2.15)$$

where τ_k^m is the average relaxation time of internal energy in mode m for the k^{th} species, and \aleph is the internal energy mode indexing set.

The various methods described above are contained in the *EGlib* transport library [18, 34] for various levels of accuracy and complexity. The cheapest model considers the transport system matrix associated with the internal energy approach while the most expensive model considers the transport system matrix associated with the translational and internal energy approach but uses temperature-dependent ratios of collision integrals and performs a direct inversion in order to evaluate the volume viscosity. All five models are fully discussed in [26].

2.3.2 Diffusion velocities

The diffusion velocities \mathbf{V} , in eq. (2.3) are quite expensive to compute in practical simulations, since one has to accurately compute the binary diffusion coefficients via the diffusion matrix. Below are different levels of approximations found in the literature which are often incorporated into flame solvers [31]:

2.3.2.1 General expression

The diffusion velocity of species i in the mixture is generally expressed as

$$\mathbf{V}_i = - \sum_{k=1}^{N_s} D_{ik} \mathbf{d}_k - D_i^T \frac{\nabla T}{T} \quad (2.16)$$

where D_{ik} is the multicomponent diffusion coefficient of species i into species k and depends on all state variables. This diffusion matrix is symmetric, that is $D_{ik} = D_{ki}$. The mass conservation constraint for the species diffusion velocities reads:

$$\sum_{i=1}^{N_s} Y_i \mathbf{V}_i = 0. \quad (2.17)$$

The vector \mathbf{d}_k is the species diffusion driving force. It takes into account gradients of species concentrations, pressure and the effects of external forces [15, 22, 35]:

$$\mathbf{d}_k = \nabla X_k + (X_k - Y_k) \frac{\nabla p}{p} + \frac{\rho}{p} \sum_{j=1}^{N_s} Y_k Y_j (\mathbf{f}_j - \mathbf{f}_k) \quad (2.18)$$

For the flame solvers presented in Chapter 4 (Sect. 4.4), the pressure induced diffusion is an option. But in most practical cases, baro-diffusion is usually negligible because the Mach number is small and the external forces \mathbf{f}_j are considered to act identically on all species. The resulting expression simplifies to

$$\mathbf{d}_k = \nabla X_k. \quad (2.19)$$

In eq.(2.16), D_i^T is the thermal diffusion coefficient of species i , while the combined term $D_i^T \nabla T / T$ is the so-called Soret or thermo-diffusion effect, which accounts for the diffusion of mass due to temperature gradients. This phenomenon is responsible to drive light species towards hot regions and heavy ones towards cold regions in a reacting flow [15, 36]. It is considered to be of significant importance in situations where light radicals such as H or H₂ often present in hydrogen combustion play a significant role. Otherwise, this term is generally ignored due to its relatively high computational cost. It is coded as an option in the tools used for this thesis work and except otherwise stated, it is considered for all hydrogen flame computations.

Due to the fact that the kinetic theory does not give explicit expressions for the transport coefficients, the diffusion matrix is often expanded into convergent series, using the Stefan-Maxwell-Boltzmann equations together with some general assumptions [18, 26, 32]. As such, different levels of approximations of the transport properties are available, depending on the truncation order.

2.3.2.2 First-order approximation

A first-order approximation, which is derived by keeping the first two terms of the series leads to the most accurate transport model used in practice for the binary diffusion coefficients [15, 32]. Here, cross-diffusion, Soret and Dufour effects are accounted for. For detailed flame computations, the resulting global computational cost is still acceptable [31].

2.3.2.3 Hirschfelder-Curtiss approximation

According to this zeroth-order approximation [35], a mixture averaged diffusion coefficient, D_i^* for the species i is given as

$$D_i^* = \frac{(1 - Y_i)}{\sum_{k=1, k \neq i}^{N_s} \frac{X_k}{\mathcal{D}_{ik}}}, \quad (2.20)$$

where \mathcal{D}_{ik} is the binary diffusion coefficient which depends only on species pair properties, pressure and temperature. It is equivalent to keeping only the first term of the series expansion of the multicomponent diffusion matrix [15]. In general, this model does not consider cross-diffusion effects. Here, for mass to be conserved, the diffusion velocity \mathbf{V}_i for species i is divided into a predictor \mathbf{V}_i^* and a corrector \mathbf{V}_c term. Using eq. (2.19), we have that

$$\mathbf{V}_i = \mathbf{V}_i^* + \mathbf{V}_c; \quad \mathbf{V}_i^* = -D_i^* \frac{d_i}{X_i} = -D_i^* \frac{\nabla X_i}{X_i}; \quad \mathbf{V}_c = -\sum_{k=1}^{N_s} Y_k \mathbf{V}_k^* \quad (2.21)$$

This approximation level is the classical one used in our solvers and in most practical combustion codes, with the corresponding fluxes expressed as

$$Y_i \mathbf{V}_i = -D_i^* \frac{W_i}{\overline{W}} \nabla X_i \quad (2.22)$$

2.3.2.4 Fick's law approximation

A much more simplified way to express the diffusion velocities is given by (see [31] and references therein):

$$Y_i \mathbf{V}_i = -D_i \nabla Y_i \quad (2.23)$$

When all the D_i are not equal, mass conservation is again violated and a correction velocity is then required.

2.3.2.5 Lewis number approximation

The Lewis number Le_k of species k compares the thermal diffusivity of the mixture and mass diffusivity of the species. When this number is assumed to be constant, then the diffusion coefficient of species k can be expressed as

$$D_k = \frac{\lambda}{\rho C_p Le_k} \quad (2.24)$$

where λ is the mixture-averaged thermal conductivity. When all Le_k values are not equal, a correction velocity is again necessary to ensure mass conservation.

2.3.2.6 Unity Lewis number approximation

In simple cases, the Lewis number can be assumed to be unity, whereby each species is considered to have the same diffusion coefficient as heat. Though this approach is very simple to implement and is widely used in turbulent flame solvers, large differences are noticeable on the flame structure and properties when compared to results where more realistic transport models are used.

2.3.3 Heat flux

The heat flux vector is given by the generic expression for multicomponent flows [8, 13–15]:

$$\mathbf{q} = -\lambda' \nabla T + \sum_{k=1}^{N_s} (\rho h_k Y_k \mathbf{V}_k) + \mathbf{q}_r - p \sum_{k=1}^{N_s} (D_k^T d_k) \quad (2.25)$$

where λ' is the partial thermal conductivity, which is different from the usual thermal conductivity λ [18]. The diffusion of heat is due to temperature gradients (first term), mass diffusion (second term) and the Dufour effect (last term). The third term \mathbf{q}_r , corresponds to the gas radiative heat flux vector, which has not been considered in this work, even though it might be important in many combustion applications. When thermal diffusion effects are neglected, λ' coincides with λ , such that (also ignoring the last term in (2.25))

$$\mathbf{q} = -\lambda \nabla T + \sum_{k=1}^{N_s} (\rho h_k Y_k \mathbf{V}_k) \quad (2.26)$$

This is the equation implemented in our code.

2.4 Chemistry models

Chemistry effects can be added in a flow by several different ways. The first and simple technique is the so-called *single-step-chemistry* in which the chemical kinetics is summed up in one global irreversible equation. In opposition to this simple case, the most costly method is the so-called *complex chemistry mechanism* where all the species in the chemical scheme being used are taken into consideration. There are also *classical reduction techniques* where only a selected number of species and reactions are retained from a given complete mechanism. Such a reduction scheme falls between the previous two. In addition to these, there are also interesting alternatives like

the so-called *chemistry tabulation techniques*, in which the chemical kinetics is computed *a priori* and stored up in look-up tables.

All these chemistry models and reduction techniques have a common measuring rod as far as the description of the elementary chemical reaction kinetics is concerned. In other words, the rate coefficients are generally based on an Arrhenius law [8]:

$$k = \mathcal{A}T^\beta \exp\left(-\frac{E_a}{RT}\right) \quad (2.27)$$

with \mathcal{A} , β and E_a being the pre-exponential factor, a temperature dependent coefficient and the activation energy, respectively. These constants are all reaction-dependent and are usually determined experimentally.

2.4.1 Single-step mechanism

A mechanism is considered to be single-step when all the intermediary radicals in the detailed chemical kinetics scheme disappear and the kinetics of the burning process is represented by a single global reaction:



where F represents the fuel, O the oxidizer and P the product. In such a relation, only the major species are represented. Even though such a crude approximation of the chemical kinetics is sufficient for theoretical studies (for example when overall characteristics of a flame such as the laminar flame speed are sought for), it is too simple to describe all the chemistry taking place in a reacting flow system. Nevertheless, it proves to be a good compromise between qualitative results and computing time, and it is still being used in some very expensive DNS, LES and RANS codes [37, 38].

2.4.2 Complete mechanism

A complete mechanism (also called complex chemistry) corresponds to a chemical scheme where all chemical kinetic processes are being taken into consideration. Here, no simplification is introduced and an equation is solved explicitly for each and every chemical species present in the chemical scheme, simultaneously with the Navier-Stokes equations. Unlike the single global reaction strategy where only the major species is predicted, combustion processes result in the formation of various intermediate species. For a chemical scheme comprising N_s species, these so-called elementary reactions are modeled by

$$\sum_{i=1}^{N_s} \nu'_{ij} \Omega_i \rightleftharpoons \sum_{i=1}^{N_s} \nu''_{ij} \Omega_i, \quad j \in [1, N_r] \quad (2.29)$$

with N_r the number of elementary reactions and Ω_i a symbol for the i^{th} species. ν'_{ij} and ν''_{ij} denote respectively, the number of molecules of type i that are consumed and produced with the elementary reaction j , with the following molar stoichiometric coefficient relation:

$$\sum_{i=1}^{N_s} \nu_{ij} W_i = 0, \quad j \in [1, N_r] \quad (2.30)$$

where $\nu_{ij} = \nu'_{ij} - \nu''_{ij}$. The resulting reaction rate of progress for reaction j is the difference between the forward and backward rates, given by

$$r_j = k_{fj} \prod_{i=1}^{N_s} n_i^{\nu'_{ij}} - k_{bj} \prod_{i=1}^{N_s} n_i^{\nu''_{ij}}, \quad j \in [1, N_r] \quad (2.31)$$

where $n_i = \rho Y_i / M_i$ denotes the molar concentration of species i while k_{fj} and k_{bj} are respectively, the forward and backward reaction coefficient/constants of reaction j , expressed as usual via the Arrhenius law (eq. (2.27)). Finally, the mass reaction rate or chemical source term of species i is given by taking the sum of all contributions from the elementary reactions:

$$\dot{w}_i = M_i \sum_{j=1}^{N_r} \nu_{ij} r_j, \quad i \in [1, N_s] \quad (2.32)$$

In practical simulations for which complex chemistry is employed, the chemical scheme has to be given, implying that the knowledge of all the species, reactions and Arrhenius constants must be available. These constants are commonly listed in so-called combustion reaction mechanism, of which the *chemkin* format [39] has become a global and practical standard.

For the numerical simulations of practical reacting flows, the use of such complex chemistry is too demanding, since large reaction mechanisms contain a large number of species and elementary reactions. For instance, typical hydrogen kinetic schemes require around 9 species and over 30 elementary reactions. Lower hydrocarbons require schemes typically around 50 species and a few hundred chemical reactions. Since a transport equation is solved for each and every chemical species in order to describe properly and accurately the combustion process, the induced numerical cost in terms of computing time and memory requirements become indeed huge and prohibitive. These limitations become more significant if we want to move from one- to multi-dimensional simulations, which of course are more instructive. For these reasons, calculations with complex chemistry are often obtained and used mainly for the validation of simpler or reduced chemical kinetics models, as well as for the understanding of the detail structure of a flame. In this thesis, direct simulations of turbulent flames have been carried out using detailed chemical kinetic schemes for hydrogen (H₂: 9 species, 38 elementary reactions) [40, 41], syngas (CO/H₂: 13 species, 67 elementary reactions) [42] and methane (CH₄: reduced scheme with 16 species, 50 elementary reactions) [43] oxidation. For completeness, we have listed explicitly the reaction mechanisms using a prescribed format, along with the values of \mathcal{A}_j , β_j and E_j in Appendix A.

To recapitulate the previous two sections, we have seen that on the one hand, a *single-step mechanism* is simple and practical, yet plagued with the inability to depict correctly the complete burning process, and on the other hand, the *complex mechanism* is on its own too demanding for use in practical combustion applications or parametric studies. Model reduction techniques are therefore useful to establish the best compromise between these two extremes and at the same time being able to generate chemical schemes which give accurate and satisfactory results. In the following sections, we discuss briefly some of the available techniques and pathways leading to reduced chemical kinetic schemes.

2.4.3 Reduced chemical kinetics schemes

There exist three main classical techniques involved in the reduction of complete mechanisms into either a *detailed mechanism* or a *semi-global mechanism*. These are the quasi-steady state assumption, the partial equilibrium assumption and sensitivity analysis.

1. The quasi-steady state assumption relies on the fact that the production and consumption rates of some very reactive intermediary species are equal. Hence the computation of corresponding intermediate radicals can be replaced by implicit relations.
2. The partial equilibrium relies on the fact that an assemble of reversible elementary reactions' forward and backward movements can be so fast that one obtains a partial equilibrium for these. As such direct algebraic relations are derived and the concentrations of these species are obtained by them.

3. Sensitivity analysis seeks to identify the rate-limiting reaction steps.

The first level of reduction stemming directly from the *complete mechanism* leads to a so-called *detailed mechanism*. It corresponds to the case where the complexity of the chemical processes have been reduced on purpose, while keeping all the main chemical pathways corresponding to imposed or solicited conditions. On a whole, at least 50-20% of the species present in the *complete mechanism* are retained.

From the *detailed mechanism*, further reduction leads to a *semi-global mechanism*, which usually considers less than five reactions involving 5-10 species, neglecting most chemical pathways.

When carefully derived, these reduced mechanisms provide a rather good estimation of the reaction rate of the flame and the major species are well captured.

2.4.4 Tabulated chemistry

Up to this point, we have outlined two principal approaches of simplifying the chemical kinetics encountered in reacting flows. The first one was the single-step approach, currently used for many theoretical studies and in expensive DNS calculations. In this model, one need not determine *a priori*, a detailed chemical mechanism. In the second approach – the chemical approach – one needs a thorough knowledge of the different chemical reactions involved, before considering quasi-steady state, partial equilibrium or sensitivity. Here, we introduce a third approach, the chemistry tabulation technique, with most models based on a mathematical analysis of the dynamical system.

Tabulated chemistry reduction techniques are the most recent development in the field of mechanism reduction, originally derived from considerations already used in dynamical system theory. They offer an attractive and promising alternative to complete reaction schemes and do serve as a smart means of introducing effects of complex chemistry phenomena in reacting flow computations. A number of prominent complex chemistry tabulation techniques have emerged in the course of the last two decades with a variety of published methods. For instance the In-Situ Adaptive Tabulation (ISAT) technique [44] is a very accurate chemistry tabulation technique. A chemical database is constructed from the direct solving of the time evolution of the species compositions and tabulated at run time and restricted to the actually accessed part of the composition space. Another example is the Intrinsic Low Dimensional Manifold (ILDM) technique [42], which is based on a local study of the characteristic times of the dynamical system associated with the reactive mixture. More recently, the Flamelet Generated Manifold (FGM) [45] and/or the Flame Prolongation of ILDM (FPI) [10] have been developed and lead finally to similar chemistry tabulation techniques. More details will be presented later on.

2.5 Summary

In this chapter, the most general mathematical formulation of a reacting flow system has been presented, consisting of the five classical Navier-Stokes equations together with a transport equation for each chemical species involved. The flow is assumed to be Newtonian and one that obeys the ideal gas properties. As such, practical constitutive relations are then established. Appropriate transport models for viscosity, species diffusion and heat flux are outlined. For the chemistry, a range of approaches on how to include chemical kinetics into the flow are stated, starting from the most accurate but expensive complex chemistry paradigm to the most simple but unpredictive models. Within this two extremes, reduced techniques can be derived, with the most promising alternative being perhaps the complete chemistry tabulation techniques, on which the following chapter is dedicated. Some of the presented models are preferred over others depending on the level of accuracy and computational resources available. To glean fundamental

insight into fine-grain turbulence–chemistry interactions, pollutant emissions, ignition/extinction phenomena, etc., studies with complex chemistry together with multicomponent transport models are usually mandatory. On the other hand, for theoretical studies such as when only general trends and characteristics of a flame are needed as in stability computations, single-step chemistry often stands out as a good compromise between quality and computing time.

Model reduction

3.1 Introduction

Complete or complex chemical mechanisms as pointed out in the previous chapter, constitute the most appropriate model for reacting flows. Here, no simplification is introduced and an equation is solved explicitly for each and every chemical species present in the chemical scheme in question, simultaneously with the classical five Navier-Stokes equations. Though being the most accurate technique, its use in the simulation of practical installations or for parametric studies is often too demanding, since large reaction mechanisms contain hundreds of species with thousands of elementary reactions and rapidly lead to unacceptable computing costs [10, 31, 46, 47]. For more realistic configurations (complex three-dimensional geometry), or when systematic studies are required (long physical times, several simulations, realistic Reynolds numbers, etc.), such computations remain completely impossible at present, even with the advent of petascale computing. There is therefore an urgent need for suitable model reduction.

Calculations with complex chemistry are obtained and used mainly for the validation of simpler or reduced chemical kinetics models, and also for the understanding of the detailed flame structure. In particular, it is very important to identify models that will simplify the numerical description of the reacting process, while preserving the coupling between chemistry, heat transfer and fluid dynamics in a quantitative manner. For instance, tabulated chemistry reduction techniques, which are the most recent development in the field of chemical kinetics reduction constitute a vital alternative to the direct use of complex reaction schemes in DNS flow solvers. Tabulated chemistry typically leads to one or two orders of magnitude reduction in computing time compared to a complete reaction scheme.

A non-negligible level of reduction could also be derived from the choice of the numerical method. With that in mind, it is easily spotted that most applications of interest, such as for example furnaces and boilers, but also inside the combustion chambers for automotive or aeronautical/ aerospace applications operate generally at quite small Mach number, at least in the region where combustion takes place. It is then unnecessary and inefficient to employ a fully compressible formulation to investigate numerically such configurations. The low-Mach number approximation allows an important speedup [48], since the stability restrictions associated in particular with the Courant-Friedrichs-Lewy condition are practically released. Moreover, the equations are considerably simplified since several viscous terms become negligible, in particular in the energy equation [49].

Thanks to these two compatible reduction approaches, a strong reduction of computing times for full three-dimensional direct simulations of turbulent flames is thereby obtainable by combining the low-Mach number approach (well suited to most configurations), with the accurate FPI reduction technique for the chemistry [50].

In the following section (3.2), a brief and non-exhaustive listing of published complex chemistry tabulation techniques are presented, followed by a step-by-step description, (with as much details as possible) of the generation and implementation of both the classical and proposed advanced FPI technique in Sect 3.4. Among other intrinsic issues, the choice of the most appropriate species (combination) for the table coordinate and the most efficient grid structure for information storage are discussed. The functionality of the chemical databases is discussed after motivating and proposing suitable modifications towards the advanced FPI, aimed at tackling flames for which mass diffusivity along iso-equivalence ratio surfaces is important. In Sect. 3.5, the low-Mach number formulation is additionally described. DNS results computed using the combined reduction techniques in a single solver will be presented in later.

3.2 Brief overview of chemistry tabulation techniques

Below is a non-exhaustive list of some of the available complex chemistry tabulation methodologies.

3.2.1 Computational Singularity Perturbation (CSP)

The CSP method is based on computational singularity perturbation techniques with the aim of developing explicit reduced mechanism by separating chemical time-scales into fast and slow subspaces [51]. It reduces the numerical stiffness of the chemical schemes. The CSP approach is advantageous in that it is automatic and very accurate. Furthermore, it delivers a reduced chemical scheme and not only tabulated data. Nevertheless, its applicability as a reduction technique in complex simulations is prohibitive due to its relatively heavy computational cost.

3.2.2 In-Situ Adaptive Tabulation (ISAT)

In many reduction methods, the database is generated in a pre-processing step. In the ISAT [44] technique, the chemical database is generated at run time. The size of such an in-situ created database is restricted to the actually accessed part of the composition space. This is a major advantage. Another merit of this technique is that the accuracy of the reduced mechanism is directly controlled by a so-called error control. Though highly accurate, fast and light, its implementation on a parallel distributed memory system is non-trivial, and the obtained speed-up is often disappointing.

3.2.3 Intrinsic Low-Dimensional manifold (ILDM)

The ILDM technique [42] is based on a local study of the characteristic time scales of the dynamical system associated with the reactive mixture. When an attracting manifold (which corresponds to a description of the complete reaction system by a smaller number of coordinates) is identified, it is tabulated and later on used in the flow simulation. The resulting look-up table makes available all the species during the simulation, even though only the equations corresponding to the table coordinates are actually solved. The method has been properly validated with CO/H₂/O₂ flames. For methane or hydrocarbon combustion, there are limitations in that the low temperature regions (where there are fast chemical times) cannot be fully captured with a reduced number (say 3) of coordinates and up to 100% error were sometimes observed for the laminar flame speed [10].

3.2.4 Flame(let) Prolongated ILDM (FPI)

In an attempt to develop a solution for a proper representation of the burning process in the low temperature region for the combustion of hydrocarbon fuels, which was a major setback of the promising ILDM technique outlined above, the FPI [10] chemistry tabulation technique was born. In this technique, the chemical kinetics is described by an ensemble of one-dimensional laminar premixed flames for different mixture compositions. Though void of a thorough mathematical backing, this technique eliminates the difficulties encountered when using the classical ILDM method. Moreover, the tabulation technique of the classical ILDM method is preserved, with the dimensions of the resulting database remaining very small, irrespective of the chemical kinetic scheme used.

The FPI method has already been applied with great success in the study of auto-ignition phenomena [52], premixed laminar flames [10], non-adiabatic partially premixed laminar flames [53], non-adiabatic turbulent premixed reactive flows [54], in the DNS of premixed turbulent V flames and as a SGS description of chemistry for the LES of ducted flames [55]. In combination with a presumed PDF of the progress variable, FPI has also been used for RANS studies of piloted premixed turbulent flames [56].

Section 3.4 of this chapter is dedicated to the FPI approach, where an advanced approach taking into account detailed transport is proposed, with a detailed account of the different steps involved in its generation and implementation for use with direct simulations of turbulent flames.

3.2.5 Flamelet Generated manifold (FGM)

The FGM method [57] is closely similar to the FPI technique in that the chemical kinetics is also described by an ensemble of 1D laminar premixed flame[let]s. The original subspace covered by the FGM method is (h, Y_c) and allows the modeling of non-adiabatic flames while that for the original FPI covered the (Y_c, Y_z) subspace and treat flames with various mixture fractions. All these terms will be defined in the subsequent sections. It should be noted that both the FGM and FPI have been improved to cover the (Y_c, Y_z) (2D) and (Y_c, Y_z, h) (3D) subspaces, respectively.

A good number of other reduction techniques can be found in the literature, such as the Rate-Controlled Constraint Equilibrium (RCCE) [58] method, which is based purely on thermodynamics. They are not discussed further here.

3.3 Attributes of a good chemical look-up table

For a chemistry tabulated reduction technique, the efficiency and usability has to go beyond the mere reduction itself. The following issues must be considered *a priori*:

1. The information storage structure of the database must be optimized.
2. The procedure for information retrieval from the database must be optimized. That is, the CPU time needed to retrieve a stored value must be minimal.
3. The accuracy of the retrieved value has to meet specific criteria.
4. The required memory needed to store all the desired data must be affordable.

These criteria and more will be examined for the case of the classical and advanced FPI technique in the following section.

3.4 FPI complex chemistry tabulation

The basis of FPI [10] consists of relating all flame quantities (species mass fractions, temperature, density, etc) to a single progress variable Y_c , which quantifies the transition between fresh and fully burnt products. This is for a given equivalence ratio of the gas mixture under consideration. We therefore have to tabulate an ensemble of one-dimensional laminar premixed flames and in this work, we will be working mostly with freely propagating laminar premixed flames. The second coordinate, Y_z depicts the local gas mixture fraction, and it is a function of the equivalence ratio Φ . So for a given Φ (Y_z), the progress variable Y_c of the flame under consideration evolves between the pure unreacted mixture ($Y_{c,min}$) and the equilibrium values ($Y_{c,max}$). The *chemkin* [39, 59, 60] complex chemistry flame solver is used to compute this spectrum of one-dimensional premixed laminar flames, used as raw data for the FPI chemistry database generation and tabulation.

3.4.1 One-dimensional premixed flame computations

The example considered here is a one-dimensional premixed freely propagating methane-air (CH_4/air) flame, varying Φ . For a stream tube of section surface A , such a flame is governed by the following equations:

$$\dot{m} = \rho u A \quad (3.1)$$

$$\dot{m} \frac{dT}{dx} - \frac{1}{c_p} \left(\lambda A \frac{dT}{dx} \right) + \frac{A}{c_p} \left(\sum_{k=1}^{N_s} \rho Y_k V_k c_{pk} \right) \frac{dT}{dx} + \frac{A}{c_p} \left(\sum_{k=1}^{N_s} \dot{\omega}_k h_k W_k \right) = 0 \quad (3.2)$$

$$\dot{m} \frac{dY_k}{dx} + \frac{d}{dx} (\rho A Y_k V_k) - A \dot{\omega}_k W_k = 0; \quad k = 1, \dots, N_s \quad (3.3)$$

The solution of the above system of equation yields the mass flow rate \dot{m} , temperature $T(x)$ and the mass fractions $Y_k(x)$ of all the species in the chemical mechanism employed. The fresh mixture species composition at an initial temperature is required for initialization, together with a boundary condition such as a fixed temperature at a given point of the grid, in order to fix the flame front. This helps to find a corresponding mass flow rate that leads to laminar flame speed S_L . It should be noted that the evolution of this system from fresh to burn gas is isenthalpic, and under the unity Lewis number assumption ($Le = 1$), it can be associated to a constant enthalpy level. In fact, such an assumption is needed since the local differential diffusion of species in the flame front region may be different, leading to enthalpy variations.

Hence, for a given Φ , the corresponding flame covers the whole range of Y_c from $Y_{c,min}$ to $Y_{c,max}$. Varying Φ results in a collection of one-dimensional laminar premixed flames and as such, we can cover the whole $(Y_z(\Phi), Y_c)$ space.

Basically, there are six steps involved in using *chemkin* to solve a typical chemical process model problem like the one above ((3.1)-(3.3)). Details of the various steps are outlined elsewhere [61]. A number of detail chemical mechanism such as the GRI 1.2 [62] scheme (involving 21 species and 300 elementary reactions), the Lindstedt [63] scheme (involving 29 species and 300 elementary reactions), etc. were employed together with their corresponding thermodynamics and transport data files.

From *chemkin*, the solution columns corresponding to the mass density, net heat released, temperature and all the mass fractions are exported for further post-processing for instance with *tecplot* [64]. So we end up with a raw solution data file of $(3 + N_s)$ columns, where N_s is the total number of species involved in the chemical reaction mechanism employed in the calculations.

3.4.2 Database implementation

First and foremost, a couple of issues need to be decided on how we want to store the 1D flame data in order to have easy access to it when needed. The table coordinates through which informations within the database will be accessed must be appropriately chosen, together with the choice of the most convenient and efficient data structure and search algorithm. Here, we explicate on these intricate attributes of look-up tables, in particular for FPI tables. We consider a table with two coordinates in what follows. Extension to higher dimensional tables is cumbersome but straight forward.

3.4.2.1 Choice of table coordinates

With the help of a small FORTRAN subroutine¹, the raw solution is read and then re-arranged into a more practical format for further analysis with/in *tecplot*. The resulting solution file contains two additional columns – the first two – which are the mass fractions (or a linear combination of mass fractions) of the species that we wish to use as the FPI table coordinates.

Though the choice of the mass fractions to be used as coordinates is arbitrary in principle, some caution is required [53]. The FPI database is intended to be a look-up table, whose values are accessed from the given coordinate values. So there must be a one-to-one mapping constraint on the mass fractions of any species which must be used as a coordinate, especially for the progress variable Y_c , which must be monotonic (in order to keep continuous track of the reaction) and a good representative of the global chemical process. In other words, any species which evolves slowly/regularly and in a monotonic way is a suitable candidate for the job.

The Y_z coordinate, which takes care of the correct description of the mixing, must be a (linear combination) of non-reactive species. Under the unity Lewis number hypothesis, the mass fraction of N_2 is constant for a given flame mixture composition. Hence Y_{N_2} is readily used to represent the local mixture composition coordinate (Y_z) in classical FPI tables. It should be noted that the value of Y_{N_2} is directly related to the equivalence ratio Φ [10, 53]. Therefore, given the equivalence ratio of the reactive mixture, we have, along the corresponding vertical line (see Fig. 3.1(a)), data points corresponding to the kinetics of the combustion ranging from the fresh ($Y_{c,min}$) to the burnt ($Y_{c,max}$) gas mixture.

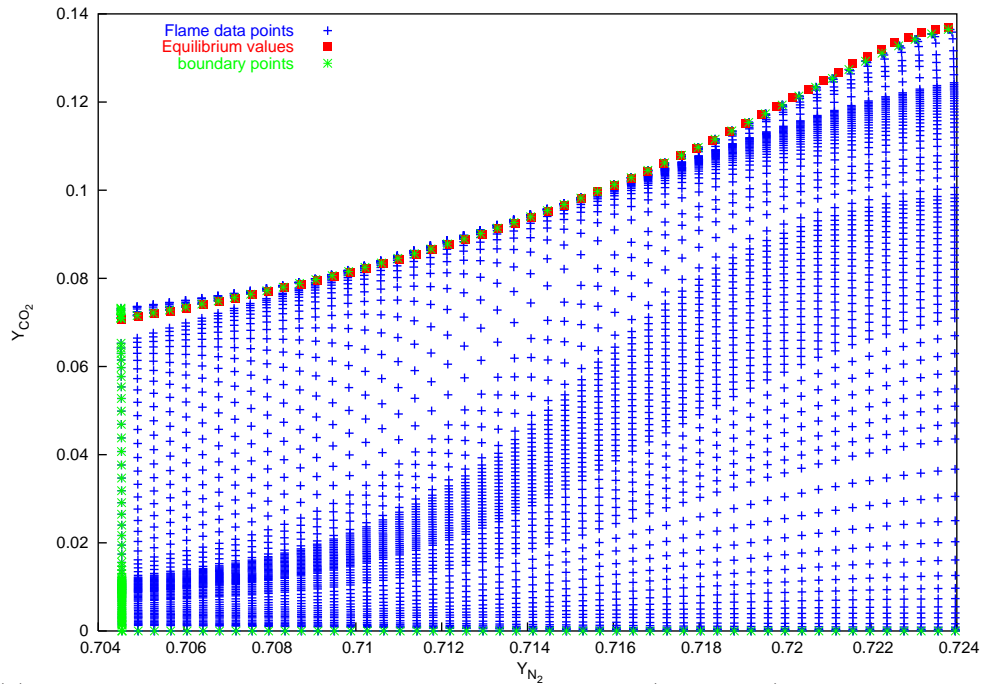
The original FPI table [10] used $Y_c = Y_{CO_2}$ (for methane or general hydrocarbon combustion) or $Y_c = Y_{H_2O}$ (for hydrogen combustion) as the reaction progress variable. It works well if one were to compute only lean flames. The monotonic constraint is violated for some tabulated quantities at higher equivalence ratios. Figure 3.1(a) shows a zoom of the flame points on the (Y_z, Y_c) space around the rich flames ($\Phi > 1$). The equilibrium points (red squares) are seen to be sometimes lower than the last flame points! Further more, a projection of the flame points on the (Y_{CO_2}, T) subspace for different Φ (see Fig. 3.1(b)) reveals that the bijectivity of the temperature profiles gives way as we move towards higher values of Φ , with clearly observed turning points. This is unacceptable and confirms the previously observed behavior.

Such an unexpected behavior of methane combustion for rich conditions at high temperature has its explanation rooted in the fact that, under such conditions, CO_2 readily decomposes into CO [53]. With such knowledge, a linear combination of the mass fractions of CO_2 and CO will therefore be a good candidate for the progress variable [53]:

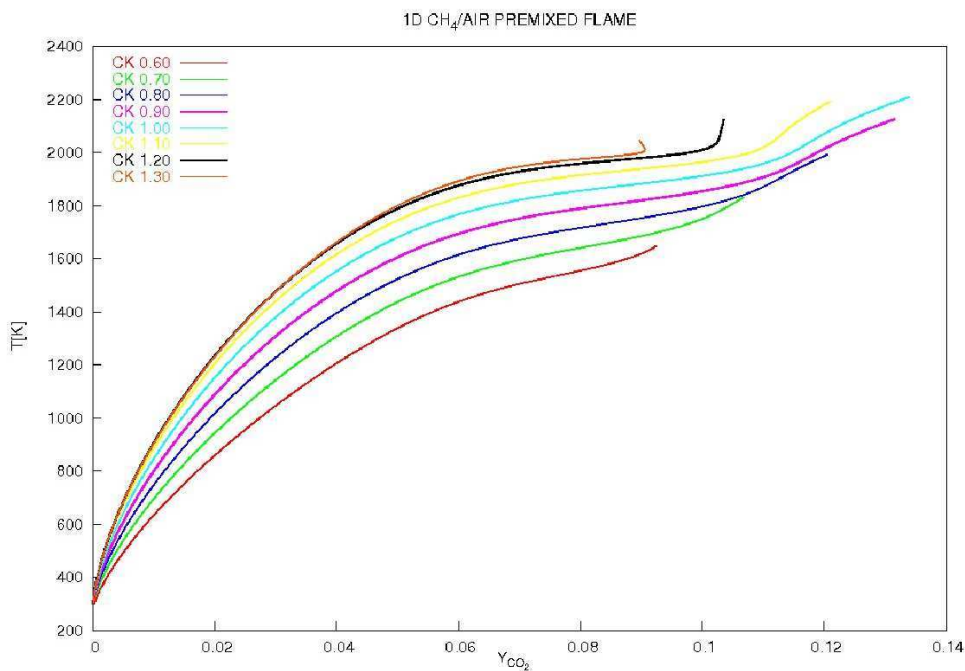
$$Y_c = Y_{CO_2} + \alpha Y_{CO}; \quad \alpha \geq 0 \quad (3.4)$$

According to eq. (3.4), the previous case then corresponds to $\alpha = 0$. In the second generation of FPI tables [53], $\alpha = 1$ was proposed and used in an effort to correct the previously observed problem. We went further to develop a tool to systematically vary the value of α so as to get an

¹freely available upon request



(a) Zoom on the projection of the flame points on the (Y_{CO_2}, Y_{N_2}) space around the rich flames ($\Phi > 1$, low Y_{N_2}). Note that the equilibrium points (red squares) are seen to be sometimes lower than the last flame points



(b) Temperature profiles versus the progress variable Y_c for different Φ (0.6 – 1.3). Note the turning points on the profiles at high temperature ($T > 1800\text{K}$) under rich mixture compositions

Figure 3.1: One-dimensional freely propagating laminar premixed methane-air flames with the progress variable $Y_c = Y_{CO_2}$ and the mixture coordinate $Y_z = Y_{N_2}$ for $0.54 \leq \Phi \leq 1.55$ (corresponding to $0.703 \leq Y_{N_2} \leq 0.744$)

optimal value and $\alpha = 1$ gave indeed the best value. With this value, 99% of the above problem was solved. Fig. 3.2(a) shows a projection of the corresponding scattered flame points of a series of one-dimensional freely propagating laminar premixed $\text{CH}_4/\text{N}_2/\text{O}_2$ flames for $0.54 \leq \Phi \leq 1.55$ (corresponding to $0.703 \leq Y_{N_2} \leq 0.744$) on the (Y_z, Y_c) subspace, using the GRI 1.2 detailed

chemical kinetics mechanism. Each vertical set of points (blue markers) constitute a single flame, covering the entire Y_c range from the fresh gas mixture ($Y_{c,min}$) to chemical equilibrium ($Y_{c,max}$) within the flammability limits of a given Y_z value. The points in green define the table boundaries. The rich and lean flammability limits of this flame correspond to $Y_z = Y_{N_2} = 0.703$ ($\Phi = 1.55$) and $Y_z = Y_{N_2} = 0.744$ ($\Phi = 0.54$). The step in equivalence ratio is $\Delta\Phi = 0.01$, resulting in 102 1D flames. Fig. 3.2(b) shows a projection of the flames on the (Y_c, T) subspace for different Φ . These modifications by using $\alpha = 1$ overcome the turning point problem to an acceptable extent in practical applications.

3.4.2.2 Choice of data structure

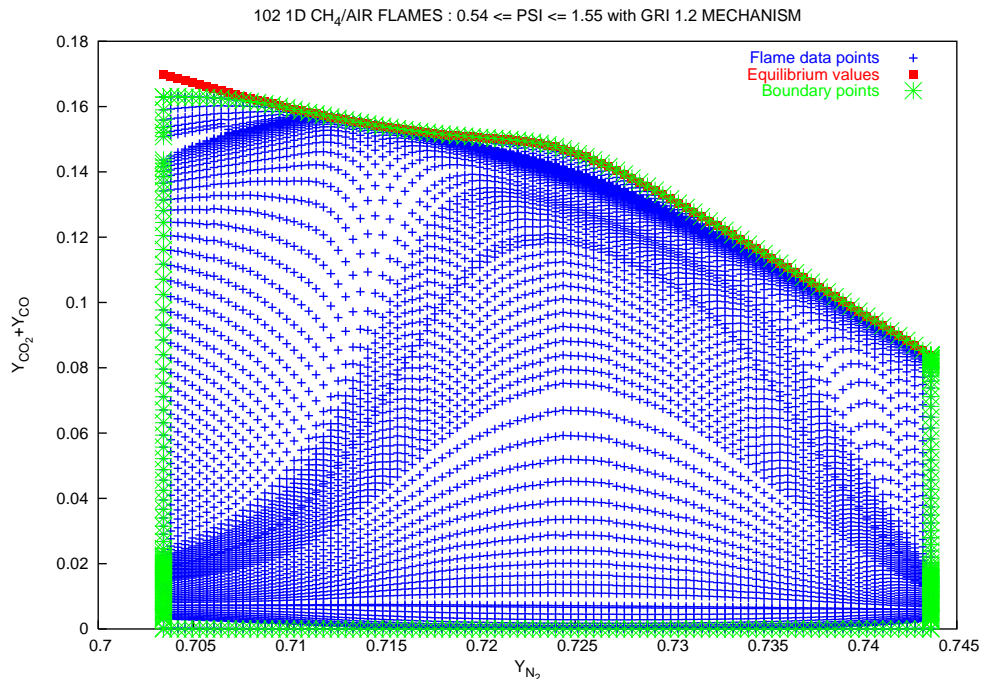
The flame data points, as shown on Fig. 3.1(a) and 3.2(a) are usually irregular along Y_c and are dictated by a proper resolution of the flame front. To be able to walk efficiently within the database, we need to determine not only the right gridding and/or meshing strategy but also one whose quality will be ideal and optimal in the implementation of an appropriate data structure for the tabulation and retrieval of information to and from the resulting database.

Classical FPI tables are built on a triangular grid (tetrahedral grid in 3D), as illustrated in Fig. 3.3. To achieve this, we use triangulation, which is a process that connects data points to form triangles. The triangulation is realized with/in *tecplot*, where we convert the irregular, I-ordered data sets into a finite-element surface zone. We therefore have N_t triangles, with each triangle made up of three nodes (vertices) and three neighbors. The data structure used for the information storage and retrieval is as follows:

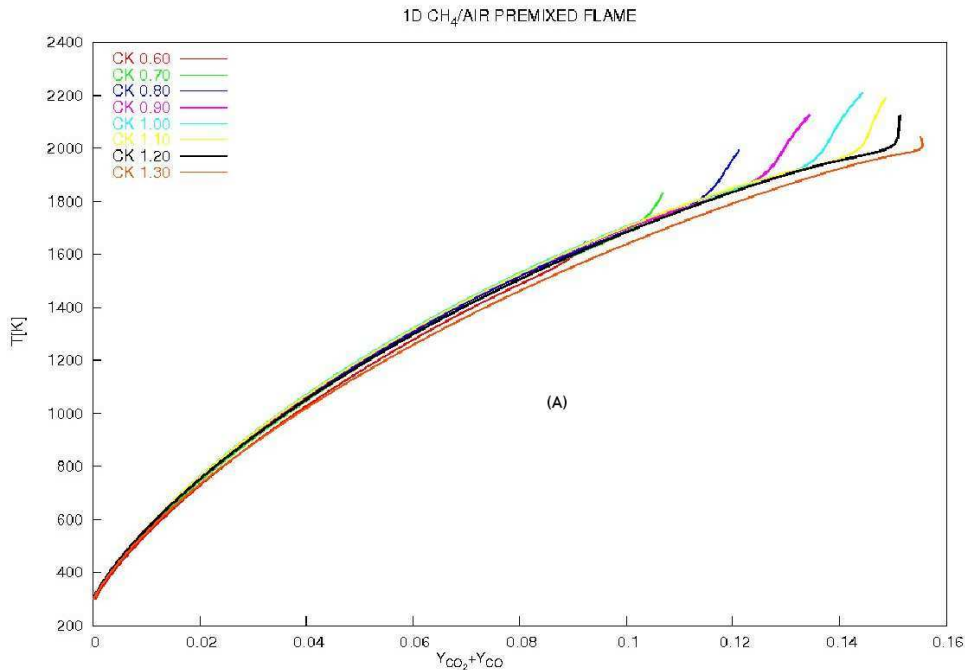
1. Each node in the triangulation has a unique identity (ID), which is an integer value.
2. Each of the N_t triangles has a unique ID, which is an integer value.
3. Each triangle contain information about the coordinates of its three vertices.
4. Each triangle knows the ID of its three neighbors and their common vertices (nodes).
5. Each node stores all possible thermo-chemical data (e.g., T , ρ , Y_i , etc.).

With the above construct, each vertex therefore contains all tabulated information. A targeted point within the database is then sought for by traversing/searching the table via its triangles, using neighbors information. When a triangle harboring a target point is located, the desired value is then approximated (in a multi-linear fashion) from the corresponding values stored in its vertices. The table is equally constructed to react decently to points that fall outside the database domain. The search and interpolation techniques are discussed in more details in [10, 53]. Even though a good triangulation with a good search algorithm is crucial for computational time speedup, we recently observed in a couple of direct simulations of turbulent flames using the FPI tabulated chemistry constructed on a triangular grid that a non negligible amount of computing time is spent in the database search routines. In the quest for a shorter resident time within the table via a more efficient gridding strategy, we tested if it is possible to transform an unstructured triangular grid into a structured rectangular grid, on which the desired thermo-chemical data is projected and stored. This is demonstrated on the sketches shown in Fig. 3.4.

In the first place, we create a rectangular grid (within *tecplot*) of $(N_x \times N_y)$ grid points, where N_x and N_y are the number of grid points in the horizontal and vertical directions, respectively, as illustrated in Fig. 3.4(a). Though N_x and N_y are free parameters, the choice of their actual values should be closely guided by the current 1D flame computations parameters. All things being equal, the number of flame data points N_p , along Y_c should be the same for all the 1D flames. Therefore, N_y should be at least equal to N_p . An N_y value slightly greater than N_p will



(a) Projection of the flame points on the (Y_z, Y_c) subspace. Each vertical set of points (blue markers) constitute a single flame, covering the entire Y_c space from the fresh gas mixture ($Y_{c,min}$) to chemical equilibrium ($Y_{c,max}$) within the given Y_z flammability limit. The square (red markers) points are the corresponding equilibrium values while the green markers define the table boundaries



(b) Profiles of temperature versus progress variable Y_c for different Φ (0.6-1.3)

Figure 3.2: One-dimensional freely propagating laminar premixed methane-air flames with the progress variable $Y_c = Y_{CO_2} + Y_{CO}$ and the mixture coordinate $Y_z = Y_{N_2}$ for $0.54 \leq \Phi \leq 1.55$ (corresponding to $0.703 \leq Y_{N_2} \leq 0.744$)

results in a more refined database. For the N_x points, we note that the stepping in Y_z is not constant, even though $\Delta\Phi$ is. So for a spectrum of N_f 1D premixed flames, a reasonable choice for the number of horizontal grid points is $N_x \geq N_f$, so that there is at least a one-to-one match between the original flame points and that on the rectangular grid. For the 102 flames shown

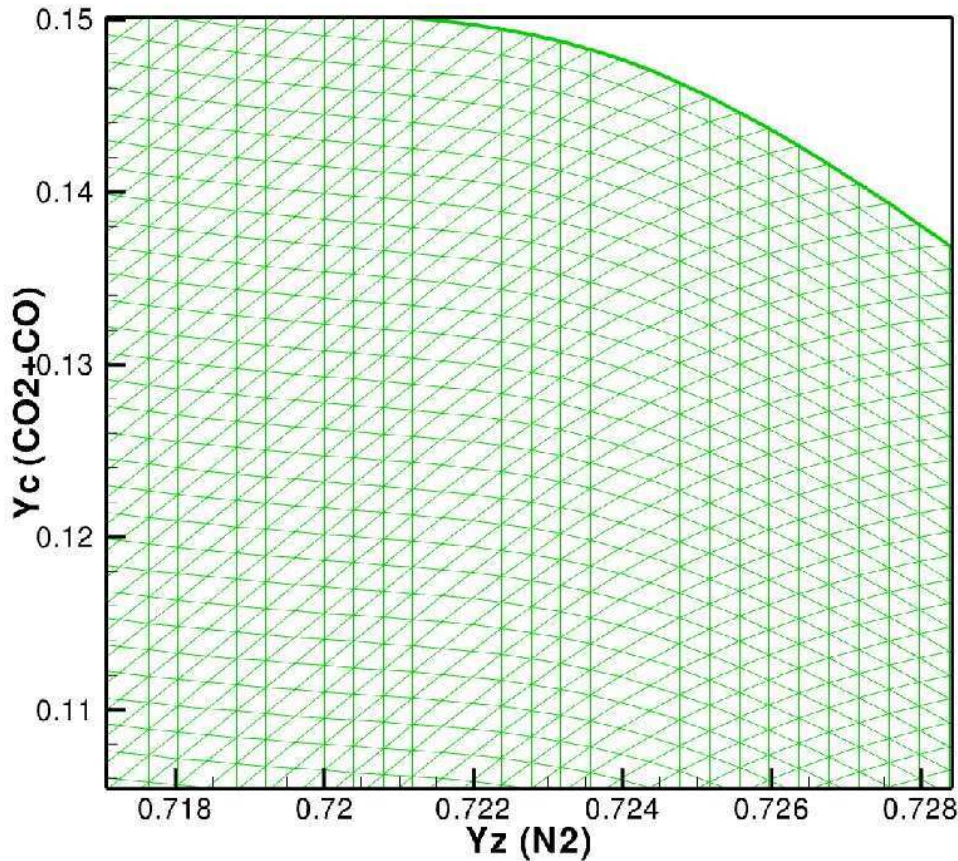


Figure 3.3: Zoom on the (Y_z, Y_c) subspace to show the triangulation of flame data points

on figure 3.2(a), $N_x \geq 150$ seems to be a good choice, with $N_y \geq 1000$.

Let L_c and L_z be the lengths **AB** and **AE**, respectively. While the length **AE** can be directly estimated from $L_z = Y_{z,max} - Y_{z,min}$, **AB** need some special attention, since each flame has a different L_c value. The first and last grid point along Y_c should therefore hold the minimum and maximum value of the various minima and maxima, respectively. That is, $L_c = \max(L_{c_i})$, where i is the number of 1D flames.

3.4.2.3 Information tabulation

All the information contained in the triangulation is then interpolated onto the rectangular grid described above, assigning a constant value, (chosen as zero), for the nodes of the rectangular grid that are outside the triangular grid region, that is, nodes located in the region bounded by **BCDB** in Fig. 3.4(a). The constant value for these outside nodes could be any real number. The choice of zero will serve as a flag when querying the database. We will return to this later on in the chapter.

On completion, the raw data, now contained on a structured grid is tabulated using a dedicated set of FORTRAN subroutines. Additional variables are computed by invoking *chemkin 2* subroutines. The user specifies in an input text file the keywords of the quantities he wants to tabulate. For instance, the keywords *ACON*, *MASS*, *MASR* and *WYPR* from the input file will instruct the tabulation routines to compute and store the thermal conductivity, all species mass fractions, mass fractions of table coordinates and the mass production rate of the table coordinates, respectively. For each keyword, the flame information from the fresh gas mixture to the fully burnt products, as well as the equilibrium responses and the boundary information are tabulated (see Fig. 3.2(a)). The data structure employed for the information storage and subsequent retrieval is shown in listing 3.1.

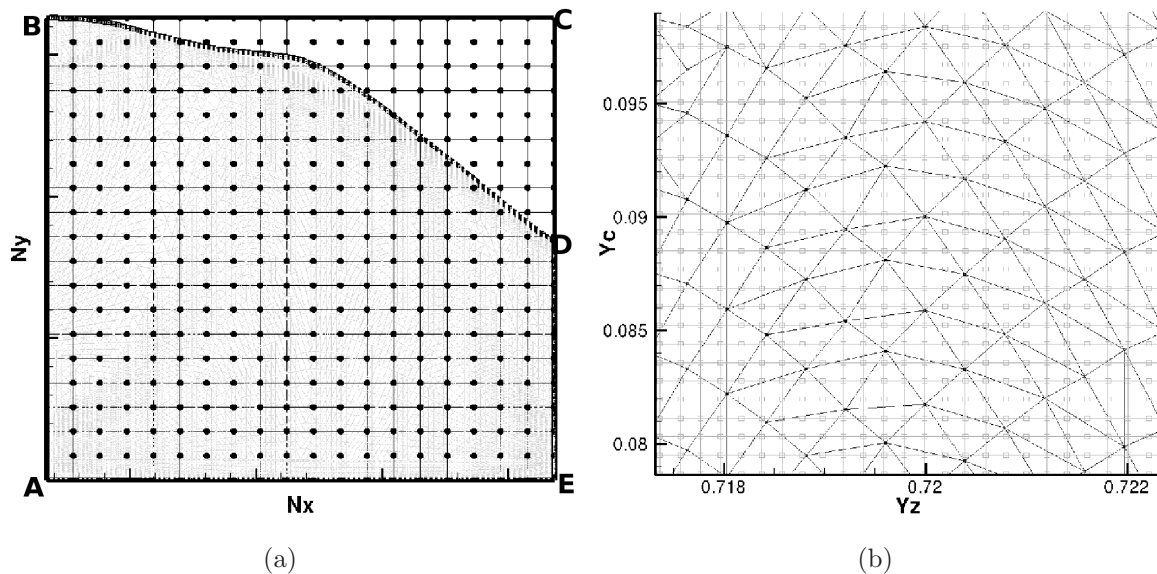


Figure 3.4: (a) Sketch of the triangular-to-rectangular grid mapping. The shaded region, **ABDEA**, defines the actual flame domain while the unshaded region, **BCDB** is where the rectangular grid nodes are outside the main flame domain. (b) Zoom on the triangulation with the regular rectangular grid in the background (gray lines).

```

1  TYPE POINT
2      REAL :: X,Y                               !NODE COORDINATES
3      REAL,DIMENSION(:),POINTER :: VALUE       !STORED VALUE
4      INTEGER :: NUMBER                         !NODE ID
5      LOGICAL :: INSIDE                        !NODE INSIDE/OUTSIDE FLAME DOMAIN
6  END TYPE POINT
7  TYPE(POINT), ALLOCATABLE, TARGET, DIMENSION(:) :: NODE

```

Listing 3.1: FPI table data structure

For all nodes within the main flame domain (region **ABDEA** in Fig. 3.4(a)), the boolean *INSIDE* is set to *true*, and *false* otherwise. To determine the location of a node as either inside or outside the main domain, we check the stored temperature value, which if inside the main domain, is non zero. It should be pointed out that this inside/outside node information is checked only once, during table initialization. The double-precision number array *VALUE* holds the actual stored value. For the mass fractions (*MASS*), for instance, its dimension is N_s , whereas for density (*RHOY*), its dimension is one. The numbering of the nodes is from left to right (**A** \rightarrow **E**), bottom to top (**A** \rightarrow **B**). The other fields are self explanatory.

3.4.2.4 Storage constraints

Suppose the Y_z and Y_c variables are discretized by N_x and N_y points respectively, and that we desire to store N flame quantities for each point in the look-up table. The overall size of the table is then $N \times N_x \times N_y$. This is a major concern, since it may lead to very large amounts of data and hence storage constraints, especially on massively parallel systems.

The thermo-chemical variables to be stored in addition to the information related to the species being used as the FPI coordinates depend entirely on how much information the user wants from the table for use in the flame solver. For an incompressible low-Mach number solver (that will be presented in sect. 4.4.2 on page 54), the basic quantities of interest are shown in table 3.1, together with the FPI subroutine names. The default unit used for the tabulation is the SI system.

Keyword	FPI routine	Dim	Explanation
TEMP	FPI_TEMPER	1	Temperature
RHOY	FPI_RHOY	1	Mass density
AVIS	FPI_AVIS	1	Viscosity of mixture
ACON	FPI_ACON	1	Mixture thermal conductivity
MMWY	FPI_MMWY	1	Mixture mean molar mass
CPBS	FPI_CPBS	1	Mixture heat capacity at constant pressure
DLE1	FPI_DLE1	1	Global diffusion coefficient for $Le=1$
ADIF	FPI_ADIF	1	Mixture-averaged diffusion coefficient
MASR	FPI_MASS_RED	2	Mass fractions of table coordinates
WYPR	FPI_WYP_RED	2	Mass production rate of table coordinates
WT	FPI_WT_RED	2	Molar masses of table coordinates
MASS	FPI_MASS	N_s	Mass fractions of all species

Table 3.1: FPI subroutine names and keywords used in the tabulation routine input file and their corresponding meaning. The third column is the number of variable(s) that the quantity holds.

Mechanism	N_s	Table Type	Stored Var.	No. of 1D Flames	N_x	N_y	Size (MB)
MILLER [65]	9	FULL	21	121	150	1000	48
	9	BASIC	14	121	150	1000	25
MARINOV [66]	9	FULL	21	103	110	1000	27
	9	BASIC	14	103	110	1000	19
GRI 1.2 [62]	20	FULL	32	102	150	1000	49
	20	BASIC	14	102	150	1000	25
	20	FULL	32	102	250	2500	205
	20	BASIC	14	102	250	2500	105

Table 3.2: FPI table memory size constraints for various kinetic schemes. For the FULL table, all the variables of table 3.1 are tabulated. In the BASIC table type, only the variables needed during the simulation are stored.

Moreover, the size of the look-up table depends also on the number of grid points in our rectangular domain, i.e., on the values of N_x and N_y . On the other hand, the number of chemically reacting species involved in the detail chemical scheme employed in the computations of the 1D flames also contribute significantly in determining the size of the resulting database. Typical values of N_x and N_y for different kinetic schemes are summarized on table 3.2. For the FULL table, all the variables of table 3.1 are tabulated, while in the BASIC table type, only the species mass fractions defining the table’s coordinates (keyword: *MASR*) rather than all N_s species (keyword: *MASS*) are tabulated.

For simulating flames using FPI look-up tables, only information related to the species defining the table coordinates is mandatory, together with a relatively small number of other thermochemical quantities. Therefore instead of tabulating the mass fractions of all the N_s species (keyword: *MASS*) present in the chemical kinetics scheme being used, we may consider only 2 (two-coordinate table) or 3 (three-coordinate table) species being used as coordinates. The same consideration applies for, say, the mass production rate (keyword: *WYP*), etc. With such considerations, we can obtain look-up tables with extremely reduced sizes (see table 3.2) for usage during the flow simulation, while reserving the much heavier FULL version for post-processing on local machines with larger memories.

Different research groups are adopting different ways of tackling this storage issue. A method was proposed of tabulating complex chemistry, referred to as the Self-Similarity Flame Tabula-

tion (S2FT) technique [67], based on FPI and taking advantage of the self-similarity behavior of species reaction rates (or mass fractions) profiles, plotted as a function of a reduced progress variable together with scaling rules, to drastically reduce the size of the chemical database compared to the classical FPI/FGM formalism. The 2D FPI table is replaced by four one-dimensional vectors. This has been validated for one-dimensional laminar premixed flames. In [68], the same idea is extended by taking advantage of self similar properties of mean FPI chemical quantities under a presumed PDF formalism for turbulent flame computations. The performance of the latter reduction procedure has been successfully investigated with RANS simulations of a turbulent jet flame [69]. It should be noted that these FPI table reduction strategies adopt a look-up table computed using the unity Lewis number hypothesis.

3.4.3 Advanced FPI

3.4.3.1 Motivation and challenges

Until now, both the classical and new FPI tables have been computed using the unity Lewis number hypothesis ($Le_k = 1$, Sect. 2.3.2.6) for the evaluation of the species diffusion velocities. For methane flames, this is expected to be a reasonable assumption. In such a simplified transport model, mass diffusivity along iso-equivalence ratio surfaces is impossible, hence imposing great restrictions on its applicability especially when flames with high diffusivities such as hydrogen-air flames are considered.

If on the other hand a more realistic transport model with $Le_k \neq 1$ is adopted in the FPI table generation stage, appropriate changes and modifications must be made both in the data tabulation/retrieval techniques and in the flame solver to ensure that

1. first of all, mass is conserved,
2. the linear combination strategy with which the progress variable is reconstructed is appropriate for all the tabulated flame variables associated with it,
3. the mass diffusivity along iso-equivalence ratio surfaces is properly captured.

Such measures, extensions and verifications are necessary when for example we desire to quantify the impact of the chemical database generated using different transport models on the turbulent flame structure. Eventually, it will also help in the direct comparison of DNS results obtained when using FPI tables computed with the same detailed chemical scheme but different transport models.

The incorporation of detailed transport into FPI tables comes with its own challenges. It goes without saying that the mass fraction of nitrogen, which under the $Le_k = 1$ approximation is constant for a given mixture composition (see Fig. 3.5(a)) is no more constant when a realistic transport model is employed. This is demonstrated in Fig. 3.5(b) where variations of Y_{N_2} along a given flame are clearly visible. Finding the most appropriate tabulation and data search techniques for such a complicated local flame point distribution has been the major difficulty. Up to now, a non unity Lewis number FPI database has been always avoided, under the argument that DNS results will know no significant differences stemming from a table with detailed transport. This issue has however not yet been given proper attention and it is worth cross-checking.

3.4.3.2 Proposed modifications

Assume that we have a FPI chemical database computed with detailed chemical and transport schemes. In what follows, we derive appropriate expressions to account for the first two modifications mentioned above and discuss its consequences on the tabulation strategy and practical implementation. The last issue regarding the choice of FPI grid/data structure was already addressed in Sect. 3.4.2.2.

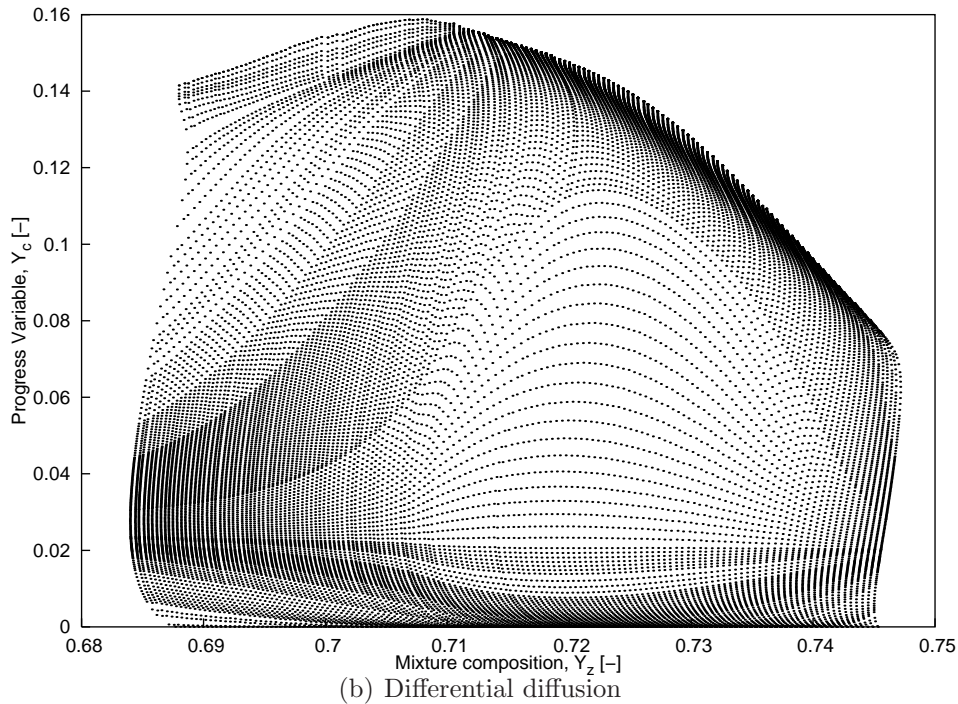
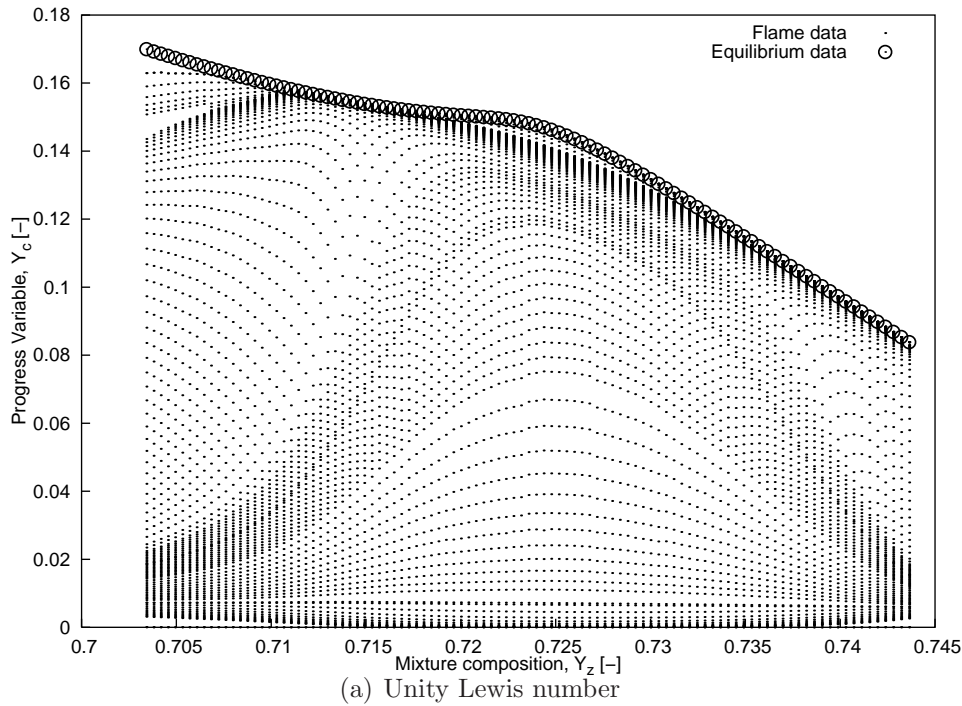


Figure 3.5: Projection of a series of 1-D freely propagating laminar premixed methane/air flames on the (Y_z, Y_c) subspace for $0.50 \leq \phi \leq 1.97$; $0.688 \leq Y_z(\phi) \leq 0.745$ and a stepping of $\Delta\phi = 0.01$. Each vertical set of points (dots) constitute a single flame, covering the entire Y_c space from the fresh gas mixture ($Y_{c,min}$) to chemical equilibrium ($Y_{c,max}$) within the given Y_z flammability limit. The \odot symbols are the corresponding equilibrium values. When using the assumption $Le=1$, each flame is aligned vertically (top), since differential diffusion is not allowed. On the other hand, each flame has a complex structure when taking into account a realistic diffusion model (bottom).

Modifications due to Y_c species combination

As mentioned before, the FPI tabulation methodology often require that we use combination of the mass fractions of some abundant species present in the complete chemical scheme to reconstruct an appropriate Y_c . This measure is taken to ensure that the variation of Y_c across

the flame front is monotonic. For example, in hydrocarbon fuels, Fiorina [53] proposed the use of a linear combination of Y_{CO_2} and Y_{CO} for Y_c .

If we assume that Y_c is reconstructed from a linear combination of $N_c \geq 1$ species, then

$$Y_c = \sum_{i=1}^{N_c} \alpha_i Y_i \quad (3.5)$$

where the α_i are scaling real constants. Such a summation implies that during the lookup table generation each tabulated property of the *new* or lump species Y_c will be made up of the corresponding quantities for the Y_i species combined together. For instance the diffusion coefficients and mass production rates of Y_c will be computed and stored as follows (to simplify the expression and analysis, we will use $N_c = 2$):

$$D_c = D_1 + D_2, \quad W_c \dot{\omega}_c = W_1 \dot{\omega}_1 + W_2 \dot{\omega}_2 \quad (3.6)$$

Consider the mass balance transport equations for Y_1 and Y_2 :

$$\partial_t(\rho Y_1) + \nabla \cdot (\rho \mathbf{u} Y_1) = -\nabla \cdot (\rho Y_1 \mathbf{V}_1) + W_1 \dot{\omega}_1 \quad (3.7)$$

$$\partial_t(\rho Y_2) + \nabla \cdot (\rho \mathbf{u} Y_2) = -\nabla \cdot (\rho Y_2 \mathbf{V}_2) + W_2 \dot{\omega}_2 \quad (3.8)$$

Upon adding eq. (3.7) and (3.8), we obtain the following transport equation for Y_c (making use of eq. (3.5) with $\alpha_1 = \alpha_2 = 0.5$):

$$\underbrace{\partial_t(\rho Y_c)}_{\text{Time}} + \underbrace{\nabla \cdot (\rho \mathbf{u} Y_c)}_{\text{Convection}} = - \underbrace{\nabla \cdot (\rho (Y_1 \mathbf{V}_1 + Y_2 \mathbf{V}_2))}_{\text{Diffusion}} + \underbrace{W_c \dot{\omega}_c}_{\text{Reaction}} \quad (3.9)$$

As can be observed from eq. (3.9), all the terms sum up linearly as desired except for the diffusion term which needs some special attention.

If we consider the Hirschfelder-Curtiss approximation from Sect. 2.3.2.3, we have that (in x -direction only)

$$Y_i V_{i_x} = -D_i^* \frac{W_i}{\bar{W}} \frac{\partial X_i}{\partial x} \quad \forall i \in N_s \quad (3.10)$$

From this equation, we see that the diffusion velocities depend on the mixture-averaged diffusion coefficients D_i^* , which are the quantities that are actually stored in the lookup table. In the classical FPI [10] (unity Lewis number approximation) the diffusion coefficients for Y_1 and Y_2 are such that

$$D_1 = D_2 = D_c \quad (3.11)$$

Consequently, eq. (3.9) simplifies to

$$\partial_t(\rho Y_c) + \nabla \cdot (\rho \mathbf{u} Y_c) = -\nabla \cdot (\rho Y_c \mathbf{V}_c) + W_c \dot{\omega}_c \quad (3.12)$$

where

$$Y_c \mathbf{V}_c = -D_c^* \frac{W_c}{\bar{W}} \nabla X_c \quad (3.13)$$

In the situation where a detailed transport model is employed for both the FPI generation and subsequently in the DNS computation, the diffusion of each species making up the progress variable must be evaluated separately before they are linearly combined, as already hinted in eq. (3.9):

$$Y_c \mathbf{V}_c = -(D_1^* W_1 \nabla X_1 + D_2^* W_2 \nabla X_2) / \bar{W} \quad (3.14)$$

We could generalize the above expressions for both the progress and mixture composition variable such that:

$$Y_c \mathbf{V}_c = - \sum_{j=1}^{N_c} D_j^* \frac{W_j}{\bar{W}} \nabla X_j \quad (3.15)$$

$$Y_z \mathbf{V}_z = - \sum_{j=1}^{N_z} D_j^* \frac{W_j}{\bar{W}} \nabla X_j \quad (3.16)$$

where N_z is the total number of species used in the reconstruction of Y_z . Most often, $Y_z = Y_{N_2}$ ($N_z = 1$).

It should be noted that, when $N_c = 1$ (a single species is used to serve as Y_c) or when a simpler transport model (such as the unity Lewis number approximation) is used, the diffusion velocities are easily recovered from eq. (3.15) and (3.16). Also, an identical value for all α_i in eq. (3.5) will not affect the above derivations.

Modifications to ensure global mass conservation

In the pre-computations leading to the series of 1D unstrained freely propagating laminar pre-mixed flames used in the construction of the FPI database, the diffusion of each species is influenced by the rest of the ($N_s - 1$) species in the system. When incorporated into a FPI-based flame solver, only the two lump species (Y_z and Y_c) are solved for. In the real mixture, the diffusion of Y_z is influenced not only by Y_c (and vice versa) but by the full system of N_s species. This has not been the case up till now.

To introduce a correction term for the diffusion velocities for such a reduced system, a closure problem arises since a predictor term will involve a summation over all the N_s species. Therefore in addition to the diffusion coefficients of the table coordinates, we equally compute and store those of all the species present in the original complete chemical system employed in the FPI table generation. The diffusion velocities can then be computed classically according to eq. (2.21).

To summarize, we have seen that to move from a simple ($Le_k = 1$) to a detailed ($Le_k \neq 1$) transport model FPI database, we have to make two indispensable modification:

1. Compute at run time, the diffusion velocities of the various species constituting the progress variable before summing them up, as opposed to the *a priori* summation via their diffusion coefficients in the chemical database.
2. Add a corrector term in the evaluation of the diffusion velocities for the table coordinates to ensure global mass conservation:

$$Y_c \mathbf{V}_c = - \sum_{j=1}^{N_c} D_j^* \frac{W_j}{\bar{W}} \nabla X_j + V_{cor} \sum_{j=1}^{N_c} Y_j \quad (3.17)$$

$$Y_z \mathbf{V}_z = - \sum_{j=1}^{N_z} D_j^* \frac{W_j}{\bar{W}} \nabla X_j + V_{cor} \sum_{j=1}^{N_z} Y_j \quad (3.18)$$

where

$$\mathbf{V}_{cor} = \sum_{k=1}^{N_s} \left(D_k^* \frac{W_k}{\bar{W}} \nabla X_k \right) \quad (3.19)$$

With the smart tabulation technique described earlier in combination with the robust information location and retrieval (described next), we computed a database which accounts for differential diffusion together with one under the unity Lewis number assumption. Results for the comparison will be presented in Chapter 6.

3.4.4 Data base functionality

In this section, we proceed to detail out the strategy used for the identification and retrieval of information within the database. Out-of-bound approximation and stand-alone verifications are then presented, followed with some comments on the relative merits when using the new data structure.

3.4.4.1 Information location and retrieval

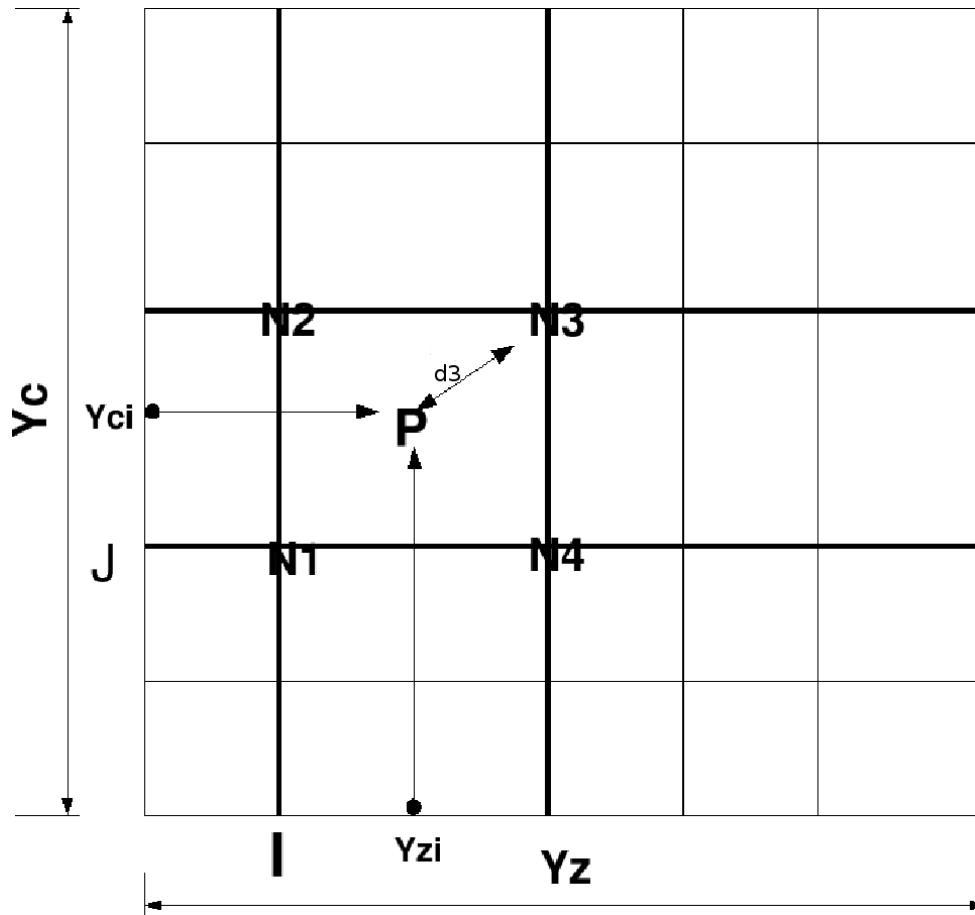


Figure 3.6: Sketch of the rectangular grid, illustrating information localization and retrieval at point $\mathbf{P}(Y_{zi}, Y_{ci})$ with nodes N_1, N_2, N_3 and N_4 of rectangle \mathbf{R} (not shown) within the database

To locate a cell within the database containing a target point, we do not need a search procedure as in the previous versions of the FPI table since our grid is now regular, with a fixed grid size given as:

$$\Delta Y_z = L_z / (N_x - 1); \quad \Delta Y_c = L_c / (N_y - 1) \quad (3.20)$$

where ΔY_z and ΔY_c are the grid size on the Y_z and Y_c coordinates, respectively.

Suppose we have a flame point \mathbf{P} , with coordinates (Y_{zi}, Y_{ci}) and that we wish to get information for this flame point. From the above discussion, \mathbf{P} is contained in a rectangle \mathbf{R} , and must be identified in an efficient manner. The four nodes (N_1, N_2, N_3 and N_4) of \mathbf{R} could all be embedded within, without or in-between the database main flame domain (see Fig. 3.4(a)). We proceed in the localization, approximation and retrieval of information at \mathbf{P} harbored by \mathbf{R} within the database as follows (see the sketch in Fig. 3.6 for the definition of the parameters used below):

1. Locate the Y_z component I , of the lower-left node N_1 , of \mathbf{R} :

$$I = \begin{cases} 1 & \text{if } Y_{zi} \leq Y_{z,min} \\ N_x - 1 & \text{if } Y_{zi} \geq Y_{z,max} \\ \text{floor} \left(\frac{Y_{zi} - Y_{z,min}}{\Delta Y_z} + 1 \right) & \text{otherwise} \end{cases}$$

2. Use I to locate the Y_c component J , of the lower-left node N_1 , of \mathbf{R} :

$$J = \begin{cases} 1 & \text{if } Y_{ci} \leq Y_{c,min} \\ I + (N_y - 1) \times N_x - N_x & \text{if } Y_{ci} \geq Y_{c,max} \\ I + \left[\text{floor} \left(\frac{Y_{ci} - Y_{c,min}}{\Delta Y_c} + 1 \right) - 1 \right] \times N_x & \text{otherwise} \end{cases}$$

3. Get the integer ID of the four nodes of \mathbf{R} :

$$\begin{aligned} N_1 &= \text{NODE}(J)\%NUMBER \\ N_2 &= \text{NODE}(J + N_x)\%NUMBER \\ N_3 &= \text{NODE}(J + N_x + 1)\%NUMBER \\ N_4 &= \text{NODE}(J + 1)\%NUMBER \end{aligned}$$

4. Determine the number of nodes of \mathbf{R} lying within **ABDEA** and **BCDB** (see Fig. 3.4):

$$\begin{aligned} N_{1out} &= \text{NODE}(N_1)\%INSIDE \\ N_{2out} &= \text{NODE}(N_2)\%INSIDE \\ N_{3out} &= \text{NODE}(N_3)\%INSIDE \\ N_{4out} &= \text{NODE}(N_4)\%INSIDE \end{aligned}$$

5. Extract the corresponding information stored on the nodes of \mathbf{R} :

$$\begin{aligned} \mathcal{V}_1 &= \text{NODE}(N_1)\%VALUE(K) \\ \mathcal{V}_2 &= \text{NODE}(N_2)\%VALUE(K) \\ \mathcal{V}_3 &= \text{NODE}(N_3)\%VALUE(K) \\ \mathcal{V}_4 &= \text{NODE}(N_4)\%VALUE(K) \end{aligned}$$

6. Approximate the value \mathcal{V}_R , at $\mathbf{P}(Y_{zi}, Y_{ci})$ in \mathbf{R} using a multi-linear interpolation:

- If two or more nodes of \mathbf{R} are inside the main domain **ABDEA**,

$$\mathcal{V}_R = \begin{cases} \mathcal{V}_n & \text{if } P(Y_{zi}, Y_{ci}) = N_n, \quad n = 1, 2, 3 \text{ or } 4 \\ \sum_{i=1}^{(n)} (\mathcal{V}_i/d_i) / \sum_{i=1}^{(n)} (1/d_i) & \text{otherwise,} \quad n = 2, 3 \text{ or } 4 \end{cases}$$

- Otherwise, \mathbf{P} is projected back unto **ABDEA**, from where \mathcal{V}_R is approximated. How this is done is explained in the next subsection.

Here, n is the number of nodes of \mathbf{R} that lie within the tabulated flame domain, and \mathcal{V}_R is the retrieved value. \mathcal{V}_i is the stored value at node N_i of \mathbf{R} . The distance between $\mathbf{P}(x_i, y_i)$ and N_i is d_i .

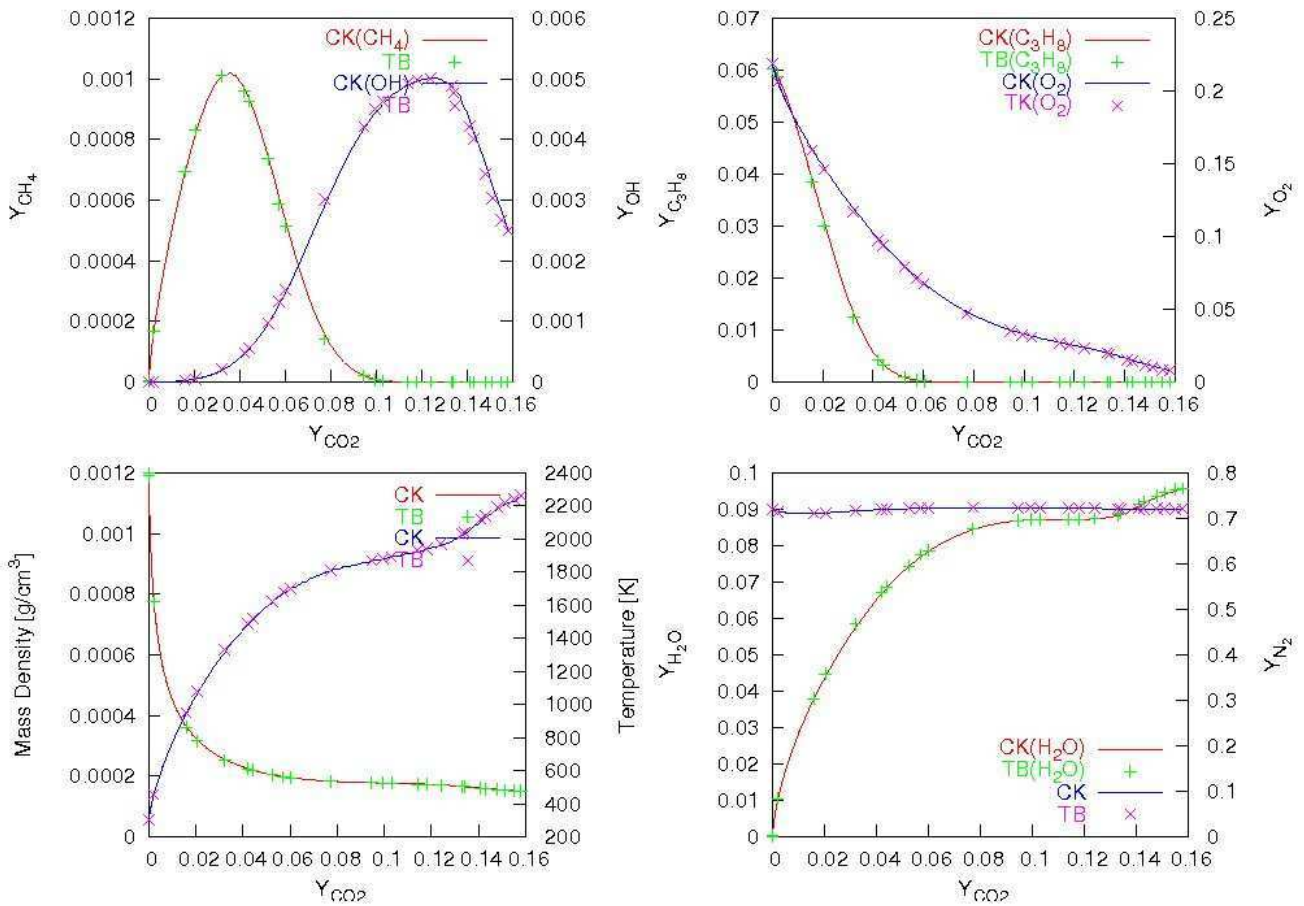


Figure 3.7: Comparison of the profiles of density, temperature and mass fractions of OH, CH₄, H₂O, C₃H₈, O₂ and N₂ of a methane–air premixed flame computed with complex chemistry (solid lines) and retrieved from FPI look-up table (color markers) parameterized by $Y_c = Y_{CO_2}$

3.4.4.2 Out-of-bound approximation

As one could easily observe from the determination of the I and J above, every point \mathbf{P} , on entering the database is handled in such a way that it ends up being confined within **ABCDEA** (see Fig. 3.4(a)). That is, if \mathbf{P} is below line **AE**, it is projected onto the corresponding Y_z value on line **AE**. The same principle is applied when \mathbf{P} falls on the left, right and above the lines **AB**, **ED** and **BD**, respectively. The challenge lies in the handling of points that fall within the region bounded by **BCDB**, which is outside the main flame domain **ABDEA**.

If \mathbf{P} is contained in a rectangle with at least three of its four nodes embedded in **BCDB**, it is projected back unto the line **BD** and the retrieved value is then approximated from the equilibrium information stored along line **BD**. The two equilibrium points used for the multi-linear approximation are those within whose x -components Y_{zi} is bounded.

3.4.4.3 Stand-alone verifications

We start off with a one-dimensional FPI look-up table parameterized by $Y_c = Y_{CO_2}$. This is just to verify the correctness of the 1D laminar premixed flames obtained with *chemkin*. We enter the table with randomly generated points sparsely spread out beyond the limits of the tabulated flame data, in order to also test the out-of-bound projections described above. The extracted points for the density, temperature and the mass fractions of some major (CH₄, O₂, H₂O, N₂) and minor (OH, C₃H₈) species, together with the original flame data are shown in Fig. 3.7. The agreement is as expected excellent.

Turning now to a full two-dimensional FPI table, one question that needed to be clarified

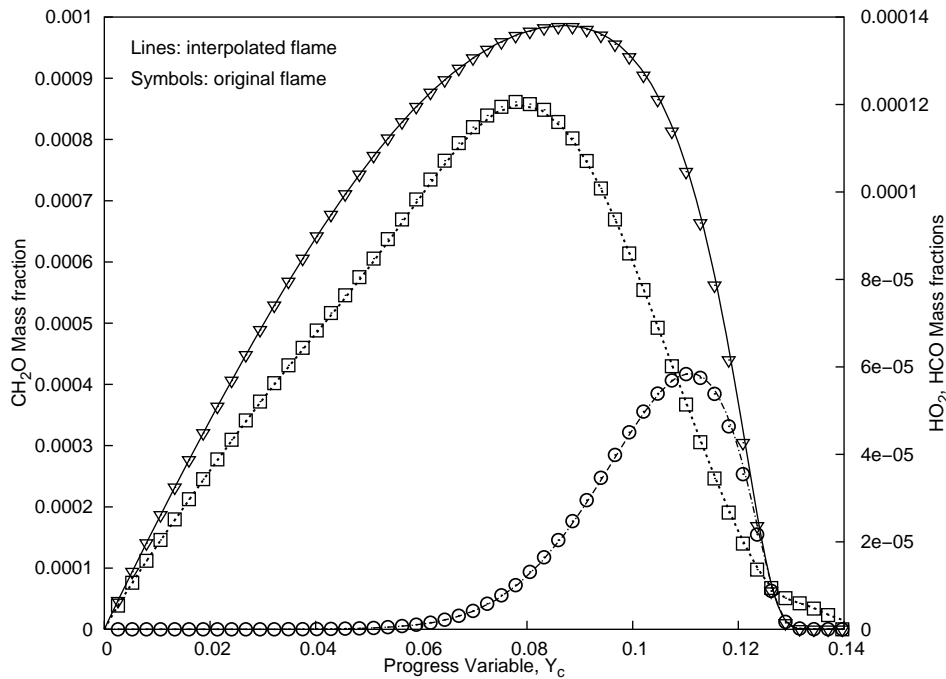


Figure 3.8: Comparison of the original flame (symbols, complex chemistry) and the interpolated flame (lines, FPI) on the rectangular grid, showing the profiles of the mass fractions of HO_2 (\square , dashed line, right axis), HCO (\circ , dash dotted line, right axis) and CH_2O (∇ , solid line, left axis) radicals, for a freely propagating laminar premixed methane/air flame projected on the progress variable Y_c

was whether vital information is not lost during the triangular-to-rectangular grid mapping/interpolation. Fig. 3.8 shows a comparison between the original and interpolated flame for the mass fractions of the CH_2O , HCO and HO_2 radicals of a freely propagating laminar premixed methane–air flame before and after interpolation. The prediction of the flame points contained on the rectangular grid compared to the original complex chemistry data is excellent. If these rather stiff radicals are fully captured, then the potentials of a chemical database constructed on such a structured rectangular grid in describing accurately the overall burning process has been demonstrated. In a flow simulation, the computed mass fractions of Y_z and Y_c are projected back onto the database at each time step, to get the proper values for the next time step. Fig. 3.9 demonstrates how the database will react for input DNS points that fall outside the database boundaries (which is a rare situation), as well as checking the accuracy of the retrieved information. The database is accessed by randomly generated points, some of which fall outside the main flame domain. Out-of-bound input points are smartly projected back onto the database and then retrieved.

3.4.5 Advantages of new FPI formulation

1. The search procedure of the previous version of FPI has been replaced with an efficient information location technique, which hinges on the rectangular grid on which information is tabulated within the database. This of course will certainly result in computational speedup, as quantified later.
2. All the mass fractions (and any other variable of interest) are now available in a single table, unlike the previous version(s), where the database used in the flow simulation and post processing were usually different, containing different tabulated quantities. This made it difficult to distinguish between an error resulting from the computations with those coming from the post processing.

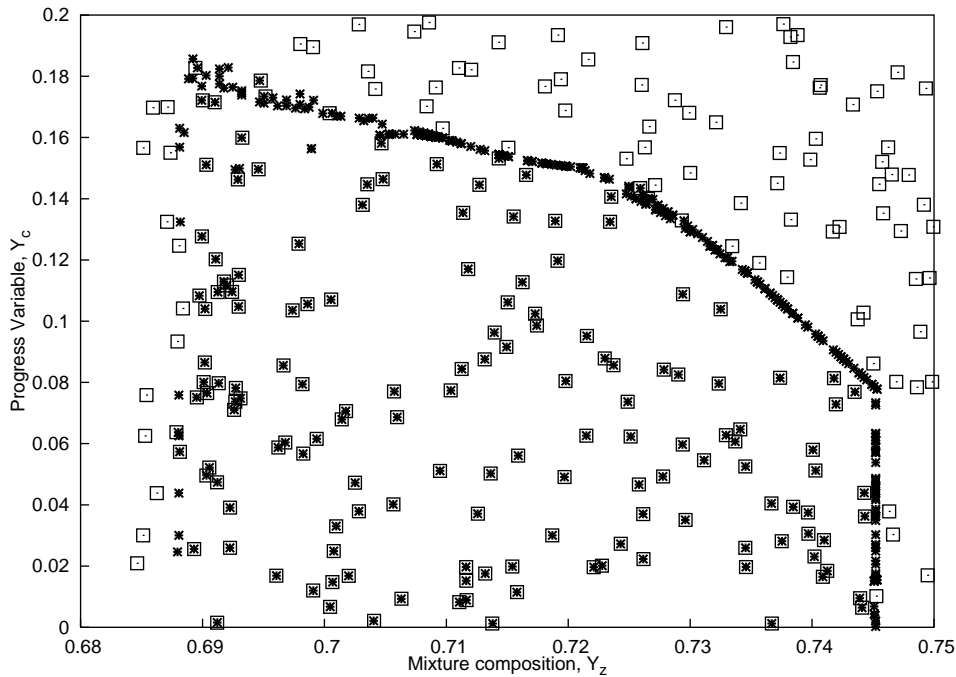


Figure 3.9: Projection of the FPI database on the (Y_z, Y_c) subspace, aimed at verifying information retrieval and accuracy. \square : randomly generated input points, $*$: retrieved information

3. With the current version, computations can be performed at any value of Y_z (hence Φ) within the database bounds.
4. Variations due to differential diffusion are now allowed for all quantities, even for a constant equivalence ratio.

3.4.6 FPI at work

In this section, we present briefly the coupling process of the look-up table with a CFD code before presenting some of the validation results in Sect. 6.2.

The CFD code in which the FPI look-up table is implemented is called π^3 (see Sect. 4.4.2 for details). The coding strategy makes it easy to implement a transport model of choice, using either the unity Lewis number assumption or mixture-averaged transport properties. Thus far, it has been assumed that the functionality of the FPI table is not intrinsic to the transport model with which it is generated.

Prior to the current changes to π^3 , it has been running with the classical FPI database constructed on a triangular grid using the unity Lewis number approximation. The same diffusion speeds are imposed on the Y_z and Y_c variables. Moreover, we impose zero diffusion for the mixture composition coordinate Y_z for pure premixed flames, purely due to numerical stability reasons. To use now FPI with differential diffusion, we simply deactivate the unity Lewis number boolean variable in the π^3 input file. Corresponding changes in the code are then automatic.

In addition to the above specifications, the search routines of the previous look-up table were suppressed and replaced with the new information localization and interpolation routines. The out-of-bound projections and approximations routines have all been replaced. With a two-coordinate look-up table (Y_c, Y_z) for a given complete chemical scheme, complex chemistry is taken into account by introducing only two conservative species equations in the solver:

$$\frac{\partial}{\partial t} (\rho Y_j) + \frac{\partial}{\partial x_i} (\rho u_i Y_j) = \frac{\partial}{\partial x_i} \left(\rho D_j^* \frac{W_i}{W} \frac{\partial X_j}{\partial x_i} \right) + \dot{w}_j \quad (3.21)$$

where $j = (c, z)$. Eq. (3.21) is formulated under the Hirschfelder and Curtiss approximation for molecular diffusion terms. Under the unity Lewis number assumption, $D_c = D_z = D = \lambda/\rho c_p$ and $\dot{w}_z = 0$ as $Y_z = Y_{N_2}$ is not involved in any reaction. The unknowns are ρ , D and \dot{w}_j . They are stored in the look-up table and can be retrieved via the computed values of Y_j . Therefore, instead of solving the full 5 (Navier-Stokes) plus N_s (species) system of equations, only $5 + 2$ (FPI coordinates) equations are solved. So, for a chemical scheme like the GRI 3.0 [62], which has 53 species, the system of coupled equations is reduced from 58 to 7 for a full 3D simulation!

At any given iteration n of the CFD solver, the computed values of the coordinates $Y_{j(n)}$ are used to enter the look-up table. The information localization and retrieval algorithm described earlier allows us to extract from this chemical database all the transport, thermodynamics and reaction coefficients needed for the next iteration step leading to $Y_{j(n+1)}$, and so on. The FPI table is generated at constant pressure and the flames are at low-Mach numbers, hence ρ is readily extracted from the database. A typical FPI Fortran subroutine call is illustrated in listing 3.2.

```
1 CALL FPIROUTINE_NAME(COORD(:) ,VAR(:) ,DIM)
```

Listing 3.2: Typical FPI subroutine call

The (input) integer DIM is the size of the (output) vector VAR(:) while the (input) vector COORD(:) holds the values of the table coordinates, whose dimension is either 2 (2D table) or 3 (3D table).

3.5 Low Mach number approximation

For most applications relying on combustion, practical devices are operated at low flow speeds and very low-Mach numbers. When trying to simulate such configurations directly an explicit time integration of Eq. (2.1)-(2.5) leads to severe time-step limitations corresponding to the most critical time-scale. This fastest characteristic time-scale is associated with the propagation of acoustic waves, leading to a wave velocity equal to the maximum of the flow speed plus the local velocity of sound. Using compressible equations for very low-Mach numbers system is then particularly inefficient [70, 71]. It is much better to consider a low-Mach number approximation which enables us to solve only the vorticity and entropy waves and neglect the acoustic ones.

The derivation of the low-Mach number equations is performed through an asymptotic expansion of the non-dimensional variables in terms of the Mach number M [72]:

$$p^* = p_0^* + Mp_1^* + \gamma M^2 p_2^* + o(M^3) \quad (3.22)$$

$$v^* = v_0^* + Mv_1^* + o(M^2) \quad (3.23)$$

$$T^* = T_0^* + MT_1^* + o(M^2) \quad (3.24)$$

where $(:)^*$ is the corresponding non-dimensional variable. Expansions (3.22)–(3.24) are introduced in the non-dimensional compressible equations and the terms of equal power of M are gathered together. It turns out that the pressure p can be split into a spatially uniform pressure $p_0(t)$ and a dynamic perturbation part $\tilde{p}(\mathbf{x}; t)$. Using this decomposition the equations for combustion at zero-Mach number can be established [15], leading to (assuming that the fields p_1^* , v_1^* and T_1^* vanish and that the ambient pressure is time independent)

$$\frac{\partial \rho}{\partial t} + \frac{\partial(\rho u_j)}{\partial x_j} = 0 \quad (3.25)$$

$$\frac{\partial(\rho u_i)}{\partial t} + \frac{\partial(\rho u_j u_i)}{\partial x_j} = -\frac{\partial \tilde{p}}{\partial x_i} + \frac{\partial \tau_{ij}}{\partial x_j} + \rho f_i, \quad i = 1, 2, 3 \quad (3.26)$$

$$\frac{\partial(\rho Y_k)}{\partial t} + \frac{\partial(\rho u_j Y_k)}{\partial x_j} = -\frac{\partial(\rho Y_k V_{kj})}{\partial x_j} + \dot{w}_k; \quad k = 1, 2, \dots, N_s \quad (3.27)$$

$$\frac{\partial(\rho e_t)}{\partial t} + \frac{\partial}{\partial x_j}(\rho u_j e_t) + \frac{\partial q_j}{\partial x_j} = 0 \quad (3.28)$$

In order to simplify the computational algorithm, it is useful to employ primitive variables for the species equations (3.27). In the same way it is easier to solve a temperature equation instead of the energy equation (3.28). The derivation of the isobaric temperature equation is again achieved by introducing the asymptotic expansions (3.22)–(3.24) in the compressible temperature equation.

Note that the low-Mach number approximation leads to the disappearance of the viscous and pressure terms in the energy and temperature equation [11]. This is due to the fact that the kinetic energy is not of the same order of magnitude as the internal energy in terms of Mach number. A specific procedure is now required to determine the hydrodynamic perturbation $\tilde{p}(\mathbf{x}; t)$. Several possibilities have been proposed in previous publications. We decide to use a pressure-projection method [72–74], which leads to the solving of eq. (3.26) in two consecutive parts. The details are given in Chapter 4 (Sect. 4.4.2).

3.6 Summary

Two powerful and highly predictive model reductions aimed at reducing the numerical complexity and user-waiting time for turbulent flame computations have been presented.

The chemistry tabulation strategy, which is an excellent alternative for the inclusion of complex chemistry effects in high fidelity direct simulations, is exemplified via the FPI tabulation approach. A full functional look-up table was developed and validated. The need for more realistic transport models in the generation of the chemical database was highlighted and modifications were proposed to this end. With a new and efficient data structure for the tabulation of flame data, such an advanced FPI table was developed and results will show a better agreement with complex chemistry results, especially for mixtures with highly diffusive radicals such as hydrogen–air flames. The advantages of both the classical and advanced FPI tables constructed with the new data structure are appealing.

The second model reduction leads to a simplified equations. Since combustion devices operate at low-Mach numbers, using incompressible equations then proved beneficial with respect to computing times, as the fastest characteristic time-scale associated with the propagation of acoustic waves is avoided. Details of the implementation of the low-Mach number system of equations for turbulent reacting flow computations will be given in the following chapter.

DNS results obtained when combining the two reduced models will be presented in Chapter 6.

Numerical combustion

4.1 Introduction

Limiting ourselves to gaseous combustion, three principal combustion modes or burning regimes can be identified both in nature and in the industry – the premixed, non-premixed (diffusion) and partially premixed modes. The first mode corresponds to a situation where a flame front propagates into a homogeneous mixture of reactants (fresh gas) while the second mode refers to a flame configuration whereby the reactants are initially separated and diffuse towards a reaction zone. In certain instances, some partial premixing of reactants may occur in a diffusion combustion before the reaction zone develops. This third case is the so-called partially premixed burning regime and exhibits some interesting characteristics such as triple and/or edge flame structures, which have been the subject of numerous studies. This kind of flame may also arise from a sudden propagation of a perfectly premixed flame through a non-homogeneous mixture. Throughout this thesis work, all the focus was on premixed and diffusion combustion.

The numerical study of any of the above turbulent combustion configurations, generally grouped under the denomination Computational Fluid Dynamics (CFD), involves the solution of basic balance equations of continuity, momentum, species and energy transport – eq. (2.1)-(2.5). Given the chemical mechanism and transport models, such equations may be solved directly without modeling turbulence or interactions between turbulence and other mechanisms like in Direct Numerical Simulation (DNS) methods. Alternatively, the equations may be averaged like in Reynolds-Averaged Navier-Stokes (RANS) or filtered like in Large Eddy Simulation (LES) formalisms, resulting in unclosed terms that need to be modeled.

With a given flame configuration and numerical strategy (DNS and/or LES), one critical issue is that of prescribing realistic initial flow-field conditions, able to mimic the main features of an actual turbulent flow. This issue is sometimes denoted as *supergrid* modeling [75]. Such initial conditions, which should be compatible with the mass and momentum conservation equations, maybe difficult to set and limit the possible configurations to be tackled [5]. Most often, the initial turbulent field is superimposed on laminar mean profiles, and in the absence of forcing, decays with time. Many turbulence turn-over times may be needed to compensate for the non-steady state situation, and to reduce the limitations of the conclusions from such simulations. An example of one such initial turbulence generation technique is the inversed FFT based method [76], which provides satisfactory and accurate initial flow field data. Nevertheless, the complexity with respect to its coding and parallelizing for fine grain supercomputing infrastructures leads to a lot of limitations for its regular usage. Alternative methods that are simple and easily generalizable are therefore needed in order to access larger computational domains and hence, higher turbulent Reynolds numbers.

This chapter begins in Sect. 4.2 with a brief outline of the outstanding characteristics of the

various burning modes considered in this work, followed by a presentation in Sect. 4.3 of the various numerical techniques used to simulate turbulent reacting flows. Emphasis is placed only on the DNS approach. Three different non-commercial flame solvers have been used at one stage or the other during this work and some major aspects of these tools will be reported in Sect. 4.4. The initial conditions, in particular, the initial turbulent field generation techniques are revisited and improved alternatives are proposed in Sect. 4.5, followed by an outline in Sect. 4.6 of the general numerical strategy used in direct simulation of reacting flows.

4.2 Combustion modes and configurations

In chapter 5, we will consider three flame configurations: 1) planar (both premixed and non-premixed); 2) spherical (premixed) flame configurations in either one-, two- and/or three-dimensions. The third setup is a premixed planar jet surrounded by a hot co-flow of burnt gases.

4.2.1 Premixed combustion

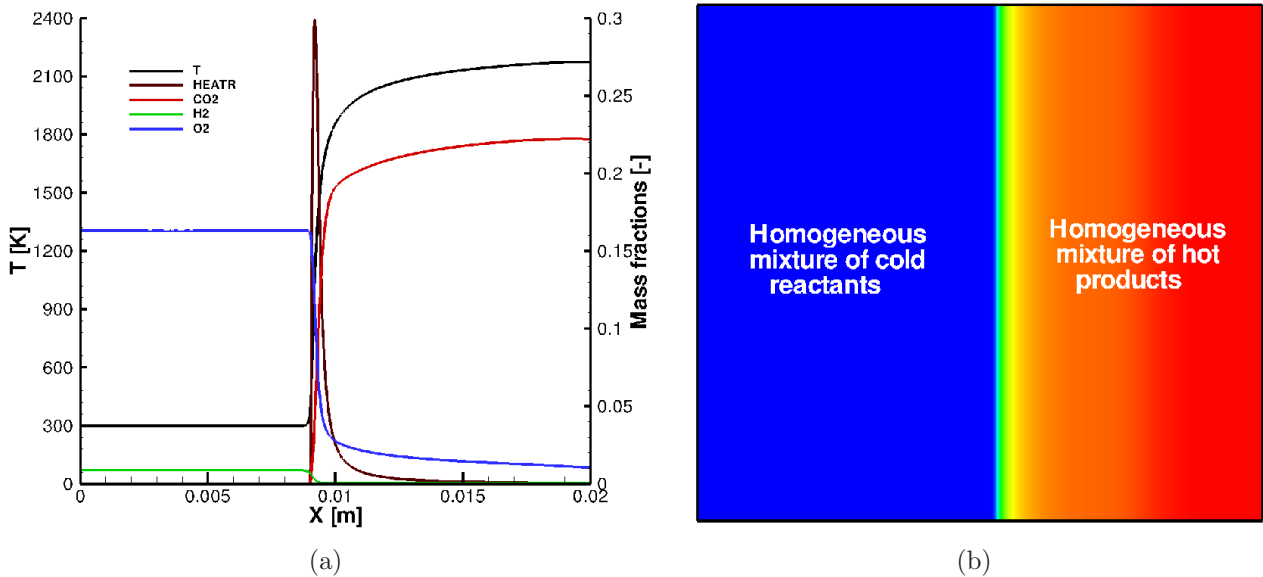


Figure 4.1: (a) Typical laminar planar premixed CO-H₂/air flame structure and (b) 2D numerical configuration showing respectively, profiles of temperature, different species mass fractions and the temperature field, computed using detailed transport and chemistry models

Premixed combustion is observed in many industrial applications. It is the combustion mode whereby the fuel and oxidizer are completely mixed before the combustion starts. Fig. 4.1(a) shows a typical laminar premixed syngas-air (CO-H₂/air) flame structure using detailed transport and chemistry. The profiles are those of temperature, heat release and the mass fractions of CO₂, H₂ and O₂. Fig. 4.1(b) shows its corresponding two-dimensional numerical configuration. The initial values corresponds to a global equivalence ratio $\Phi = 1.12$, defined as the ratio of the actual fuel/air ratio to the stoichiometric fuel/air ratio:

$$\Phi = \frac{(Y_F/Y_O)}{(Y_F/Y_O)_{st}}; \quad \text{Pre-mixture mode} = \begin{cases} \text{lean} & \text{if } \Phi < 1 \\ \text{stoichiometric} & \text{if } \Phi = 1 \\ \text{rich} & \text{if } \Phi > 1 \end{cases}$$

In premixed burning, an unburnt and a burnt region of the flame is clearly visible, separated

by a thin flame front, which is positioned around the peak heat release rate value (around $x = 0.01$ m in Fig. 4.1(a)).

Beside the planar premixed configuration above, another commonly studied configuration is the spherical premixed flame kernel. Fig. 4.2 shows the typical flame profiles, this time in the reaction progress variable space, defined in terms of reduced temperature [5]:

$$C = \frac{T - T_u}{T_b - T_u} = \begin{cases} 0 & \text{fresh gas mixture} \\ 1 & \text{burnt gases} \end{cases} \quad (4.1)$$

where T_u and T_b are the unburnt and burnt gas temperatures, respectively. C is a non-dimensional variable which describes the local chemical state between unreacted and fully reacted mixture. For a sufficiently large radius, the corresponding flame structure is more or less the

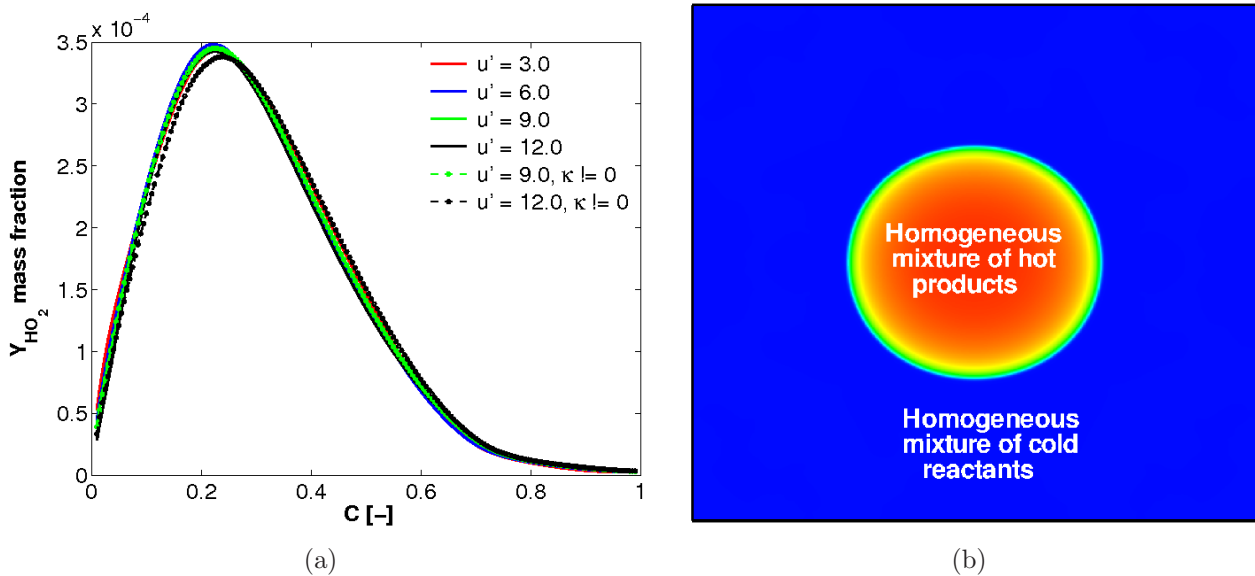


Figure 4.2: (a) Typical turbulent spherical premixed CH₄/air flame structure and (b) 2D numerical configuration showing respectively, profiles of the mass fraction of HO₂ species in the progress variable space and the 2D temperature field, computed using detailed transport and chemistry models

same as that of the planar configuration. In both cases, a strong temperature gradient is often observed as the flame front is traversed. As the flame front propagates towards the fresh gases (due to the imbalance between diffusion of heat and chemical consumption), the reactants (O₂, H₂, CO, CH₄) are consumed and products (CO₂, H₂O) are formed.

Premixed combustion phenomena have a characteristic velocity scale, S_L – the laminar burning velocity (typically 0.1 – 2.0 m/s) and a characteristic length scale, δ_{th} – the flame thickness. These parameters are used to define different regimes in premixed combustion regime diagrams (see for example [6]). The diagrams are usually based on the comparison between the turbulent and chemical length scales and time scales with regimes defined based on different non-dimensional parameters.

A strong advantage of the premixed combustion mode is in its capacity to reduce the production of NO_x under lean conditions. On the other hand, combustion instabilities and safety issues lead to new difficulties. Due to the self-propagating nature of premixed flames, complex and often difficult techniques are sometimes needed to anchor the flame front in a fixed position for proper application. Examples of premixed combustion include lean-burn gas turbines and homogeneous charge spark ignition engines.

4.2.2 Non-premixed combustion

In non-premixed or diffusion combustion, the fuel and oxidizer are initially separated. Both mixing and burning processes occur in the combustion chamber. Figure 4.3(a) shows a typical laminar non-premixed flame structure in physical space, while Fig. 4.3(b) depict the corresponding two-dimensional numerical configuration of the same CO/H₂-air system considered above. The mixture fraction Z is a key parameter analogous to the reaction progress variable. It plays

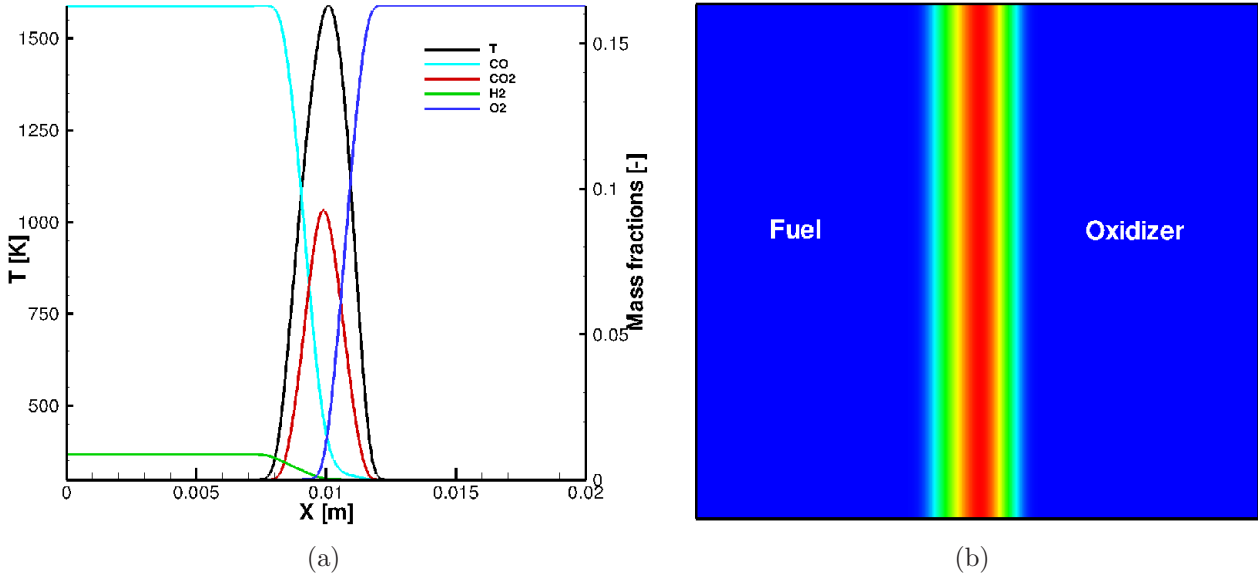


Figure 4.3: (a) Typical laminar non-premixed CO-H₂/air flame structure and (b) 2D numerical configuration showing respectively, one-dimensional profiles of temperature and different species mass fractions and the temperature field, computed using detailed transport and chemistry models

a vital role in the description and analysis of non-premixed combustion. It is a non-dimensional variable that describes the level of mixing between the reactants in the flame front and allows a formal decoupling between turbulent mixing on one hand and a description of the local flame structure in the mixing space (or Z -space) on the other hand. For hydrogen combustion, there exists a well-established definition [77]:

$$Z = \frac{0.5(Z_H/W_H) + (Z_O^\infty - Z_O)/W_O}{0.5(Z_H^\infty/W_H) + (Z_O^\infty/W_O)} = \begin{cases} 0 & \text{pure oxidizer} \\ 1 & \text{pure fuel} \end{cases} \quad (4.2)$$

where W denotes molar weight, Z_j the mass fraction of element j in the mixture, and ∞ initial compositions on oxidizer and fuel sides. In the present work, most of the analysis of diffusion flames will be carried out in the Z -space.

In non-premixed combustion, the time for turbulent mixing is usually much longer than the chemical time scale [6]. As a result, the mixing process is often the rate-controlling process. It is observed that the reaction rates of non-premixed combustion are closely related to the state of mixing [7]. Diffusion flames are different from their premixed counterpart in that they have no characteristic velocity nor length scale. The flame thickness is also not constant and depends on the local flame properties. Non-premixed combustion does not exhibit a self-induced propagation mechanism as in premixed flames.

Due to the high temperatures often present in the resulting flame front, this burning mode has the disadvantage of producing more pollutants. But on the other hand, the resulting flames are very stable and fuels can often be stored beyond their flammability limits. Examples of appliances in which non-premixed combustion is present include diesel engines and furnaces, where the fuel is supplied separately.

Approach	Advantages	Drawbacks
RANS	<ul style="list-style-type: none"> - coarse numerical grid - geometrical simplification (2D flows, symmetry, etc) - reduced numerical costs 	<ul style="list-style-type: none"> - only mean flow field - models required
LES	<ul style="list-style-type: none"> - access to unsteady features - reduced modeling impact (compared to RANS) 	<ul style="list-style-type: none"> - models required - 3D simulations required - needs accurate codes - numerical costs
DNS	<ul style="list-style-type: none"> - no models for turbulence-combustion interactions - tool for modeling investigations 	<ul style="list-style-type: none"> - prohibitive numerical costs (fine grids, very accurate codes) - limited to academic problems yet

Table 4.1: Comparison between the RANS, LES and DNS approaches for numerical simulations of turbulent reacting flows

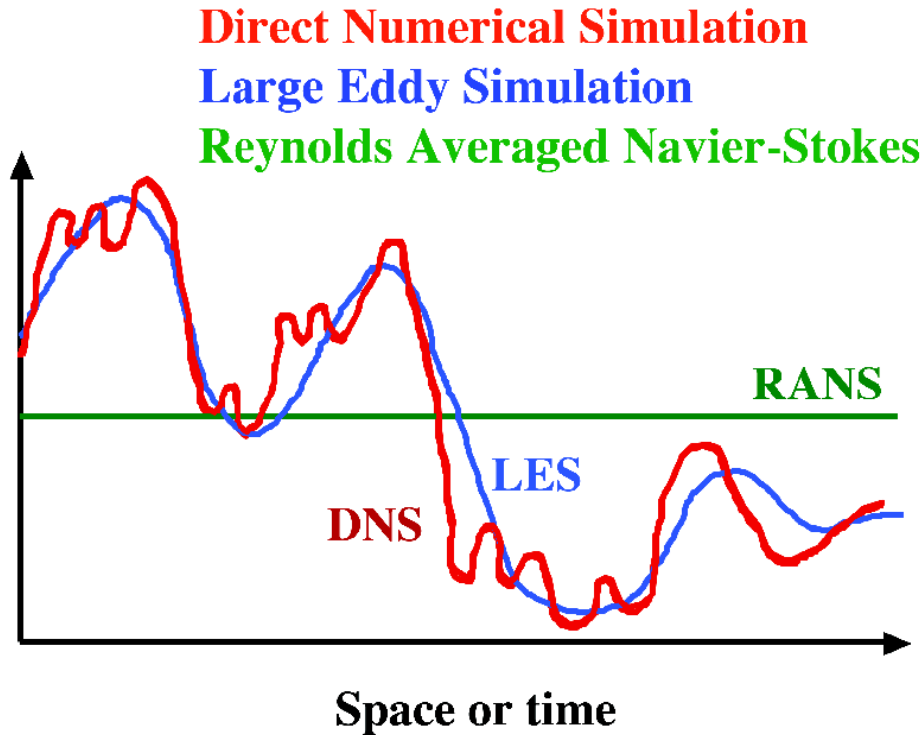


Figure 4.4: Schematic picture of differences between the RANS, LES and DNS approaches for numerical simulations of turbulent combustion: RANS delivers only a mean value, LES part of the fluctuations, DNS the exact solution.

4.3 Numerical combustion approaches

The major Computational Fluid Dynamics (CFD) strategies for turbulent combustion simulation include Reynolds-Averaged Navier-Stokes (RANS), Large Eddy Simulation (LES) and Direct Numerical Simulation (DNS) methods. A comparison between these three approaches is summarized in Table 4.1 [1] and Fig. 4.4. In this section, a brief outline is presented for the RANS and LES techniques (for which we encourage the interested reader to consult appropriate references such as [5]), while a detailed presentation is given here and in the following sections for the DNS approach, since it is the simulation strategy used through out this thesis work.

4.3.1 Reynolds-Averaged Navier-Stokes (RANS)

The RANS approach obtains the mean flow field by solving the averaged governing equations [5–7, 78, 79]. Each quantity Q is decomposed into a mean value \overline{Q} and a deviation Q' away from the mean: $Q = \overline{Q} + Q'$, where $\overline{Q'} = 0$. The instantaneous balance equations may be ensemble or time-averaged to derive the transport equations for \overline{Q} . This Reynolds averaging procedure leads to unclosed terms such as $\overline{u'Q'}$, which need to be modeled. This method has been widely used in simulations of non-reacting turbulent flows. In turbulent combustion, because of the fluctuations in density caused by heat release, Reynolds averaging generates unclosed terms including fluctuation correlations involving density. To avoid explicitly modeling such correlations, a Favre (mass-weighted) averaging of Q is introduced.

A RANS simulation solves for the averaged quantities, providing the statistical means of scalars associated with turbulent flames. Because of the strong unsteady mixing effects observed in turbulent combustion, such mean properties are not always sufficient to describe the flames. It only serves the purpose of identifying trends. As an alternative, Large Eddy Simulation may be used.

4.3.2 Large Eddy Simulation (LES)

The LES [2] approach is a compromise between the extremely expensive DNS and (perhaps overly) simple RANS methods. It explicitly computes the large scale structures (like in a DNS) that are larger than the mesh size, while modeling the effects of small scale structures as in RANS. Although its application in turbulent combustion [3] is still at an early stage (relative to its wide use in non-reacting flows), it remains a promising method because of the following features:

- Compared to DNS, LES only solves for large structures, which is computationally more affordable.
- The unsteady large scale mixing is simulated, instead of being averaged as in RANS.
- LES might capture the instabilities caused by the interactions between heat release, hydrodynamic flow and acoustic waves.

The balance equations for LES are derived via a spatial filtering of the instantaneous balance system (2.1)-(2.5) [5]. That is, in LES, a quantity Q is filtered in the spectral space where components larger than a given cut-off frequency are suppressed, or in the physical space where weighted averaging of the quantity is performed in a given volume. Q may be decomposed into a filtered component \overline{Q} and a fluctuating component Q' such that $Q = \overline{Q} + Q'$. From the filtered balanced equations, the unclosed terms include Reynolds stresses, the species and enthalpy fluxes, filtered laminar diffusion fluxes and filtered chemical reaction rates. Reynolds stresses are usually evaluated using a subgrid scale (SGS) turbulence model. Common SGS models include Smagorinsky models [80] and dynamic Smagorinsky models [81–83]. In a standard dynamic procedure, the coefficients of the SGS model are solved by assuming that they are the same at the grid and test-filter level. The dynamic subgrid models usually have better performance. A comprehensive review of LES for turbulent combustion is presented in [4].

LES has been successfully used to study a wide variety of turbulent reacting flows. Since neither RANS nor LES resolves the smallest scales, at which the rate-controlling molecular mixing processes and chemical reactions occur, the formulations of these two methods both require modeling of these scales. Therefore, most of the RANS combustion models may be modified and applied in LES.

A compressible LES turbulent flame solver called *AVBP* will be briefly presented in Sect. 4.4.3, though used during this thesis work for DNS-like simulations.

4.3.3 Direct Numerical Simulations

Direct Numerical Simulation (DNS) is the most powerful tool to predict and simulate compressible turbulent flows since it literally resolves the system of equations describing the physical processes. In other words, DNS consists in solving exactly all the physical space and time scales embedded in the representative system of equations, without any model for turbulence. A combustion DNS must thus provide an exact solution for both fluid dynamics and flame structure. In particular, the balance equations (2.1)-(2.5) are solved directly after discretization. Meshes used in DNS need to be fine enough to resolve correctly both the largest and smallest eddies in the turbulent flow. For a computational domain of size L discretized by N grid points in each coordinate direction, the typical cell size is $\Delta x = L/(N - 1)$. Comparing the largest and smallest scales in the flow is equivalent to relating the turbulent Reynolds number (Re_t), the integral (l_t) and Kolmogorov (η_k) length scales:

$$\text{Re}_t = \frac{u' l_t}{\nu}; \quad \eta_k \simeq \frac{l_t}{\text{Re}_t^{3/4}} \quad (4.3)$$

where u' and ν are the root mean square (rms) velocity and kinematic viscosity, respectively. Therefore, the size of the computational domain should be at least of the order of the integral scale ($L \geq l_t$) while the mesh size should be less than the Kolmogorov ($\Delta x < \eta_k$) [5].

A resolution constraint is equally imposed by the chemical scales present in the chemical scheme used. The flame thickness δ_{th} must extend across a number of grid points Q , such that $L \simeq (N/Q)\delta_{th}$. Defining a mechanical time scale $\tau_t = l_t/u'$ and a chemical time scale $\tau_c = \delta_{th}/S_L$, the Damköhler number (Da) is related to the Reynolds number by

$$\text{Re}_t \text{Da} = (l_t/\delta_{th})^2 \quad (4.4)$$

leading to the grid condition $\text{Re}_t \text{Da} < (N/Q)^2$ [5]. Typical spatial resolutions range around 20 μm for multi-dimensional, multi-component direct simulations. Temporal resolution are generally governed by conditions such as the CFL and Fourier constraints.

From all indications, the computational cost to resolve all these relevant continuum scales, which might differ in order of magnitude by up to three decades, is very high. To simulate a real flow with large Reynolds number, the number of cells needed can be overwhelming [84]. Moreover, the number of scalars that need to be solved for in turbulent combustion is often very large. A detailed chemical kinetic system might include tens or hundreds of species and reactions. Lastly, the boundary and initial conditions of a practical system are often difficult to define in DNS. Consequently, DNS is mostly used to analyze turbulent flames in simple and/or canonical configurations [85–87] such as homogeneous isotropic turbulent flows and mixing layers.

Even though this method requires prohibitive numerical costs for practical configurations, it offers an excellent complement to experiments in order to assess the importance of various physical mechanisms and obtain complementary information on flame structure. Moreover, it serves as a tool for fundamental studies of the micro-physics of turbulent reacting flows and the development and validation of reduced model description used in macro-scale simulations of engineering-level systems. Hence it goes a long way to improve turbulent combustion modeling [7, 11, 31, 37, 38, 46–48, 50, 88–96, 96–107].

To summarize, a good DNS can be referred to as a *numerical microscope* or *numerical experiment* if and only if it can

- resolve all relevant continuum scales in the representative equations,
- provide a high-fidelity computer-based observation of the micro-physics of chemistry-turbulence interactions,

Code	Tabulated chemistry	Complete reaction scheme
Compressible	$\pi^3\text{C}$	<i>Parcomb</i> (2D)
Low-Mach number	π^3	<i>Parcomb</i> (3D)

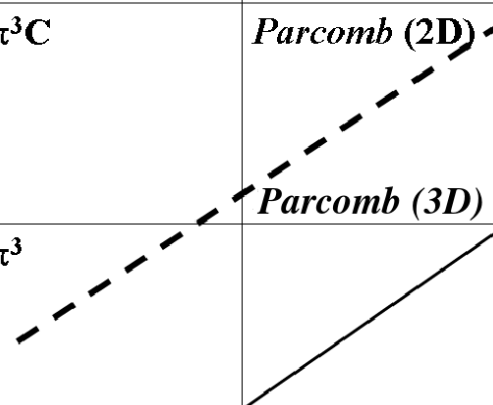

Growing accuracy & numerical cost

Figure 4.5: Main characteristics of the *parcomb* and π^3 DNS code families employed in this work

- tackle building-blocks and canonical configurations, and
- offer low error tolerance via efficient high-order discretization methods.

These attributes and more will be cross-examined below, for practical direct simulations using three different DNS solvers.

4.4 Employed research tools

Two DNS and one LES/DNS specific and dedicated numerical research codes have been used to obtain the results presented later. All three codes were employed for fundamental studies of turbulent reacting flows. Though the *parcomb* and π^3 DNS code families are very similar in their building bricks and global structure, they also show noticeable differences depending on the specific problem that must be investigated. The *parcomb* family considers only complete reaction schemes, while the π^3 family relies on tabulated chemistry to describe reaction processes. In addition, both compressible and low-Mach number formulations are available for the π^3 family. The final specialization of the different codes is shown in Fig. 4.5. Towards the end of the thesis, the industrial LES/DNS solver *AVBP*, was used in conjunction with a DNS-like gridding to simulate a three dimensional spatially developing turbulent lean premixed methane–air Bunsen flame at CERFACS. Since all codes have been used at some point during this thesis, the common features and main differences are discussed in what follows.

4.4.1 Compressible DNS solver: *parcomb*

The two-dimensional version of *parcomb* was originally developed by Thévenin and co-workers [31, 49, 108–111], corresponding to the available computing power on supercomputers at that time (almost 20 years ago). The current derived three-dimensional version has been rewritten in modular FORTRAN 95 and in collaboration with ONERA [112]. *parcomb* has been widely used over the last two decades to investigate various properties of turbulent flames (see for example [49, 110, 113]). In what follows, we present details of the recently upgraded modules and numerics at the University of Magdeburg, focusing mostly on code structure, parallel I/O, parallel performance and optimization.

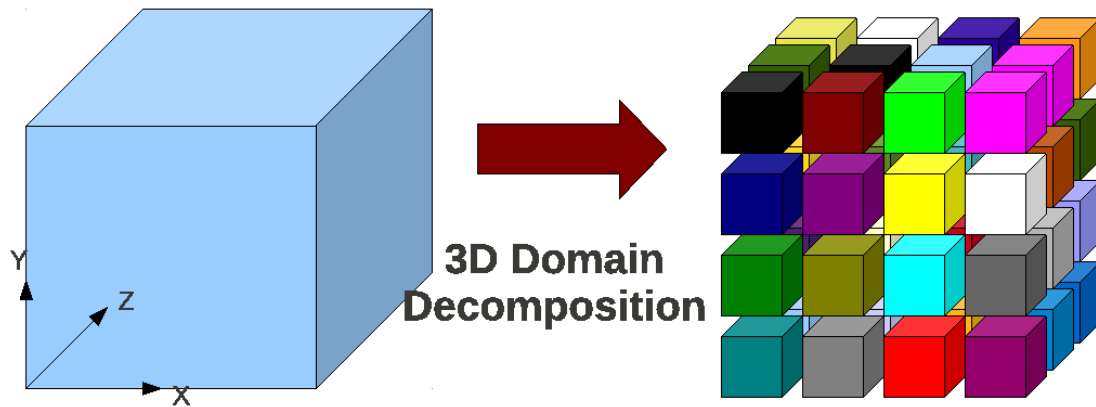


Figure 4.6: *parcomb*: a block partitioning domain decomposition into $4 \times 4 \times 3 = 48$ MPI task in memory

4.4.1.1 Numerical method

parcomb is a finite-difference DNS code that solves the full compressible Navier-Stokes equations for multicomponent reacting flows with detailed and accurate physical and chemical models. The parallelization of *parcomb* relies on three-dimensional domain-decomposition. Each node thus controls a sub-domain of the global computational domain, consisting of blocks as illustrated schematically in Fig. 4.6. Derivatives are computed using centered explicit schemes of order six except at boundaries where the order is progressively reduced to four. During the upgrading process, an improved numerical scheme, the *skew-symmetric* formulation [114] was implemented for the convective terms, in order to further increase stability. According to this scheme, the derivative of a general convective term can be written as:

$$\frac{\partial(\rho u_j)}{\partial x_j} = \frac{1}{2} \frac{\partial(\rho u_j)}{\partial x_j} + \frac{a}{2} \frac{\partial(\rho u_j)}{\partial x_j} + \frac{\rho u_j}{2} \frac{\partial a}{\partial x_j} \quad (4.5)$$

As a consequence, the transported quantities are globally conserved for a given viscosity approaching zero.

Time integration is performed in an explicit manner with a fourth-order Runge-Kutta scheme, since implicit methods do not seem to be beneficial for our problems [115] and prove to be difficult to parallelize efficiently. The time step is controlled by two independent mechanisms. A Courant-Friedrichs-Levy (CFL) condition and a Fourier condition (for the diffusion terms) are tested in order to ensure the stability of the explicit integration.

Boundary conditions are treated with the help of the Navier-Stokes Characteristic Boundary Condition (NSCBC) technique [76], extended to take into account multicomponent thermodynamic properties [116]. This allows in particular to obtain non-reflecting conditions at the boundaries.

Transport coefficients and chemical kinetics are treated following methods similar to those used in the standard packages *chemkin* and *transport* [39, 59]. *Parcomb* employs complete reaction schemes to describe chemical reactions. During this thesis, direct simulations of turbulent flames have been carried out using detailed chemical kinetic schemes for hydrogen (H_2 : 9 species, 38 elementary reactions) [40], syngas (CO/H_2 : 13 species, 67 elementary reactions) [42] and methane (CH_4 : reduced scheme with 16 species, 25-step reactions) [43] oxidation.

The numerical domain employed when using *parcomb* to investigate turbulent flame properties is a two-/three-dimensional square/cubic box of dimension L_{box}^2/L_{box}^3 , typically a few centimeters in each direction. Figs. 4.1(b) and/or 4.3(b) are examples of typical numerical configuration employed for two-dimensional computations. Often, a fixed mesh is used in each direction, with a typical spatial resolution between 20–50 μm , necessary to resolve accurately all intermediate chemical radicals as well as the dissipation scale of turbulence. For (turbulent)

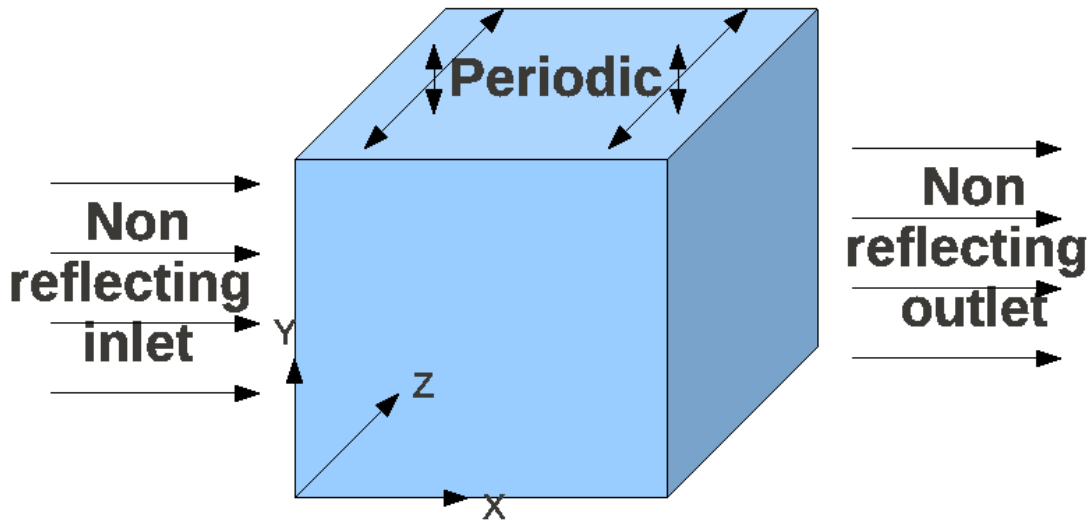


Figure 4.7: Sketch of a 3D computational domain showing typical boundary conditions

planar premixed computations, the left-hand boundary condition is usually a subsonic inlet with imposed value of velocity, while the right-hand boundary condition is a non-reflecting subsonic outlet, both implemented using the NSCBC technique. The remaining boundary conditions are periodic. These are all illustrated in Fig. 4.7. *parcomb* has been used within this thesis work to investigate both premixed and non-premixed flames burning hydrogen, syngas or methane with detailed models.

4.4.1.2 Data Input/Output enhancement

The computations realized with *parcomb* on massively parallel computers are large and I/O-intensive. The first straight forward and traditional I/O approaches in parallel applications is when simulated data from each participating processor is sent to a master processor, which collects them and writes out to disk as a single file. Next to this is the situation where each process writes its sub-array to a new and separate file at each checkpoint. This often requires an additional post-processing step, without which restarts must use the same number of processors. The most efficient approach is when each processor calculates its position in a shared file and writes its array individually in a canonical order. As such there is only one file created per checkpoint, regardless of the number of MPI processes used.

The first two approaches are simple, but offer poor performance (single process writes to one file) and/or are awkward and not inter-operable with other tools (each process writes a separate file). In this section, we focus on how to achieve high performance by moving from sequential to parallel I/O (MPI-IO), demonstrated by its implementation into *parcomb*.

Sequential I/O

In this approach, all MPI processes send their data (sub-array) to a root process P_0 , and P_0 then writes it to the file. The procedure is illustrated by the schematic diagram in Fig. 4.8(a). Such an I/O strategy could proved advantageous in situation where

- The parallel machine may support I/O only from one process (i.e. no common file system).
- Some I/O libraries may not be parallel.
- Resulting single file is handy for **ftp**, **mv**, etc.
- Big blocks improve performance.

- Short distance from original, serial code.

A major and crippling disadvantage of this I/O paradigm is that its lack of parallelism limits code scalability and performance. This single node bottleneck rapidly outweighs all the above advantages in the light of today's HPC capabilities.

Semi-Parallel I/O

In a slightly improved approach, each process writes its chunk of data/sub-array to a separate file at each checkpoint, as illustrated in Fig. 4.8(b). Such a measure offers some parallelism and relative gain in performance. On the other hand, we end up with lots of small files to manage together with the difficulty of reading back these data files from a possibly different number of MPI processes for a restart.

Parallel I/O

The optimal file I/O technique would be to have each MPI process of a parallel application to have write and/or read access to a common/shared file at the same time. Such a scenario is illustrated in Fig. 4.8(c). Writing is then likened to sending a message and reading to receiving a message, making MPI a good setting for such a process. One outstanding advantage of using such a robust parallel I/O is that it provides high performance and a single solution/data file that can be used directly with many different visualization tools.

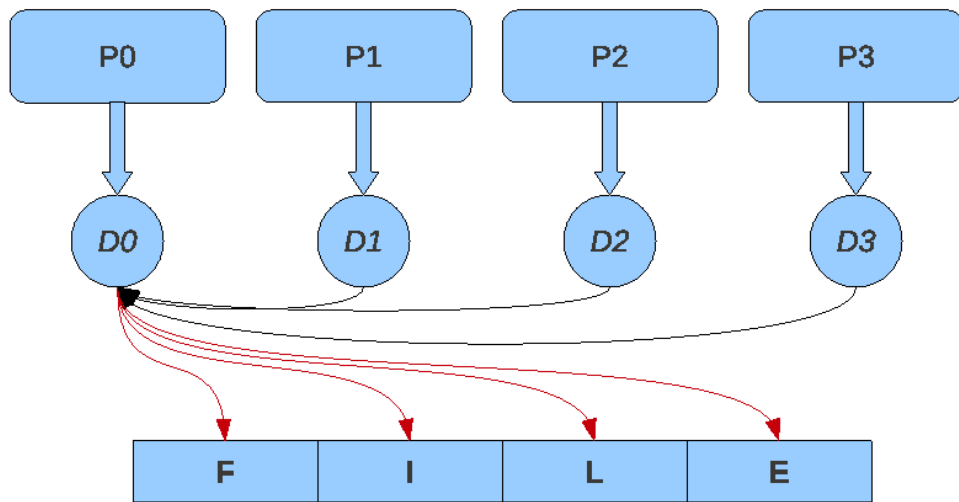
I/O implementation and performance

The functionality of the parallel read and write procedures via MPI I/O have been properly added into *parcomb*. It is a recommended option to the originally sequential I/O via Fortran read/write functions. We measured the execution time for dumping restart files for all the primitive variable in a typical production size computation where the load per process is kept constant at $50 \times 50 \times 50$ grid points. Figure 4.9 compares the dumping time with number of computing cores for the sequential and full parallel I/O procedures. The overall measured file writing times show a huge reduction when using MPI-IO. The performance is significant and gets better with increasing number of parallel processes. When using 320 computing cores, writing/reading of solution/restarting data files for a given file dumping/retrieval instance with MPI-I/O outperforms its sequential counterpart by over 50% in terms of measured CPU time, offering considerable enhancements for parallel performance and a speedup in the overall computing time.

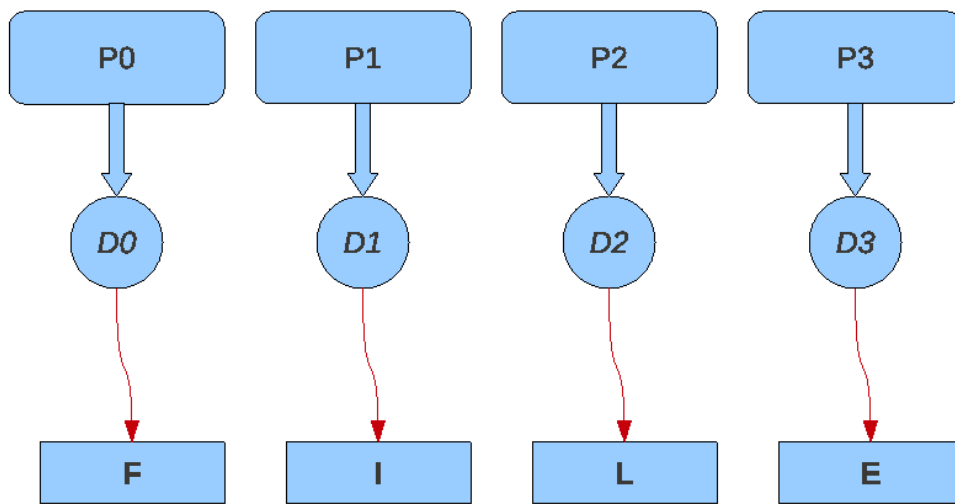
4.4.1.3 Parallel performance and optimization

A general overview of the single- and multi-processor performance of *parcomb* is shown for the *IBM POWER5 cluster (HPCx)* system at EPCC, Scotland (which provides a total of 1536 processors, delivering at least 6 Tflop/s sustain) and the *IBM BlueGene/P (BABEL)* system at IDRIS, France (offering 40960 cores PowerPC 450 for a total peak performance of 139 Tflops). Similar experiments have also been carried out on the vector *CRAY/X2 (HECToR)* machine at EPCC.

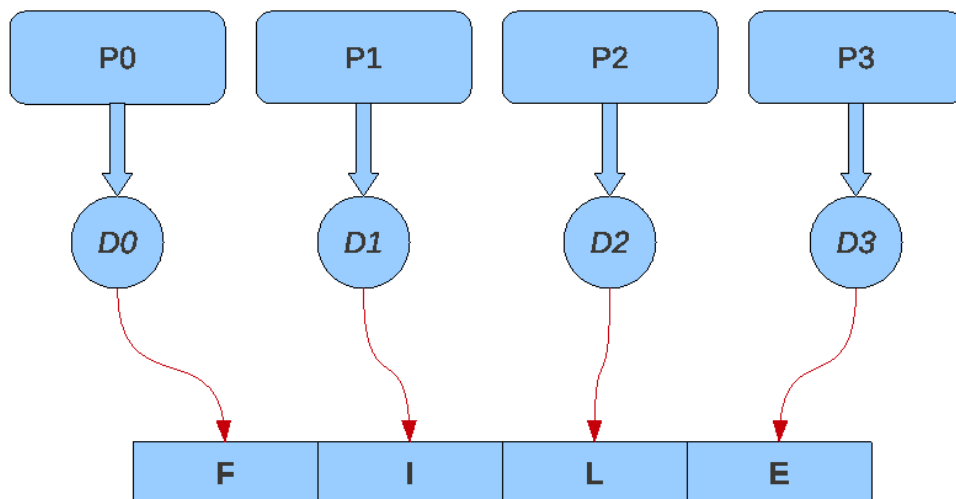
The code performance and scaling is hereby evaluated by simulating a three-dimensional laminar spherical premixed flame kernel evolution with time. Flames with both detailed CO-H₂ and H₂ chemistry, consisting of 13 and 9 chemical species, respectively, together with a multicomponent molecular transport model were simulated. The problem size is kept at $50 \times 50 \times 50$ grid points per core, which is a typical load per MPI process in production simulations. The code performance is measured in terms of scaled world clock time (WCT) per number of time steps.



(a) Sequential I/O



(b) Semi-parallel I/O



(c) Parallel I/O

Figure 4.8: Data Input/Output strategies

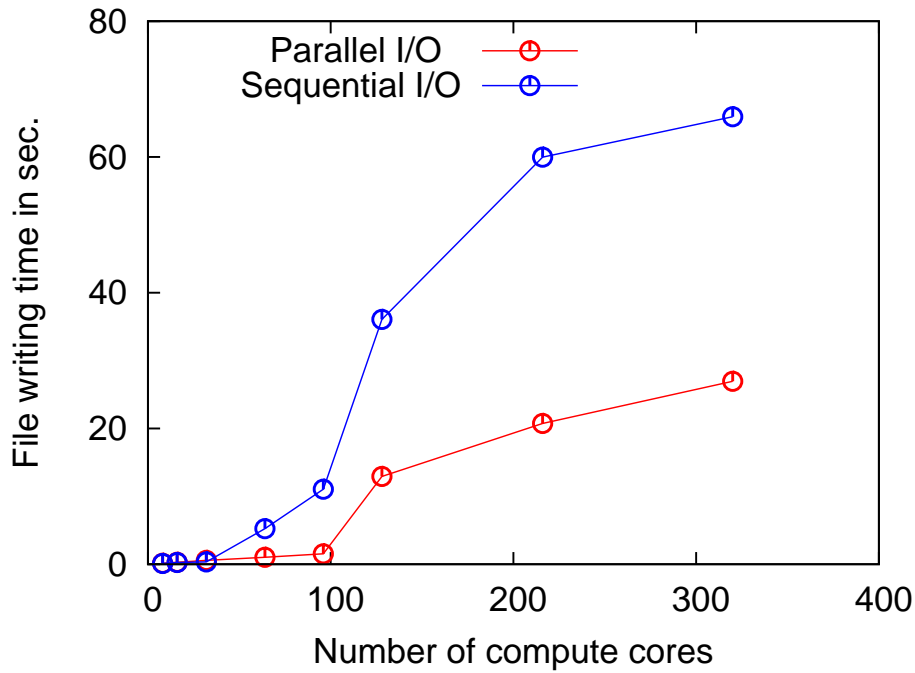


Figure 4.9: *parcomb*: Restart file dumping time vs. number of computing processors for the sequential and full parallel I/O

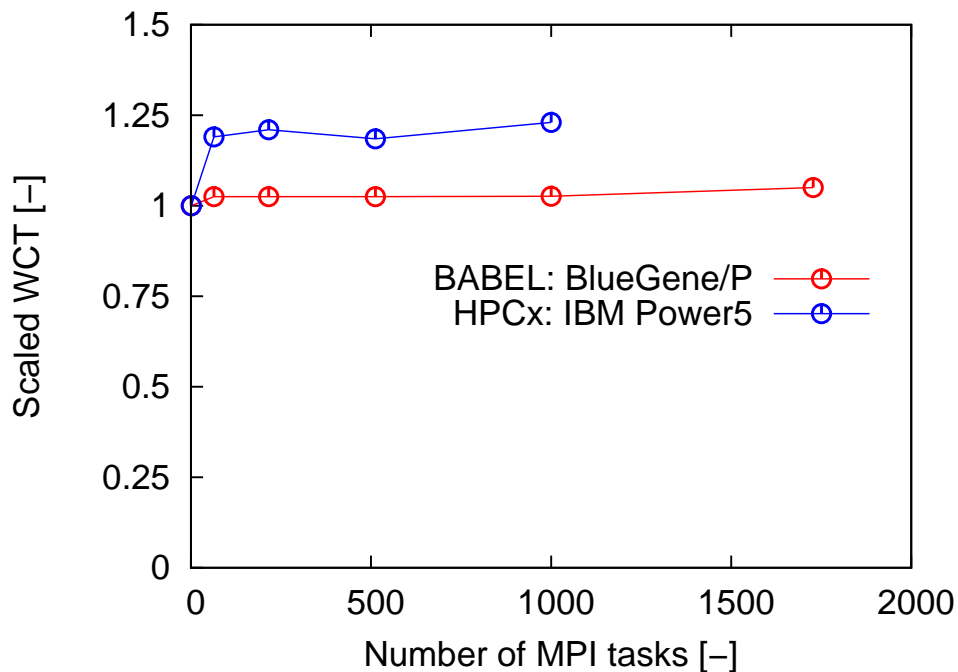


Figure 4.10: *parcomb* parallel scaling on the *IBM BlueGene/P* and *IBM POWER5* for a full 3D simulation

Single-processor performance

The *hpmcount* utility of the Hardware Performance Monitor (HPM) Toolkit is used in conjunction with *parcomb* to provide information on execution time (WCT), hardware performance counters, hardware metrics and resource utilization statistics. The Flop rate (flops/WCT) or simply the famous MFLOP/s metric is the quantity of great interest. From the given values and the peak performance of the system stated above, the percentage of peak performance attained with *parcomb* on the HPCx system is directly computed to be 13.4%. According to IBM, if a real-world application obtains a performance exceeding 10% of theoretical peak performance,

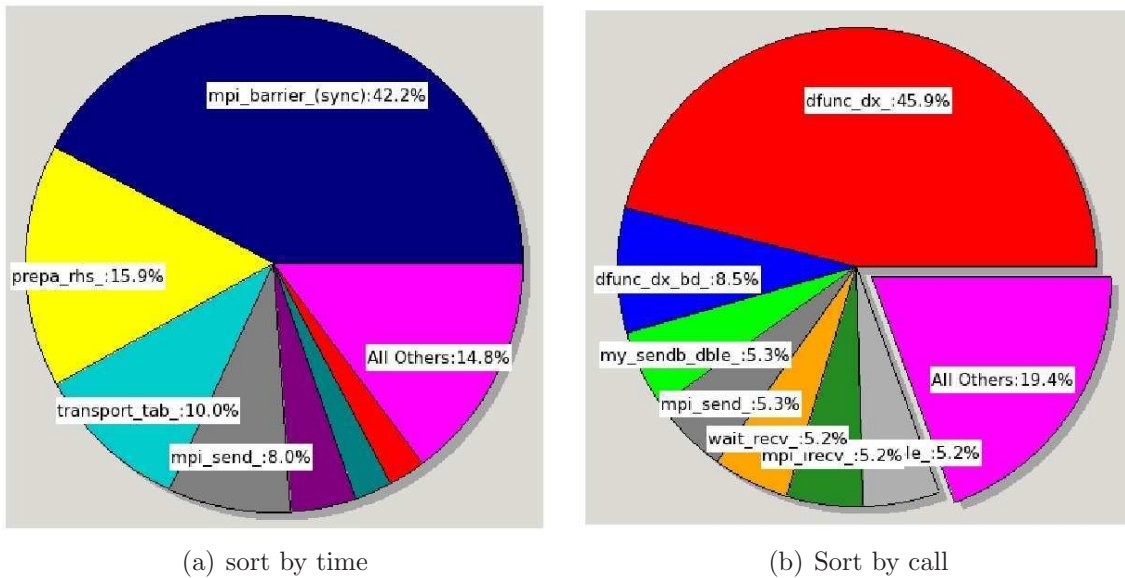


Figure 4.11: *parcomb* subroutines profiling

then that application is making good use of the machine resources. Hence *parcomb*'s performance is within a good range.

Multi-processor performance

It should be noted that, since the problem size per MPI task is kept constant, the parallel scaling experiments demonstrated in the following plots are a weak one. A perfect parallel scaling would manifest itself as a flat scaling curve, meaning that the cost of computations does not increase when larger number of processors are utilized. Fig. 4.10 demonstrates and compares the performance scaling for a full 3D problem on *HPCx* and *BABEL*. The scaled WCT is plotted against the number of cores used. The performance is near perfect between 64 and 1024 processes and is far much better on the BlueGene/P for the same number of processors. As already mentioned, the domain is increased with increasing processor number, hence all runs have the same resolution of $20 \mu\text{m}$ and load of 50^3 points per MPI task. We can comfortably claim that the scalability of *parcomb* on both systems is near perfect for the number of processes considered. There is an extra cost incurred when passing from a single to multiple processes, definitely due to the MPI inter-process communication. This cost is higher on *HPCx*. On the other hand, a relatively higher performance is observed on both machines when 512 cores are employed. One possible explanation could be that 512 processes (which corresponds to a half rack on *BABEL*) fits squarely into a *TORUS* connection (forming a perfect cube), thereby reducing inter-node communication.

Subroutine profiling

A graphical representation of the profiling (sorted by execution time and by number of calls) of each of the most expensive routines in *parcomb* is shown in Fig. 4.11. Such information is vital as to which routines need source level optimization. It is interesting to note that the most solicited routine is among the least time consuming routines.

4.4.2 Incompressible DNS solver: π^3

In this subsection, we present briefly a second-generation three-dimensional DNS code, π^3 [50, 95, 117, 118], written in modular Fortran 95. A strong reduction in computing times is achievable

by combining two reduced models for the numerics and chemistry. Two versions of the code exist – a compressible (suitable in particular for flame/acoustic investigations) and an incompressible (low-Mach number) version. All the comments in this thesis are for the latter and most efficient version. We refer the reader to Sects. 3.4 and 3.5 of chapter 3 for a detailed outline of the physical models and numerical methods employed in π^3 , in particular, the FPI chemistry reduction technique and the low-Mach number formulation, respectively.

4.4.2.1 Numerical method

π^3 is also an explicit finite difference solver and uses similar numerical techniques to compute spatial derivatives and to perform time-integration. But the low-Mach number approximation leads to a two-stage integration of the momentum equation (3.26).

Starting from the (known) momentum value at step n , the prediction step is first used to estimate the new momentum terms and is written, using standard notations:

$$(\rho \mathbf{u})^* = (\rho \mathbf{u})^n + \Delta t [-\nabla \cdot (\rho \mathbf{u} \otimes \mathbf{u}) + \nabla \cdot \boldsymbol{\tau}] \quad (4.6)$$

We then solve a Poisson equation for the pressure fluctuation \tilde{p} , using a finite-difference estimation of density changes:

$$\nabla^2 \tilde{p} = \frac{1}{\Delta t} \left[\left(\frac{\partial \rho}{\partial t} \right)^{n+1} + \nabla \cdot (\rho \mathbf{u})^* \right] \quad (4.7)$$

Finally the momentum values are corrected to take into account the actual pressure value by

$$(\rho \mathbf{u})^{n+1} = (\rho \mathbf{u})^* + \Delta t [-\nabla \tilde{p}] \quad (4.8)$$

The pressure splitting is also introduced in the state law for perfect gas, which becomes $p_0 = \rho r T$. It can be seen in this equation that we therefore suppress the coupling between the fluctuating pressure \tilde{p} and the density. As a consequence, the Euler system is modified and acoustic waves are neglected.

This methodology is an extension to reactive flows of algorithms employed for incompressible non-reactive flows [72]. The dilatation induced by heat release is taken into account through the introduction of the density variation term $(\partial_t \rho)^{n+1}$. This term is evaluated numerically in the code using a third-order backward finite-difference formulation:

$$\left(\frac{\partial \rho}{\partial t} \right)^{n+1} = \frac{1}{\Delta t} \left[\frac{11}{6} \rho^{n+1} - \frac{6}{2} \rho^n + \frac{3}{2} \rho^{n-1} - \frac{2}{6} \rho^{n-2} \right] \quad (4.9)$$

In this approach the continuity equation is a constraint, which is taken into account through the dilatation term $(\partial_t \rho)^{n+1}$. It is known that the finite-difference approximation of this term can lead to numerical errors [119] and other techniques have been proposed. For example, a velocity divergence constraint can be derived from the continuity equation and introduced in a Poisson equation with variable coefficients. We do not use this more complex method here. We have observed that, in real cases involving viscous flows and thermal conductivity, the error introduced by the numerical approximation of $(\partial_t \rho)^{n+1}$ is negligible compared to the magnitude of physical effects. The procedure is described in detail in [11], and similar low-Mach number methods have been successfully applied by other authors to various reacting flows [120–126]. Boundary conditions are simply given by the Neumann (zero-gradient) and Dirichlet (constant value) conditions, since characteristic boundary conditions cannot be used here.

4.4.2.2 Poisson solver

The global accuracy of results obtained with π^3 depends on the level of accuracy obtained when solving the Poisson equation for pressure, which is a key point of the low-Mach number formulation. In the present study, we investigate only configurations that involve periodic and inlet/outlet boundary conditions. Generally, we use spectral methods along periodic directions while fourth-order compact schemes [76] corresponding to the classical Padé approach are employed along stream-wise directions for non-reflecting inlet/outlet conditions. In what follows, the various steps are given for the case with periodic boundary conditions in all directions (we refer the interested reader to [11] for the case with inlet/outlet or mixed boundary conditions). For the all periodic case, the integration of the Poisson equation is simply performed as follows:

$$\frac{\partial^2 \tilde{p}}{\partial x^2} + \frac{\partial^2 \tilde{p}}{\partial y^2} + \frac{\partial^2 \tilde{p}}{\partial z^2} = f(x, y, z) \quad (4.10)$$

where x , y and z are the spatial co-ordinates and f is the source term given in the right-hand-side of eq. (4.7). On a uniform 3D grid, the algorithm for the sequential Poisson solver consist of five main steps:

1. Diagonalize $\frac{\partial^2 \tilde{p}}{\partial x^2}$ by performing a FFT in the x -coordinate direction (FFT _{x}).
2. Repeat step 1 for the y - and z -coordinate directions (FFT _{y} and FFT _{z}). At this stage, eq. (4.10) can be rewritten in the Fourier space as [11]:

$$-\theta_x^2 \hat{\hat{p}} - \theta_y^2 \hat{\hat{p}} - \theta_z^2 \hat{\hat{p}} = \hat{\hat{f}}(\theta_x, \theta_y, \theta_z) \quad (4.11)$$

where θ_x , θ_y and θ_z are the wave numbers in the x , y and z directions respectively, and $\hat{\hat{\cdot}}$ denotes the Fourier transform.

3. Finalize the direct inversion of eq. (4.11) in the Fourier space by dividing the source term by the sum of the wave numbers squared:

$$\hat{\hat{p}} = - \left[\frac{\hat{\hat{f}}(\theta_x, \theta_y, \theta_z)}{(\theta_x^2 + \theta_y^2 + \theta_z^2)} \right] \quad (4.12)$$

4. Perform an inversed FFT in the z -coordinate direction (FFT _{z} ⁻¹).
5. Repeat step 4 in the y - and x -coordinate directions (FFT _{y} ⁻¹ and FFT _{x} ⁻¹) to transform back to the physical space.

The direct and reverse FFT's are performed using an existing library [127] with a high level of vectorization.

4.4.2.3 Parallelization

The parallelization of π^3 was realized during the present thesis work. As in *parcomb*, it relies on domain-decomposition, but this time only along the y -direction in space, projected onto a corresponding one dimensional processor topology. Each processing core thus controls a sub-domain of the global computational domain as illustrated schematically in Fig. 4.12, for nine planes of data distributed across three processes P_0 (blue), P_1 (green) and P_2 (yellow).

The integration procedure then consists of two successive steps, repeated until the end of the computation. First, each processor carries out an integration step on its own sub-domain independently from the others. Then, all processors communicate the new boundary values

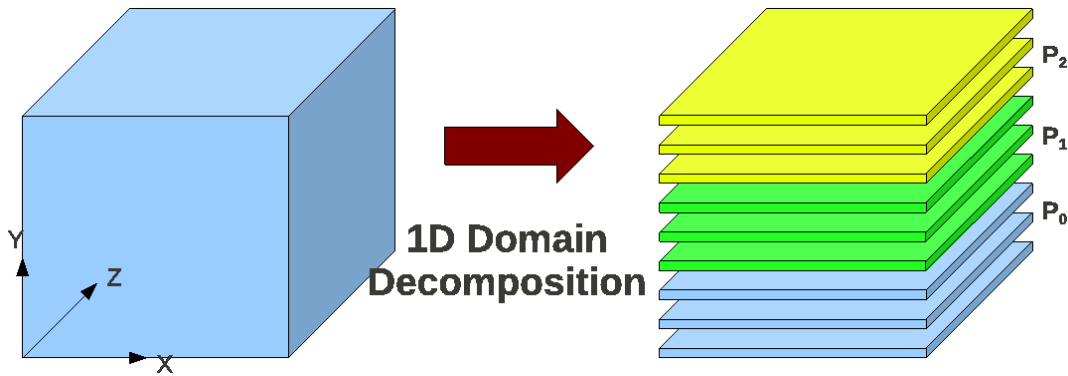


Figure 4.12: π^3 : domain decomposition of nine data planes across three processors P_0 (blue), P_1 (green) and P_2 (yellow)

to their direct neighbors. The next integration step can afterward be started. The grid is equipartitioned among the processors along the y -direction. All communications rely on the Message-Passing Interface (MPI) [128].

We assume that before starting the solution of the Poisson system for the multi-processor case, each MPI task have available in its local memory all nodes and/or planes at some subset of physical space location describing \tilde{p} and f . The layout of memory across processes before and after data exchange is illustrated in Fig. 4.13, again for nine planes of data distributed across three processes P_0 (blue), P_1 (green) and P_2 (yellow). The data in each plane is divided (not shown) into the same number of approximately equal-sized blocks of data, with the number of blocks equating the number of MPI processes involved. The data blocks are ordered by block index.

With such a data distribution, the FFT_x and FFT_z are performed concurrently by each processor on each of its three data planes with no need for communication. Memory is then exchanged across processes (via message passing) in a block transpose and the data is eventually ordered and oriented into vertical x -slices as shown in Fig. 4.13(right). FFT_y is then performed in parallel on each x -slice. The block transposition is the most time-consuming and network contention stage in the algorithm. After dividing the source term by the wave number squared in the Fourier space (see eq. (4.12)), FFT_y^{-1} is then performed on each x -slice. Before performing the FFT_z^{-1} and FFT_x^{-1} , the data is once more block transposed back to its original horizontal y -slice decomposition. This parallel algorithm can be summarized as follows:

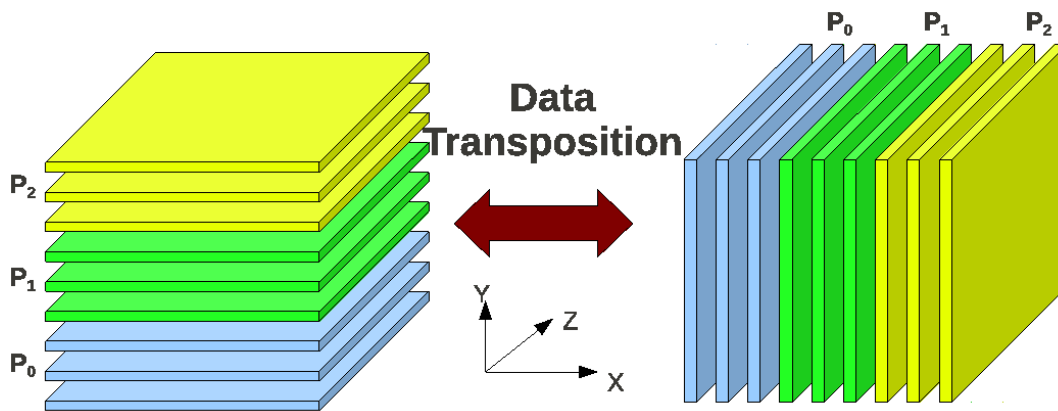


Figure 4.13: π^3 : Arrangement of nine data planes of memory, distributed across three processors, before (left) and after (right) transposition/exchange

1. Perform locally a FFT in the x -coordinate direction (FFT_x).

2. Repeat step 1 for the z -coordinate direction (FFT_z).
3. Transpose the data from a y -slice to an x -slice decomposition.
4. Perform locally a FFT in the y -coordinate direction (FFT_y).
5. Divide the source term by the sum of the wave numbers squared.
6. Perform an inversed FFT in the y -coordinate direction (FFT_y^{-1}).
7. Transpose the data from an x -slice to a y -slice decomposition.
8. Perform an inversed FFT in the z - and x -coordinate direction (FFT_z^{-1} and FFT_x^{-1}).

4.4.2.4 Parallel performance

We define a speedup S_p and parallel efficiency P_e in computing time when using the above algorithm relative to single processor computations as

$$S_p = \frac{T_{1,w}}{T_{n,w}}; \quad P_e = \frac{T_{1,c}}{T_{n,c}} \times 100 \quad (4.13)$$

where T_1 and T_n are the observed elapsed times on a single and n processors, respectively. The second subscripts w and c stand respectively for the wall and CPU times. The experiments were performed on Linux cluster *karman* at the Institute of Fluid Dynamics and Technical Flows, University of Magdeburg. The problem contains $50 \times 400 \times 50$ grid points and was run for at least 300 time steps. Since the minimum number of grid points per processing core is seven, we could not go beyond 40 processors. Here, the amount of data per processor decreases with increasing number of processing cores.

A measure of S_p , P_e and other parallel performance parameters of the implementation for several decompositions is shown in table 4.2. The speedup is observed to vary from 1.72 on 2 processors up to 13.23 for 40 processors. The slow rise in S_p with increasing processors is definitely due to the declining number of floating-point operations per processor compared to the amount of inter-processor data exchanged [129]. Also, computational speed up is already considerable. The 40 CPU run completes in an elapse time of about 26 times less than the single CPU run, although the scaling with CPU is less than linear, as portrayed by the recorded parallel efficiencies.

No. CPU	Wall time per time-steps (hours)	Speedup	Parallel efficiency (%)
$1 \times 2 \times 1$	25.6	1.0	100
$1 \times 2 \times 1$	14.2	1.8	95
$1 \times 4 \times 1$	7.1	3.6	91
$1 \times 8 \times 1$	4.3	5.9	84
$1 \times 16 \times 1$	2.6	9.7	75
$1 \times 20 \times 1$	1.5	16.7	68
$1 \times 40 \times 1$	1.0	25.2	53

Table 4.2: Speedup and parallel performance of the parallel algorithm for several processor decompositions

4.4.3 Compressible LES/DNS solver: *AVBP*

AVBP [130] is a parallel CFD code that solves the laminar and turbulent compressible Navier-Stokes equations in two and three space dimensions on unstructured and hybrid grids. While initially conceived for steady state flows of aerodynamics, the major area of applications is now the modeling of unsteady (reacting) flows. These activities are strongly related to the rising importance paid to the understanding of the flow structure and mechanisms leading to turbulence. The prediction of these unsteady turbulent flows is primarily based on the LES approach. A single-step chemistry model allows to study reacting flows in combustion for complex configurations

The handling of unstructured or hybrid grids is one key feature of *AVBP*. With the use of these hybrid grids, where a combination of several elements of different type is used in the framework of the same mesh, the advantages of the structured and unstructured grid methodologies are combined in terms of gridding flexibility and solution accuracy. In order to handle such arbitrary hybrid grids the data structure of *AVBP* employs a cell-vertex finite-volume approximation. The basic numerical methods are based on a Lax-Wendroff or a Finite-Element type low-dissipation Taylor-Galerkin discretization in combination with a linear-preserving artificial viscosity model.

AVBP is built upon a modular software library that includes integrated parallel domain partition and data reordering tools, handles message passing and includes supporting routines for dynamic memory allocation, routines for parallel I/O and iterative methods. *AVBP* is highly portable to most standard platforms including PCs, work stations and mainframes and has proven to be efficient on most parallel architectures.

Mesh related aspects of *AVBP* are handled by the multi-function grid-preprocessor *HIP*. This proprietary grid manipulation tool allows various operations such as generic solution interpolation between two grids, grid cutting or merging, grid validation, adaptive local grid refinement, grid extrusion or the creation of axi-symmetric grids. The above information can be summarized as follows [130]:

- **Flow configurations:** two and three dimensional flows, external and internal flows; compressible inviscid or viscous flows, steady and unsteady flows.
- **Grid types:** unstructured grids composed of triangles or tetrahedral; unstructured grids with quadrilaterals or octahedral; hybrid grids (additionally prisms and pyramids) and derived elements with "hanging points".
- **Combustion:** premixed and diffusion flames, combustion instabilities, unsteady turbulent combustion using LES; mixing; dynamic models for flame thickening, multiple species; reactive multi-phase flows.
- **Turbulence:** unsteady turbulence simulations based on LES (filtered Smagorinsky and Wale SGS models), k-epsilon RANS turbulence model, wall-functions for LES and RANS, sampling of temporal solution fields.
- **Numerical method:** centered finite-volume cell-vertex space discretization, Lax-Wendroff, SUPG and upwind weighted-residual approaches; linear preserving artificial viscosity model; Runge-Kutta multi-stage time stepping; Finite-Element type Taylor-Galerkin TTGC third order low-dissipation schemes for LES; large choice of non-reflecting characteristic boundary conditions for unsteady flows and internal configurations, pulsed inlet conditions.
- **Parallel computing:** optionally master-slave or SPMD model for shared and distributed memory parallel platforms, implementation on IBM SP4, SGI Origin series 3000, Compaq Dec Alpha, PC clusters under Linux, Sun workstations and Cray XD1; message-passing is based on the Integrated Parallel Macros (IPM - User's Guide and Reference Manual) of CERFACS.

- **Mesh aspects:** moving grids for piston-engine applications, isotropic and anisotropic local grid refinement, recursive refinement on multiple levels, de-refinement, automatic adaptation based on gradient of flow features.
- **Code engineering aspects:** extensive Code Validation Program, version and file management under CVS, on-line documentation (Users Manual and Hand Book), interfaces to commercial grid generation and visualization tools: ICEM-CFD, GridGen, Centaur, Ensign, FieldView, TecPlot, etc.

First applications of *AVBP* for DNS will be discussed later in this document.

4.5 Novel turbulence generation strategies

The generation of an appropriate field for the initial velocity fluctuations for use in turbulent combustion simulations is one complex yet very important issue. Generally, the generation of fluctuation fields, say pseudo-turbulent velocity fields in three dimensions consists of generating fluctuating signals and then transforming them in such a way as to satisfy the Reynolds-stress-tensor or a prescribed energy spectrum of real turbulence. The base method for turbulence generation in *parcomb* is the inverse Fast Fourier Transform (FFT) technique [49], whereby a FFT is applied on a prescribed von Kármán energy-spectrum with Pao correction. The underlying algorithms of this technique together with relevant comments regarding its practical implementation and validation are given in the *parcomb* user manual [131].

Although the FFT technique gives accurate and satisfactory initial turbulent velocity fields, the complexity level in coding, parallelizing and constraint for use with equidistant Cartesian grids has pushed researchers to hunt for alternative turbulence generation techniques. In this respect, Klein *et al.* [132] and Kempf *et al.* [133] have developed two sister turbulence generators based on digital filters and random noise diffusion, respectively, having applicability and simplicity in mind. These methods are detailed out in Sects. 4.5.1 and 4.5.2. For each, a brief theory is outlined together with the underlying algorithms and comments regarding their implementation in *parcomb*. DNS validation results are presented later in Chapter 5.

4.5.1 Digital Filtering (DF) technique

This technique was proposed in [132]. It introduces a simple, flexible and accurate approach of generating artificial initial velocity data (at the inlet plane) for DNS and/or LES computations. The method can be divided into two steps:

1. Provisional three-dimensional signals are generated for each velocity component based on a prescribed two-point statistics (length scale, energy spectrum).
2. Possibly transform the generated signals in a way to satisfy the Reynolds-stress-tensor in case of non homogeneous isotropic turbulence.

In what follows, we will restrict ourselves only on the first point stated above, since it is sufficient to obtain homogeneous turbulence in a box, which is our purpose.

4.5.1.1 Brief theory

For simplicity and better understanding, we consider a one-dimensional case. Let U_{m_x} be a series of random data with $\overline{U_{m_x}} = 0$ and $\overline{U_{m_x}U_{m_x}} = 1$. The signal is convoluted with a digital, linear

and non-recursive filter such that

$$u_{m_x} = \sum_{n=-N_x}^{N_x} b_n U_{m_x+n}; \quad b_k = \frac{\tilde{b}_k}{\left(\sum_{j=-N_x}^{N_x} \tilde{b}_j^2\right)^{1/2}}; \quad \tilde{b}_k = \exp\left(-\frac{\pi k^2}{2n_x}\right) \quad (4.14)$$

where b_k is the filter coefficient. Assuming that Δx is the homogeneous grid spacing, the desired length scale is computed as $l_x = n_x \Delta x$. The half width of the filter kernel is specified by N_x . This relation is extended to three-dimension by the convolution of three one-dimensional filters:

$$b_{ijk} = b_i b_j b_k \quad (4.15)$$

A numerical error estimate

$$\max_k \left| \exp\left(-\frac{\pi k^2}{4n_x}\right) - \frac{\sum_{j=-N_x+k}^{N_x} b_j b_{j-k}}{\sum_{j=-N_x}^{N_x} b_j^2} \right| \leq 0.001 \quad (4.16)$$

is imposed on this approximately valid formulation such that

$$N_x \geq 2n_x; \quad n_x = 2, \dots, 100. \quad (4.17)$$

In other words, the filter width should be large enough to capture twice the length scale. This last inequality and n_x value range in Eq. (4.17) are crucial for the proper functionality of the overall technique.

4.5.1.2 Algorithm

The corresponding algorithm to generate a homogeneous turbulence in a box is as follows ($i = x, y, z$):

1. Choose for each coordinate direction a length scale $l_i = n_i \Delta i$ and a filter half width N_i , such that $N_i \geq 2n_i$.
2. Initialize and store three random fields U_m between -1 and 1 , with dimensions $[-N_x+1:M_x+N_x, -N_y+1:M_y+N_y, -N_z+1:M_z+N_z]$, where $M_x \times M_y \times M_z$ is the size of the computational grid.
3. Compute the filter coefficients b_i according to eq. (4.14) and (4.15).
4. Apply the filter operation on the random data (U_m) according to eq. (4.14):

$$u_m(i, j, k) = \sum_{i'=-N_x}^{N_x} \sum_{j'=-N_y}^{N_y} \sum_{k'=-N_z}^{N_z} b(i', j', k') U_m(i+i', j+j', k+k') \quad (4.18)$$

5. Normalize the random fields to a zero mean: $u_m = u_m - \bar{u}_m$
6. Scale the random data to a target mean fluctuation u' : $u_m = u_m \cdot \left[\frac{u'}{U_{rms}}\right]$, where U_{rms} is the rms value of the generated random field.
7. Add the velocity fluctuations to the base velocity field: $U = U + u_m$

The above turbulence generator has been partially implemented in *parcomb* and works on equidistant meshes. Its extension to irregular grids, which are typical of applications involving complex geometries is non trivial. Moreover, the parallelisation of the filters across processor boundaries for multi-core computations is not yet completed. For these reasons, the following alternative and closely related technique has been considered.

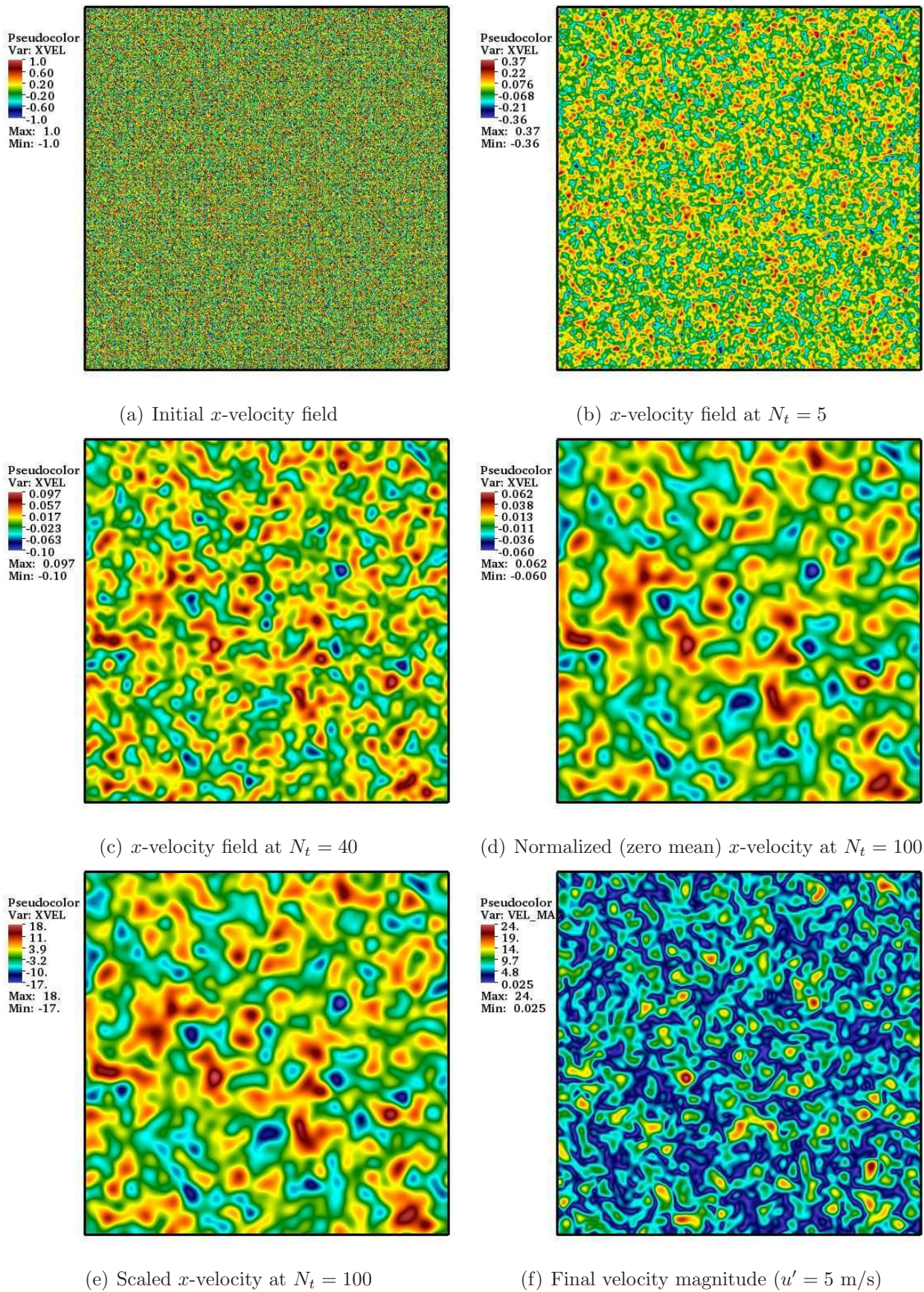


Figure 4.14: Graphical representation of the Random Noise Diffusion technique algorithm

4.5.2 Random Noise Diffusion (RND) technique

This method presents an artificial way of generating initial fluctuations for DNS by creating velocity fields that satisfy a given Reynolds-stress-tensor and length scale. It is based on physical space and according to the authors [133], it features greater flexibility, efficiency and applicability, and can be used even for complex geometries with arbitrary grids. It relies on a diffusion process that converts white noise into a signal that features the required length scale.

4.5.2.1 Brief theory

As with the previous method (Sect. 4.5.1), three fields of random noise U_i are generated and normalized such that $\bar{U}_i = 0$. For unstructured grids, the cell sizes can be compensated for by scaling with the inverse-root of the cell volume ($V_{\mathbf{i}}^{-1/2}$), where $V_{\mathbf{i}}$ is the volume of cell $\mathbf{i} = (i_x, i_y, i_z)$. Next, the small structures in the fields U_i are removed by applying diffusion, so that the larger scales become dominant. For instance, in the x -direction:

$$\frac{\partial U_i}{\partial t} = D \frac{\partial^2 U_i}{\partial x_j^2} \quad (4.19)$$

It is claimed [133] that for a given diffusion coefficient D , the resulting length scale increases with the time for which diffusion is applied according to

$$L^2 \approx 2\pi N_t D \Delta t \quad (4.20)$$

where Δt and N_t denote the size and the number of time steps, respectively. It should be noted that inhomogeneous length scales can be obtained by applying an inhomogeneous diffusion coefficient field.

Since diffusion occurs in physical space, the method can be applied to arbitrary grids and its implementation in a CFD code is straight forward, since the later features diffusive transport anyway.

Since our main interest is to obtain homogeneous turbulence in a box, the supplementary step to ensure that the resulting fields satisfy a given Reynolds-stress-tensor is not necessary. Our aim is simply to initialize a velocity field with arbitrary values which conform to a desired length scale.

4.5.2.2 Algorithm

Below is an outline of the various steps discussed above (as implemented in *parcomb*). A graphical representation of the important steps is given in Fig. 4.14.

1. Choose the method parameters (diffusion coefficient D , an appropriate time-step Δt and the number of iterations N_t) according to eq. (4.20). To get the most appropriate values, some experimentation is required, as further discussed below.
2. Initialize and store three random fields with $-1 \leq U_i \leq 1$, with dimensions of the computational grid. This is illustrated by Fig. 4.14(a) where the x -component of the velocity field of the white noise is plotted.
3. With unstructured grid, multiply the fields with $1.0/\sqrt{V_{\mathbf{i}}}$ ¹
4. Apply diffusion for N_t time steps by solving eq. (4.19). This is demonstrated in Fig. 4.14(b,c) for $N_t = 5$ and $N_t = 40$, respectively.

¹This step is omitted during the implementation with the simple reason that *parcomb* uses exclusively structured Cartesian mesh.

5. Normalize U_i to a mean value $\overline{U}_i = 0$ (see Fig. 4.14(d)).
6. Scale the random data to a target mean fluctuation, u' , as shown in Fig. 4.14(e)
7. Finally, superimpose the fluctuations onto the base velocity field. This is portrayed by Fig. 4.14(f) where the velocity magnitude is plotted for $u' \approx 5.0$ m/s (the base velocities are $u_x = u_y = u_z = 0.0$).

All the above steps are done in parallel together with MPI communications, especially in step 4. The procedure is exemplified in Fig. 4.15, where serial and parallel executions of the technique are displayed for two- and three-dimensional setups, using up to 64 computing cores. The above turbulence generator has been successfully implemented in *parcomb* as the default technique. It is very handy and scales on thousands of computing core. Except otherwise stated, it is the technique employed for the computations presented later.

4.5.3 A *posteriori* investigation of generated fluctuating fields

Using the above pseudo-turbulent field generators, in particular the **RND** technique, a number of test computations have been performed, with the main objective of checking their proper implementation in the DNS solvers, to verify their stability when using the resulting fluctuating velocity fields and finally to ensure that the impact of the turbulence on the flow/flame structure and vice versa are appropriate. All the measurements presented here were performed on *HPCx*: IBM POWER5 system at EPCC (Edinburgh) and on *karman*: Linux-based PC-cluster at LSS (Magdeburg). It is built with Opteron quad-core nodes with 32 GB memory/node and an Infiniband connection, with a peak performance of roughly 5 Tflop/s. The entire cluster contain 68 computing and 2 I/O nodes with 8 computing cores each (560 cores in total).

4.5.3.1 General flow field

Fig. 4.16 shows the resulting vorticity fields for a square domain with side length $L = 5$ mm and a mesh of 201×201 grid points. The initial fluctuations are generated for successively higher values of the number of diffusion iterations, N_t at a constant rms speed $u' = 2$ m/s. This is to check the influence of N_t on the initial vortical structures and its subsequent effect on the flame structure. The vortical structures get as expected larger when increasing the number of diffusion steps. Values of N_t computed directly from Eq. (4.20) tend to be too large. Some experimentation is therefore required to figure out the most appropriate N_t value for a given computational domain size. Generally, from my experience, a value of $N_t \geq 100$ is recommended. Note also that the diffusion coefficient D may not be equal to the real mixture diffusion coefficient of the system. From our experience, a value of $D \approx 1.0 \times 10^{-8}$ is a good initial guess.

In the second test, we consider a larger domain ($L = 3.0$ cm) and monitor the long term effect of the generated fluctuations at a constant value of $N_t = 200$. The temporal evolution of the vorticity contours are shown in Fig. 4.17. The color scale for all subplots is kept constant ($|\omega| \leq 50000$). The turbulent fluctuating velocity is $u' = 8$ m/s, integral length scale $l_t = 2.4$ mm and $Re_t = 1340$. Turbulent parameters (rms of velocity fluctuations, longitudinal integral length scale, turbulent kinetic energy and the energy spectrum of the system) have been determined in a post-processing step from instantaneous snapshots of the flow field using the *AnaFlame* post-processing toolbox [134, 135] and are shown in Fig. 4.18. It is observed from Fig. 4.18(a) that the value of the post-processed rms of velocity fluctuations is slightly smaller by 7.5% compared to the prescribed value of 8 m/s at $t/\tau = 0$. It decays with time by up to 27% of the initial value at $t/\tau = 6.67$. The same trend is directly echoed by the turbulent kinetic energy of the system as plotted in Fig. 4.18(b). On the other hand, the longitudinal integral length scale, as shown in Fig. 4.18(c) start off with a value 12.5% lower than that initially prescribed. An

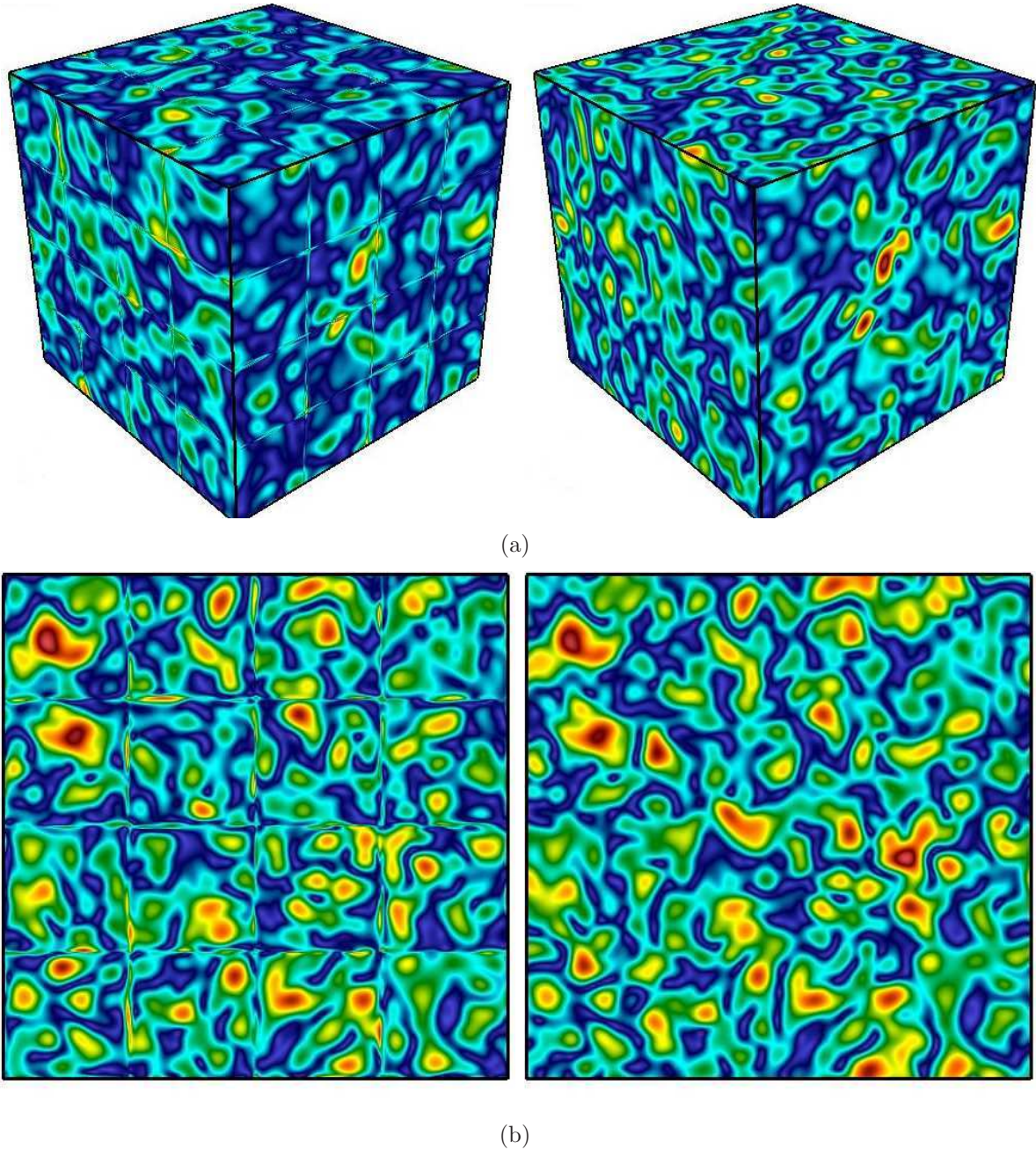


Figure 4.15: Graphical representation of the serial (left) and parallel (right) Random Noise Diffusion technique algorithm for (a) three- and (b) two-dimensional configuration after a few diffusion iterations using several processors.

overall gradual increase can be observed from the time profile, which stabilizes after $t/\tau = 4.0$. These are natural readjustments which depend on the actual computational domain size. Note, that, in real DNS computations, the interval $0.5 < t/\tau < 2.0$ is usually the only interesting one.

4.5.3.2 Energy spectrum and length scales

The evolution of the kinetic energy spectrum ($E(k)$, log-log scale) in decaying 2D turbulence from the above example is plotted in Fig. 4.18(d) against the wave number. The different curves are for different times after initialisation. The spectrum spreads and the peak moves to smaller k with time. The general tendency is geared towards the lowering of $E(k)$ at high wave number (small vortices region) where the turbulence is dissipated by viscosity and raising it at low k .

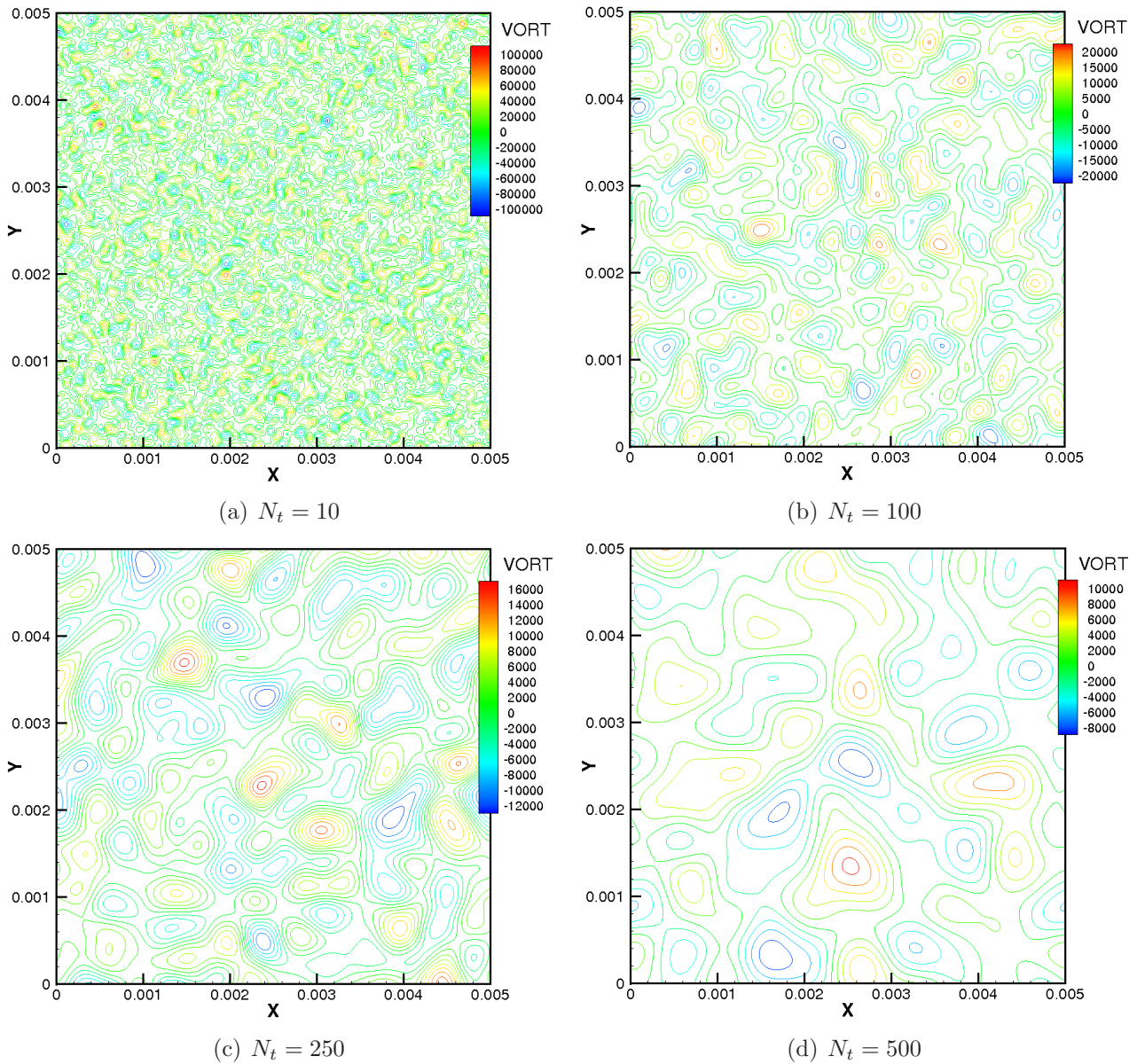


Figure 4.16: Random noise diffusion technique: Instantaneous vorticity field for different values of the diffusion steps, N_t . Domain dimensions are in meters

This is typical of 2D turbulence [136]. The time decay of the energy is gradual and reasonable. The initial field ($t/\tau = 0.0$) shows some fluctuations in its energy spectrum, which disappear after a few iterations ($t/\tau = 0.17$).

Also plotted in Fig. 4.18(d) are fits of the theoretical slope for 2D turbulence (proportional to k^{-3}). There is an excellent qualitative agreement of the profiles with classical 2D turbulent energy cascade diagrams [2]. The spectral slopes for large wave numbers are very close to -3 for each of the selected curves apart from the very first one.

Both u' and l_t (via the domain size L) have also been varied simultaneously and Fig. 4.19 displays the instantaneous temperature fields for a syngas diffusion flame for increasing Re_t at $t = 2.0\tau$ for four computations. The effect of Re_t on the flame structure is as expected. There is a steady move from today's easily accessed mild turbulence conditions (Fig. 4.19(a) & 4.19(b)) with only slight contortions to more realistic ones (Fig. 4.19(c) & 4.19(d)) for increasing Reynolds numbers. This leads to considerable structural modifications of the flame, as will be demonstrated in the next chapter.

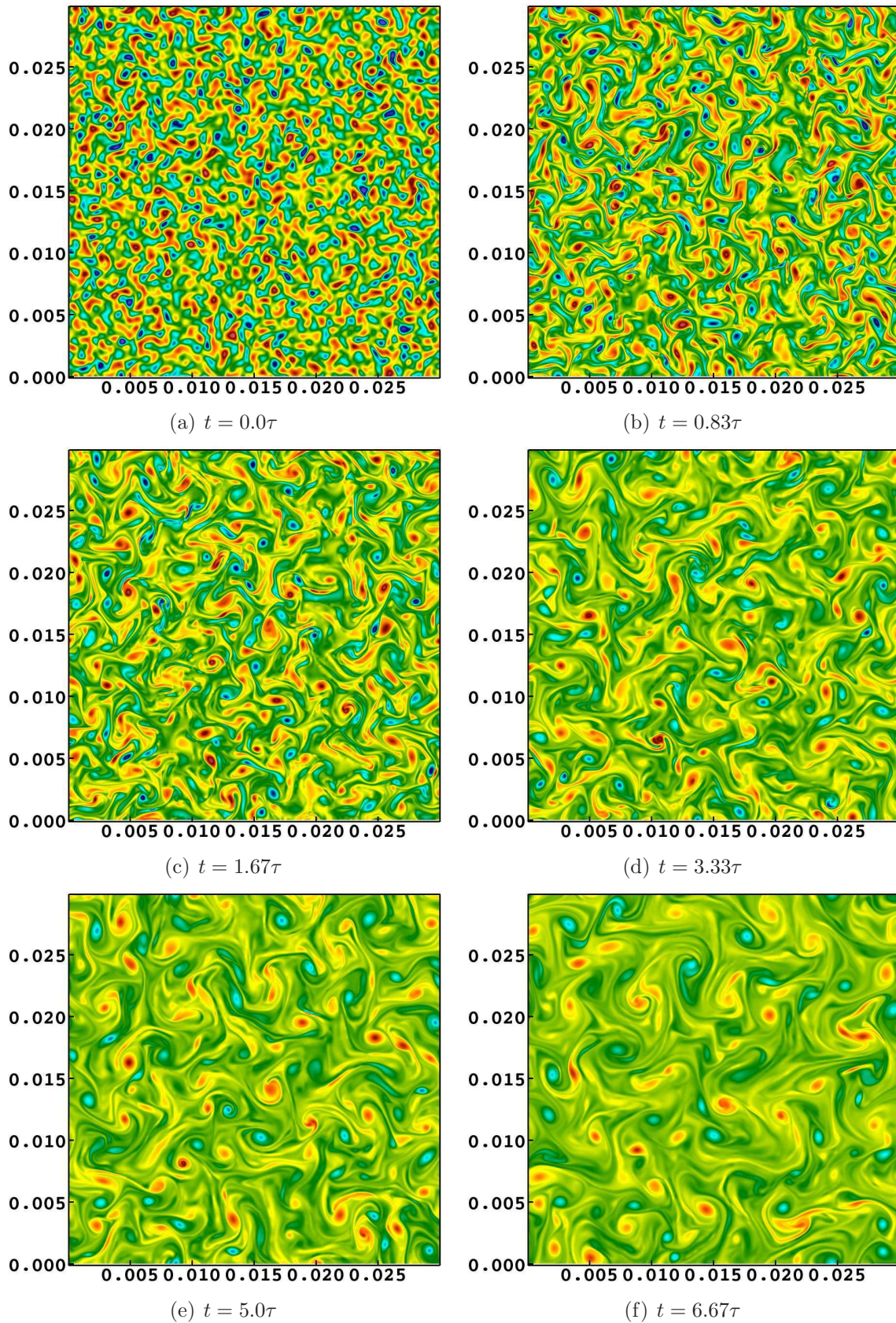


Figure 4.17: Random noise diffusion technique: Temporal evolution of a 2D vorticity field generated with $u' = 8$ m/s, $l_t = 2.4$ mm and leading initially to $Re_t = 1340$. Domain dimensions are in meters

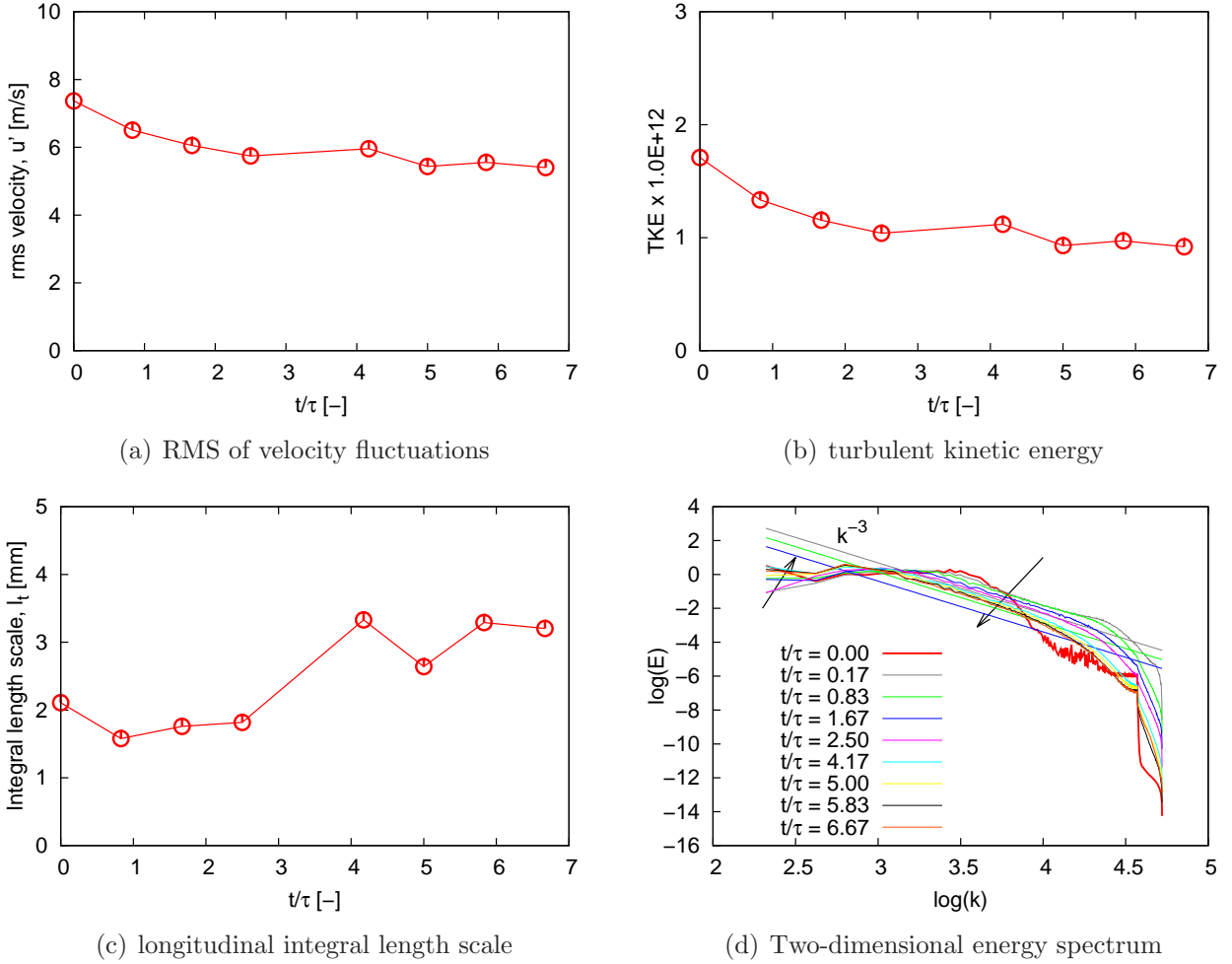


Figure 4.18: Random noise diffusion technique: Turbulent parameters of an initial two-dimensional turbulence field with $l_t = 2.4$ mm, $u' = 8.0$ m/s and $L = 3.0$ cm at different time instances. The arrows point in the direction of increasing time

4.5.3.3 Incompressibility

The dilatation, defined as the divergence of the velocity

$$\theta = \nabla \cdot \mathbf{U} = \frac{\partial u}{\partial x} + \frac{\partial v}{\partial y} + \frac{\partial w}{\partial z} \quad (4.21)$$

provides a measure by which density fluctuations associated to turbulent fluctuations \mathbf{u}' can be characterized. The vorticity, defined as

$$\omega = \frac{1}{2} \nabla \times \mathbf{U} \quad (4.22)$$

and dilatation fields of a turbulent velocity field with $u' = 6.0$ m/s after $t = 50 \mu\text{s}$ are shown in Fig. 4.20. Certainly, at the start of the simulation, the maximum level of the dilatation is comparable to that of the vorticity. At this instant in time, acoustic noise is significant. At later times, when all the acoustic waves are supposed to have left the computational domain (if we are working with non-reflecting boundary conditions), the level of the dilatation will reduce remarkably compared to the vorticity level, as evidenced from the snapshots in Fig. 4.20 after $t = 50 \mu\text{s}$. Their maxima are decreasing and increasing functions of time and turbulence intensity, respectively.

The level of vorticity and dilatation equally characterizes the incompressibility of the generated velocity fluctuations. The generated signal should be purely vortical ($\theta = 0$). Of particular

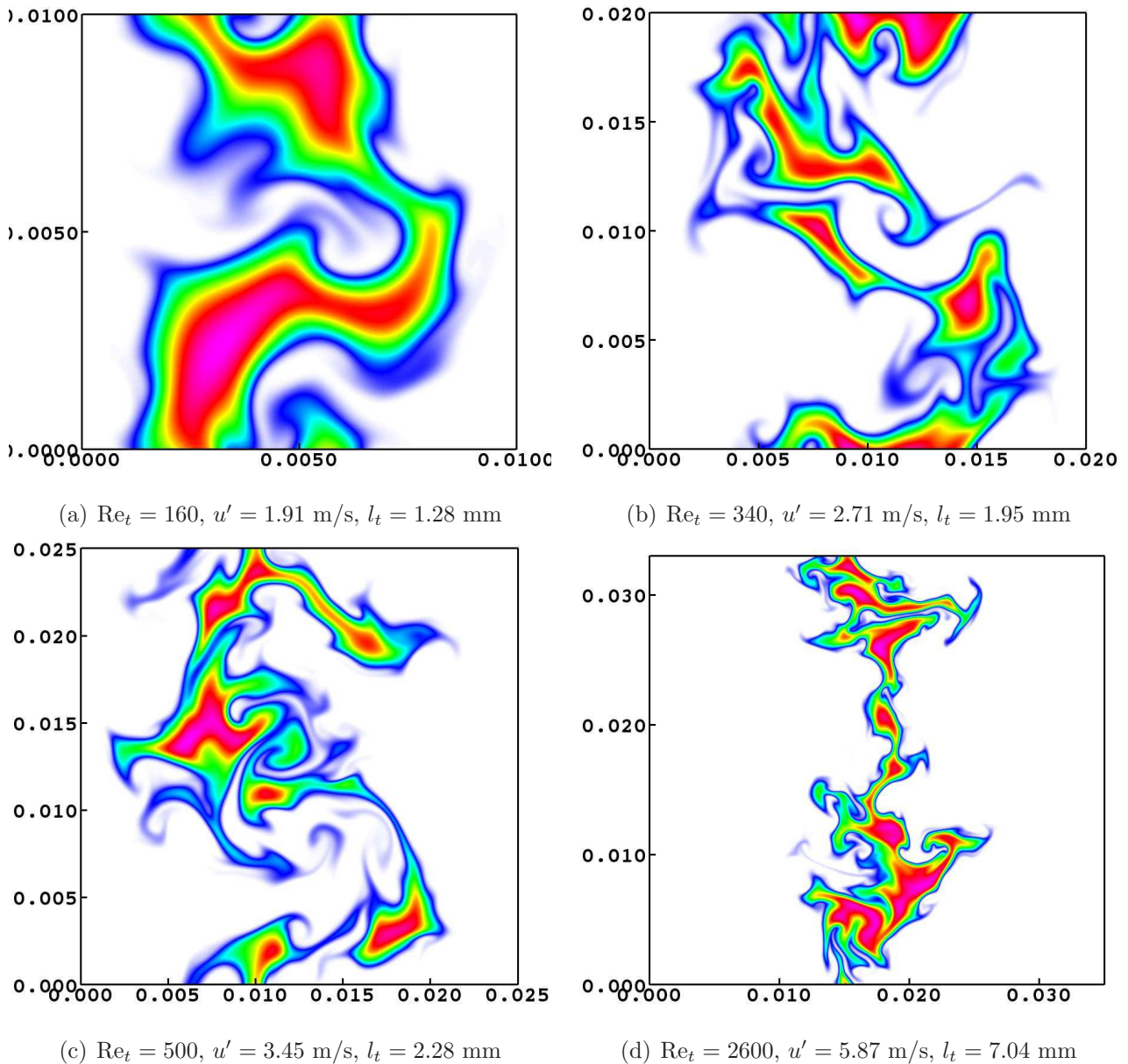


Figure 4.19: Instantaneous iso-contours of temperature at $t = 2.0\tau$ for a CO-H₂ diffusion flame for different integral length scales l_t , turbulence intensities u' , and turbulent Reynolds numbers Re_t . Note the different domain sizes (in meters)

interest is the incompressibility rate, which compares the dilatation to the vorticity, θ/ω . Its time evolution for three different rms velocities is compared in Fig. 4.21 up to $t = 4\tau$. Beside indicating which fraction of the turbulent energy is transformed into acoustic energy, this quantity also serves as a test for the quality of the turbulence generator. This ratio should ultimately be zero for a pure incompressible turbulent flow field. But as can be seen, this is never the case, due to noise generated by the initial and boundary conditions. Its maximum value is observed at $t = 0$. After readjusting the flow, this ratio decreases well below unity with increasing simulation time. In other words, dilatation levels stay much lower than vorticity levels, as already pointed out from Fig. 4.20.

In general, the initial turbulence generators seem to be working as intended, producing the expected effects on the flame and vice versa. With the two approaches presented and validated above, it becomes possible to implement efficiently a fully parallel generation of turbulent fields on massively parallel machines, unlike the serial complex inverse FFT-based algorithm used in

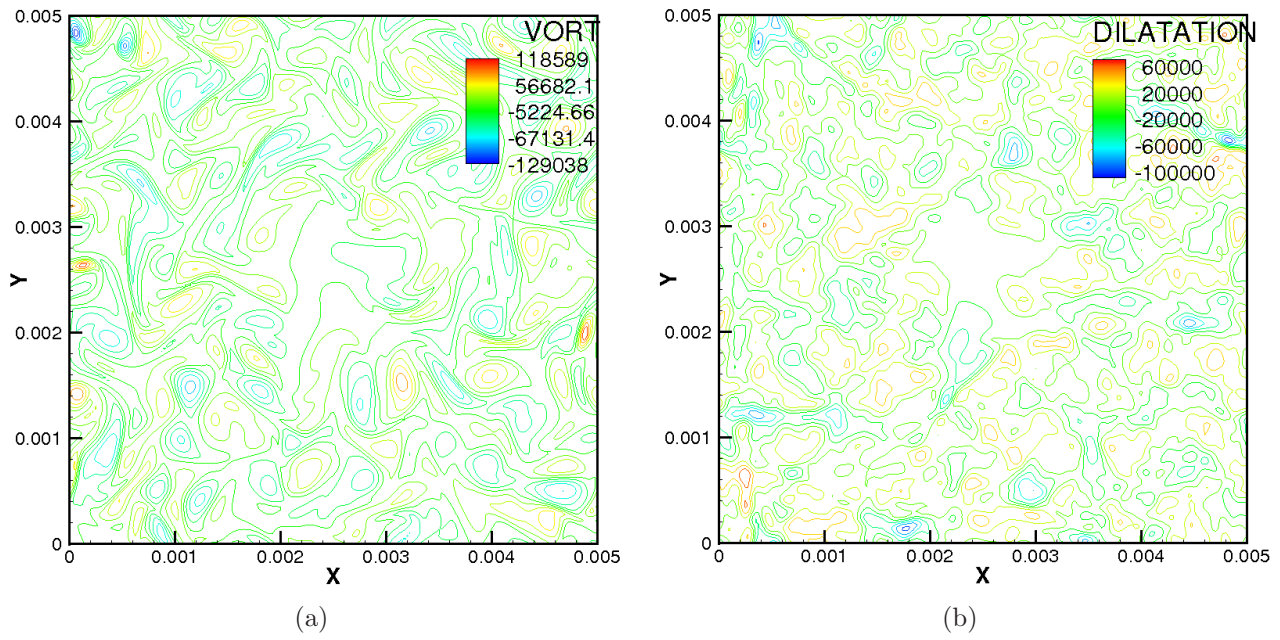


Figure 4.20: (a) Vorticity and (b) dilatation fields of a turbulent velocity field with $u' = 6.0$ m/s after $t = 50 \mu\text{s}$

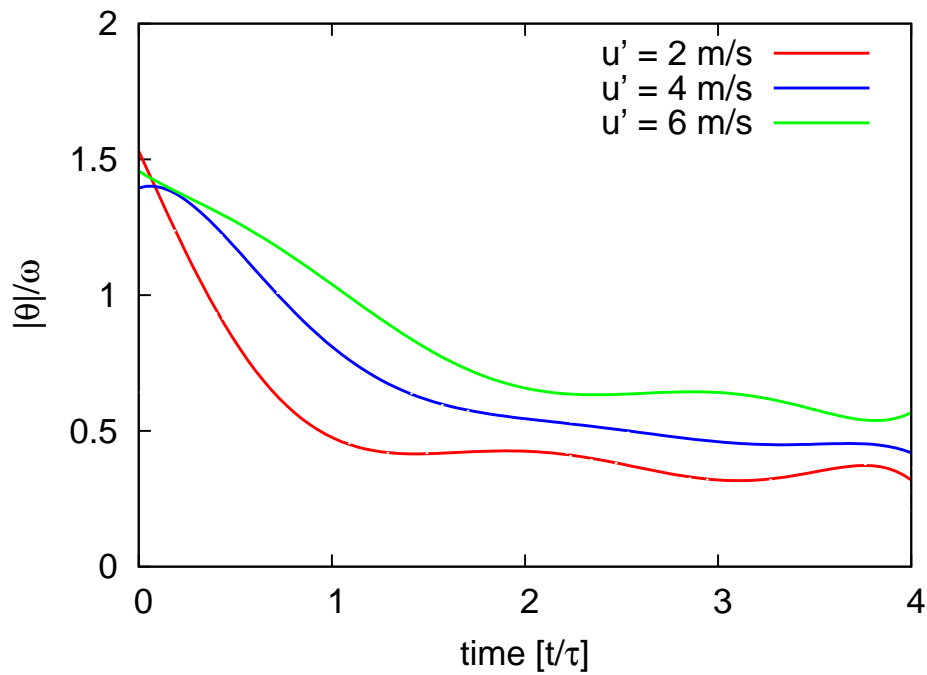


Figure 4.21: Temporal evolution of the compressibility rate $\theta_{max}/\omega_{max}$ for different rms velocities u'

previous versions of the code [111]. In this manner, much higher values of Re_t are now accessible.

4.6 Numerical combustion solution strategy

Our analysis of turbulent flames and of flame/turbulence interactions using DNS follows always the same procedure. First, a laminar flame configuration is determined, either using a first DNS computation when considering detailed chemistry, or using a simple estimation when relying on tabulated chemistry. Then, the obtained laminar solution is transposed to a two- or three-dimensional configuration, with fuel (resp. fresh gases) on one part of the numerical domain, the other part consisting of oxidizer (resp. burnt gases). A field of synthetic homogeneous isotropic turbulence, based on either the classical turbulent energy spectrum of Kármán with a Pao correction for near-dissipation scales [49, 110, 137] or on the newly implemented parallel technique [28, 132, 133, 138] is then superposed on top of this laminar configuration as exemplified in Fig. 4.22 (cf. Fig. 4.17) for a planar double diffusion methane flame configuration. The turbulence properties are imposed by the user in order to obtain the highest possible Reynolds number in the domain, considering its limited size and the really achieved spatial resolution [134]. The turbulence parameters are checked by a separate post-processing of the initial solution as in the previous section. For the results shown later in Chapter 5, this leads to a Reynolds number based on the integral scale equal to $Re_t = 100 - 7000$. The integral scale of turbulence is $l_t = 1.0 - 5.0$ mm, with a turbulent fluctuation velocity $u' = 0.5 - 22.0$ m/s and a value of the unburnt mixture viscosity dependent on the fuel under consideration. The characteristic time-scale of the large turbulent structures is then $\tau = 9.6 - 0.5$ ms.

When iterating the DNS computation in time, a turbulent flame develops into the numerical domain (e.g., Fig. 4.22(a-c)). This computation is carried out until reaching equilibrium between chemistry and turbulence (in a statistical sense), which is known to occur at a time around $t \geq \tau$ from the literature [120] (e.g., Fig. 4.22(d-f)). At that time, the structure of the resulting turbulent flame can be analyzed and used for model testing and development.

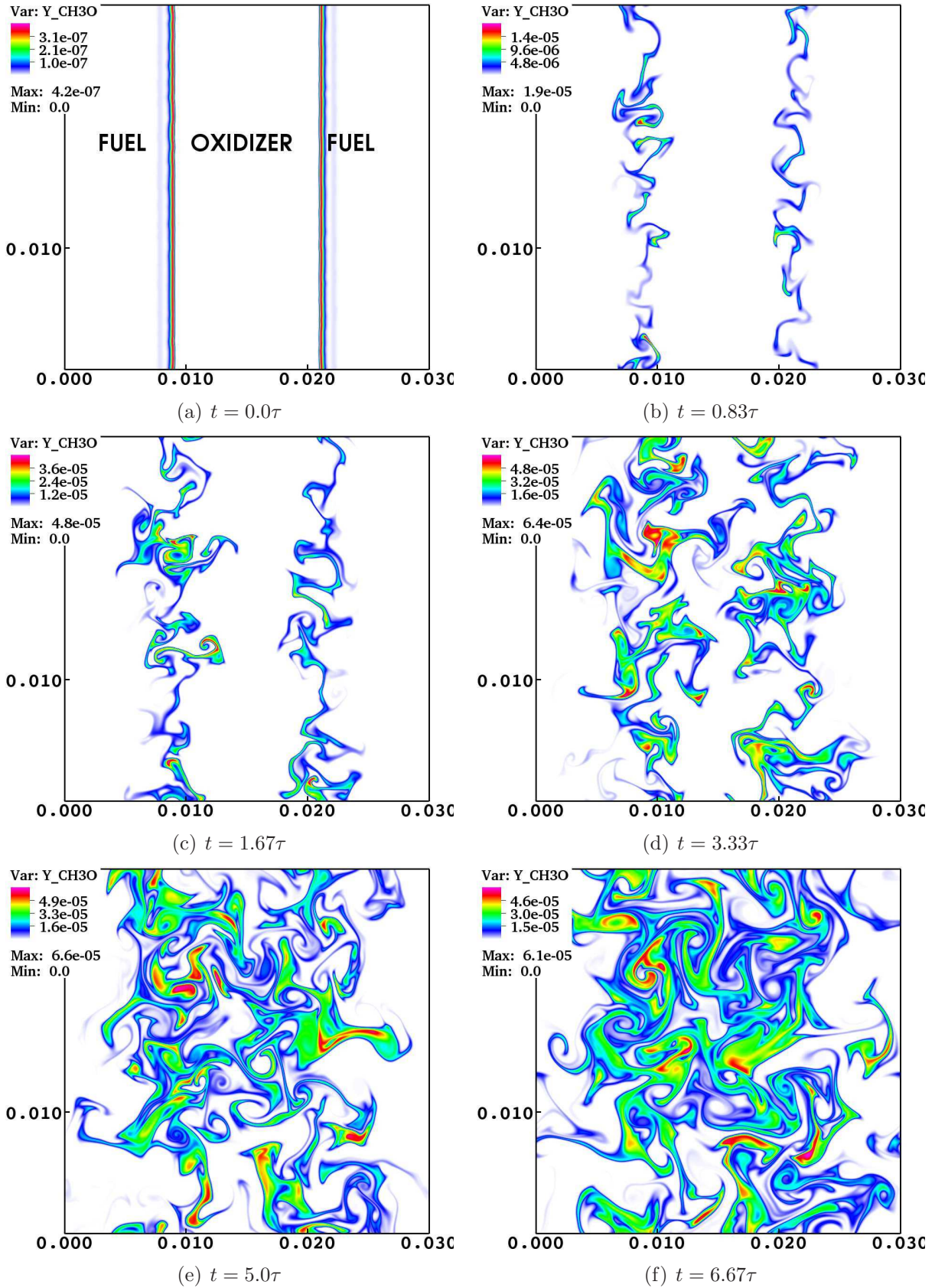


Figure 4.22: Temporal evolution of the contours of the CH_3O radical in a CH_4 double diffusion flame configuration for $\text{Re}_t = 1340$. The initially planar laminar flame (a) is superposed with an initial turbulent field (cf. Fig. 4.17) and allowed to evolve with time, resulting in flame wrinkling (b) from which useful statistics are collected at a statistically stable stage (c-d)

4.7 Summary

Turbulent combustion simulation is challenging because of the coupling of complex phenomena such as fluid dynamics, chemical reactions, radiation, phase changes, *etc.* Depending on the characteristics of the combustion processes, different numerical methods and techniques, subject to various levels of approximations can be used to approach this problem.

In this chapter, the outstanding characteristics of the three principal modes of combustion, namely premixed, non-premixed and partially premixed burning have been briefly described. The main similarities and differences between the various modes are stated. While the fuel and oxidizer are completely mixed before combustion starts in premixed flames, the fuel and oxidizer are initially separated in diffusion flames. The characteristic velocity and length scales observed in premixed combustion are non-existent in non-premixed burning. Premixed flames have a strong capacity to reduce the production of NO_x under lean conditions, unlike non-premixed flames with high temperature flame fronts. On the other hand, combustion instabilities and storage difficulties are frequently encountered in premixed burning, while diffusion flames are very stable and fuels can easily be stored.

We presented the various numerical techniques, (RANS, LES and DNS) used to simulate turbulent reacting flows, with emphasis placed on the DNS approach. DNS stands out as the most powerful tool to predict and simulate compressible turbulent flows since it directly resolves the system of equations describing the physical processes. Even though it requires prohibitive numerical costs for practical configurations compared to the other two approaches, it offers an excellent complement to experiments in order to assess the importance of various physical mechanisms and obtain complementary information on the micro-physics of turbulent flame structures.

Some major aspects of three different flame solvers used during this work were then presented. Their underlying numerical methods, newly upgraded/implemented modules, single- and multi-processor performance and optimization were discussed. We saw that efficient and fully parallel data input/output (I/O) is a major issue towards fine-grain parallelism. The traditional I/O approaches must be replaced by fully parallel I/O to achieve high parallel scaling and performance.

Then, two simple, flexible and accurate turbulence generators based on digital filtering and random noise diffusion have been derived, implemented and parallelized on massively parallel computers, thereby alleviating the problem size restrictions imposed by inverse FFT based techniques.

These modifications, among others, pave the way towards exploring turbulent flames with increased grid sizes, Reynolds numbers, larger number of time steps and ensemble averaging, leading to a high statistical reliability. Consequently, turbulent combustion computations can now be considered under more realistic conditions using DNS.

CHAPTER

5

Results and discussions

Most of the results presented in this chapter have been published in the following peer-reviewed journal articles:

1. **G. Fru**, G. Janiga, and D. Thévenin. Impact of volume viscosity on the structure of turbulent premixed flames in the Thin Reaction Zone Regime. *Flow, Turbulence and Combustion*, 1–28, **2011**. 10.1007/s10494-011-9360-1
2. **G. Fru**, G. Janiga, and D. Thévenin. Direct numerical simulation of the impact of high turbulence intensities and volume viscosity on premixed methane flames. *Journal of Combustion*, Article ID 746719, 12 pages, **2011**
3. **G. Fru**, D. Thévenin, and G. Janiga. Impact of turbulence intensity and equivalence ratio on the burning rate of premixed methane–air flames. *Energies*, 4(6):878–893, **2011**.

5.1 Introduction

In this chapter, some of the major results obtained in the course of this thesis work are presented. For all the non-premixed flame configurations considered below, the flame is first ignited in a laminar one-dimensional configuration using numerical catalysis [111], whereby a threshold temperature, $T_{th} > T_u$ is used in the evaluation of the species source term in the species transport equation as long as the system temperature $T < T_{th}$. The initialization of the multi-dimensional premixed flame computations are from one-dimensional profiles with the same mixture composition and starting conditions. For both the planar premixed and non-premixed setups, the resulting one-dimensional profiles are collected at a time $t \approx 1.0 - 2.0$ ms, linearly extended in the remaining directions and then superimposed with a homogeneous time-decaying isotropic turbulent field using the techniques outlined in Sect. 4.5. The DNS results are mostly analyzed using conditional statistics based on the mixture fraction given by Eq. (4.2) for diffusion flames or on the reaction progress variable given by Eq. (4.1) for premixed flames, since the local structure of a flame is best described with such statistics, and also because many turbulent combustion models rely directly or indirectly on conditional variables [7]. A recently developed post-processing toolbox [134, 135, 139] is used for most of the analysis.

The first two sections focus on the analysis of numerical data for non-premixed (Sect. 5.2) and premixed (Sect. 5.3) combustion computed with detailed physico-chemical models using *parcomb*, the code presented in Sect. 4.4.1. Therefore, only the boundary and initial conditions specific to a given flame configuration need to be outlined. Except otherwise stated, the mixture-averaged transport model is employed in all the numerical experiments reported in these sections, coupled with the detailed chemical mechanisms listed in Appendix A for the flames burning hydrogen (A.1), syngas (A.2) and methane (A.3) in air.

In Sect. 5.2, a series of non-premixed combustion cases are considered, first for turbulent

flames at relatively low turbulent Reynolds number. The data is analyzed toward improving turbulent models based on presumed probability density functions (PDF) widely used in RANS and LES codes. In the second case, a series of computations aim at evaluating the impact of both the turbulent intensity and the volume viscosity transport term on the diffusion flame structure burning hydrogen and syngas in air. The impact of including volume viscosity effects in the system of flow equations on both laminar and turbulent flames is quantified, as well as its influence at higher turbulent Reynolds numbers.

In Sect. 5.3, results from a series of parametric studies to investigate the influence of turbulence intensity, mixture equivalence ratio and volume viscosity on premixed flames and their burning rates are discussed. Highly turbulent methane–air flames in both planar (Sect. 5.3.2) and spherical (Sect. 5.3.3) premixed configurations are extensively investigated. In Sect. 5.3.4, a systematic study is dedicated to the influential role played by the volume viscosity transport term on initially spherical premixed combustion burning hydrogen, syngas and methane fuels in air. The ignition and subsequent development of such a premixed flame-kernel under the influence of a turbulent flow field is an excellent configuration which allows turbulent flames to be studied well away from the influence of external perturbations such as walls and artificial boundary conditions. From a fundamental point of view, it offers the possibility to study highly complex multi-scale flows involving fully coupled physical processes. Simultaneously, it has direct practical relevance in a number of industrial cases including spark-ignition internal combustion engines and gas turbine re-ignition, as well as safety issues [140].

The nomenclature for the various cases or group of cases is with upper case letters, for instance *case A*, *case B*, etc. If a case involves sub-cases, then we have *case A1*, *A2*, etc. Furthermore, if a sub-case contain several variants, then we write *case A1a*, *A1b*, etc.

5.2 Non-premixed combustion

Non-premixed flames correspond to situations where the reactants are not initially mixed and originate from two separate streams. Mixing must bring them together for combustion to take place. A general overview of this burning mode was given in Sect. 4.2.2. The analysis of the results in this section is subdivided into two cases, depending on the turbulent diffusion flame phenomena under investigation. A detailed outline specific for each of the two cases is given below.

5.2.1 Problem setup and initialization

case A: Planar H₂-air flames (impact on presumed PDF-based models)

In the first configuration, we consider a single three-dimensional turbulent hydrogen-air flame simulation. A detailed chemical scheme involving 9 species and 19 reversible elementary reactions [40] is used to describe H₂ oxidation (see Appendix A.1 for details). The initial conditions correspond to a global mixture ratio $\phi = 0.8$. The stoichiometric mixture fraction given by theory is then $Z_s = 1/(1 + \phi) = 0.56$. The computational domain is a cube of 1.0 cm side with a uniform grid spacing of 50 μm (8 million grid points). The NSCBC [116] boundary conditions are employed in the x -direction (non-reflecting boundaries with pressure relaxation), while periodicity is assumed along the y - and z -directions. The initial turbulent field for the results presented afterwards has been generated assuming a turbulent kinetic energy distribution given by a von Kármán spectrum with Pao correction [110]. The characteristic viscosity of the mixture is $\nu = 1.55 \cdot 10^{-5} \text{ m}^2/\text{s}$. The turbulent integral scale l_t , velocity fluctuation u' , turbulent Reynolds number $\text{Re}_t = l_t u' / \nu$ and eddy turn-over time $\tau = l_t / u'$ for the generated turbulence

are given in Table 5.1.

Parameter	<i>Case A</i>	<i>Case B1</i>	<i>Case B2</i>	<i>Case B3</i>	<i>Case B4</i>
Fuel	Hydrogen	Hydrogen	Hydrogen	Hydrogen	Syngas
L (cm)	1.00	0.80	0.80	2.00	2.00
l_t (cm)	0.16	laminar	0.13	0.48	0.48
u' (m/s)	2.05	laminar	5.00	6.00	6.00
τ (ms)	0.76	laminar	0.26	0.80	0.80
Re_t	205	laminar	419	1 858	1 858
Φ	0.80	0.80	0.80	0.80	1.12
<i>DIM</i>	3D	1D	2D/3D	2D/3D	2D/3D

Table 5.1: *Case A & B:* Initial turbulence and flame parameters

case B: Planar H₂- and CO/H₂-air flames (impact of volume viscosity, κ)

In order to check the impact of volume viscosity, three non-premixed flames involving different fuels are considered (see Sect. 2.3.1 for a general introduction on volume viscosity).

Case B1:

In the first setup of the second case, a planar hydrogen/air flame is considered in a one-dimensional setup. The same chemical scheme [40] as above is used to describe H₂ oxidation with similar initial flame and boundary conditions. The aim here is twofold: check the influence of volume viscosity on the laminar flame structure and furnish stable input profiles for the subsequent turbulent multi-dimensional computations. The remaining simulation parameters are displayed in Table 5.1.

Case B2:

The laminar one-dimensional profiles from *case B1* are collected at $t = 1.0$ ms and then used as initial profiles for the turbulent multi-dimensional computations. The turbulent Reynolds number based on the integral scale is $Re_t = 419$ which is relatively low compared to the other cases considered here but higher than in *case A*. The turbulent integral scale l_t and the velocity fluctuation u' are given in Table 5.1.

Case B3:

To quantify the influence of the turbulence intensity on the flame structure with and without volume viscosity, *cases B2* has been repeated identically but with a much higher value of Re_t . Therefore, *case B3* corresponds to $Re_t = 1\,858$, a value more than four times higher than in *case B2* (see Table 5.1).

Case B4:

The next configuration considers a turbulent flame burning synthetic gas in air (CO/H₂-air). The reaction scheme employed contains 13 species and accounts for 67 individual reactions [42] (see Appendix A.2 for details of the employed chemical scheme). The initial conditions correspond to a stoichiometric CO/O₂ ratio with slight H₂ enrichment at $T_u = 300$ K, leading to $\Phi = 1.12$ and $Z_s = 0.47$ (see Table 5.1). Unlike the other cases in this group, this case has been repeated four times with different turbulence fields initialized with different random seeds but having the same scales for both $\kappa \neq 0$ and $\kappa = 0$. Furthermore, three additional computations for the $\kappa \neq 0$ case with κ substituted by $\kappa/2$, $\kappa/4$ and $\kappa/8$ have also been realized to make the study more comprehensive. In this manner, the statistical significance [12] of the obtained results is increased and it is possible to eliminate the influence of any other intermittent and transient phenomena (initial and/or boundary conditions, numerics, etc.) but turbulence.

For all setups in *cases A & B*, an appropriate nitrogen complement is added everywhere. The computational domain in *case B* is discretized with a uniform spatial resolution of $25\mu\text{m}$,

necessary to resolve correctly not only the smallest vortical structures but also stiff radicals like CH_2O or H_2O_2 . The computations for *case A* were performed at ONERA (France), using a total number of 125 processors from a parallel cluster HP SC-2 (≈ 2 Tflops/s peak performance) and required approximately 12 500 hours of processor time. Using 512 cores of the *IBM HPCx Power5* system at EPCC Edinburgh (peak performance of ≈ 6 Tflop/s sustain), corresponding DNS computations for *case B* require up to 10 days of user waiting time with $\kappa = 0$. This computing time is almost doubled when taking into account volume viscosity. In what follows, all results are presented for $t \approx \tau$ and $t = 2\tau$ for *case A* and *case B*, respectively, corresponding to equilibrium conditions between turbulence and chemistry in time decaying turbulence [120].

Corresponding results for these two cases were presented at the seventh ERCOFTAC workshop on Direct and Large Eddy Simulation (DLES7) in Trieste, Italy [141] and at the 32nd International Symposium on Combustion in Montreal, Canada [142], respectively.

5.2.2 General turbulent flame structure

The typical turbulent flame structure is exemplified in Fig. 5.1 where the general view of the configuration, showing the instantaneous iso-surface of the mass fraction of H_2 is displayed. The mixing zone is clearly visible, extending around the center of the domain. Also shown is the iso-fluctuation of heat release colored by the flame index (see Eq. (5.1)) [143] within the mixing layer. This index is used as a segregation factor to distinguish between the different reaction

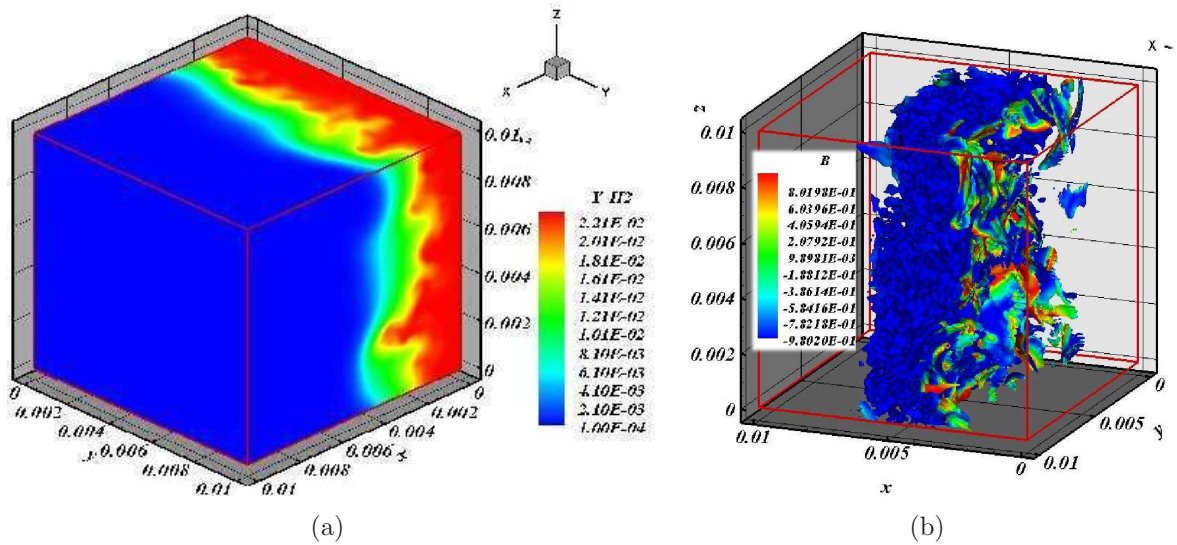


Figure 5.1: *Case A*: Turbulent diffusion hydrogen-air flame structure: (a) distribution of H_2 mass fraction and (b) iso-fluctuations of heat release colored by the flame index defined by Eq. (5.1)

zones co-existing in the system. It is based on the scalar product of the local gradient of fuel and oxidizer mass fractions, and has been widely used to support the analysis of simulation results [101, 102, 104]. It is classically defined as:

$$\xi = \nabla Y_F \cdot \nabla Y_O, \quad (5.1)$$

where Y_F and Y_O are the fuel and oxidizer mass fractions, respectively. According to this segregation index, a flame is purely premixed when $\xi \simeq 1$, pure non-premixed when $\xi \simeq -1$ and partially premixed when $-1 \ll \xi \ll 1$. The maximum (dashed line), mean (solid line) and minimum (dash dotted line) values of the flame index conditioned by the mixture fraction is shown in Fig. 5.2(a) for the present DNS results, excluding the regions with $Z \leq 0.05$ (considered as pure oxidizer) and $Z \geq 0.95$ (pure fuel). A large region in Z -space around $Z = Z_s$ is dominated

by pure non-premixed conditions, as expected for this globally non-premixed configuration. A non-negligible amount of partially-premixed zones are nevertheless visible on the fuel side (around $Z \simeq 0.81$) and, to a lesser extent, on the oxidizer side (around $Z \simeq 0.13$). For these same conditions the peak of conditional flame index lies systematically around 1, showing locally the presence of fully premixed conditions. These two regions, just outside of the main reaction zone, correspond to the burning conditions most strongly disturbed by interaction with the turbulence.

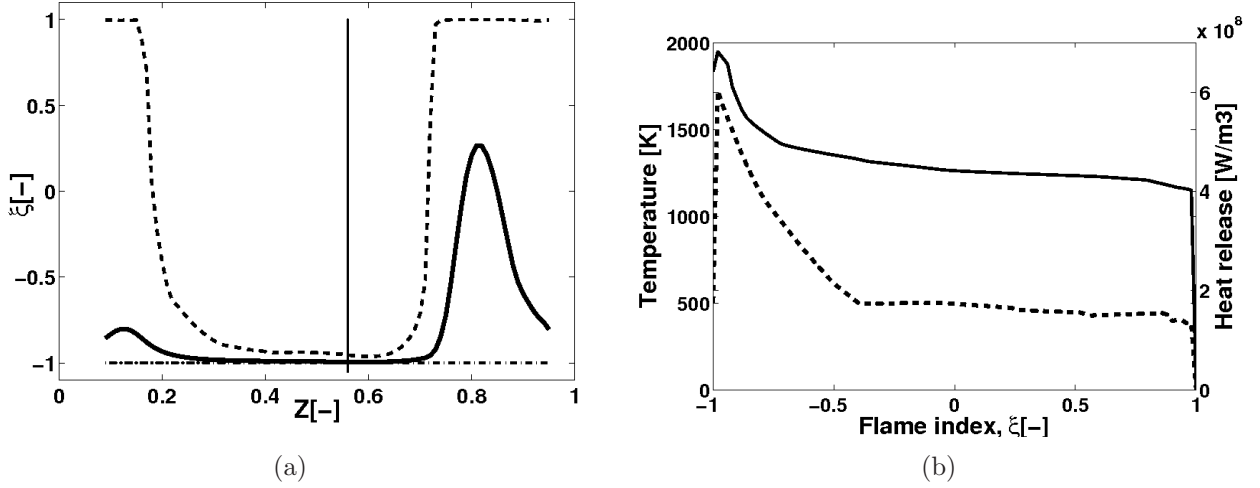


Figure 5.2: *Case A:* Profiles of (a) maximum (dashed line), mean (solid line) and minimum (dash dotted line) flame index ξ conditioned by the mixture fraction and (b) maximum temperature (solid line, left scale) and heat release (dashed line, right scale) conditioned by the flame index ξ at $t \approx 1.0\tau$. $\xi \simeq 1$: pure premixed; $\xi \simeq -1$: pure non-premixed; $-1 \ll \xi \ll 1$: partially-premixed. The solid vertical line corresponds to the stoichiometric mixture fraction, Z_s

Figure 5.2(b) shows the maximum values of temperature and heat release conditioned by the flame index at the same time instance. As expected, most of the heat release takes place in a non-premixed mode, though the peak of conditional heat release and temperature is found for a value of ξ slightly higher than -1 . For $\xi > -0.5$ a slowly decreasing plateau is observed, followed by a sharp drop both of heat release and temperature when approaching $\xi = 1$. Figure 5.3 shows the evolution of the mean value of temperature and heat release conditioned by the mixture fraction Z . Considering Figs. 5.2 and 5.3, it becomes clear that the partially-premixed combustion regimes observed in Fig. 5.2(a) relatively far from the stoichiometric conditions are associated with a comparatively low level of heat release. These partially-premixed regimes correspond to low-intensity burning regions at the periphery of the main reaction zone. Globally, 64% of the heat released by the chemical reactions in the whole computational domain takes place in the non-premixed mode. Figure 5.3 reveals also that the region associated with the highest conditional mean temperature and heat release does not lie exactly at $Z = Z_s$, but slightly on the oxidizer side.

5.2.3 Impact on presumed PDF-based turbulent flame models

Modeling correctly the PDF of mixture fraction in turbulent reacting flows is an essential issue [5–7]. For most models and in particular when using the RANS approach, the form of this PDF is usually presumed, using either β - or γ -functions as given by Eqs. (5.2) and (5.3), respectively:

$$\tilde{P}_\beta(Z; \mathbf{x}, t) = \frac{Z^{a-1}(1-Z)^{b-1}}{\Gamma(a)\Gamma(b)}\Gamma(a+b) \quad (5.2)$$

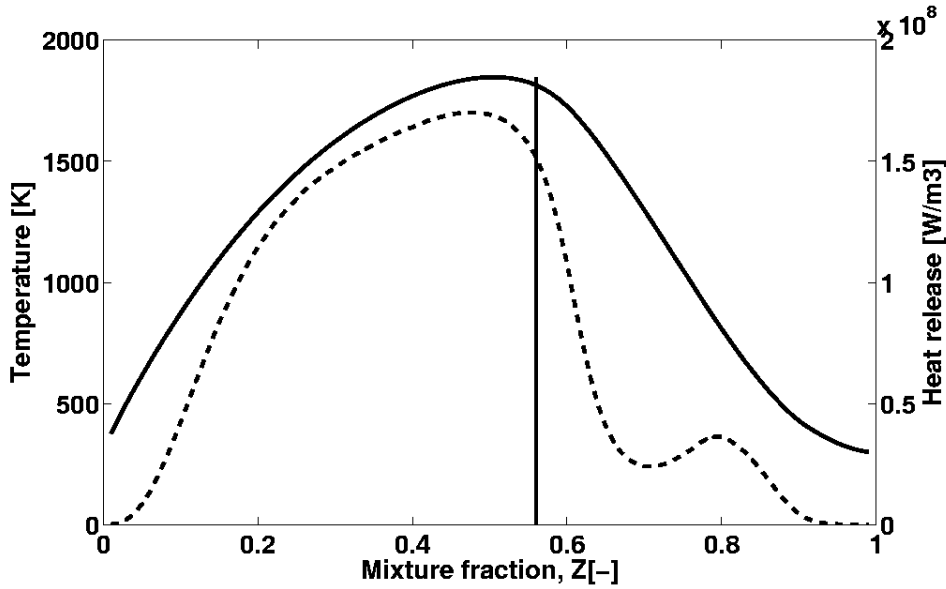


Figure 5.3: *Case A:* Plots of mean temperature (solid line, left scale) and heat release (dashed line, right scale), conditioned by the mixture fraction Z at $t \approx 1.0\tau$. The solid vertical line corresponds to the stoichiometric mixture fraction, Z_s

$$\tilde{P}_\gamma(Z; \mathbf{x}, t) = \frac{Z^{c-1}}{d^c \Gamma(c)} \exp(-Z/d) \quad (5.3)$$

where Γ denotes the γ -function. The parameters a , b , c and d are determined using the Favre-averaged mean \tilde{Z} and variance $\widetilde{Z'^2}$ of the mixture fraction:

$$a = \tilde{Z}\alpha_1; \quad b = (1 - \tilde{Z})\alpha_1; \quad \alpha_1 = \frac{\tilde{Z}(1 - \tilde{Z})}{\widetilde{Z'^2}} - 1$$

$$c = \alpha_2; \quad d = \alpha_2 \tilde{Z}; \quad \alpha_2 = \frac{\tilde{Z}}{\widetilde{Z'^2}}$$

When using turbulent combustion models, \tilde{Z} and $\widetilde{Z'^2}$ are usually obtained through supplementary, approximate transport equations. On the other hand, these quantities are readily available from the DNS data, considering the y - and z -directions as homogeneous, corresponding to separate realizations. For this analysis the central part of the numerical domain in x -direction (flame zone) is separated in 9 identical cubic sub-regions with a side length of 1/3 cm (roughly twice the integral scale of turbulence). This dimension is typical for the grid size employed in the RANS computation of a turbulent flame. In each sub-region the Favre-averaged mean \tilde{Z} and variance $\widetilde{Z'^2}$ of the mixture fraction are computed by post-processing the DNS data and are afterwards used to reconstruct the PDF of Z following Eqs. (5.2) and (5.3). These reconstructed PDF are compared with the exact PDF obtained from the DNS data within the corresponding sub-regions, plotted in Fig. 5.4 for six of the nine (except the third, fifth and seventh) slabs. The numbering is from left-to-right, top-to-bottom. All functions are normalized to obtain a probability of 100% over the full Z -axis. The obtained agreement is quantified by computing the correlation between the exact and reconstructed curves using Matlab. The correlation coefficients are listed in Table 5.2. The correlations demonstrate the superiority of the β -function for reconstructing the PDF. Without any exception, the correlation associated with the β -function is considerably higher than with the γ -function. As a whole, the reconstruction with the β -function is in quite good agreement with the exact PDF, as observed for example in Fig. 5.4(d). Nevertheless, in one from the 9 boxes (or 11%) the agreement with both reconstructions is quite poor (Fig. 5.4(f)). This is the only case where the exact PDF exhibits three clear peaks. It is known that a good

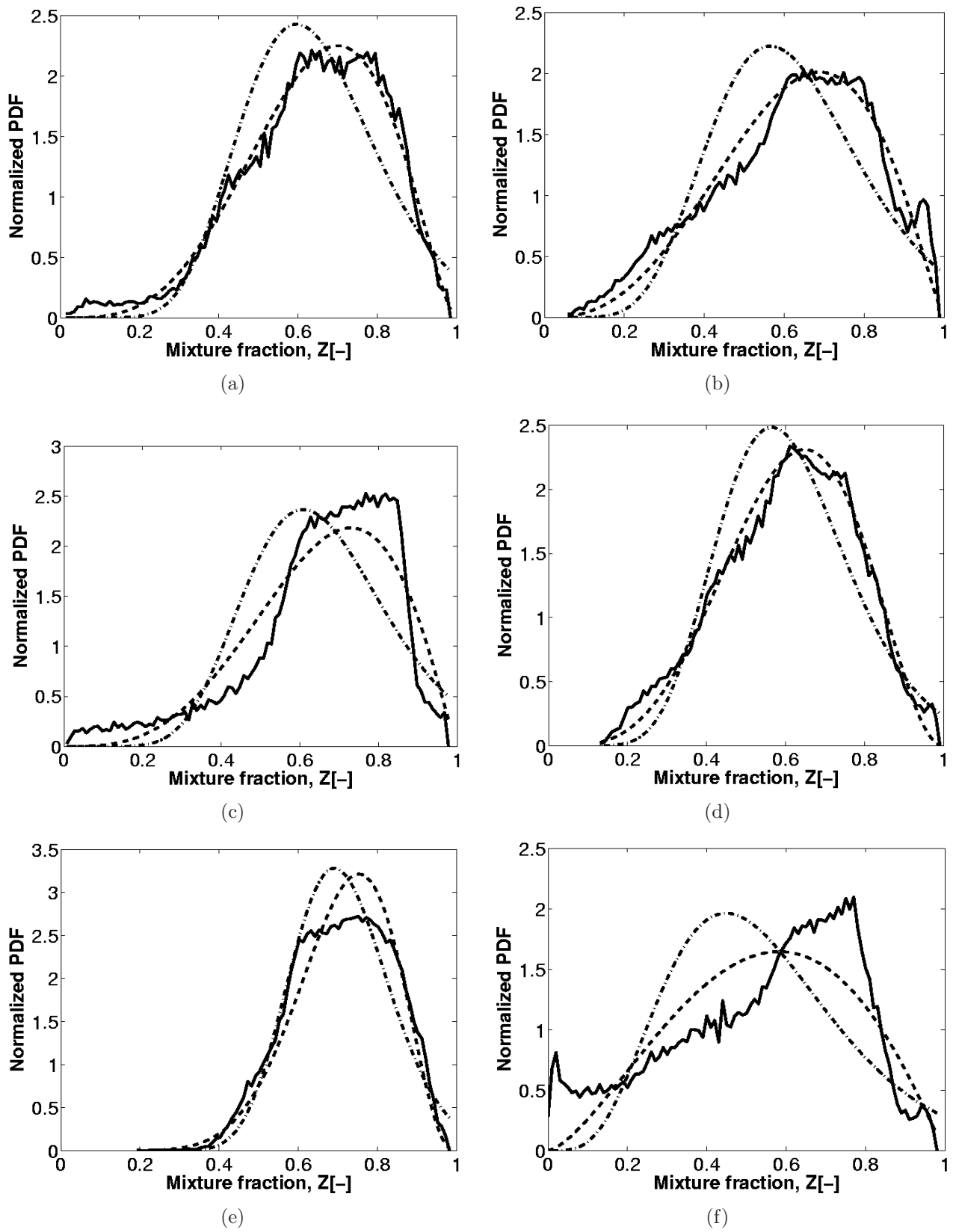


Figure 5.4: *Case A:* PDF of mixture fraction Z in the different sub-regions for six of the nine slabs. DNS: solid line; reconstruction with a β -function: dashed line; reconstruction with a γ -function: dash-dotted line

Sub-region	1	2	3	4	5	6	7	8	9	full slab
β -function	0.99	0.98	0.93	0.95	0.98	0.99	0.96	0.98	0.82	0.93
γ -function	0.91	0.85	0.63	0.81	0.94	0.93	0.82	0.96	0.56	0.77

Table 5.2: *Case A:* Correlation coefficients between the exact PDF obtained from the DNS data and the reconstructed PDF using the β - and γ -functions

reconstruction is not possible using β - or γ -functions in such cases. The correlation obtained when carrying out the analysis for the full slab composed of the nine sub-regions is also given in Table 5.2, demonstrating again the superiority of the β -function reconstruction.

5.2.4 PDF of scalar dissipation rate

The scalar dissipation rate χ is critical to quantify the interaction between mixing and reaction in a non-premixed flame [6]. It represents directly the local mixing intensity and is thus an essential element of all turbulent non-premixed combustion models. It is defined [110] as

$$\chi = 2D|\nabla Z|^2; \quad D = \lambda/(\rho C_p) \quad (5.4)$$

A plot of χ conditioned by the mixture fraction Z is shown in Fig. 5.5(a).

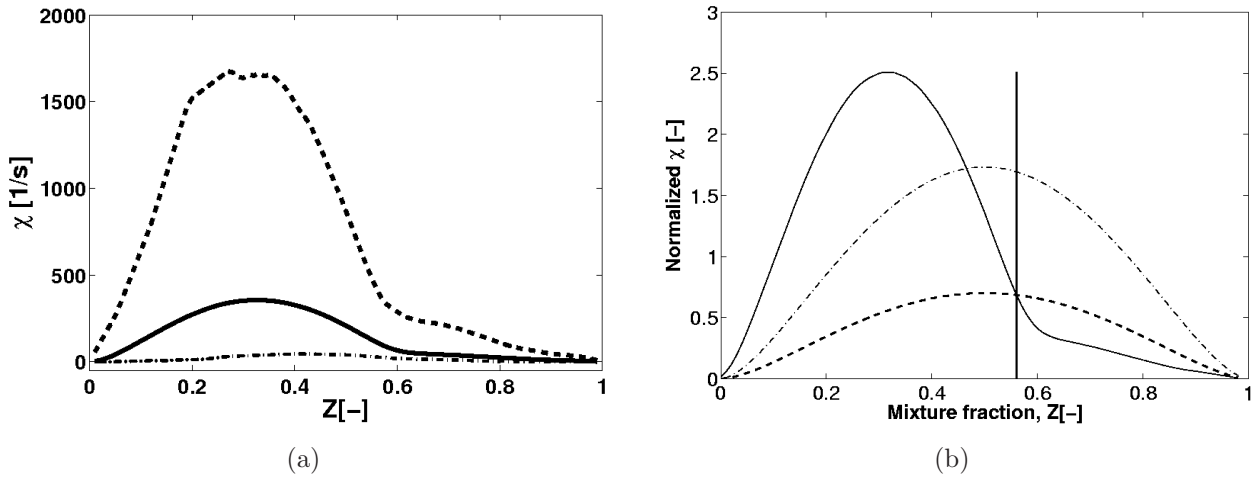


Figure 5.5: *Case A:* (a) Plots of the mean (solid line), maximum (dashed line) and minimum (dash-dot line) of the scalar dissipation rate χ conditioned by the mixture fraction Z and (b) Normalized conditional mean scalar dissipation rate $\tilde{\chi}$ versus mixture fraction Z at $t \approx 1.0\tau$. DNS results: solid line; Eq. (5.5): dash-dotted line; scaled model following Eq. (5.6): dashed line. The solid vertical line corresponds to the stoichiometric mixture fraction, Z_s

The peak conditional scalar dissipation rate appears on the oxidizer side, confirming previous observations (see for example [31] for the analysis of two-dimensional DNS results). The maximum value of χ is four times the mean value, illustrating the considerable variation of scalar dissipation rate found in practice for one value of the mixture fraction. The peak value found in the present DNS computation ($\chi_{max}^{3D} \approx 1600 \text{ s}^{-1}$) is much higher than those observed in previous 2D simulations of our group corresponding to the same conditions, for which a peak value $\chi_{max}^{2D} \approx 900 \text{ s}^{-1}$ has been found. This confirms previous observations concerning differences between 2D and 3D direct simulations (see for instance [95]). Corresponding differences are also observed for the peak heat release values.

Concerning the modeling of scalar dissipation rate, a detailed analysis is proposed in particular in [6]. Starting from the consideration of two specific configurations (counterflow flame,

unsteady mixing layer), it is suggested that the dependency of χ on mixture fraction should follow a law of the type

$$\chi(Z) = \mathcal{A} \exp(-2[\text{erfc}^{-1}(2Z)]^2), \quad (5.5)$$

where \mathcal{A} is a constant that depends on the specific flame configuration being studied and $\text{erfc}(x) = 1 - \text{erf}(x)$ is the complementary error function, erfc^{-1} being its inverse. The mean scalar dissipation rate conditioned by the mixture fraction $\tilde{\chi}_Z$ is modeled by relating it to that at $Z = Z_s$ following [6]:

$$\tilde{\chi}_Z = \tilde{\chi}_s \frac{f(Z)}{f(Z_s)}, \quad (5.6)$$

where $f(Z)$ is the exponential term in Eq. (5.5) and $\tilde{\chi}_s$ is the conditional mean scalar dissipation rate at $Z = Z_s$. The corresponding PDF are plotted in Fig. 5.5(b), together with the exact distribution obtained from the DNS. The observed agreement is quite poor (correlation coefficient of 0.457 between the DNS results and the scaled model). In particular, the obtained distribution of $\tilde{\chi}$ is not at all symmetrical, being highly skewed on the oxidizer side. Model modifications might therefore be needed to take into account such non-symmetrical distributions.

5.2.5 Impact of volume viscosity

Analysis for *case B* is hereby considered. For each computation, the experiment is performed at least twice with exactly the same initial and boundary conditions including turbulent features, except for the fact that the volume viscosity terms are deactivated in one but activated in the other simulation.

5.2.5.1 Laminar flame structure

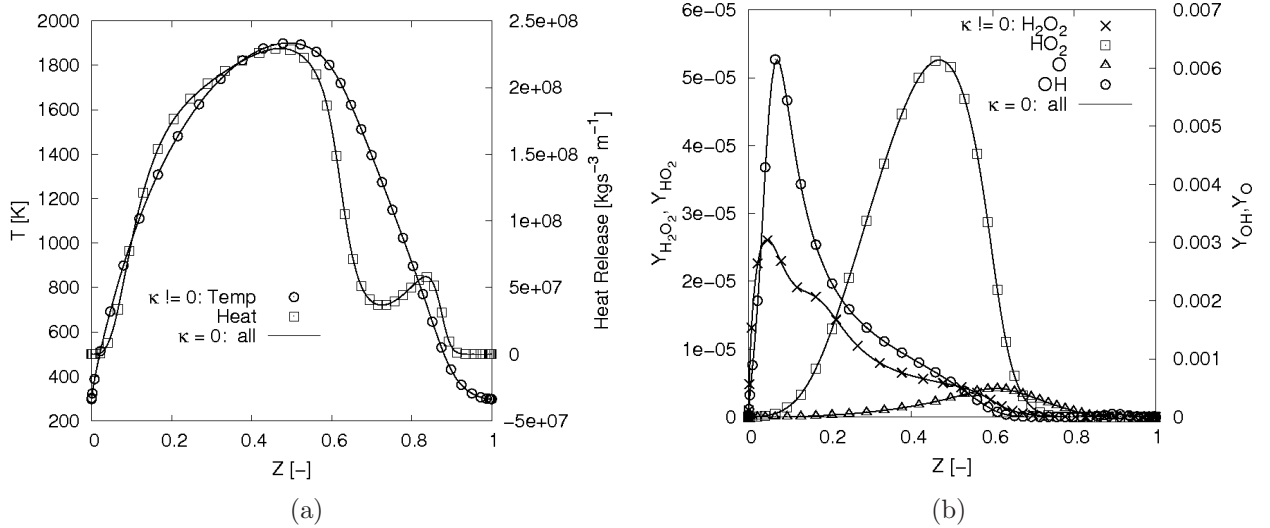


Figure 5.6: *Case B1*: Comparison of one-dimensional laminar non-premixed hydrogen-air flame showing instantaneous profiles of (a) temperature and heat release and (b) the mass fractions of HO_2 , H_2O_2 , O and OH with (symbols) and without (line) volume viscosity at $t = 1.0$ ms

Figure 5.6 shows the one-dimensional laminar flame structure from *case B1*. The results are plotted as a function of the mixture fraction Z as defined in [77]. The instantaneous profiles of the temperature, heat release rate and the mass fractions of OH , O , H_2O_2 and HO_2 are shown at $t = 1.0$ ms with (symbols) and without (line) taking into account volume viscosity. At that time, the non-premixed hydrogen-air flame is chemically very active. It is nevertheless impossible to differentiate the two numerical results in Fig. 5.6. All fields are quantitatively

identical with relative differences below 1%. The other considered cases show the same results. Hence, volume viscosity has no apparent effect on the laminar flame structure. This is due to the fact that the dilatation term is approximately zero in this computation, with a peak Mach number below 0.001. These observations fully confirm the findings of [23], stating that when numerical simulations are performed with identical boundary conditions and at low-Mach numbers, the quantitative differences between simulations are extremely small whether or not the volume viscosity is included. Nevertheless, this theoretical observation is valid only for instantaneous comparisons. It is therefore interesting to check now the long-time influence of turbulence on this finding.

5.2.5.2 Temporal evolution of turbulent flame

Laminar profiles obtained in one-dimensional computations like that described in the previous section are now used as initial estimates to start the turbulent computations. Since it is con-

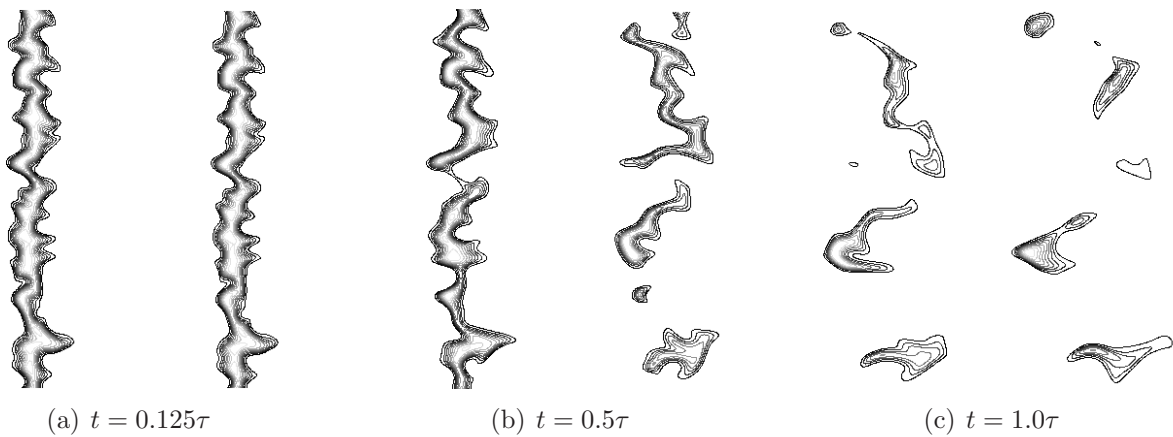


Figure 5.7: *Case B4*: Time evolution of the iso-levels of the mass fraction of OH (zoomed around $0.005 \leq x \leq 0.015$ for $z = 0$) for CO-H₂/air at (a) $t = 0.125\tau$ (b) $t = 0.5\tau$ and (c) $t = 1.0\tau$ with (left) and without (right) taking into account volume viscosity κ . The iso-levels are identical

sidered in many experimental studies, it is interesting to visualize the mass fraction of the OH radical in order to characterize the evolution of the reaction zone. Its temporal evolution is compared in the plane $z = 0$ in Fig. 5.7 at times $t = 0.125\tau$, 0.5τ and 1.0τ for *Cases B4*, when the volume viscosity effects are taken into account or not. The flame becomes increasingly wrinkled and distorted with time as it interacts with the initial turbulent velocity field. There is neither a qualitative nor a noticeable quantitative difference between the two fields up to $t = 0.125\tau$. The same observation goes for all other species and variable fields (not shown), apart from κ of course. With increasing time, the form of the flame begins to differ visibly for the two simulations. This is obvious for $t = 1.0\tau$ but is already clearly seen at $t = 0.5\tau$. The difference becomes more and more considerable with increasing time. When volume viscosity effects are present, the OH front becomes totally ruptured, with the development of isolated flame pockets. Without considering volume viscosity, the rupturing of the flame front starts somewhat later. Similar structural differences can also be observed (not shown) on the instantaneous fields of temperature and heat release rate after interacting with the turbulent field.

5.2.5.3 Normal profiles through the turbulent flame

In order to have a closer look of the impact of volume viscosity on the local flame structure, we have defined straight lines across the flame front at various locations along the y -direction from which flame normal profiles have been extracted for *case B2*. The position of the various normals are shown in Fig. 5.8. In what follows, only the profiles along lines L₁, L₃ and L₅ are

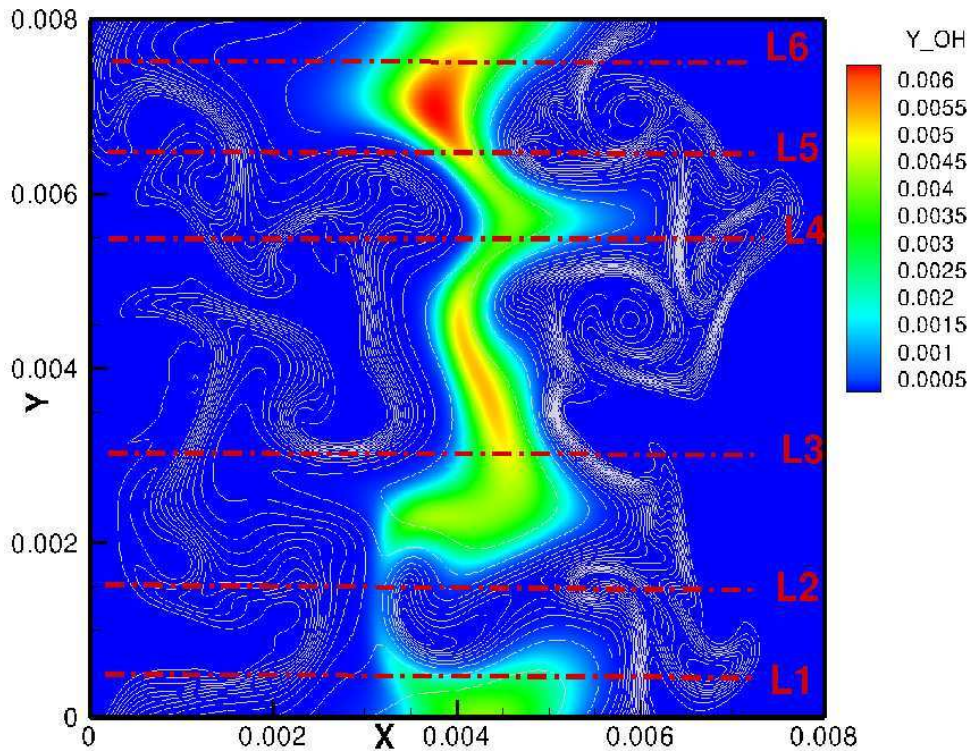


Figure 5.8: *Case B2:* Instantaneous isolevels of density (thin white lines) and instantaneous field of OH species mass fraction at $t = 2\tau$. L_1 - L_6 are line cuts across the flame front at which information is extracted for further analysis

presented. Those for lines L_2 , L_4 and L_6 show a similar behavior and are therefore not shown in the interest of space.

The turbulent flame normal profiles from the computations with and without the volume viscosity of the heat release rate, κ , κ/μ ratio and the mass fractions of HO_2 and H_2O are plotted in Figs. 5.9, 5.11 and 5.11 for lines L_1 , L_3 and L_5 , respectively. The differences in the profiles between the simulations with and without the volume viscosity, as portrayed by these profiles are striking. The local peak values of the heat release rate, the active radical (HO_2) and the abundant species (H_2O) are under estimated when volume viscosity is ignored. Approximately 64% and 42% difference in the peak values of HO_2 and heat release, respectively, is observed along L_1 . The differences decreases to 25% and 33% along L_3 and even further to 20% and 10% along L_5 . The temperature profiles (not shown) are also affected, with differences well above 30 K on certain lines. It is also observed that the similarity in the profiles for the two experiments gets enhanced along those lines where the local peak temperature is much higher. For instance, the profiles for line L_5 (Fig. 5.11) where the local peak temperature rises above 1800K are both qualitatively and quantitatively alike, in contrast to line L_1 (Fig. 5.9) and L_3 (Fig. 5.10) where the local peak temperatures are below 1700K.

The lowest local peak heat release value with and without volume viscosity occurs along line L_1 and increases to L_5 . The same is true for the local peak values of the mass fractions and temperature. Along line L_5 , where we have the highest local peak heat release, species mass fractions are less sensitive to the presence of volume viscosity.

Together with the above flame profiles, we have plotted on Figs. 5.9(b), 5.10(b) and 5.11(b) the variation of the volume viscosity coefficient κ and the ratio κ/μ along each of the afore mentioned normals. Interesting enough, κ and κ/μ are every where far from zero. The peak value of κ , appearing away from the pure fuel and pure oxidizer ends, is very much affected by the turbulence. It is always less than the laminar peak value of $3.0 \cdot 10^{-4}$ kg/m.s. On the other hand, the ratio κ/μ remains more or less around 6 as in the laminar case (not shown).

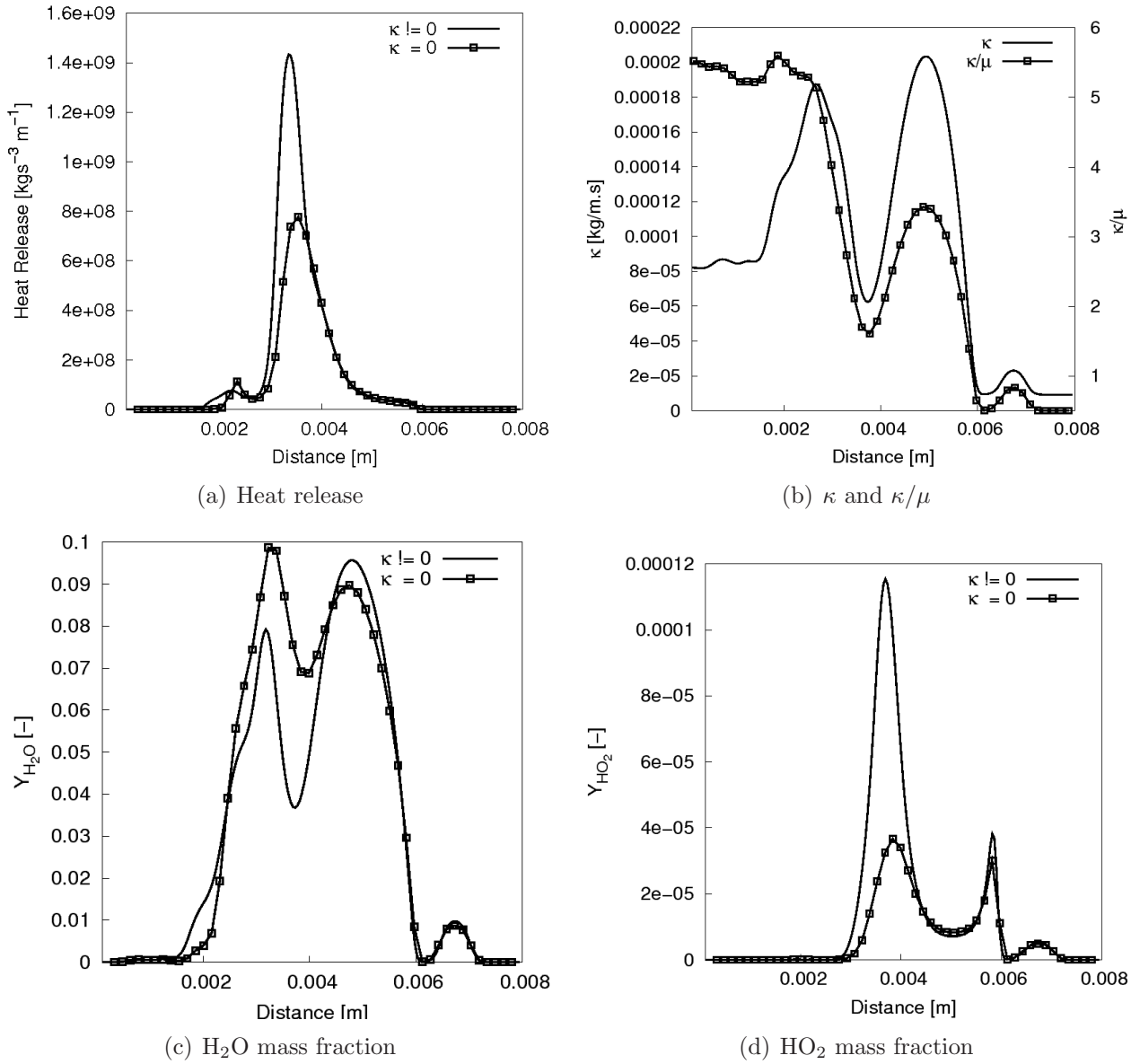


Figure 5.9: *Case B2*: Comparison of the normal profiles of (a) heat release rate, (b) κ and κ/μ , (c) H₂O and (d) HO₂ mass fractions along line L_1 , with (line) and without (line-symbol) volume viscosity

These results demonstrate that, when coupled with turbulence, volume viscosity effects lead to considerable differences both considering the evolution of the corresponding turbulent flame and the local instantaneous flame profile. This is not in contradiction with the findings described in the previous section. Indeed, starting from identical conditions at a time t_0 , the variable fields obtained with or without volume viscosity show no difference at first, as expected for such low-Mach number simulations with identical boundary conditions [23]. Nevertheless, the chaotic nature of turbulence leads to realizations diverging from each other with increasing integration time. Even a minor local difference is sufficient to obtain a completely different evolution at a later time.

It might nevertheless be assumed at first that these differences are only local and do not impact global flame properties. This will be the subject of the next section.

5.2.5.4 Global turbulent flame properties

To this effect, important integral properties of turbulent flames have been computed and compared when taking into account or disregarding volume viscosity. Qualitatively, the findings are

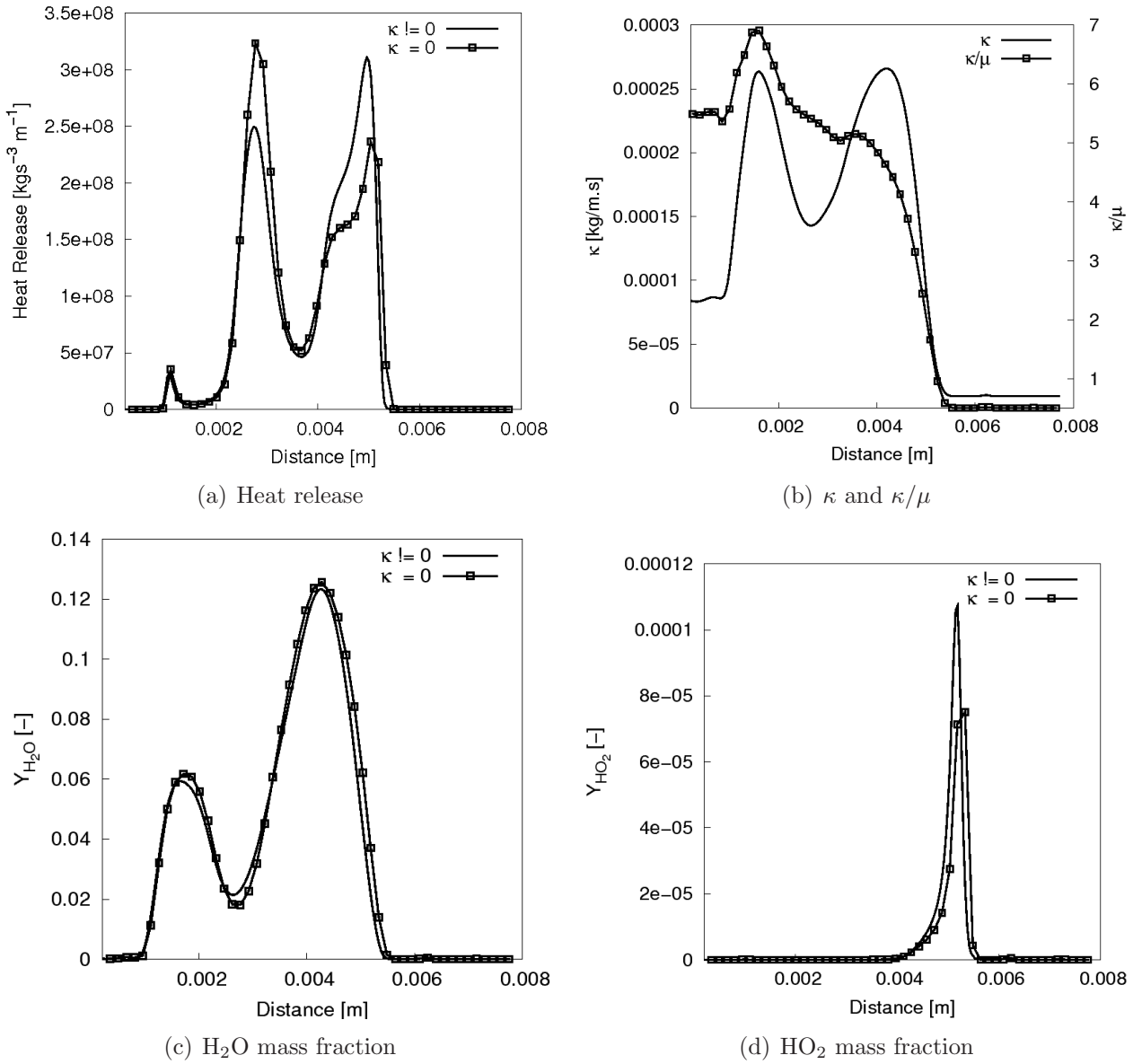


Figure 5.10: *Case B2*: Comparison of the normal profiles of (a) heat release rate, (b) κ and κ/μ , (c) H₂O and (d) HO₂ mass fractions along line L₃, with (line) and without (line-symbol) volume viscosity

similar for all properties, so that only flame surface area and mean temperature are shown in what follows for the first three cases while the fuel consumption and integrated heat release rates are considered for *case B4*.

Figure 5.12(a) shows the increase with time of the flame surface area S_f for both hydrogen (*Case B2 & B3*) and syngas (*Case B4*) flames with and without volume viscosity. In other words, this figure presents the scaled value of $|S_f/S_{f,0}(\kappa = 0) - S_f/S_{f,0}(\kappa \neq 0)|$ vs. time, where $S_{f,0} = S_f(t = 0)$. Initially, this difference is obviously zero. For the present study, the flame surface area has been defined as the area of the isosurface of the stoichiometric mixture fraction Z_s . It can be seen that volume viscosity indeed leads to considerable modifications of this global quantity. As expected, the difference is at first negligible, with noticeable deviations starting for $t \simeq 0.1 - 0.3\tau$.

Similar findings are observed in Fig. 5.12(b), showing the evolution with time of the difference in mean flame temperature with or without volume viscosity. To compute this quantity, the flame front is defined as explained previously (isosurface of stoichiometric mixture fraction). The instantaneous temperature is then extracted along the flame surface, and the values are averaged in space and shown in Fig. 5.12(b) as $|T_{av}(\kappa = 0) - T_{av}(\kappa \neq 0)|$. At low Reynolds

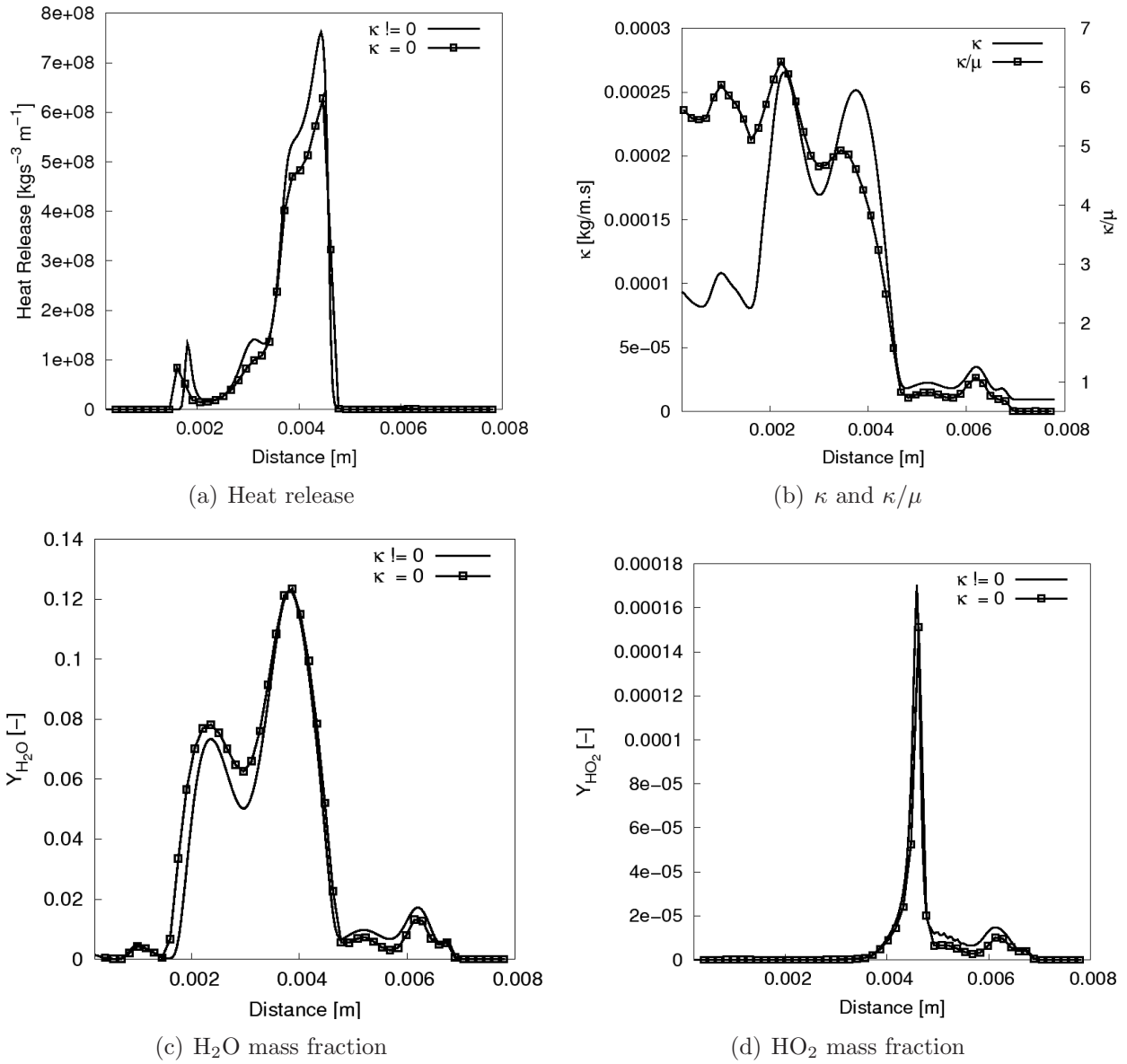


Figure 5.11: *Case B2*: Comparison of the normal profiles of (a) heat release rate, (b) κ and κ/μ , (c) H_2O and (d) HO_2 mass fractions along line L_5 , with (line) and without (line-symbol) volume viscosity

number (*Case B2*), differences become first noticeable for $t \geq 0.5\tau$. The modification of the global flame properties is again slightly larger for the syngas flame than for the hydrogen flame at the end of the simulation.

From a theoretical point of view, the effect of volume viscosity could be maximum for hydrogen flames, since the volume viscosity of hydrogen is highest. This is not confirmed by the present simulation, since *Case B4* (syngas flame) leads to comparable variations with *Case B3* (hydrogen flame at the same turbulence level). Of course, synthetic gas involves also hydrogen combustion so that the impact of volume viscosity might be large as well. Pending further investigations with in-between composition simulations, we presume that the syngas shows a more pronounced effect than the pure H_2 flame due to their different global mixture ratios of 1.12 and 0.8, respectively. As such the level of flame surface distortion by the turbulence will be different and hence lead to, for instance, different flame surface area growth rates.

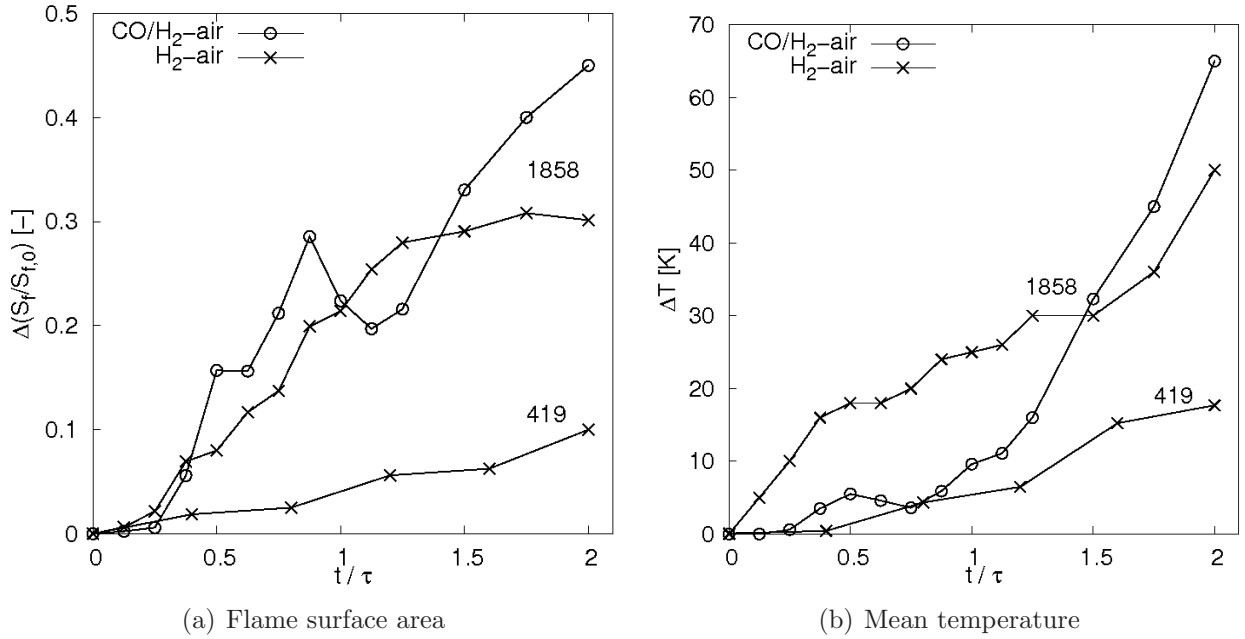


Figure 5.12: *Case B:* Temporal evolution of (a) the difference in scaled flame surface area and (b) mean flame temperature for both H₂/air (*Cases B2 & B3*) and CO-H₂/air (*Case B4*) turbulent non-premixed flames at low (*Case B2*, $Re_t = 419$) and high (*Cases B3 & B4*, $Re_t = 1858$) Reynolds numbers

5.2.5.5 Conditional and PDF analysis

Many turbulent combustion models rely on conditional values and PDF analysis, very often based on the mixture fraction. It is therefore interesting to check as well such quantities in order to quantify a possible impact of volume viscosity. For instance, the instantaneous profile of the mass fractions of H₂O₂ and HO₂ and the mean temperature conditioned on the mixture fraction Z are shown in Fig. 5.13 and Fig. 5.15(b) at $t = 1.5\tau$ for *Case B3* and *Case B4*, respectively. These conditioned species profiles lead to peak modifications between 20 and 35%.

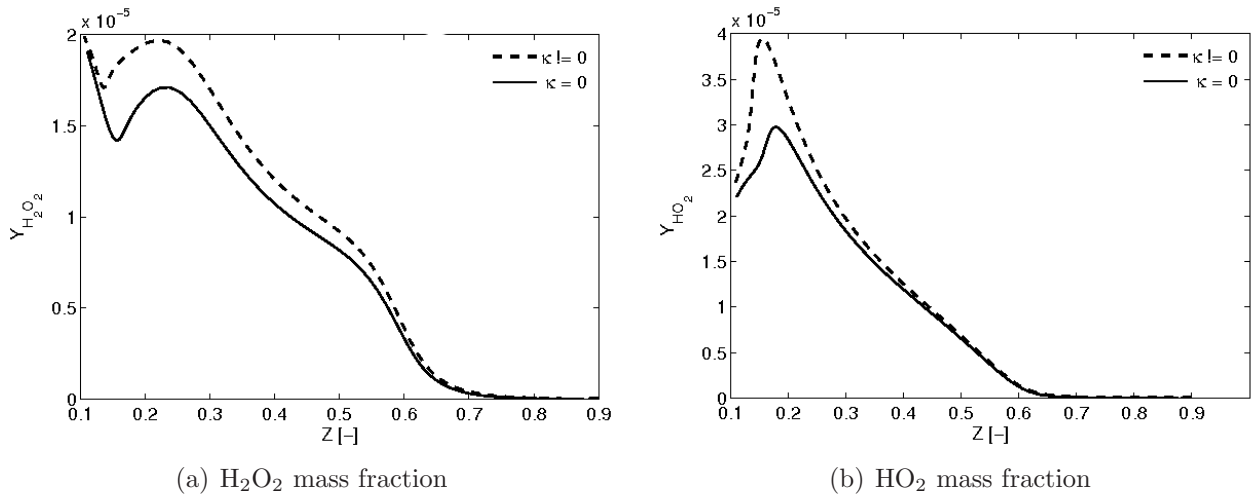


Figure 5.13: *Case B3:* Instantaneous ($t = 1.5\tau$) mass fraction profiles conditioned on the mixture fraction Z with and without taking into account volume viscosity κ

The conditional mean temperature on the other hand shows a peak difference of more than 100 K (Fig. 5.15(b)). These snapshots all demonstrate a noticeable impact of volume viscosity for conditional values. Neglecting volume viscosity systematically results in an underestimation of the peaks of conditional temperature, heat release and mass fraction profiles, which are stronger on the oxidizer side of the domain and at higher turbulent intensity. Since such results,

averaged over time or over several realizations support further model testing and improvement, working with realistic transport models accounting for volume viscosity effects appears to be essential.

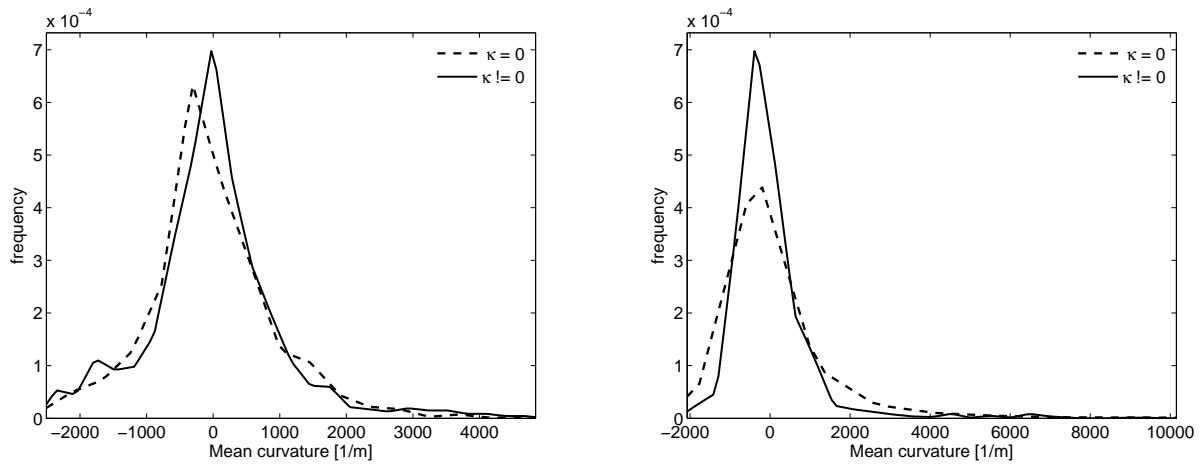
Pdfs of the flame mean curvature and local tangential and normal strain rates extracted along the flame front at two different time instances ($t = 1.0\tau$ and $t = 2.375\tau$) are shown in Fig. 5.14. These characteristics control in particular extinction limits and are therefore vital for modeling purposes. When plotted along the flame surface, they show large differences with and without volume viscosity. The peak pdfs for both the curvature and strain rates are underestimated in the absence of volume viscosity effects, leading eventually to associated modifications of the local burning rates.

From the above analysis, it is obvious that even global flame properties are noticeably modified when taking into account volume viscosity. In turbulent reacting flows at low-Mach number, the instantaneous local impact of volume viscosity might be very small, but it will nevertheless lead to completely different evolutions due to the chaotic nature of turbulence. Of course, it is well understood that any kind of perturbation (initial and/or boundary conditions, numerics, etc.) in a turbulent flow will definitely lead to different realizations. Therefore in order to dismiss the attribution of the observed differences induced by the volume viscosity to any other intermittent and transient phenomena but turbulence, and/or also to establish the statistical significance [12] of the above results, the experiment for *case B4* (CO-H₂/air) has been repeated four times with different turbulence fields initialized with different random seeds but having the same scales for both $\kappa \neq 0$ and $\kappa = 0$. Furthermore, computations with κ substituted by $\kappa/2$, $\kappa/4$ and $\kappa/8$ have also been realized to sustain a logical conclusion of this study. As an example, the measure of the relative increase in flame surface area and conditional maximum mean temperature due to κ are presented in Fig. 5.15. The $\kappa \neq 0$ and $\kappa = 0$ profiles are the average of the corresponding four realizations, with the error bars corresponding to the minimum and maximum value of the four runs at a given time instance. The same trend as presented above is observed for both flame properties. For both sets of computations, the scaled κ profiles progressively tend towards the $\kappa = 0$ solution – a convincing result which strongly supports and endorses our previous claims.

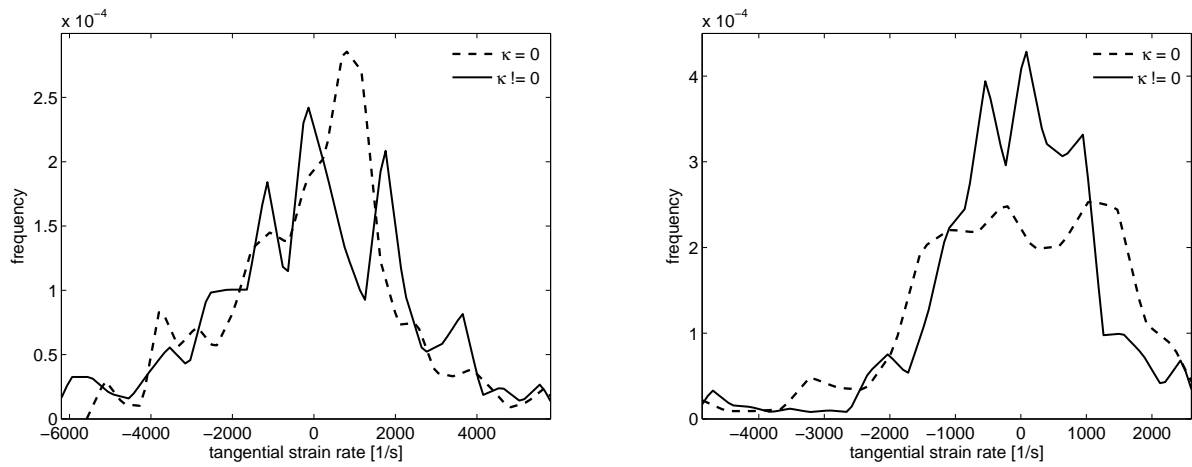
5.2.5.6 Influence of turbulent intensity

Varying turbulent intensity could lead to different findings. On one hand, a higher Reynolds number should lead to larger differences if the chaotic nature of turbulence explains the findings presented up to now. On the other hand, many authors assume that laminar transport processes become negligible for highly turbulent conditions. In the latter case, differences could become smaller for increasing Re_t . As can be seen in Fig. 5.12, by comparing *Case B2* and *Case B3*, which are identical apart from Re_t , the observed differences indeed grow when increasing the Reynolds number. When multiplying Re_t by roughly a factor of 4, the differences are magnified by a factor of the same order of magnitude at a non-dimensional time $t = 2\tau$.

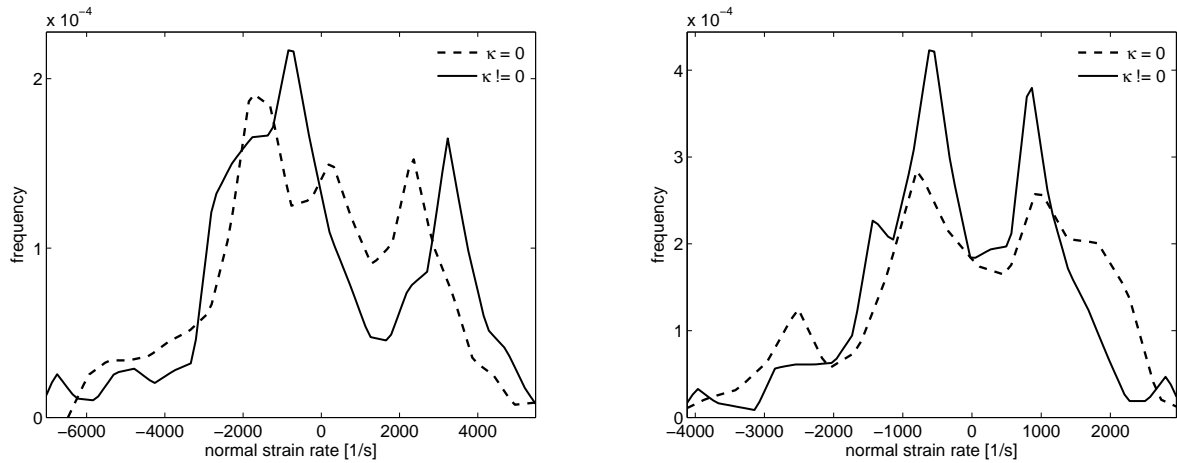
As a consequence, these first computations tend to demonstrate that the influence of volume viscosity is even more important for a higher turbulence intensity. The generality of this observation has to be confirmed by further comparisons. A first explanation for this observation can be found by looking back at Fig. 2.1 where the temporal variation of the maximum value of κ and of the ratio κ/μ as obtained from *case B2* & *B3* are plotted. It can be observed there that the peak value of κ/μ increases noticeably when increasing the Reynolds number from 419 to 1858. This comes from a coupling process; the differences in the spatial fields of temperature and mass fractions observed when taking into account volume viscosity lead to higher peak values for κ/μ in the corresponding simulations, increasing again the influence of this term. Clearly, a physical explanation for this observation would be very interesting and is the subject of our present work.



(a) Mean curvature



(b) Tangential strain rate



(c) Normal strain rate

Figure 5.14: *Case B3:* PDFs of (a) mean curvature, (b) tangential and (c) normal strain rates along flame surface with (solid line) and without (dashed line) volume viscosity at two different time instances – left: ($t = 1.0\tau$) and right: ($t = 2.375\tau$)

5.2.6 Summary

A three-dimensional Direct Numerical Simulation of a turbulent non-premixed diluted H_2 /air flame has been performed using detailed models for chemical reactions and molecular diffusion. The analysis of the results reveal that different combustion regimes (non-premixed, partially-

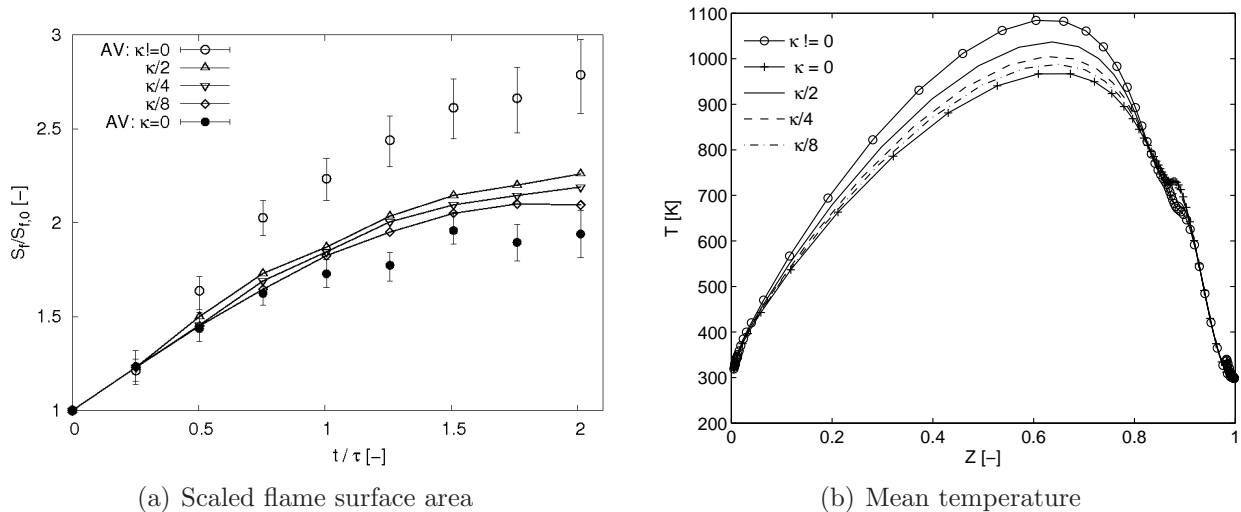


Figure 5.15: Case B4: Temporal evolution of the scaled flame surface area (a) and instantaneous ($t = 1.5\tau$) mean temperature conditioned on mixture fraction (b) for various CO-H₂/air turbulent non-premixed flames at $Re_t = 1858$

premixed, premixed) coexist, as quantified by using the segregation index. Nevertheless, two-thirds of the heat release take place in the non-premixed mode, as expected for this globally non-premixed configuration. The PDF of the mixture fraction can be quite well reconstructed using a β -function and the mean and variance of Z . Typical correlation values above 0.9 are obtained for 90% of the cases. The γ -function leads to a much poorer approximation. Finally, the distribution of the scalar dissipation rate conditioned by the mixture fraction has been considered. The obtained results are highly non-symmetrical, which cannot be reproduced by the simplified models considered here.

In a second instance, hydrogen-air and syngas-air flames have been analyzed in order to quantify the impact of volume viscosity on the flame properties. It has been shown that no differences are found in laminar, one-dimensional computations, confirming theoretical findings for such low-Mach number conditions. On the other hand, the chaotic nature of turbulence amplifies small instantaneous differences with time, eventually leading to completely different evolutions. As a consequence, taking into account volume viscosity leads to noticeable differences even before reaching the characteristic turbulent time τ . This effect is clearly visible locally, changing for instance the local flame structure. But it is also observed with a considerable magnitude on all global flame properties and increases with time. This observation is not limited to pure hydrogen flames, but is observed as well when using syngas (CO/H₂) as a fuel. For these hydrogen-containing fuels, the influence of volume viscosity appears to grow with the turbulent Reynolds number due to the fact that the peak value of κ/μ increases as well. The inclusion of volume viscosity effects in multi-component multi-dimensional turbulent non-premixed flame computations is therefore recommended for all hydrogen-containing fuels.

In Sect. 5.3.4, an analogous analysis will be conducted this time for premixed flames burning not only hydrogen and syngas but also methane – a non hydrogen-containing fuel – to investigate if the flame structure in the premixed mode also shows any convincing modifications in the presence of volume viscosity.

5.3 Premixed combustion

Now, we move on to tackle combustion phenomena in the premixed mode introduced in Sect. 4.2.1. Initially planar and spherical premixed flame configurations have been computed for lean to stoichiometric pre-mixtures under increasingly high turbulence intensities. In addition to the

hydrogen and syngas fuels used in the previous sections, flames burning methane as fuel are equally considered in this burning mode. Two main challenges have therefore been addressed – increasing the chemical complexity and turbulence intensity – at the same time, thanks to the combined ground breaking advances in high performance computing and the new turbulence generation techniques and parallel I/O enhancement presented in Chapter 4. The various groups of considered parametric cases are presented in Sect. 5.3.1 for the two configurations, together with some notes concerning the retained methane oxidation mechanism. Sections 5.3.2 – 5.3.4 are devoted to the analysis of the major results before a short summary in Sect. 5.3.5.

5.3.1 Problem setup and initialization

Case C: Planar CH₄-air flames (influence of Re_t)

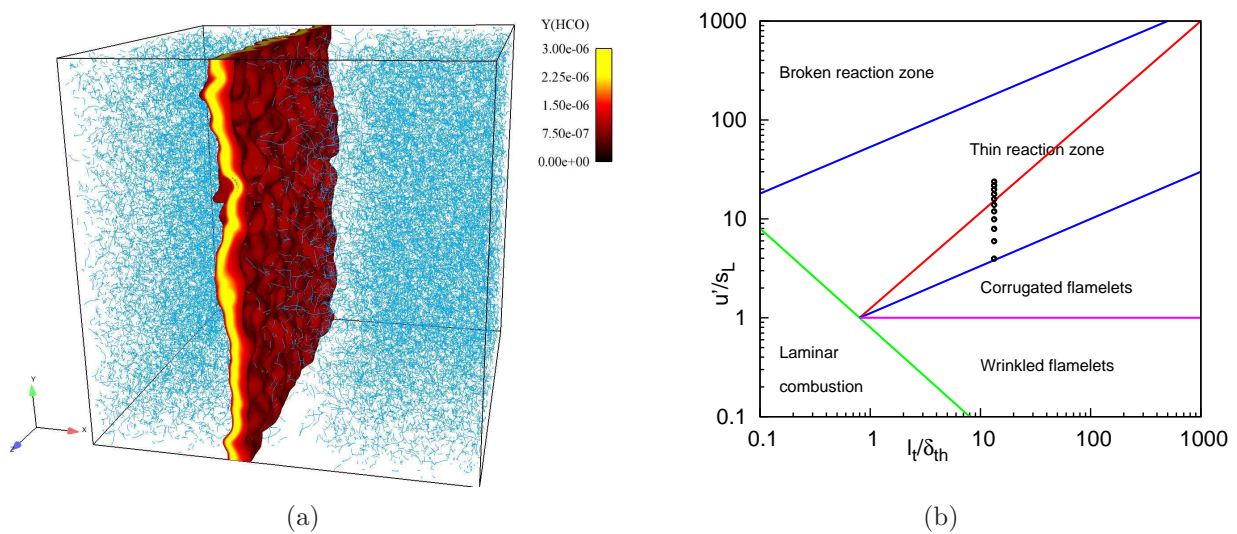


Figure 5.16: Case C: (a) Computational domain showing instantaneous HCO iso-contour surrounded by vortex cores and (b) Modified combustion diagram of Peters [6] with positions of current DNS

An initially planar stoichiometric premixed methane-air flame is considered in a high-intensity turbulent environment using a skeletal reaction mechanism that will be presented shortly. The initial mixture composition considered in the present and subsequent cases at the same mixture ratio is $Y_{\text{CH}_4} = 0.055$ and $Y_{\text{O}_2} = 0.22$ at $T_u = 300$ K on the fresh gas side, with an appropriate nitrogen complement. Smooth initial profiles are imposed with the help of hyperbolic tangent functions.

One of the main objectives in this case is to carry out a parametric study to investigate the effect of successively increasing turbulence intensity on the premixed flame structure. Vital use has therefore been made of the new and parallel turbulence generators in order to increase in a flexible and robust manner the turbulent Reynolds number Re_t based on the integral scale on fine-grain parallel systems.

Twelve numerical experiments at increasing turbulent intensities (all within the Thin Reaction-Zone (TRZ) regime of premixed combustion according to the modified regime diagram of Peters [6], as illustrated in Fig. 5.16(b)) have been realized. The fluctuating velocities u' , turbulent Reynolds number Re_t and eddy turn-over time τ are given in Table 5.3. The characteristic viscosity of the mixture, $\nu = 1.56 \cdot 10^{-5}$ m²/s, the integral length scale $l_t = 0.48$ cm, problem configuration, domain size $L = 2.0$ cm (Fig. 5.16(a)), number of grid points per coordinate direction $N = 801$ (hence a uniform spatial resolution of 25 μm), mixture equivalence ratio $\Phi = 1.0$ and initial flame profiles are identical for all computations.

Case	C1	C2	C3	C4	C5	C6	C7	C8	C9	C10	C11
u' (m/s)	1.00	2.00	3.00	4.00	5.00	6.00	7.00	8.00	9.00	10.0	12.0
τ (ms)	4.77	2.39	1.59	1.19	0.95	0.80	0.68	0.60	0.53	0.48	0.40
Re_t	305	610	916	1 221	1 527	1 832	2 137	2 443	2 748	3 054	3 665
Ka	0.77	2.16	3.98	6.12	8.56	11.25	14.18	17.32	20.67	24.20	31.82

Table 5.3: Case C: Initial turbulence parameters

After letting the flame get a stable structure in a laminar one-dimensional configuration, the resulting profiles are collected at $t = 1.0$ ms. They are then linearly extended in the remaining directions and finally superimposed with a homogeneous isotropic turbulent field computed with the method described above.

Case D: Spherical CH_4 -air flames (impact of Re_t and κ)

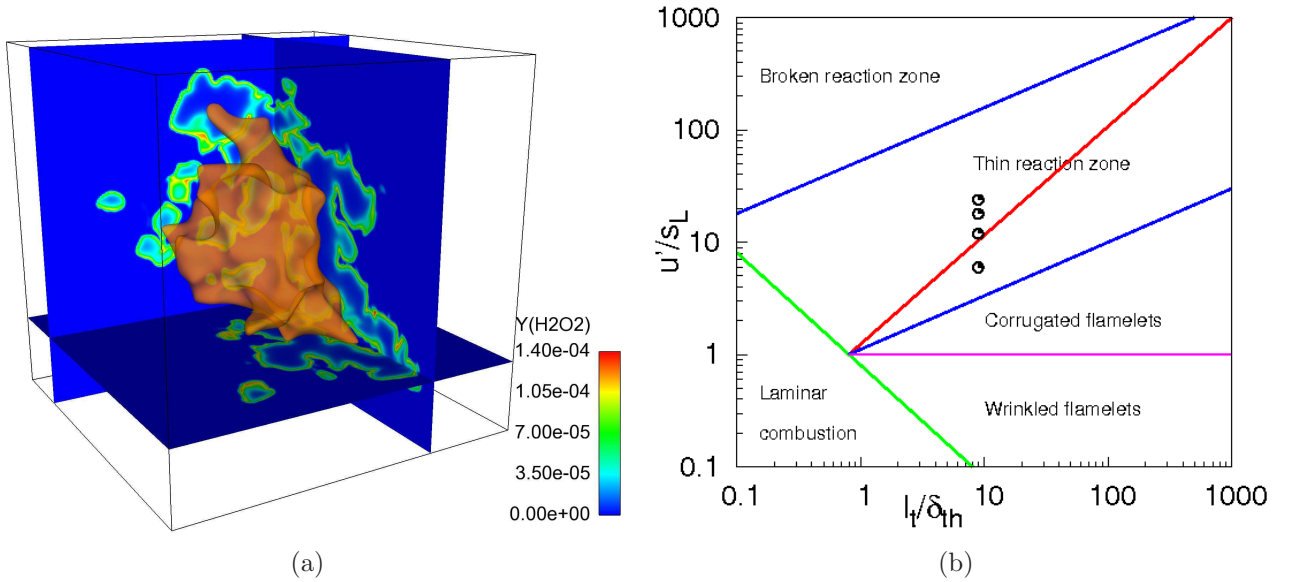


Figure 5.17: Case D: (a) General view of the configuration for the direct simulation, showing an iso-surface of temperature with H_2O_2 slices revealing the heavily wrinkled flame front after interacting with the three-dimensional time-decaying homogeneous isotropic synthetic turbulent velocity field for 0.8 ms and (b) Modified combustion diagram of Peters [6, 144] with positions of current DNS

A stoichiometric spherical premixed methane-air flame is considered in all computations, within a cubic computational domain of sides $L = 3.0$ up to 4.0 cm and a uniform grid spacing of $26 \mu\text{m}$, allowing a sufficient resolution of all spatial scales for all configurations considered. Methane oxidation is modeled with the same scheme as in case C.

The initial system is a stationary hot ($T_b \approx 2200$ K) perfectly spherical laminar flame-kernel of initial radius $r_o = 5.0$ mm, located at the center of the computational box and surrounded by a fresh atmospheric premixed mixture of methane and air at an unburnt temperature $T_u = 300$ K. The initial profile of any primitive variable Φ is prescribed according to

$$\Phi = \Phi_o + \frac{\Delta\Phi}{2} \left[1 - \tanh \left(s \cdot \left(\frac{r - r_o}{r_o} \right) \right) \right] \quad (5.7)$$

where $\Delta\Phi$ is the difference between the initial values, Φ_o in the fresh and burnt gas mixture. The constant s is a measure of the stiffness of the fresh/burnt gas interface. In this range, the influence of s is confined to the very early part of the simulation and therefore does not impact

the analysis presented below at later times. The initial mass fraction values are $Y_{CH_4} = 0.055$ and $Y_{O_2} = 0.220$ at T_u outside the kernel, and $Y_{CO_2} = 0.120$ and $Y_{H_2O} = 0.137$ at T_b within.

case	u'/S_L	τ (ms)	Re_t	Ka
D1	5.95	3.18	615	4.87
D2	11.90	1.60	1 230	13.78
D3	17.86	1.06	1 845	25.31
D4	23.81	0.80	2 460	38.97

Table 5.4: Case D: Initial turbulence parameters

To investigate the influence of the turbulent Reynolds number Re_t based on the integral scale on the flame structure, the same calculations were repeated with exactly the same initial pseudo-turbulent structures and initial composition, but with successively higher turbulent velocity fluctuations. The rms velocity fluctuation u' , the turbulent Reynolds number Re_t , the eddy turn-over time τ used to quantify flame/turbulence interaction for time-decaying turbulence [120] and the Karlovitz number $Ka \approx [(u'/S_L)^3(l_t/\delta_{th})^{-1}]^{1/2}$ are given in Table 5.4. The characteristic viscosity of the mixture, $\nu = 1.56 \cdot 10^{-5} \text{ m}^2/\text{s}$, the laminar flame speed $S_L = 0.504 \text{ m/s}$, the laminar flame thermal thickness $\delta_{th} = (T_b - T_u)/\max|\nabla T| = 0.36 \text{ mm}$ and the integral scale $l_t/\delta_{th} = 8.89$ are all constant for all simulations presented here. As in the previous case, these turbulence characteristics places all the flames considered here within the TRZ regime [6, 144] as illustrated in Fig. 5.17(b).

The general view of the configuration is illustrated in Fig. 5.17(a), where an iso-surface of temperature with H_2O_2 slices are shown, revealing the heavily wrinkled flame front after interacting with the three-dimensional time-decaying homogeneous isotropic synthetic turbulent velocity field for 0.8 ms.

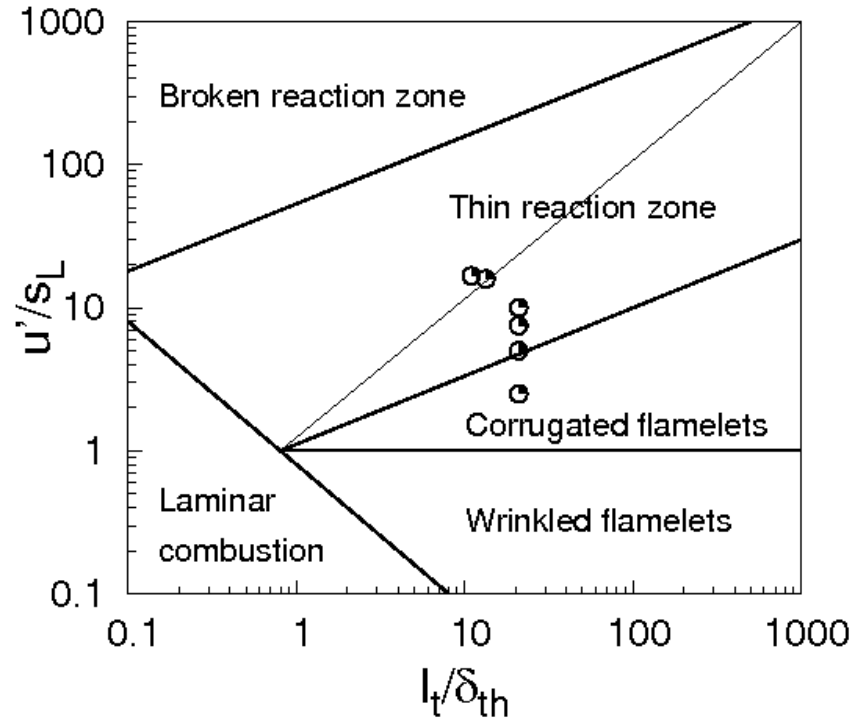
Case E: Spherical H_2 -, CO/H_2 - and CH_4 -air flames (impact of κ)

Cases	Fuel	l_t/δ_{th}	τ (ms)	u'/S_L	Re_t	Ka
E1	all three	laminar	laminar	laminar	laminar	laminar
E2	H_2	6.52	2.4	2.5	548	1.55
E2a	H_2	6.52	1.2	5.0	1 095	4.38
E2b	H_2	6.52	0.80	7.0	1 643	8.04
E2c	H_2	6.52	0.60	10.0	1 219	12.38
E3	$CO-H_2$	3.41	0.60	16.7	1 219	36.85
E4	CH_4	4.17	0.60	15.8	1 219	30.98

Table 5.5: Case E: Initial turbulence and flame parameters

In order to thoroughly check the impact of volume viscosity this time on flames burning in the premixed mode, several pairs of numerical experiments of initially perfectly spherical, laminar premixed flame kernels expanding in time by interacting with a homogeneous isotropic field of turbulence are performed, for three different fuels, namely hydrogen (H_2), syngas ($CO-H_2$) and methane (CH_4), with their oxidation in air modeled by the detailed reaction schemes outlined in Appendix A.1, Appendix A.2 and Appendix A.3, respectively. These particular fuels are chosen partly because of the interesting range of their κ/η ratios as displayed in Table 2.1. This ratio for the hydrogen species is 25 times that of methane at 300 K. Intuitively, we expect that statistics and profiles from a computation using a fuel composed of a mixture of hydrogen and carbon-monoxide will fall between the case with pure hydrogen and methane.

Figure 5.18: *Case E:* Modified combustion diagram of Peters [6, 144] with positions of current DNS



In all the considered cases, each side of the computational domain measures $L = 3.0$ cm, with a constant and uniform grid spacing of $25 \mu\text{m}$. Table 5.5 present a summary of the flame parameters, with all symbols preserving their usual meaning. The initial system is a stationary hot spherical laminar stoichiometric flame-kernel of initial radius $r_o = 3.0$ mm, located at the center of the computational domain and surrounded by a fresh atmospheric pre-mixture of the fuel at T_u . The initial profile is then prescribed according to Eq. (5.7). Moreover, all the computed flames fall within the TRZ regime [6, 144] as illustrated in Fig. 5.18. It is the regime in which it is believed that small turbulent eddies are capable of penetrating and disrupting the preheat zone but fall short of doing so on the reaction zone because of an order of magnitude disparity in the thickness of these flame layers. Almost all modeling approaches in the TRZ regime are hinged on this school of thought, whereas for some practical fuels like natural gas, the preheat layer is only approximately three times thicker than the reaction layer. This is just one of the several common assumptions adopted for the description of turbulent flame structures and dynamics within this regime, often based on theoretical analysis of the flame structure via activation energy asymptotics. We will be focusing on the impact of volume viscosity on flames in the TRZ regime, but some other issues will equally be addressed in parallel, such as determining whether turbulent flames get thicker or thinner in the TRZ regime with increasing turbulence intensity. Specific details associated to each of the considered cases are:

case E1:

In the first pair of simulations, laminar stoichiometric premixed flames are considered for the three fuels. The initial profiles for the different fuel–air pre-mixtures are specified below while describing the turbulent computations in *cases E2, E3 and E4*.

case E2:

The next set of numerical experiments are realized at increasing turbulent intensities with hydrogen–air pre-mixtures. The same methane scheme is employed. The initial system is a stationary hot ($T_b \approx 1900$ K) spherical laminar flame-kernel of initial radius r_o . The initial mass fraction values are $Y_{H_2} = 0.0291$ and $Y_{O_2} = 0.233$ at T_u outside the kernel and $Y_{H_2O} = 0.243$ at $T_b = 1900$ K within. With these values, the laminar flame thermal thickness based on maximum temperature gradient and flame speed are $\delta_{th} = 0.327$ mm and $S_L \approx 2.1$ m/s, respectively. For all the four pairs of realizations (*case E2, E2a, E2b and E2c*), both the fuel and initial

mixture composition are the same. Each setup is superimposed with a homogeneous isotropic time decaying turbulent field at $t = 0.0$, generated by one of the previously described techniques. The flow parameters, u' , Re_t and τ are summarized in Table 5.5. The mixture viscosity $\nu = 1.56 \cdot 10^{-5} \text{ m}^2/\text{s}$, integral length $l_t = 0.48 \text{ cm}$ and initial flame profiles are identical for all computations in this group. The general view of the configuration is illustrated in Fig. 5.17(a). With this case, and in conjunction with *case E1*, the influence of the turbulence intensity on the flame structure, coupled with volume viscosity effects can be systematically quantified.

Within this group, the dataset is further enhanced (following the pattern in *case B*) with additional simulations by repeating *case E2a* and *case E2b* in order to make the study more comprehensive and support the resulting conclusions. In the first instance, the volume viscosity for *case E2a* ($u' = 4 \text{ m/s}$) is systematically substituted by $\kappa^* = \kappa/2$, $\kappa^* = \kappa/4$ and $\kappa^* = \kappa/8$. Here, we seek to determine whether if the volume viscosity were to be scaled down as such, the averages will progressively tend towards the $\kappa = 0$ solution or not. This will be the most logical conclusion. In the second instance, ensemble averaging is used in order to increase the statistical significance of the results by repeating the same "numerical experiment" and then averaging the observations. This is the only option since we are employing time decaying turbulence, unlike time averaging associated with spatially developing turbulence. To this effect, the computations for *case E2b* are equally repeated four times with different turbulence fields initialized with different random seeds but having the same initial intensity ($u' = 6 \text{ m/s}$) for both $\kappa \neq 0$ and $\kappa = 0$. Since a random number generator is used to determine the phases [11], each DNS is associated with the same global properties of turbulence (spectrum, correlations, fluctuations, Reynolds number . . .) but corresponds to a different initial condition in space, and thus to a different evolution (realization) of the flame. We therefore have a richer dataset of five pairs of additional simulations (five with and five without κ) for statistics. Although a stationary flame configuration is necessary to compute long-time averages, these further experiments will provide statistical significance [12] to the results obtained here and back any conclusions. Moreover, the attribution of any observed differences induced by the volume viscosity on the turbulent flame structure to any other intermittent and transient phenomena such as initial and/or boundary conditions, numerics, etc. can then be systematically ruled out.

case E3:

The next configuration considers a flame burning syngas (50% CO and 50% H₂) in air. This fuel was chosen because it is a key subset of higher hydrocarbon fuels and because of its practical relevance. Moreover, the syngas fuel provides an in-between composition case between the previous pure hydrogen fuel and the non-hydrogen containing fuel case (*case E4*) – methane. This case is equally interesting since it would verify if the averages will progressively go from the pure H₂–air mixture to the CO–H₂–air mixture or otherwise, mindful of the values of the κ/η ratio reported in Table 2.1. The initial fuel mass fraction in the previous cases is now evenly shared with the carbon monoxide species with similar initial conditions. That is, the initial mass fraction values are $Y_{H_2} = 0.01455$, $Y_{CO} = 0.01455$ and $Y_{O_2} = 0.233$ at T_u outside the kernel and $Y_{CO_2} = 0.02286$, $Y_{H_2O} = 0.13152$ at $T_b = 1765 \text{ K}$ within. With these values, the laminar flame thermal thickness based on maximum temperature gradient and flame speed are $\delta_{th} = 0.44 \text{ mm}$ and $S_L \approx 0.42 \text{ m/s}$, respectively.

case E4:

In the last setup, a stoichiometric spherical premixed methane-air flame is considered at the same turbulence intensity as in *cases E2c* & *E3* above. Unlike the previous cases involving hydrogen and synthetic gas, this case will provide useful information on the controversy surrounding the influence of the volume viscosity term on the turbulent flame burning a non hydrogen-containing fuel. The initial flame composition is identical to that of *case D* while the flow and flame parameters specific to the case are given in Table 5.5.

Case F: Spherical CH₄-air flames (impact of Re_t on burning rate)

Φ	T_b (K)	T_u (K)	Y_{CH_4}	Y_{O_2}	Y_{CO_2}	Y_{H_2O}	S_L (m/s)	δ_{th} (mm)	Ka
1.0	2 230	300	0.055	0.220	0.137	0.120	0.507	0.36	0.94–96.7
0.9	2 140	300	0.049	0.221	0.133	0.111	0.426	0.40	1.27–81.4
0.8	2 002	300	0.044	0.223	0.122	0.099	0.329	0.46	2.01–105.2
0.7	1 844	300	0.039	0.224	0.108	0.088	0.228	0.56	3.84–159.7
0.6	1 669	300	0.034	0.225	0.093	0.076	0.136	0.78	9.84–409.2

Table 5.6: *Case F*: Initial flame and flow parameters

In the last case in this series, direct simulations are used to investigate systematically pre-mixed methane–air mixtures under successively higher turbulence intensities using detailed physicochemical models, with the aim of supplying complementary data of turbulent consumption speed S_c (which is an interesting measure of the turbulent burning velocity S_T) as a function of turbulence intensity u'/S_L [145–147].

It is then possible to determine in particular if and how the turbulent Reynolds number directly affects S_c for a given turbulence intensity; and if the still controversial [147–152] ”bending zone” and ”quenching limit” on the S_c curves versus u'/S_L can be captured numerically. The setup and range of parameters to be explored mimic combustion vessel experiments similar to those of Abdel-Gayed *et al.* [147, 149–151] and Bradley [152]. The computational settings are similar to those used in [37] for a single-step reaction mechanism and unity Lewis number assumption. In the present study, both the three-dimensional and turbulent nature of the flame–kernel evolution together with a skeletal reaction scheme and multi-component transport models are considered. All computations are within a cubic computational domain of sides $L = 4.0$ cm (see e.g, Fig. 5.17(a)) and a uniform grid spacing of $35 - 20 \mu\text{m}$ for the mild to the most intense turbulent cases, respectively, ensuring the full resolution of the smallest (Kolmogorov) scales, since their length decreases with increasing Re_t.

The initial mixture composition (Y_i), prescribed burnt (T_b) and unburned (T_u) temperatures, laminar flame speed S_L , thermal flame thickness $\delta_{th} = (T_b - T_u)/\max|\nabla T|$ and a Karlovitz number estimate $\text{Ka} \approx [(u'/S_L)^3(l_t/\delta_{th})^{-1}]^{1/2}$ for the various mixture equivalence ratios (Φ) are given in Table 5.6. The given range for Ka corresponds to the different turbulence intensities, as defined below. The initial system is a hot ($T = T_b$) perfectly spherical laminar flame-kernel of initial radius $r_o = 5.0$ mm, located at the center of the computational box and surrounded by a fresh premixed atmospheric mixture of methane and air at T_u . The initial mass fraction values of Y_{CH_4} and Y_{O_2} at T_u , and Y_{CO_2} and Y_{H_2O} at T_b are prescribed outside and within the kernel, respectively. These initial values for any primitive variable ϕ are transformed into smooth profiles according to eq.(5.7) In all cases, an appropriate nitrogen complement is added everywhere at start.

To investigate systematically the influence of Re_t on the fuel consumption rate, the calculations for a given Φ were repeated with exactly the same initial composition, but with an initial pseudo-turbulent velocity field at successively higher intensity. The eddy turn-over time $\tau = l_t/u'$, u' and Re_t for the various cases are given in Table 5.7, while $l_t = 3.2$ mm is kept constant and $\nu \approx 1.56 \cdot 10^{-5}$ m²/s. *Case 1* is not really turbulent and will not be discussed any further. Note also that not all the cases shown here are realized for every Φ given in Table 5.6, due to the higher sensitivity of the leaner mixtures to increasing turbulence intensity, as will be demonstrated later. For the mixtures with $\Phi = 0.6$ & 0.7 , only *cases 1 – 7* are considered, while for $\Phi = 0.8$ and 0.9 , only *cases 1 – 8* and *1 – 9* are performed, respectively.

Based on the above turbulence characteristics, it is clear that a wide range of turbulence Reynolds numbers have been explored with more than 90% of the investigated combustion

cases	1	2	3	4	5	6	7	8	9	10	11	12
u' (m/s)	1.0	2.0	4.0	6.0	8.0	10.0	12.0	14.0	16.0	18.0	20.0	22.0
τ (ms)	3.20	1.60	0.80	0.53	0.40	0.32	0.27	0.23	0.20	0.18	0.16	0.15
Re_t	205	410	821	1 231	1 641	2 051	2 462	2 872	3 282	3 692	4 103	4 513

Table 5.7: Case F: Initial turbulence parameters

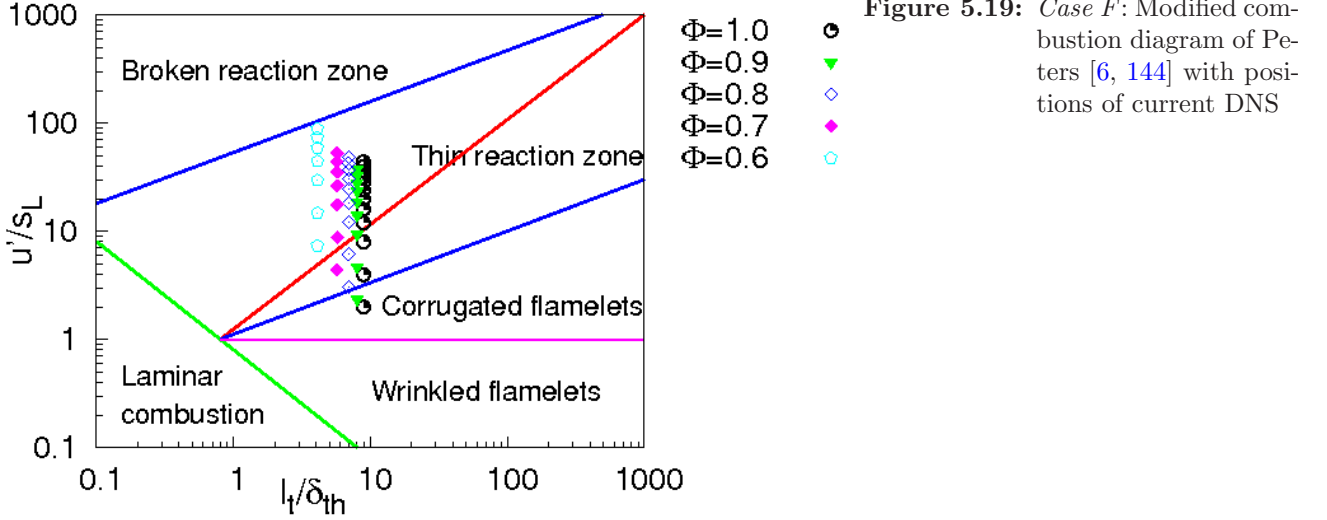


Figure 5.19: Case F: Modified combustion diagram of Peters [6, 144] with positions of current DNS

phenomena covering the Thin-Reaction Zone (TRZ) regime, according to the modified regime diagram of Peters [6, 144], as illustrated in Fig. 5.19.

For the presented computations, our local Linux-based PC-cluster has been employed in a single-user mode. It is built with Opteron quad-core nodes with 32 GB memory/node and an Infiniband connection, with a peak performance of roughly 5 Tflop/s, reserved exclusively for this project. Additionally, three HPC systems across Europe (*BABEL*-IDRIS in France, *HPCx*- and *HECToR*-EPCC in Scotland) were employed, with up to 4096 computing cores. Typically, 10 days of computing time are needed for the lowest grid resolution (35 μm spacing) to reach $t/\tau = 1$ for $\phi = 0.6$. The longest computation requires about two months. While the fully resolved system was simulated, only a reduced grid was saved for post-processing. For all results presented below, the simulations have been carried out up to a non-dimensional time $t \geq 1.3\tau$ as recommended for DNS relying on time-decaying turbulence [120].

Methane oxidation reaction mechanism

After testing many methane schemes, a 16-species 25-step skeletal reaction mechanism was finally retained [43, 153] to describe methane oxidation in air. It provides accurate results for lean up to stoichiometric conditions and has been successfully employed for large-scale direct simulations of two-dimensional non-premixed methane jet flames [154] and premixed methane-air flames [28, 138]. However, it would be inadequate for methane-rich flames due to the absence of C_2 and higher carbon-chain reactions, the reason why $\Phi \leq 1.0$ for all the methane computations reported here. A run down of the scheme in the chemkin form is tabulated in Appendix A.3.

The scheme was further tested with *parcomb* by simulating one- and two-dimensional stoichiometric premixed methane-air flame. The initial flame composition is as previously stated. Fig. 5.20 shows the laminar profiles of the heat release rate, temperature and species mass fractions at $t = 2.0\text{ms}$. Both the major (Fig. 5.20(b): CH_4 , O_2 , H_2O , CO_2) and minor (Figs. 5.20(c): OH , CO , CH_3) species mass fractions show no oscillations.

Figure 5.21 shows the temporal evolution of the mass fraction of CH_2O species in a 2D turbulent case. The initial profile (Fig. 5.21(a)) is that of a stationary planar laminar flame.

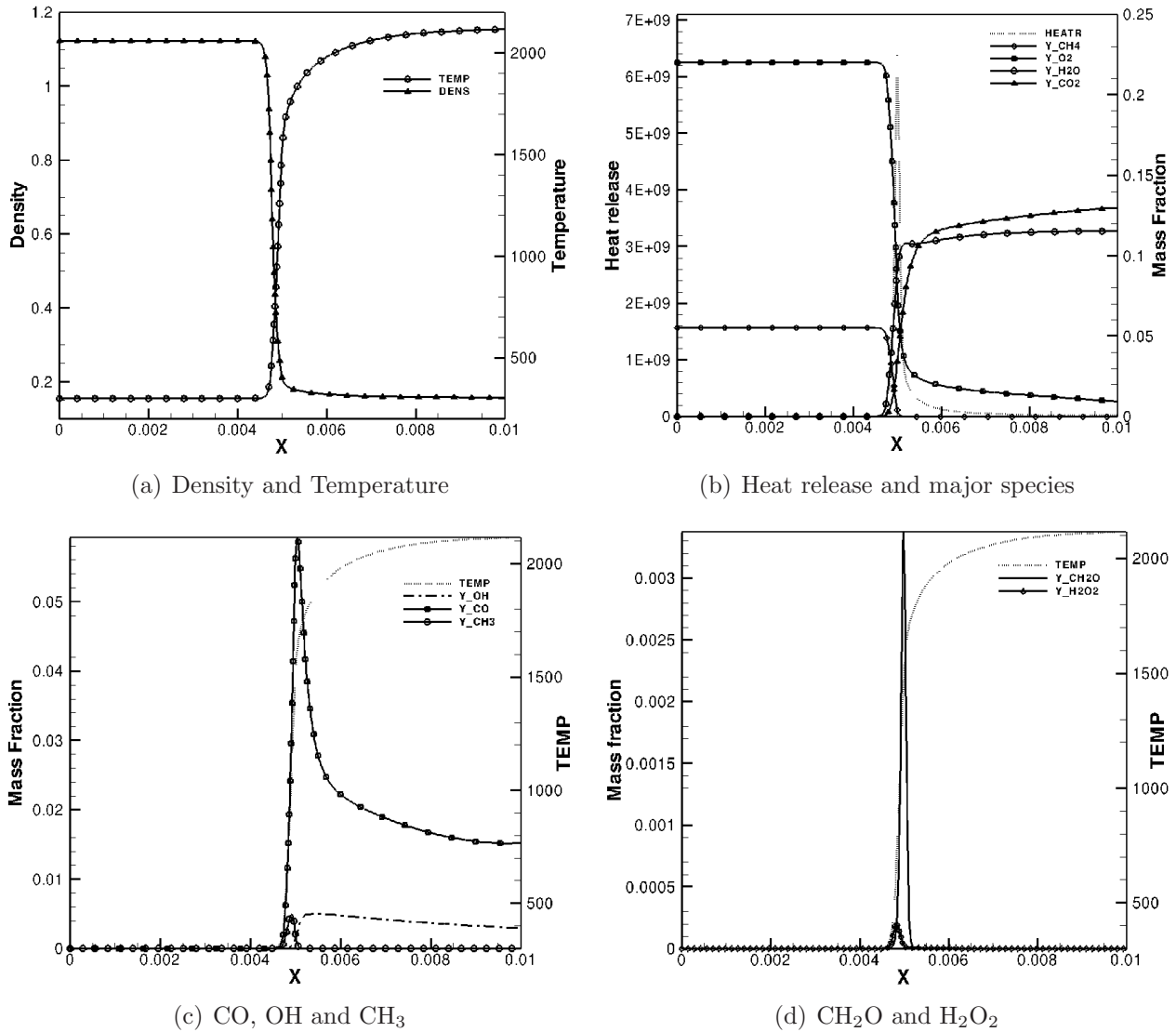


Figure 5.20: Laminar profiles of a one-dimensional methane-air premixed flame at $t = 2.0$ ms

The initially homogeneous turbulence field, as shown by the iso-levels of the vorticity field (thin white lines in the background) decays with time. The flame is stretched, curved and increases in surface area by the interaction with the turbulence. As time evolves, the flame front becomes less and less wrinkled due to dissipation of turbulence and the concurring process of mutual flame annihilation [155].

In Fig. 5.22 the spatial distribution of the temperature, heat release and the mass fractions of CH_4 and CO species after an interaction time of $t = 2\tau$ are shown. The flame front is depicted here by the isolevels (thin white lines) of the mass fraction of CH_3 species.

5.3.2 Highly turbulent planar methane flames

The results outlined in this section for the computations of *case C* were presented at the eighth ERCOFTAC workshop on Direct and Large Eddy Simulation (DLES8) in Eindhoven, the Netherlands [138].

5.3.2.1 General turbulent flame structure

Highly turbulent conditions (Re_t up to 3665) have been accessed. The instantaneous flame structure is exemplified in Fig. 5.23, where the instantaneous reaction progress variable (eq. (4.1))

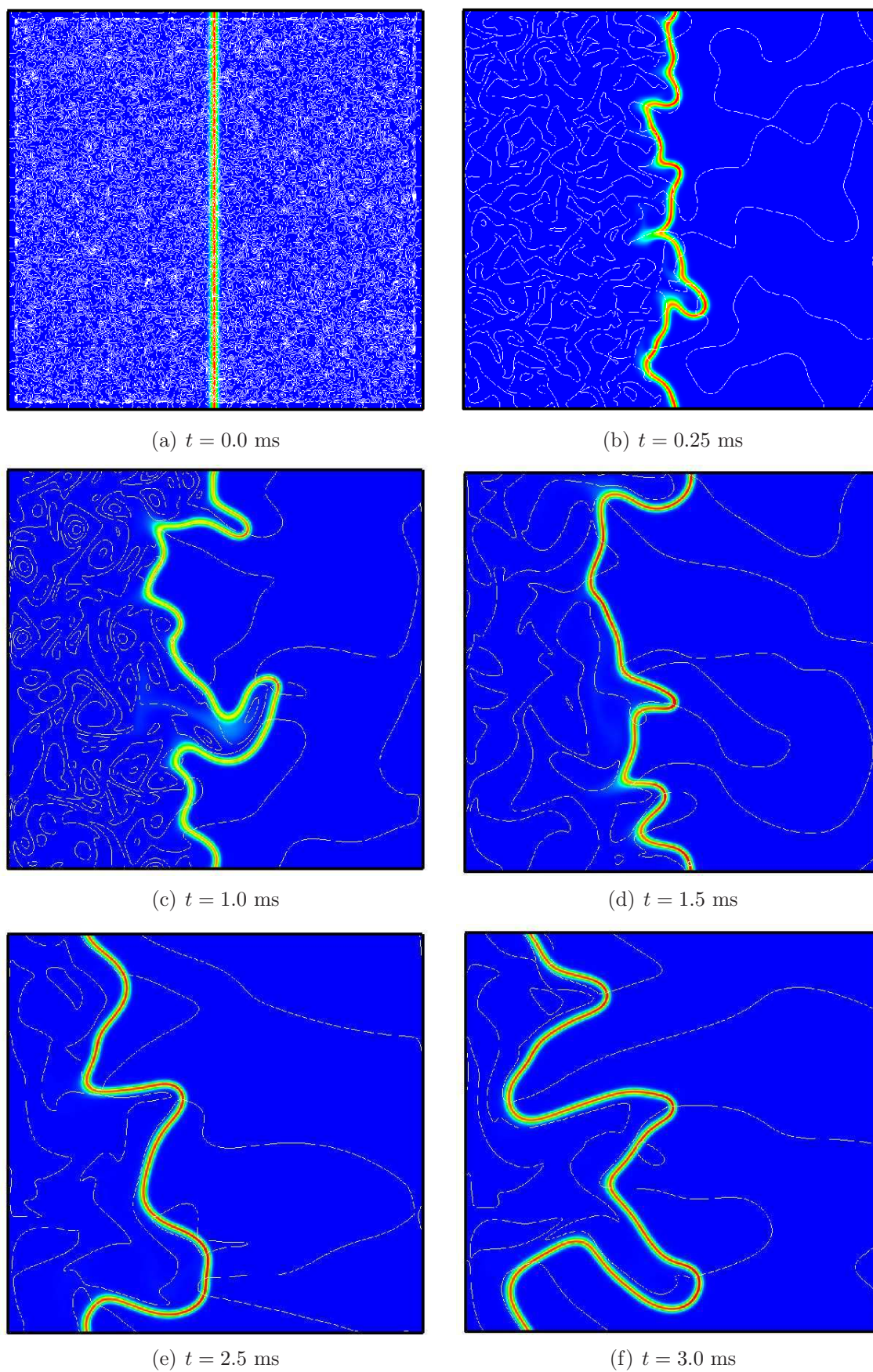


Figure 5.21: Time evolution of the mass fraction of CH_2O species in a planar premixed CH_4 -air flame, under the influence of a time decaying turbulent field

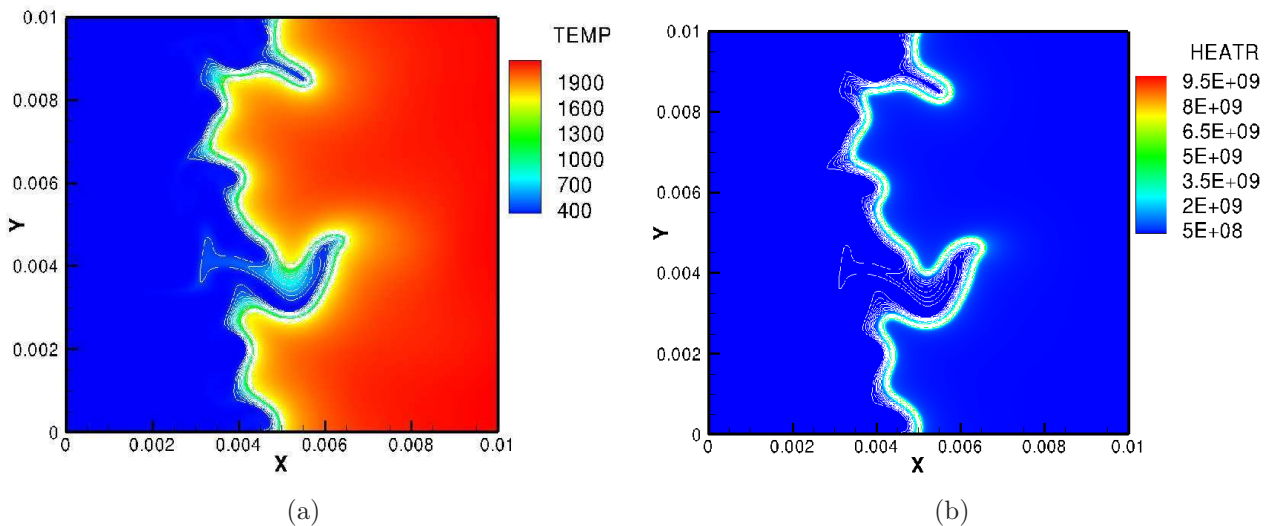


Figure 5.22: Instantaneous spatial distribution of (a) temperature and (b) heat release fields with isolevels of CH_3 mass fraction (thin white lines, depicting the flame front) in a premixed CH_4 -air flame after interacting with a turbulent velocity field for $t = 2\tau$

is plotted at the same non-dimensional time for four different turbulent intensities ($\text{Re}_t = 305, 1527, 3054$ and 3665). The initially planar flame is wrinkled by the superimposed turbulent field soon after initialization. Previously, DNS easily accessed mild turbulence conditions such as the one shown in Fig. 5.23(a) where the flame is only slightly contorted. Comparing the twelve cases, it is observed that the amount of wrinkling increases strongly from Case 1 to 6 and tends to saturate afterwards. This is an indication that Re_t should exceed noticeably 1000 in order to reach realistic conditions, depending of course on the application. For higher values of Re_t , considerable structural modifications are observed, in particular flame–flame interactions, leading to pinch off as evident in the higher Re_t snapshot in Fig. 5.23(b–d). For highly turbulent cases, pinch off and mutual annihilation of flame surface due to interactions are found to be a dominant mechanism limiting the flame surface area generated by wrinkling due to turbulence.

Another interesting observation is the overall displacement of the turbulent flame front within the computational domain with time. The conventional behavior of a laminar premixed flame front, steadily migrating towards the fresh gas mixture is observed only under low Reynolds number conditions (see Fig. 5.21 and Fig. 5.23(a,b)). This propagation is not visible at realistic Re_t values, such as seen in Fig. 5.23(c,d), at least for the short time scales considered here.

5.3.2.2 Effect on flame thickness

In the literature, both experiments and numerical simulations report contradictory claims on the impact of turbulent stirring on flame thickness, highlighting the need for further studies. DNS data is hereby analyzed to determine if the flame thickness actually increases or decreases with increasing turbulent intensity. The reciprocal of the magnitude of the flame progress variable gradient, $|\nabla C|^{-1}$, provides a measure of the flame thickness when averaged over fixed intervals of C . The normalized conditional mean of $|\nabla C|$ is plotted in Fig. 5.24 for six different turbulent intensities (Cases 3, 4, 5, 7, 9 & 11). The obtained profiles decrease with turbulent intensity. Hence, flame thickening is observed. Within the reaction zone ($0.3 \leq C \leq 0.7$), a comparison of the last three Cases in Fig. 5.24 shows a relatively slow rate of decrease compared to the first three cases. Between Cases 10 and 12, the increase becomes almost negligible. This might indicate that any further increase in turbulence intensity beyond a threshold level does not result in thicker flames. Our observations are in agreement with those by Chen *et al.* [156] in a parametric study considering a slot-burner Bunsen flame with lean premixed combustion of

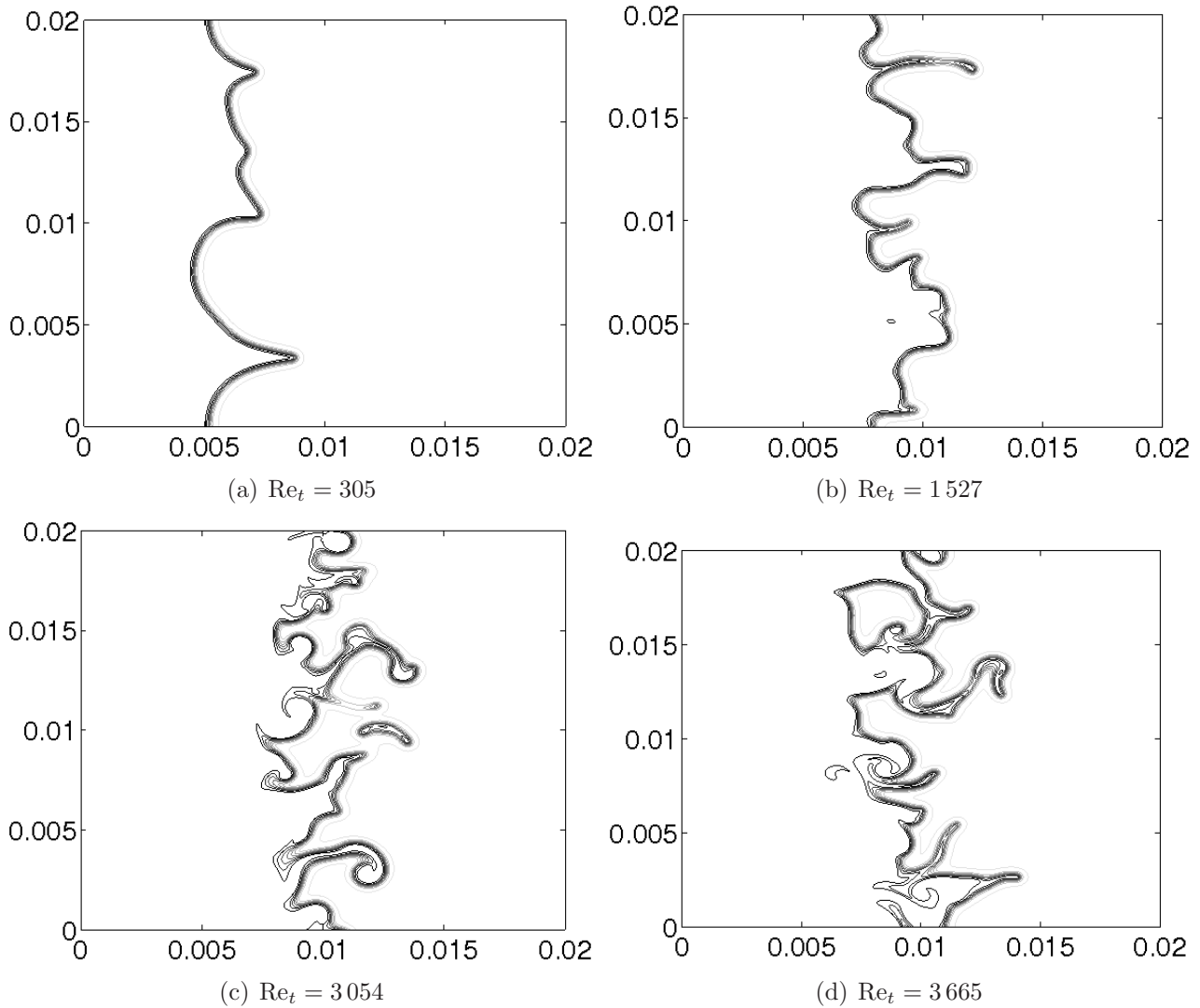


Figure 5.23: *Case C:* Instantaneous iso-surface of the temperature field for different Re_t

methane.

5.3.2.3 Conditional and PDF analysis

The influence of turbulence on the flame structure can be further quantified by probability density functions (PDF). For instance, the local tangential and normal strain rates extracted along the flame front (defined as the isosurface of the reaction progress variable $C = 0.5$ (see eq. (4.1))) for different Re_t are shown in Fig. 5.25(a & b). The peak PDF of the local tangential strain rate is highly flattened when increasing turbulence intensity. The local normal strain rate shows two peaks under mild turbulent conditions, merging into a single peak at higher Re_t . Large modifications are also observed for instance in the PDF of the mean flame curvature. These characteristic quantities control in particular extinction limits and are therefore vital for modeling purposes. When plotted along the flame surface, they show large differences with increasing turbulence intensity, leading to associated modifications of the local burning rates.

In addition to the preceding conditional analysis, other conditional values have been computed for different variables characterizing the flame behavior, like temperature, heat release rate and species mass fractions, as a function of turbulence intensity and are shown in Fig. 5.25(c & d). Such statistical analysis are of central importance for many turbulent combustion models. For the few parameters considered, in all cases, maximum, mean and rms profiles are clearly underestimated under mild turbulent conditions compared to realistic values of Re_t . For

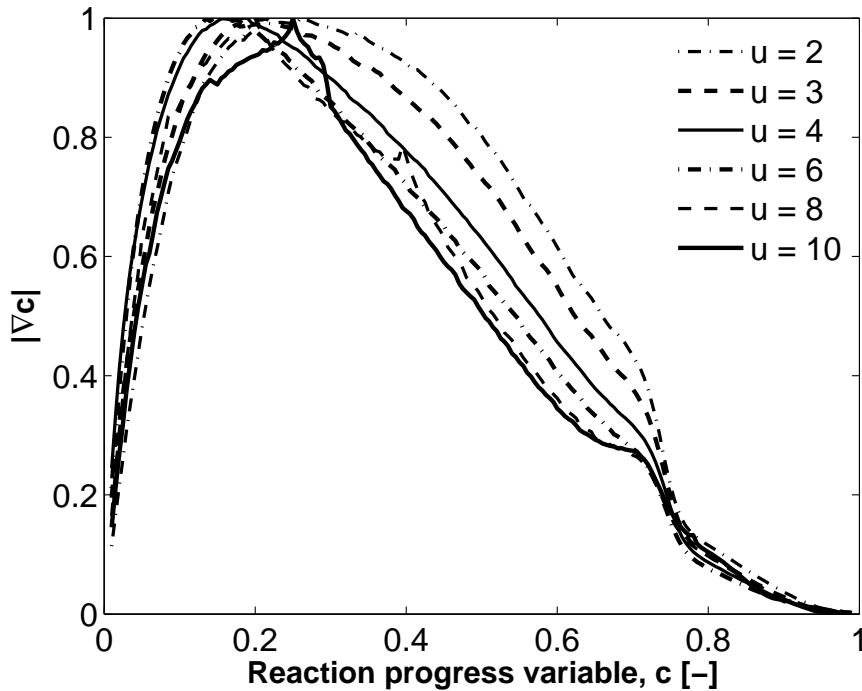


Figure 5.24: Case C: Conditional mean of $|\nabla C|$ for different and increasing Re_t

instance, the rms of the mass fraction of HO_2 conditioned on C show an additional peak around $C = 0.2$, a feature unknown when $u' < 7$ m/s. This is definitely not a spurious effect of the boundary conditions as the domain is large enough with non-periodic boundary along x -axis (see Fig. 5.23(d)). Since such results, averaged over time or over several realizations support further model testing and improvement, working with realistic turbulent conditions appears to be important.

5.3.3 Highly turbulent spherical methane flames

The obtained DNS datasets from case D are processed again using the in-house post-processing library *AnaFlame* [134, 135] to quantify the influence of high turbulence intensities and volume viscosity on premixed methane flames [157]. For cases D3 & D4, each experiment is performed twice with exactly the same initial and boundary conditions including turbulent features, except for the fact that the volume viscosity terms are deactivated in one but activated in the other. Furthermore, ensemble averaging is used in order to improve the statistical significance of the results. Due to the high computational cost and limited resources, only case D3 is repeated. These further computations will provide statistical significance to the results obtained here [12]. In what follows, all profiles shown for case D3 are therefore the average of the six realizations.

Instantaneous solutions are analyzed in terms of conditional statistics of quantities relevant for modeling such as temperature, heat release and selected mass fractions illustrating the turbulence-impaired flame structure. The impact of volume viscosity is assessed by comparing the above profiles for each of the twin computations of cases D3 & D4.

5.3.3.1 Laminar flame structure

First, a laminar case was computed in a smaller computational box ($L = 3.0$ cm) with the same initial mixture composition as in the turbulent cases. The instantaneous iso-contours of the mass fraction of H_2O_2 at different times ($t = 0.1, 0.25$ and 0.5 ms) with and without volume viscosity are shown in Fig. 5.26. The concentric circles correspond, respectively, to the three time

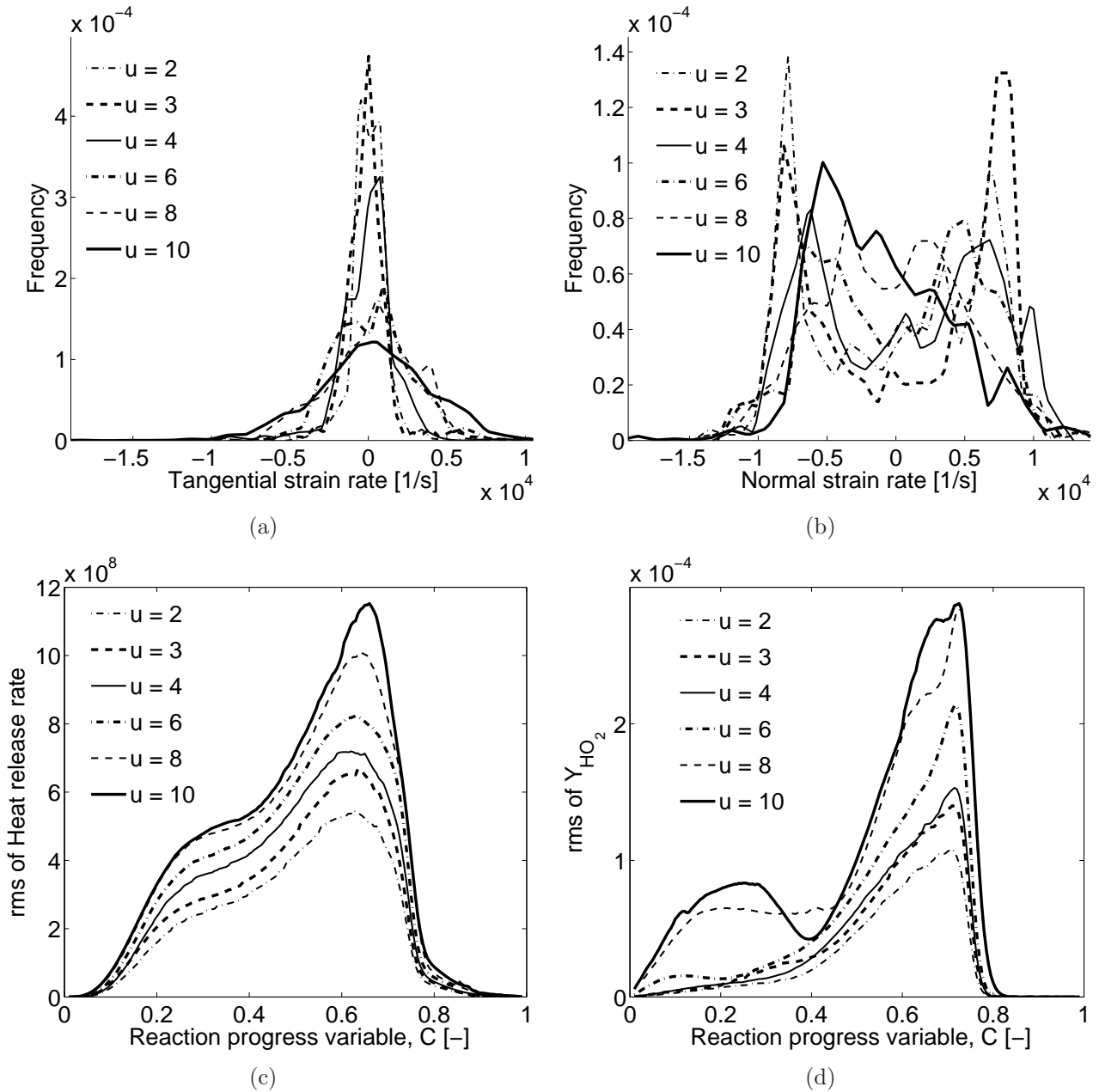


Figure 5.25: Case C: Stoichiometric premixed methane-air flame: PDF of (a) tangential and (b) normal strain rates, and conditional rms of (c) heat release and (d) the mass fractions of HO_2 for different Re_t

instances (with increasing radii). As a complement, the flame structure is shown in Fig. 5.27 against the reaction progress variable (eq. (4.1)). Corresponding temporal evolution of the fuel consumption (S_C) and integrated heat release (H_r) rates (defined later) are shown in Fig. 5.28. The instantaneous profiles of the temperature, heat release rate and the mass fractions of OH, O, H_2O , H_2O_2 and HO_2 are shown at $t = 1.0$ ms with (circled points) and without (solid line) taking into account the volume viscosity transport term. The same plotting style applies for the temporal profiles in Fig. 5.28. It is absolutely impossible to differentiate the two numerical results in Figs. 5.26 – 5.28 both in physical and progress variable space, even for flame radicals like H_2O_2 and HO_2 as well as global flame quantities like S_C and H_r . All fields are qualitatively and quantitatively identical with relative differences well below 1% at all points. All other analyzed quantities (figures not shown) are identical as well. Hence, volume viscosity has no effect on the laminar premixed methane-air flame structure. This is due to the fact that the dilatation term is approximately zero in this computation, with a peak Mach number below 0.001.

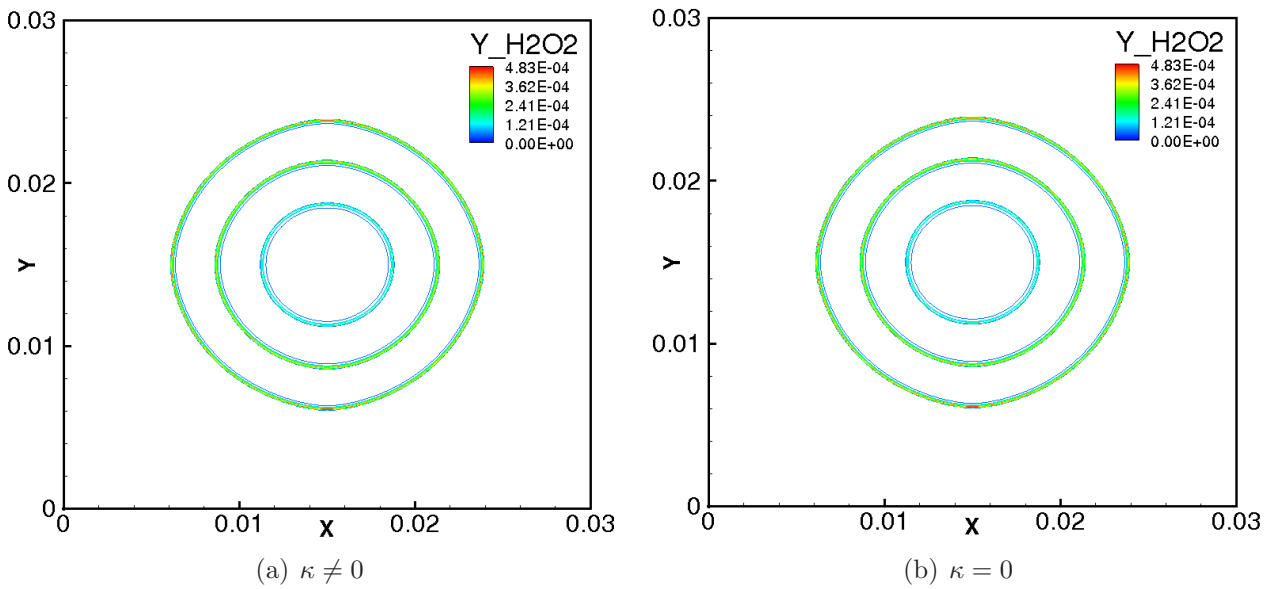


Figure 5.26: Instantaneous contours of the mass fraction of H₂O₂ (along the $z = 1.5$ cm plane) at different times ($t = 0.1, 0.25$ and 0.5 ms) with (a) and without (b) volume viscosity. The concentric circles correspond, respectively, to three time instances with increasing radii

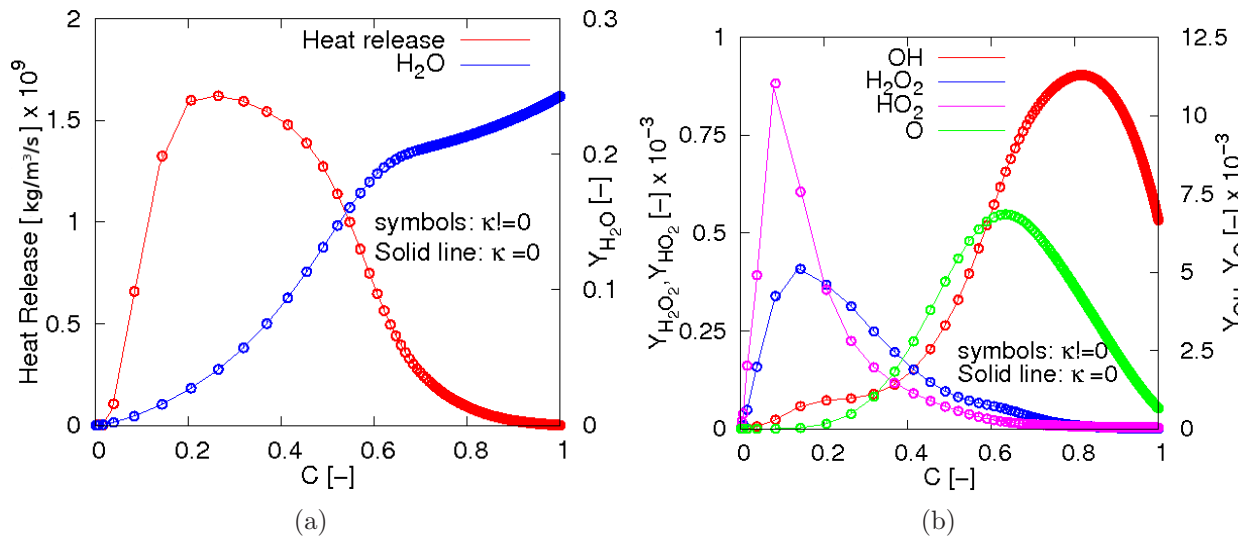


Figure 5.27: Instantaneous profiles of laminar premixed methane-air flame with (circle points) and without (solid line) volume viscosity in the reaction progress variable space, showing the (a) heat release rate and H₂O mass fraction, and (b) HO₂, H₂O₂, O and OH radicals at $t = 1.0$ ms

The above observations are not surprising and fully confirm the findings in [23], stating that when numerical simulations are performed with identical boundary conditions and at low-Mach numbers, the quantitative differences between simulations are extremely small whether or not the volume viscosity is included. Nevertheless, it is interesting to check now the long-time influence of the chaotic fluctuations induced by flow turbulence on this finding.

5.3.3.2 General turbulent flame structure

Highly turbulent conditions (Re_t up to 2460) have been accessed during this project. The effect of turbulence on the physical structure of the flame is first investigated through examination of primitive variables. The temporal evolution of the iso-contours of temperature are shown in Fig. 5.29 for the most turbulent realization (*case D₄*) without accounting for volume viscosity effects, where a cut through the instantaneous iso-contour of the variable illustrates the physical

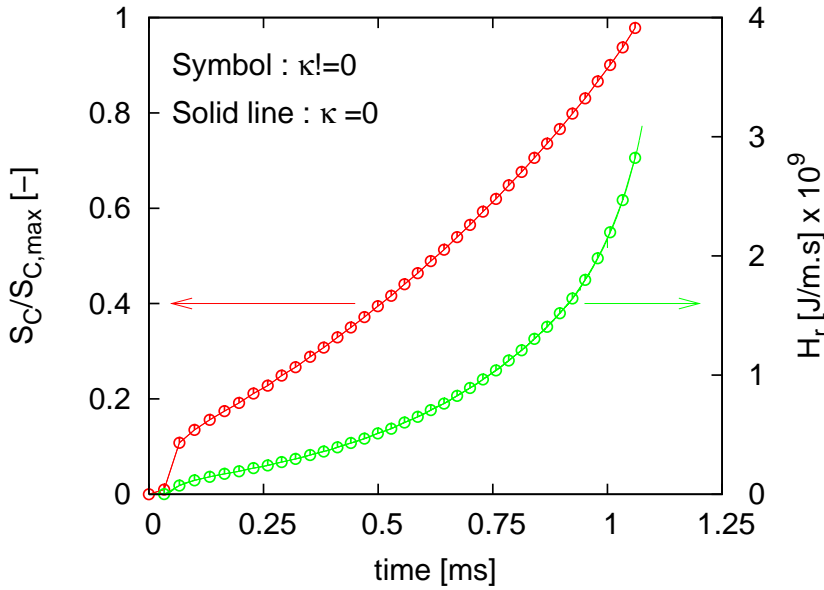


Figure 5.28: Temporal evolution of the laminar fuel consumption and integrated heat release rates for the laminar case with (circle points) and without (solid line) volume viscosity

flame structure at different non-dimensional times ($t = 0.005\tau, 0.25\tau, 0.5\tau, 0.75\tau, 1.0\tau$ and 1.2τ). The initially perfectly spherical laminar flame kernel is progressively and heavily distorted and stretched with time by the very strong turbulent field to the extent that local extinction becomes important. From $t > 0.5\tau$, the turbulent flame structure is marred with numerous perforations (in the form of burnt gas pockets in the fresh mixture and fresh gas pockets within the burnt gas) and edge flame-like structures [158] appearing within the burnt gas mixture at various locations, shapes and sizes. Mutual flame annihilation, extinction and re-ignition processes lead to a very complex flame topology.

The iso-contours of the OH radical follow those of the temperature and are shown in Fig. 5.30 at the same non-dimensional time $t = 1.2\tau$ for *cases 1 – 4* when increasing turbulence intensity ($Re_t = 615, 1\,230, 1\,845$ and $2\,460$) for computations where the volume viscosity effects are not accounted for. The OH radical is a widely employed flame marker, often used to define the location of the turbulent flame front [159]. Previously, DNS mostly accessed mild turbulence conditions such as the one shown in Fig. 5.30(a), where the flame is only slightly contorted. When increasing turbulent stirring, flame–flame interactions begin to appear, eventually initiating the formation of fresh gas pockets within the burnt gas mixture as exemplified in Fig. 5.30(b). Moving on to the most turbulent cases shown in Fig. 5.30(c,d), the amount of wrinkling increases strongly, with considerable structural modifications observed in the form of discontinuous flame fronts, which were hard to figure out from the temperature iso-contour plots on Fig. 5.29. These changes are a first indication that Re_t should ultimately exceed noticeably 1 000, in order to reach realistic conditions, depending of course on the application and on the corresponding regime for turbulent combustion. The obtained flame topology results from local flame extinctions induced by intense turbulence straining and the combined effect of fresh gas islands creation and flame–flame interactions, which eventually lead to flame pinch-off. At high turbulence, pinch-off and mutual annihilation of flame surface are found to be a dominant mechanism limiting the flame surface area generated by wrinkling due to turbulence. Such flame–flame interactions are very important for combustion device designers, being for instance partly responsible for combustion-induced noise [160, 161]. The obtained non-linear relation between turbulent flame speed and turbulence intensity will be quantified in details in the near future by post-processing systematically corresponding DNS. The contours of other major and minor species exhibit similar patterns to those of the temperature or OH fields and are therefore omitted in the interest of space.

For a first assessment of the impact of the volume viscosity on the turbulent flame structure,

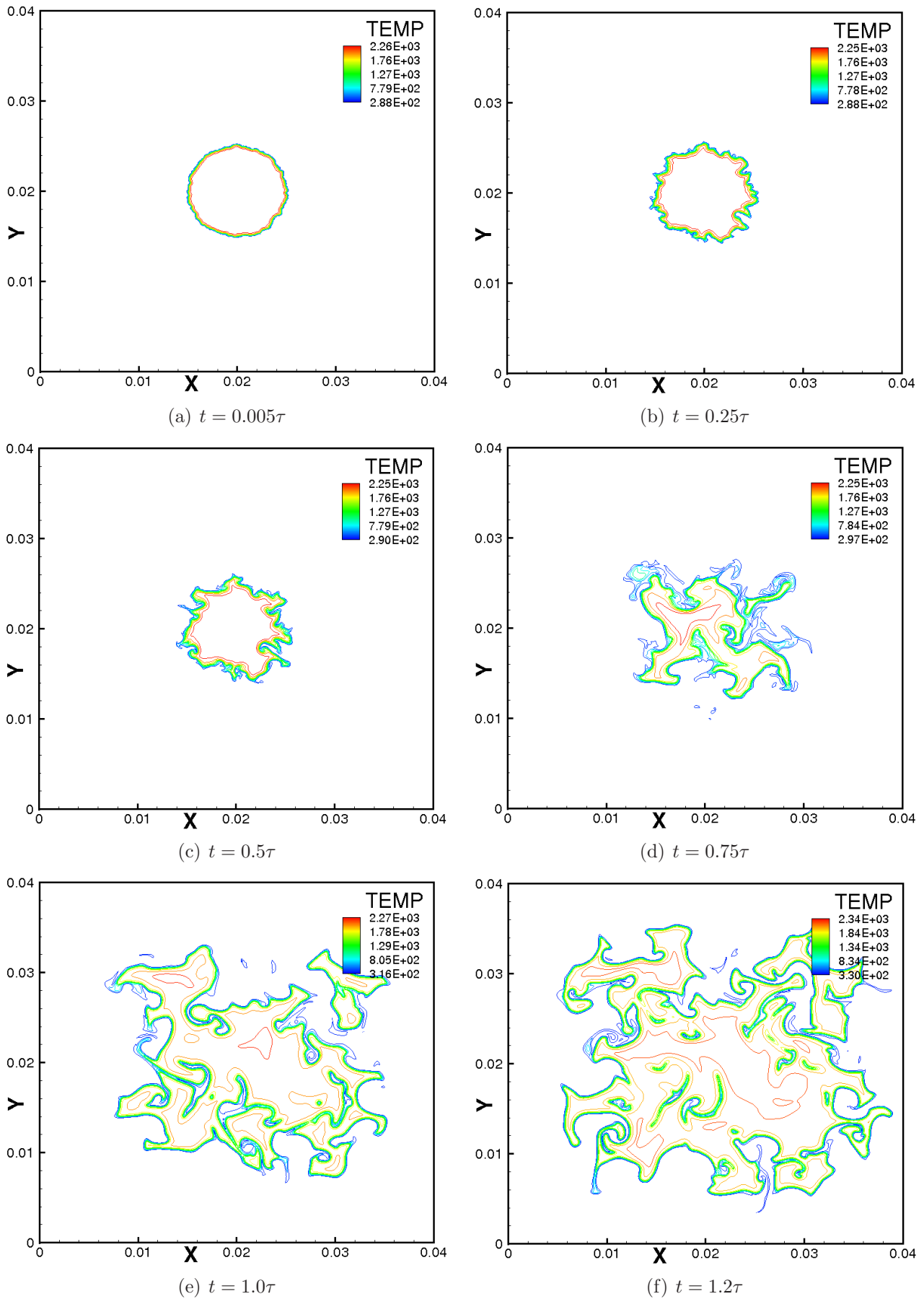


Figure 5.29: Time evolution of the iso-contours of temperature (along the $z = 2.0$ cm plane) for case D_4 (without volume viscosity)

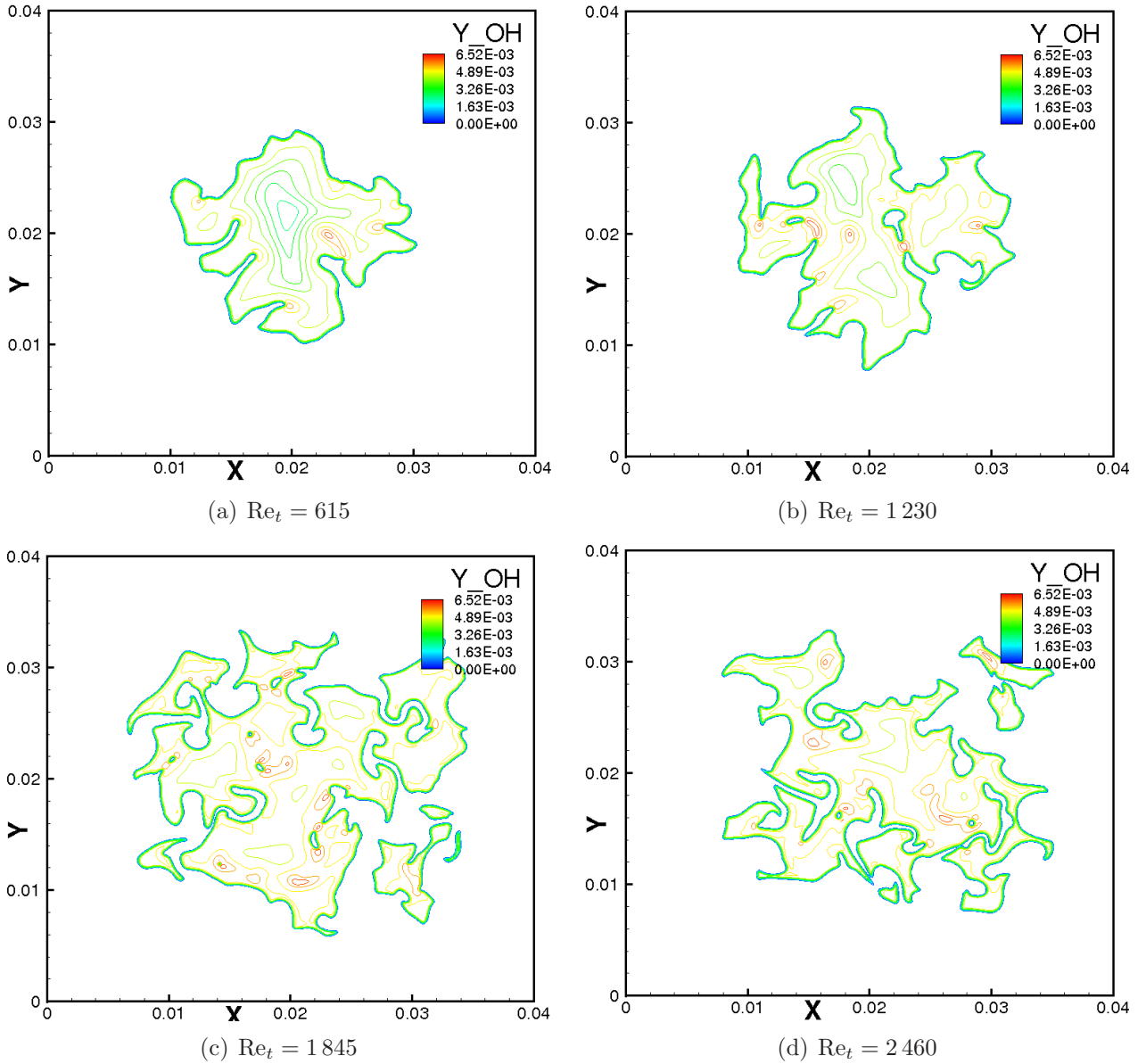


Figure 5.30: Instantaneous iso-contours of OH mass fraction (along the $z = 2.0$ cm plane) when increasing turbulent Reynolds number Re_t at $t = 1.2\tau$. Identical colors are used for all plots

Fig. 5.31 depicts the instantaneous flame front as defined by the iso-contours of the mass fraction of OH for *case D3*, with and without volume viscosity effects at the same time instance $t = 1.2\tau$. The differences in both the structure and peak values are small.

5.3.3.3 Global turbulent flame properties

Two particularly important global flame quantities – the burning rate S_C and the volume-integrated heat release rate H_r (used earlier for the laminar case) – have been tracked throughout each of the experiments and will be systematically compared to check the impact of volume viscosity on the evolution of the premixed methane flame kernel. S_C is an interesting measure of the turbulent burning speed [162] – a parameter of central importance to burner designers relying on premixed turbulent combustion. Here, the burning rate is defined following [163] as the volumetric rate per unit flame area at which the fuel is consumed $\dot{\omega}_f$, and when suitably scaled, serves as a measure of the burning velocity of the flame [164, 165]:

$$S_C \propto -\frac{W_f}{\rho_f Y_f} \int \dot{\omega}_f dV \quad (5.8)$$

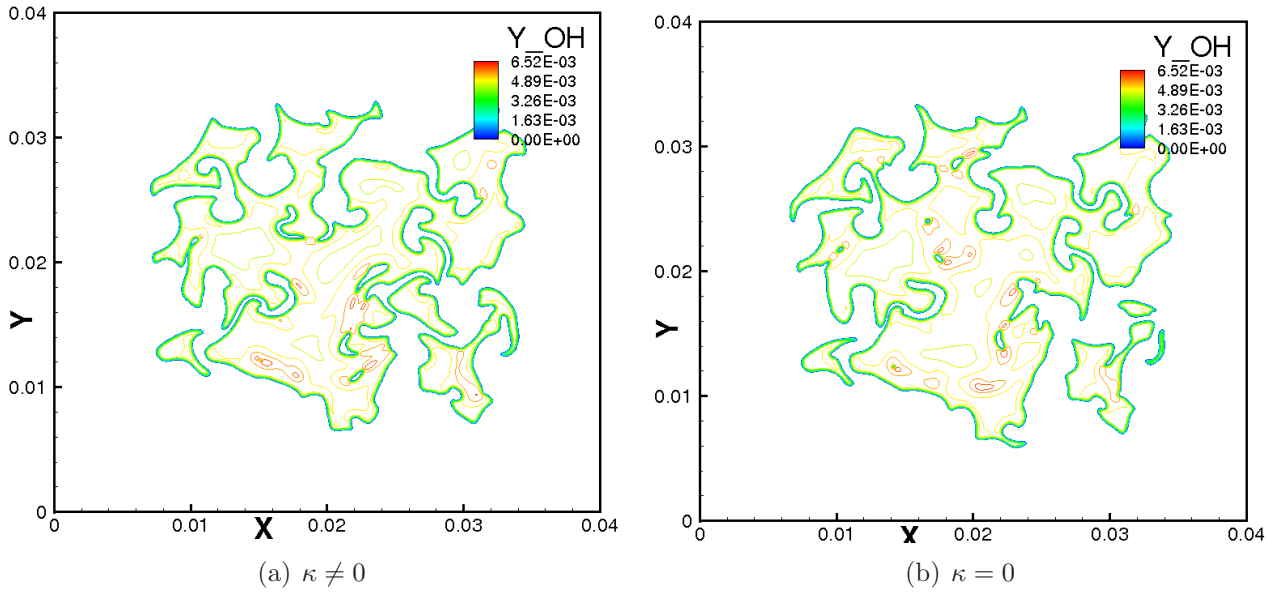


Figure 5.31: Instantaneous flame front defined by the iso-contours of the mass fraction of OH (along the $z = 2.0$ cm plane) for case $D3$ at $t = 1.2\tau$ with (a) and without (b) volume viscosity effects

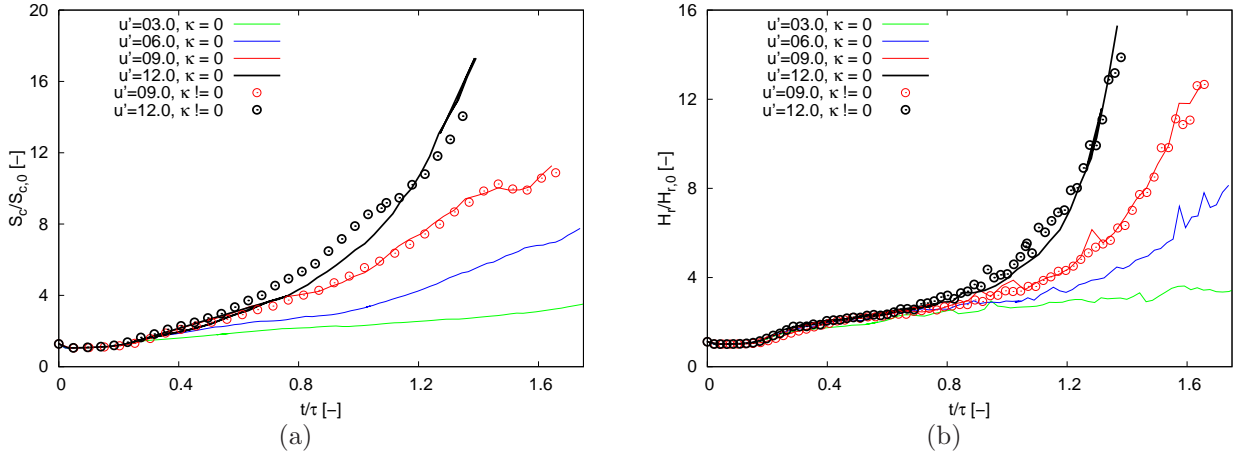


Figure 5.32: Temporal evolution of the scaled (a) fuel consumption and (b) volume-integrated heat release rates at different turbulence intensities for stoichiometric premixed methane-air flames with (circle points: cases $D3$ & $D4$) and without (solid line: Cases $D1 - D4$) volume viscosity effects

where ρ_f and Y_f are the density and mass fraction of the fuel in the fresh gas mixture, respectively. H_r is computed as

$$H_r = \int \left(- \sum_{k=1}^{N_s} h_k \dot{w}_k \right) dV \quad (5.9)$$

Both quantities are scaled by their respective initial laminar values.

The temporal evolution of these two global quantities are shown in Fig. 5.32 for cases $D1 - D4$. The computations with volume viscosity for case $D3$ & $D4$ are also shown on the same figure with circled symbols. Initially, H_r is approximately constant up to about $t \approx 0.2\tau$ after which it increases steadily for about 0.1τ . At $t \geq 0.3\tau$ the profiles for the various cases take noticeably different courses depending on the level of turbulence stirring. The turbulent profiles progressively turn exponential with time (at a pace increasing rapidly with increasing Re_t). Increasing the initial turbulent velocity fluctuation from 3 to 12 m/s leads to an increase in the total heat release normalized by its laminar value from 2 to 16 at $t/\tau = 1.4$. The observation is similar for the burning rate, as expected for this combustion regime. A clear saturation effect

is not yet observed on these DNS results, highlighting the need for simulations at even higher Reynolds numbers and possibly at other mixture equivalence ratios.

Considering now the effect of volume viscosity, the temporal profiles show no noticeable impact of this term. For *case D4* (single DNS realization), slight instantaneous differences appear, probably due to insufficient statistics. This is confirmed by the fact that, for *case D3* (for which the simulations have been averaged over six realizations), the profiles are identical in the presence or absence of κ .

5.3.3.4 Conditional analysis

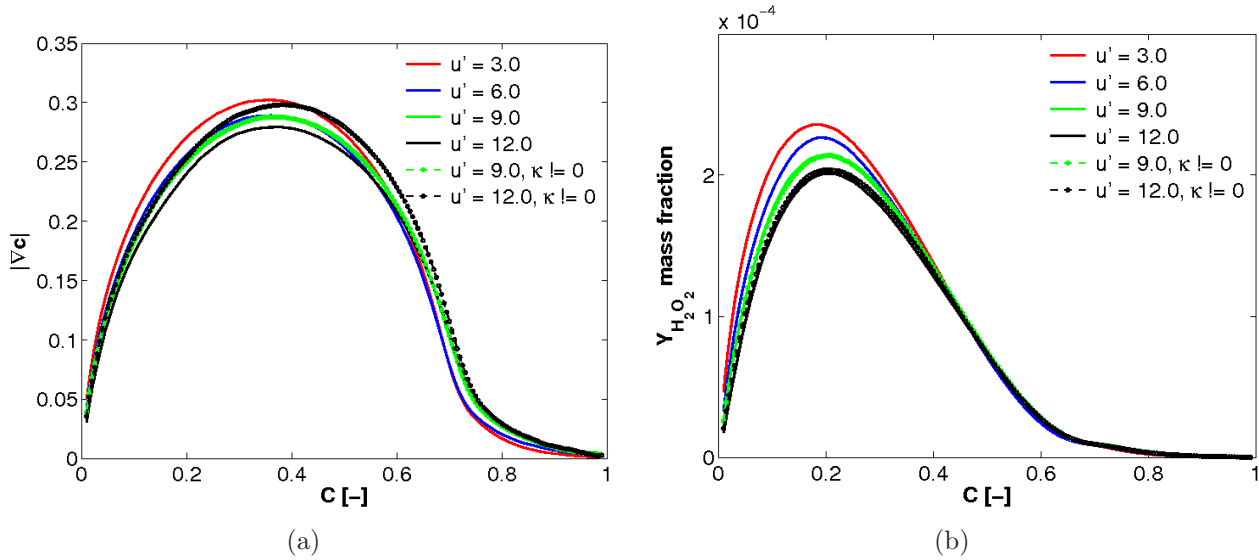


Figure 5.33: Conditional profiles of mean (a) progress variable gradient, $|\nabla C|$ and (b) mass fraction of H_2O_2 , conditioned on the progress variable C at $t = 1.2\tau$ for stoichiometric premixed methane-air flames with (dashed-dotted line: *cases 3 & 4*) and without (solid line: *Cases D1 – D4*) volume viscosity effects

Conditional analysis is of central importance for many turbulent combustion models. Hence, conditional mean values have been computed for different variables characterizing flame behavior as a function of turbulence intensity (Fig. 5.33). The conditional mean of the progress variable gradient $|\nabla C|$ is of particular interest, since its inverse gives a measure of the flame thickness in analogy to the thermal flame thickness [156]. The conditional profiles of mean $|\nabla C|$ and H_2O_2 mass fraction show a noticeable dependency on turbulence intensity, with progressively lowered peaks. The decrease of the conditional mean $|\nabla C|$ reveals that flame thickening is predominant, especially around $0.1 \leq C \leq 0.7$ (the active flame region) when increasing Re_t . Conditional mean profiles for the most sensitive minor radicals (H_2O_2) as well as major species (not shown) are identical with or without volume viscosity, irrespective of ensemble averaging. Volume viscosity effects are noticeable on the mean $|\nabla C|$ profile for *case D4* (single DNS realization). Again, this appears to be a statistical artifact, since all conditional mean profiles for *case D3* (averages over several realizations) show no influence of κ , whatsoever.

5.3.3.5 Effect of equivalence ratio

In the computations for *case F*, lean to stoichiometric mixture compositions of methane-air flames were realized. This section and the next (Sect. 5.3.3.6) contain some of the findings, with further details presented in [166].

Figs. 5.34 and 5.35 show the iso-contours of temperature and mass fraction of CH_3O computed with the same mixture equivalence ratio $\Phi = 0.8$ for *case F7*, illustrating the physical

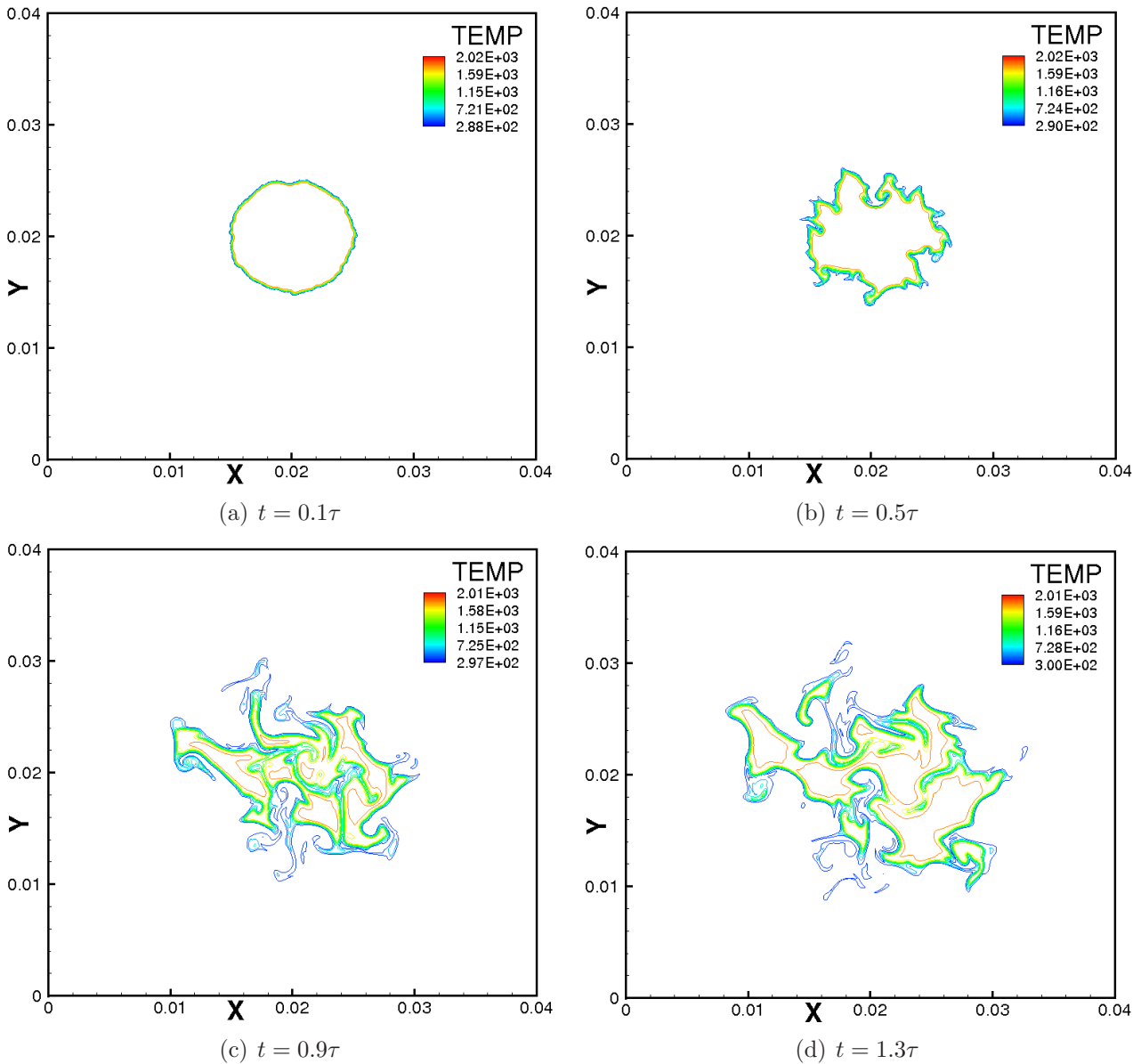


Figure 5.34: Case F7: Time evolution of the iso-contours of temperature for mixture equivalence ratio $\Phi = 0.8$ at $t = 0.1\tau$, 0.5τ , 0.9τ and 1.3τ

flame structure at different non-dimensional times $t = 0.1\tau$, 0.5τ , 0.9τ and 1.3τ . Considering the temperature field, the initial laminar spherical flame (Fig. 5.34(a)) is progressively being distorted and stretched (Fig. 5.34(b)) by the very strong turbulent field with time, leading to the creation of islands (in the form of both hot and fresh gas pockets) and edge flame-like structures (Fig. 5.34(c)–5.34(d)) [158] at various locations within the computational domain and for various shapes and sizes. For a high turbulence intensity, local flame extinction and flame-flame interactions become important. The temporal evolution of the iso-contours of the minor radical CH_3O is shown in Fig. 5.35 for the same Φ and Re_t values. The wrinkling effect induced by turbulence follows the patterns of the temperature field but shows much stronger disruptions at later times ($t = 0.9$ – 1.3τ). Such events are usually not observed when looking at integrated quantities, like temperature, illustrating the importance of a detailed description of chemical processes. Considering CH_3O as a measure of flame activity, local extinction events can be tracked with a good temporal and spatial resolution. Numerous fresh gas islands and flame pinch-off events are visible (Fig. 5.35(c)), evidencing local flame extinctions. Looking at the mass fraction values, the peak species mass fraction rises soon after its formation from $1.24 \cdot 10^{-5}$ at $t = 0.1\tau$ to $6.47 \cdot 10^{-5}$ at $t = 0.5\tau$, after which it drops to $5.76 \cdot 10^{-5}$ at $t = 0.9\tau$, then down to $3.12 \cdot 10^{-5}$

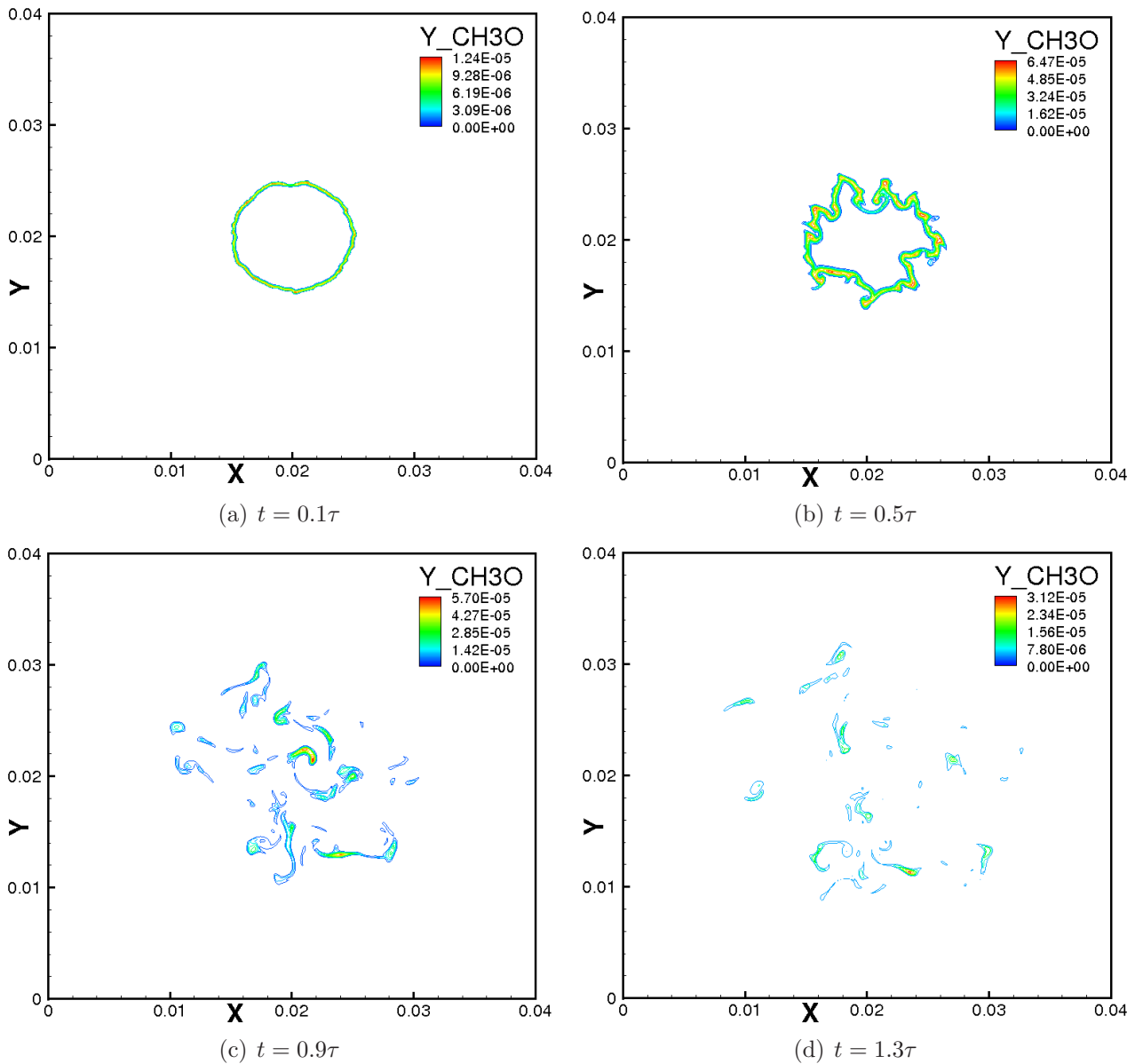


Figure 5.35: case *F7*: Time evolution of the iso-contours of the mass fraction of CH_3O for mixture equivalence ratio $\Phi = 0.8$ at $t = 0.1\tau$, 0.5τ , 0.9τ and 1.3τ

at $t = 1.3\tau$.

The iso-contours of most major and minor species exhibit qualitatively similar patterns to those of the temperature or CH_3O fields, respectively. They are therefore not shown in the interest of space.

Snapshots of the iso-surface of the mass fraction of the oxygen atom is shown in Fig. 5.36 for different Re_t values at the same time $t = 1.3\tau$ and mixture ratio $\Phi = 0.9$. In the past, DNS easily accessed mild turbulence conditions such as the one shown in Fig. 5.36(a) – 5.36(c) where the flame is only slightly contorted. Comparing the snapshots in Fig. 5.36, it is observed qualitatively that the amount of wrinkling increases strongly from Fig. 5.36(a) to 5.36(c) and tends to saturate afterwards (compare in particular Fig. 5.36(d) with Fig. 5.36(e)). For higher values of Re_t , considerable structural modifications are observed, in particular flame–flame interactions, leading to pinch off as evident in the higher Re_t snapshots in Figs. 5.36(c) – 5.36(e). The resulting turbulent flame structure is then marred with numerous perforations. Further increase in turbulence intensity leads to a further increase of pinch off and mutual annihilation effects, thereby limiting further increase in the flame surface area. Consequently, it drops steadily as evidenced in Figs. 5.36(f) – 5.36(i), indicating the growing importance of extinction processes,

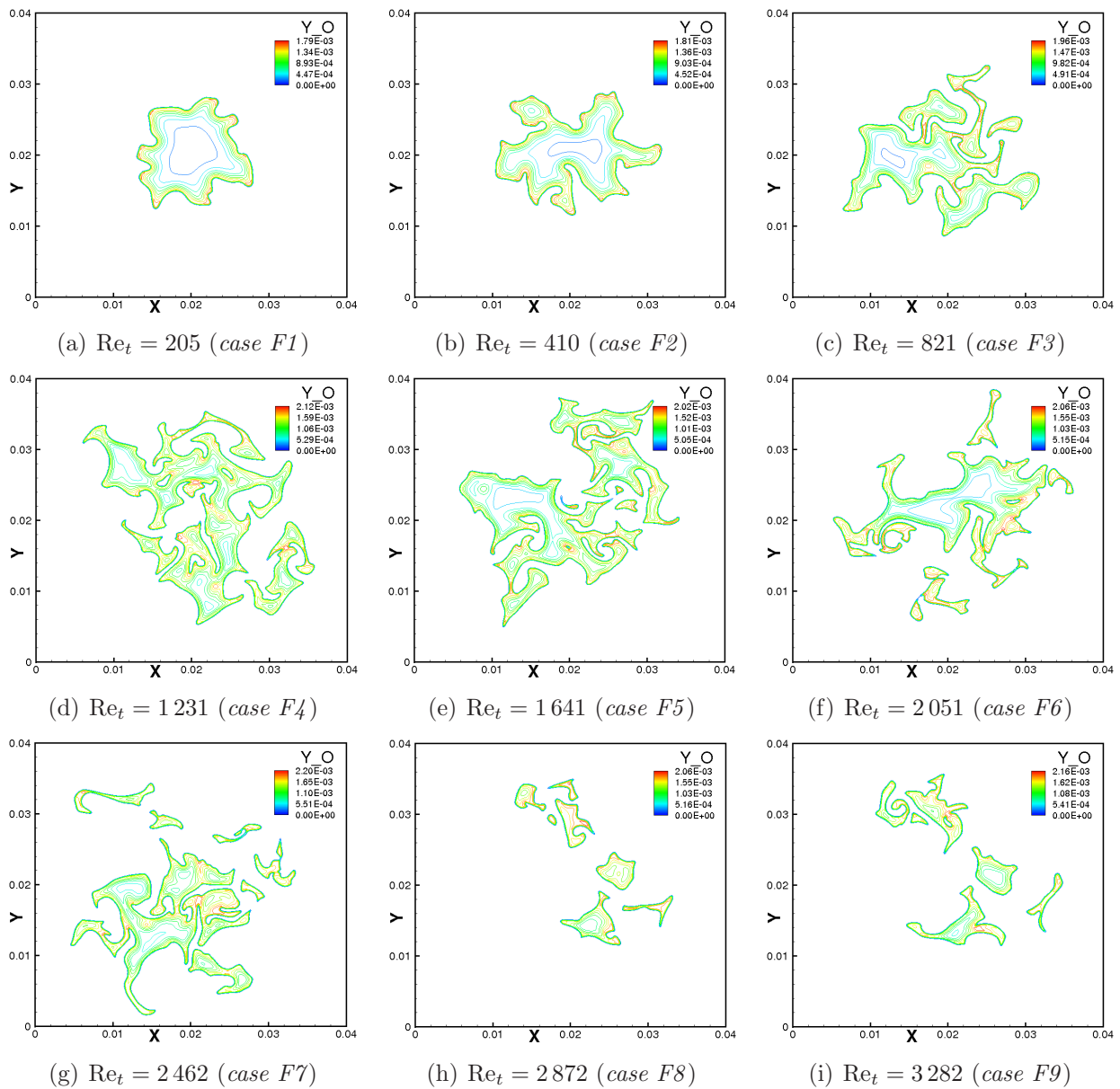


Figure 5.36: *case F*: Instantaneous iso-surface of the mass fraction of O for different integral Reynolds number Re_t at the same mixture equivalence ratio $\Phi = 0.9$ and same time $t = 1.3\tau$

as also observed experimentally in combustion vessel experiments [147, 151].

To show the effect of the equivalence ratio on the turbulent flame structure, Fig. 5.37 presents the instantaneous iso-contours of the mass fraction of OH (*case F6*) for different mixture equivalence ratios $\Phi = 0.7, 0.8, 0.9$ and 1.0 at the same time $t = 1.3\tau$. The color scale is kept identical for all plots. The lower flame activity when decreasing the equivalence ratio can easily be seen in this figure, explaining again why local flame extinction is systematically observed earlier at lower values of Φ . Since the employed chemical scheme has only been validated for lean to stoichiometric conditions, similar studies for rich conditions cannot be presented yet.

5.3.3.6 Turbulent burning velocity

Now, the time evolution of the turbulent burning velocity as a function of the turbulence intensity is investigated in moderate to intense turbulent flows for various Φ . Following [162], it is emphasized that different definitions of S_T may be useful in different contexts. In the present simulations, the consumption speed S_c is defined following [163–165] and already given in Eq. (5.8). The associated scaling area has been obtained in a post-processing step using

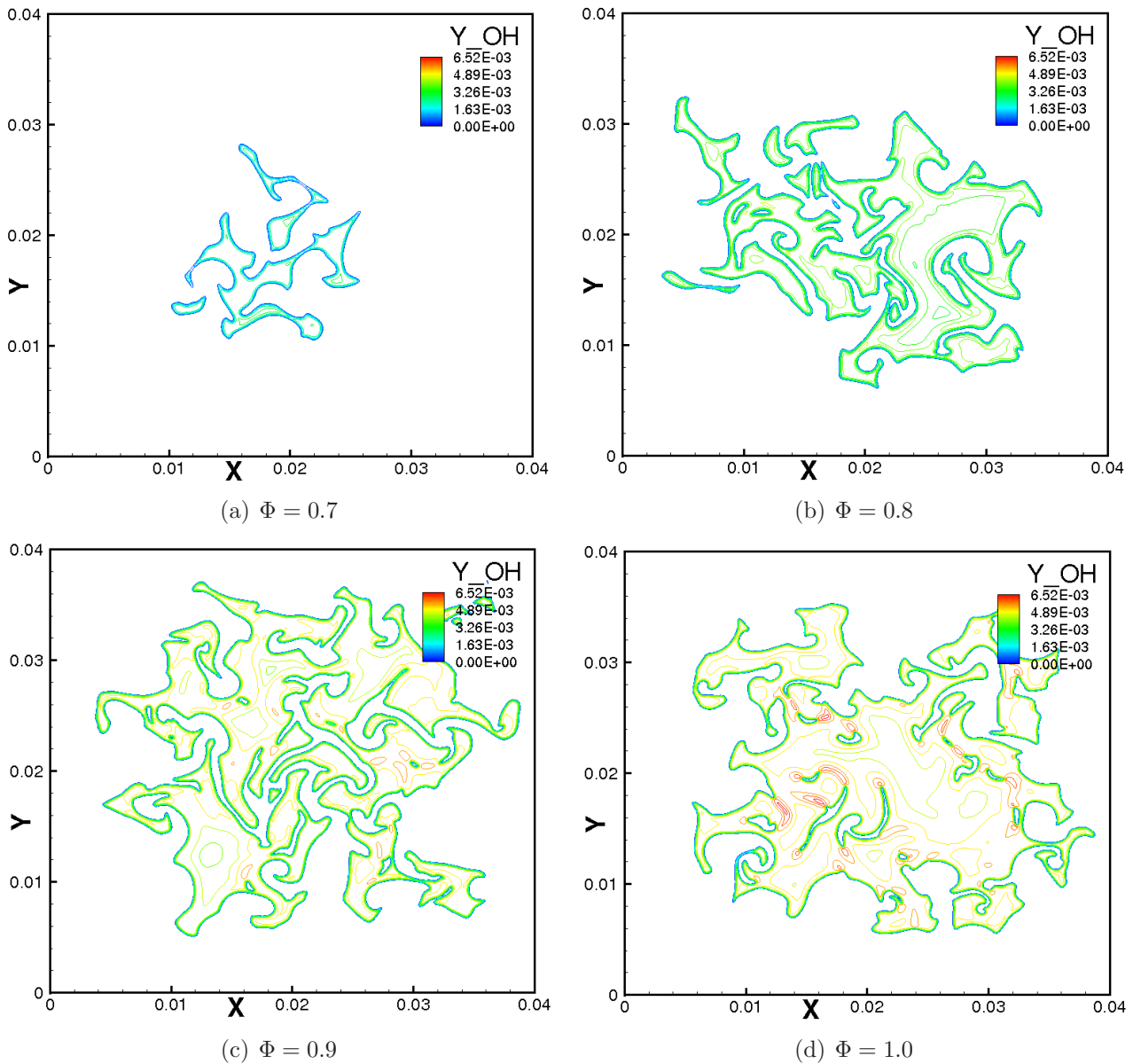


Figure 5.37: case *F6*: Instantaneous iso-contours of the mass fraction of OH for different mixture equivalence ratios Φ at the same time $t = 1.3\tau$

AnaFlame [134]. It is chosen as the area of a suitable iso-contour of the reaction progress variable C , (defined following [5] in terms of reduced temperature) representing the wrinkled flame front. For instance, a choice of $C = 0.6$, corresponding to the position of maximum heat release in the laminar flame could be adopted. Thus the value of S_c is not unique. We note also that ensemble averaging would be needed to provide a mean isosurface scaling area, which could account further for flame wrinkling effects. The computed fuel consumption rate is then directly related to the overall burning rate (by scaling with this area), and constitutes an interesting measure of the burning velocity. In all results shown, S_c is scaled by its initial value $S_{c,0}(t = 0)$ (before starting the interaction with the prescribed field of turbulence) at the corresponding equivalence ratio.

This global flame parameter is of primary importance to burner designers as far as the characterization of premixed turbulent combustion is concerned. Its prediction remains a challenge for turbulent premixed combustion modelers [8]. Most existing models are still phenomenological in nature and often fail beyond the flammability limits, whenever the pre-mixture is either too lean or too rich to sustain a flame in the mean.

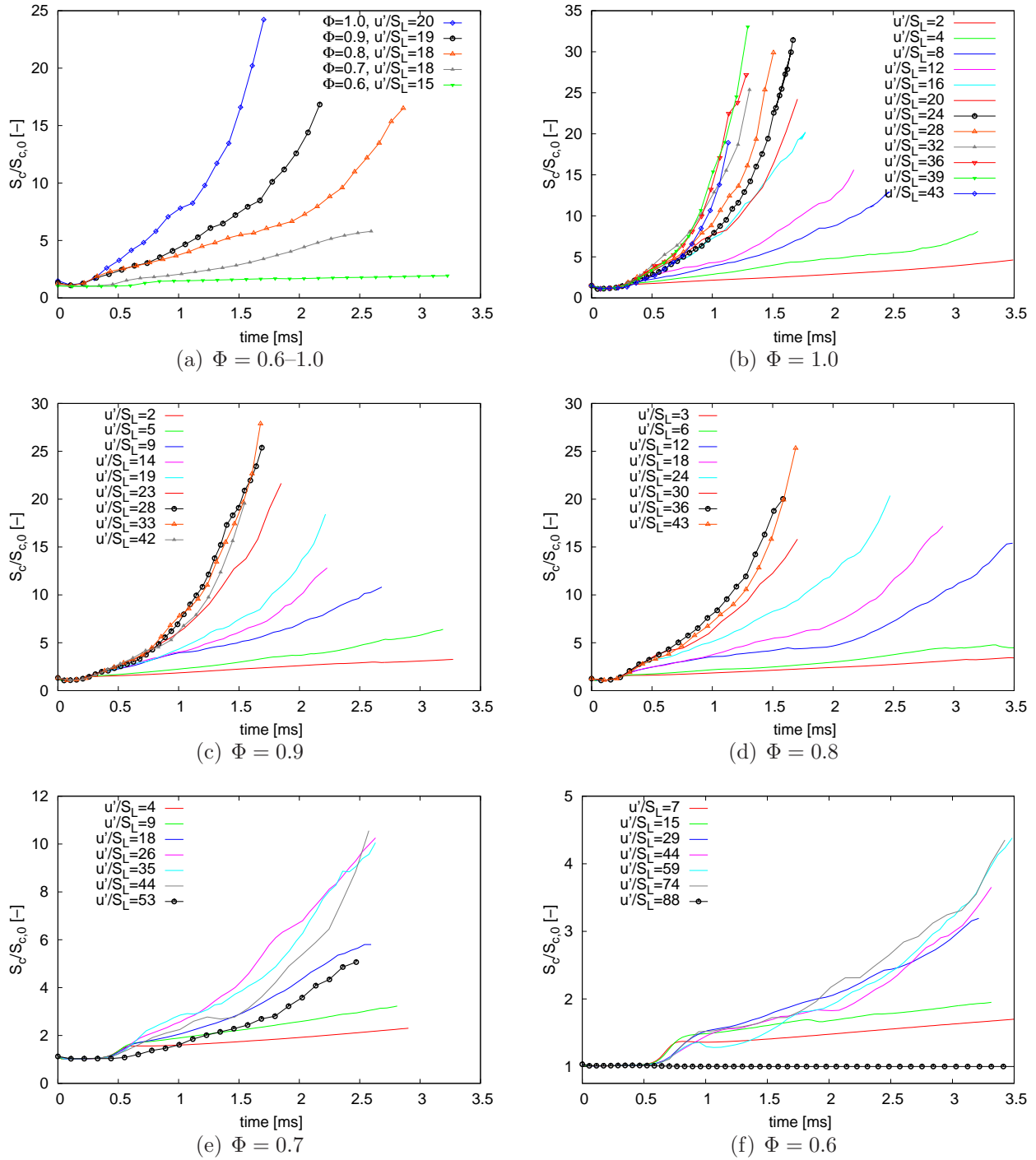


Figure 5.38: *Case F:* Temporal evolution of the volume-integrated fuel (CH_4) consumption rate S_c (normalized by their laminar flame value at the corresponding equivalence ratio and at $t = 0$) for different turbulence intensities u'/S_L and mixture equivalence ratios Φ

The temporal evolution of the consumption speed is shown in Fig. 5.38 for the various cases. Initially, it remains nearly constant up to $t \approx 0.3$ ms and $t \approx 0.6$ ms for $\Phi = 1.0$ and $\Phi = 0.6$, respectively, after which it increases steadily. Under the same flow conditions, the time required by the leaner mixtures to sustain and propagate a flame front is delayed relative to the richer ones, as expected. After a successful take-off, the profiles for the various cases take different courses depending on the turbulence intensity u' , mostly with a steady increase in slope. For a given value of u'/S_L (which is the parameter mostly used for modeling purposes), the gradient of the profiles increases with increasing Φ as shown in Fig. 5.38(a), where all the profiles for the five mixture compositions are plotted together for a nearly constant value of u'/S_L . Also, it is

obvious that the leaner the mixture, the lower the fuel consumption rate and vice versa. Note the progressive exponential nature of the curves associated with the richer mixtures ($\Phi \geq 0.9$) under highly turbulent conditions. However, as the turbulence intensity further increases, a maximum in S_c is observed. This critical (or saturation) rms velocity will be denoted u'_s . As found in the DNS, the richer the mixture, the higher the scaled saturation velocity: u'_s/S_L is about 29.0 for $\Phi = 0.6$ and up to 39.0 at stoichiometry. Increasing u' beyond u'_s , the obtained temporal profiles of S_c first cluster together (e.g., Figs. 5.38(b) & 5.38(c) for $\Phi = 1.0$ & 0.9) before declining steadily (e.g. Figs. 5.38(d) & 5.38(e) for $\Phi = 0.8$ & 0.7). This scenario is a well known phenomena observed in several combustion vessel experiments and termed "bending effect" [5, 167]. Whether such a decline persist until the flame reaches global quenching (the so called "quenching limit", also observed in many experiments) for too intense turbulence, will be the subject of further studies. Figure 5.38(f) includes a case for which, due to a high initial turbulence level ($u'_s/S_L = 88$), the pre-mixture is unable to propagate and slowly fades out. The present DNS results thus confirm the theoretical and experimental assertions that turbulence cannot increase burning rates indefinitely [152, 168]. Furthermore, leaner methane–air mixtures (e.g. $\Phi = 0.6$ at $u'/S_L \geq 74.0$) exhibit a greater decline in S_c with increasing u'/S_L than do richer ones.

Since high volumetric heat release rates in compact burners at low stoichiometries are often required, combustion in a highly turbulent medium is often necessary [169]. Intense turbulence stirring usually results in flames that burn and/or propagate faster and release higher amounts of energy in the form of heat. However, the obtained results show that optimum conditions exist, depending on mixture stoichiometry, above which the resulting flames will be weakened by a further increase in turbulent stirring.

5.3.4 Impact of volume viscosity

In this section, the DNS results for *case E* have been systematically analyzed using *AnaFlame* [134, 135, 139] in order to quantify the influence of volume viscosity. The findings have been presented in a number of conferences [28, 170] and articles [157, 171, 172]. For each considered case, the experiment is performed at least twice with exactly the same initial and boundary conditions including turbulent properties, except for the fact that the volume viscosity terms are deactivated in one but activated in the other simulation. The numerical results are presented in the following two subsections first for laminar (Sect. 5.3.4.1), then for turbulent (Sect. 5.3.4.2) computations.

The same global flame quantities – S_c and H_r – have been tracked throughout each of the experiments and will be compared and contrasted to assess the influential rule played by volume viscosity for the evolution of premixed flame kernels.

Instantaneous DNS solutions are analyzed in terms of conditional statistics and Probability Density Functions (PDF) for relevant quantities such as temperature, heat release, selected mass fractions, as well as concerning the response of the flame front to curvature and strain. The effect of initial turbulence intensity and Reynolds number are studied in the light of the presence/absence of the volume viscosity transport term.

5.3.4.1 Laminar flame structure

The compositional and physical structure of the laminar premixed flames are shown in Fig. 5.39 for the methane–air mixture in physical space (Fig. 5.39(a)) and syngas–air mixture in the reaction progress variable space, C (Fig. 5.39(b)) for *case E1*. The instantaneous profiles of the temperature, heat release rate and the mass fractions of OH, O, H, H_2O_2 and HO_2 are shown at $t = 1.5$ ms with and without taking into account the volume viscosity transport term. At this time, the premixed flame is chemically very active. It is nevertheless impossible to differentiate

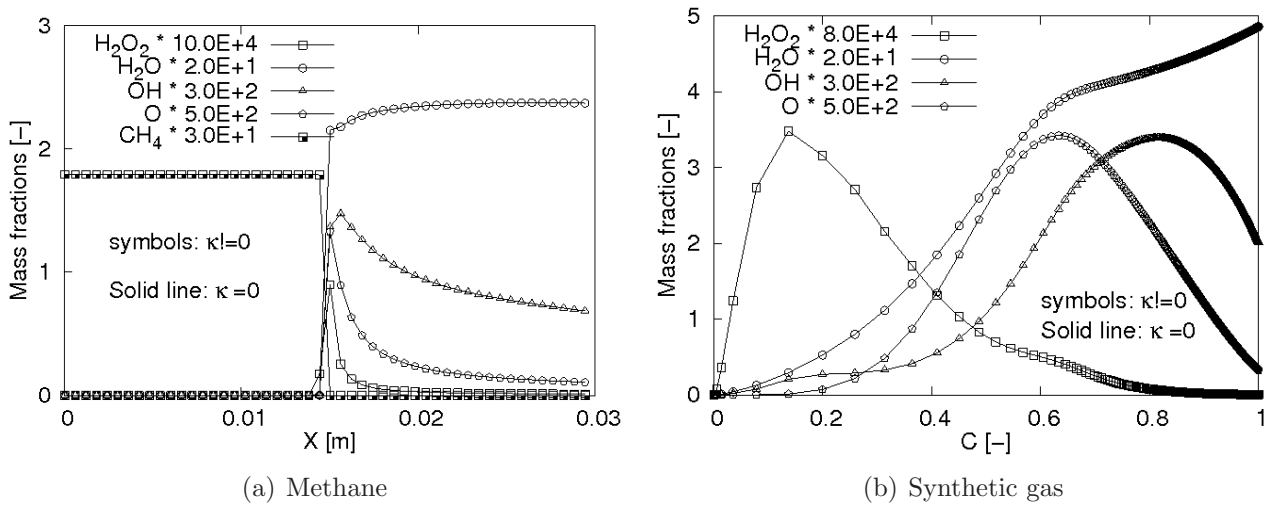


Figure 5.39: *Case E1*: Instantaneous profiles of laminar premixed flames, showing mass fractions of (a) H_2O_2 , H_2O , OH , O and CH_4 in physical space and (b) H_2O_2 , H_2O , OH and O in the progress variable space, with (symbols) and without (line) volume viscosity at $t = 1.5$ ms

the two numerical results in Fig. 5.39 both in physical and progress variable space, even for minor flame radicals like H_2O_2 and HO_2 . All fields are qualitatively and quantitatively identical with relative differences below 1%. Similar profiles for all the other variables show the same results, even in the presence of curvature (laminar flame kernels). The time evolution of the burning speed and integrated heat release rates are shown in Fig. 5.40(a) for the hydrogen–air computation of *case E1*. In Fig. 5.40(b), the conditional profile of the heat release rate (extracted along the flame front defined by the isolevel of $C = 0.5$) is shown conditioned on the reaction progress variable for the syngas–air mixture at $t = 1.5$ ms. As can be observed, the two solutions are again identical for these global quantities. Hence, volume viscosity has no apparent effect on the laminar flame structure irrespective of the considered fuel. This is due to the fact that the dilatation term is approximately zero in this computation, with a peak Mach number below 0.001. The conclusion from Sect. 5.2.5.1 for non-premixed combustion are also valid here.

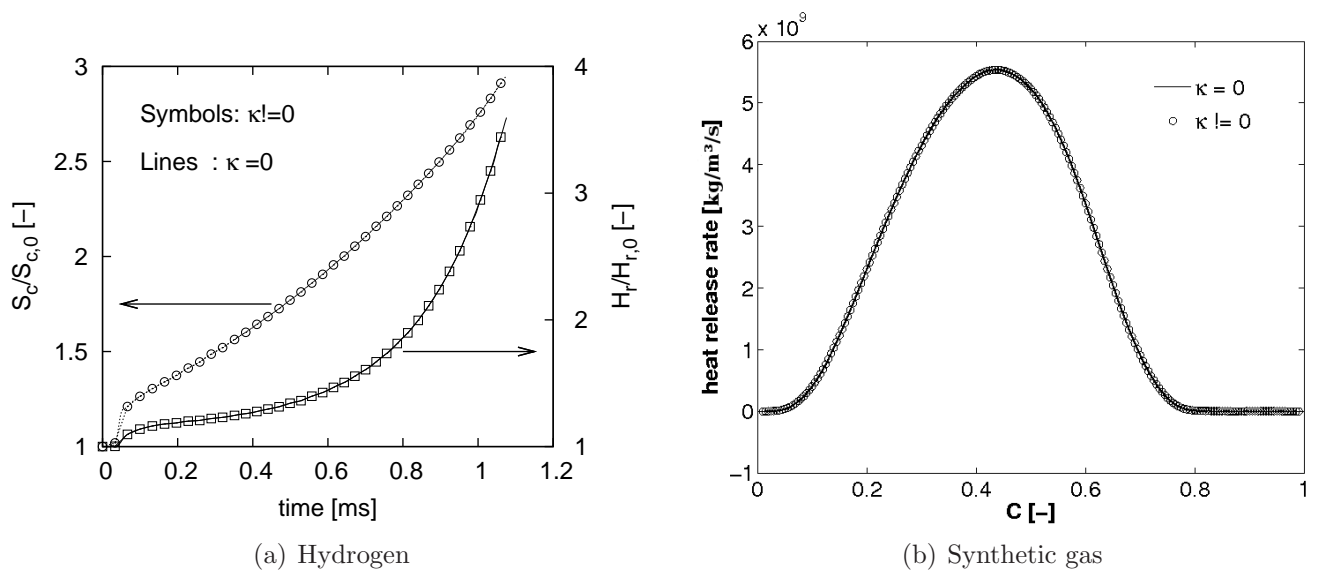


Figure 5.40: *Case E1*: (a) Temporal evolution of the laminar fuel consumption and integrated heat release rates and (b) heat release profile in the progress variable space at $t = 1.5$ ms with (symbols) and without (lines) volume viscosity

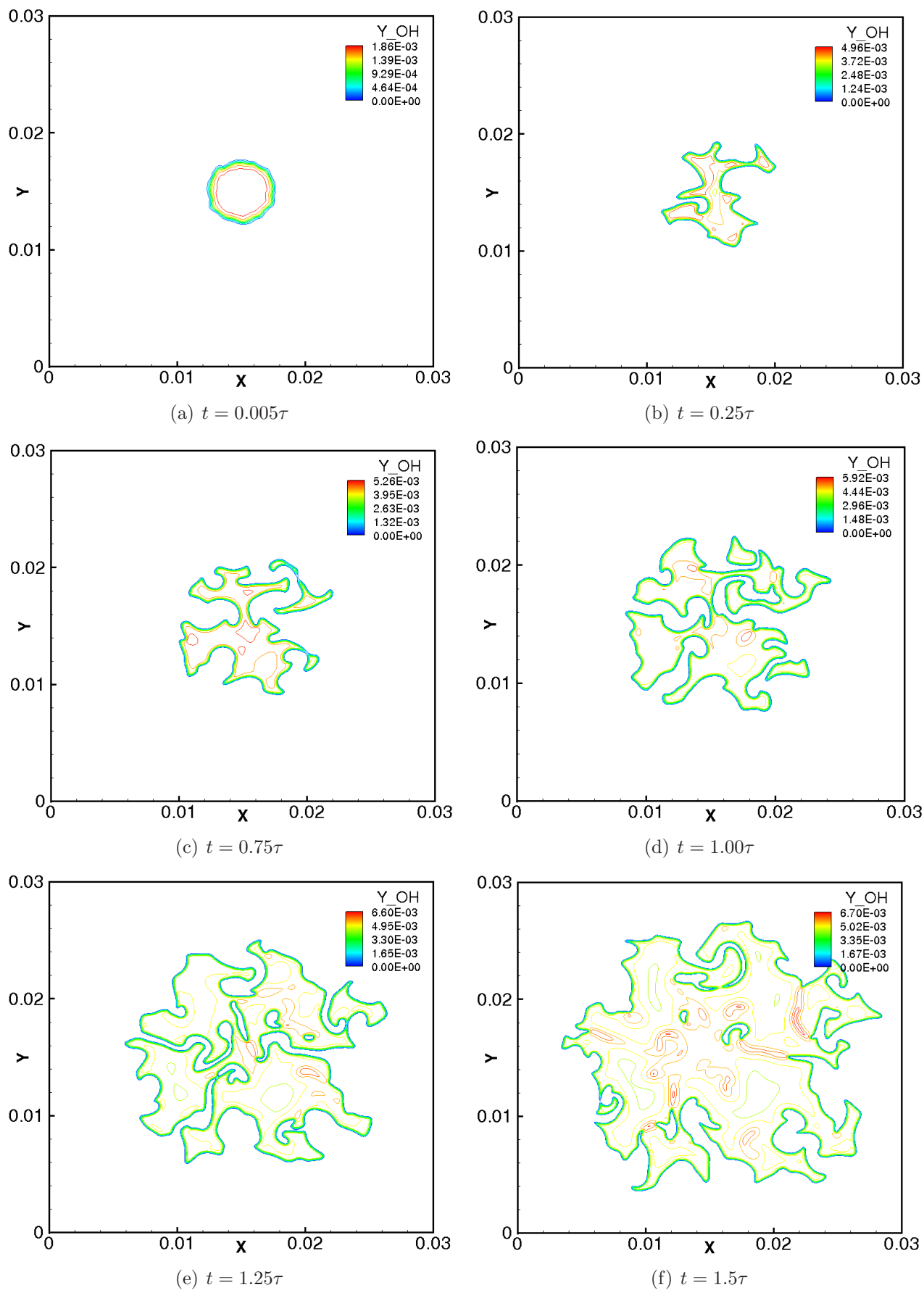


Figure 5.41: case E_4 : Instantaneous contours of the mass fraction of OH in the $z = 0$ plane for the methane flame at different times, in the absence of volume viscosity effects

5.3.4.2 Turbulent flame structure

Laminar profiles like those described in the previous section are now used as initial estimates to start the turbulent computations by adding corresponding perturbations to the flow velocity. Iso-contours of several flame quantities for the turbulent cases are shown in Figs. 5.41 to 5.43 in the plane $z = 0$. The physical flame structure at different times is visualized by the iso-contours of the mass fraction of OH from *case E4* (methane flame), since OH is known to be an interesting flame marker [159] and has been considered in many experimental studies. The initially spherical flame kernel is wrinkled by the superimposed turbulent field soon after initialization (Fig. 5.41(a-b)) and severely stretched and strained with time. The amount of wrinkling and distortion increase with increasing interaction time. For high values of Re_t , considerable structural modifications of the turbulent flame structure have been observed [138], in particular many flame–flame interactions leading to pinch off and pockets, as evident in the snapshots in Fig. 5.41(c,d,e,f). Such mutual annihilation events of flame surface due to interaction with turbulence are found to be a dominant mechanism limiting the flame surface area generated by wrinkling under turbulent conditions.

To highlight and assess the qualitative effect of volume viscosity on the developing turbulent flame kernel structure in space and time, the temporal evolution of the iso-contours of temperature is compared in the plane $z = 0$ in Fig. 5.42 at times $t = 0.25\tau$, 1.0τ and 1.5τ for *Cases E2d*, where results from computations with and without volume viscosity effects are shown. The flame becomes increasingly wrinkled and distorted with time as it interacts with the initial turbulent velocity field in a similar manner to that explained earlier for *case E4*. There is no large quantitative difference between the two temperature fields up to $t = 0.25\tau$. The same observation holds for all other species and variable fields (not shown), apart from κ of course. With increasing time, the form of the flame begins to differ visibly for the two simulations at selected locations. This is obvious for $t = 1.0\tau$ but is indeed already seen at $t = 0.25\tau$ when looking at isolated details of the temperature distribution. The differences becomes more and more considerable with increasing time. When volume viscosity effects are present, the flame front develops and consumes isolated flame pockets faster than when it is absent. The temperature iso-lines distribution is noticeably different for the two cases at $t = 1.5\tau$, together with a maximum temperature difference of up to 30K locally.

In Fig. 5.43, the instantaneous iso-contours of the mass fraction of OH for *case E2d* (hydrogen), *case E3* (syngas) and *case E4* (methane) are compared after interacting with the turbulent field during $t = 1.5\tau$. The observed local difference for OH in *case E2d* confirms the previous observations based on temperature. These results demonstrate that, when coupled with turbulence, volume viscosity effects lead to noticeable differences in the evolution of the corresponding turbulent flame with increasing duration. This is not in contradiction with the findings described in the previous section. Indeed, starting from identical conditions at a time t_0 , the variable fields obtained with or without volume viscosity show no difference at first, as expected for such low-Mach number simulations with identical boundary conditions [23]. Nevertheless, the chaotic nature of turbulence leads to realizations diverging from each other with increasing integration time. Even a minor local difference is sufficient to obtain a completely different evolution at a later time. However, the same instantaneous OH iso-contours for the turbulent flames burning syngas (*case 3*) and methane (*case 4*) at the same non-dimensional time and turbulence intensity show no noticeable difference, especially for the methane flame, demonstrating that volume viscosity plays a very minor role for such fuels. This is expected for methane for which κ/η is 25 times less than for hydrogen at 300 K (see again Table 2.1). The syngas case shows only very small disparities and falls between *case E2d* and *case E4*.

Such local differences do not necessarily lead to a modification of the global turbulent flame properties and might therefore be irrelevant for practical purposes. This issue will be the subject of the next section.

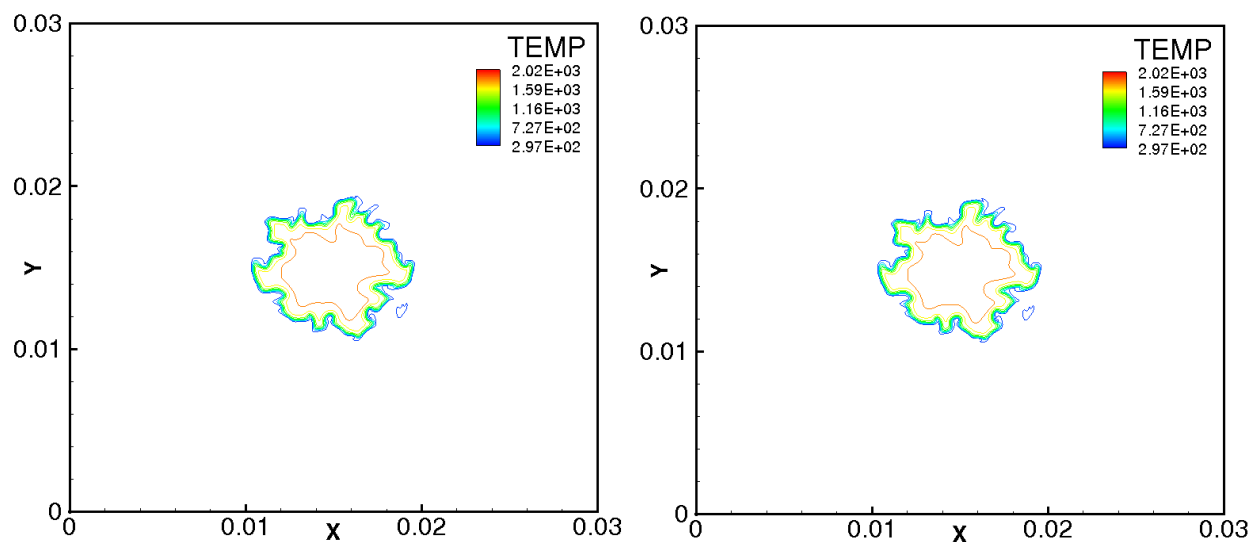
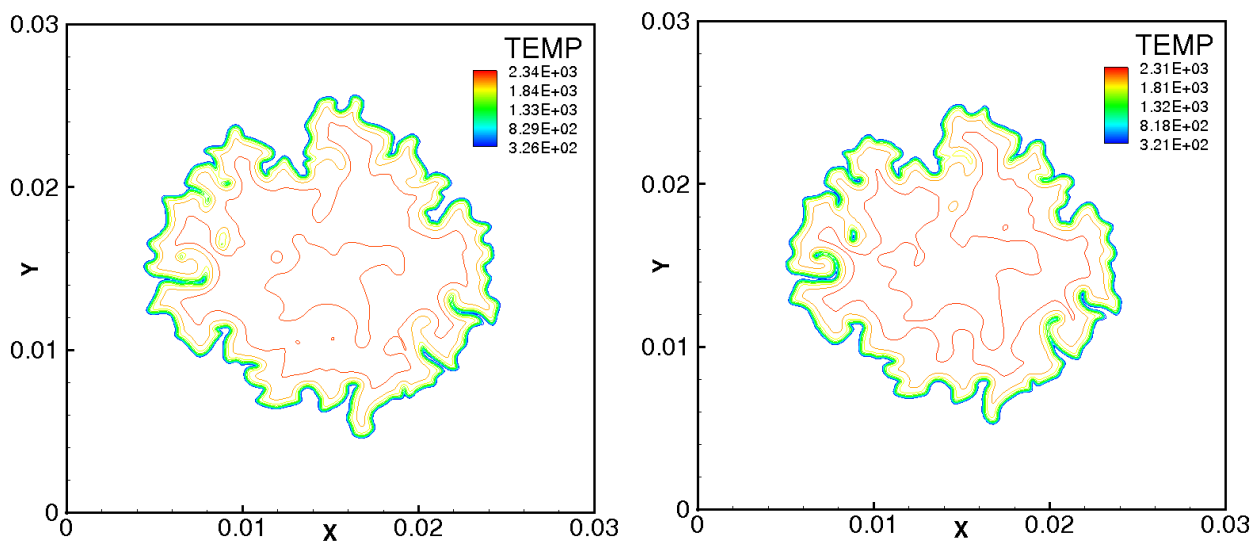
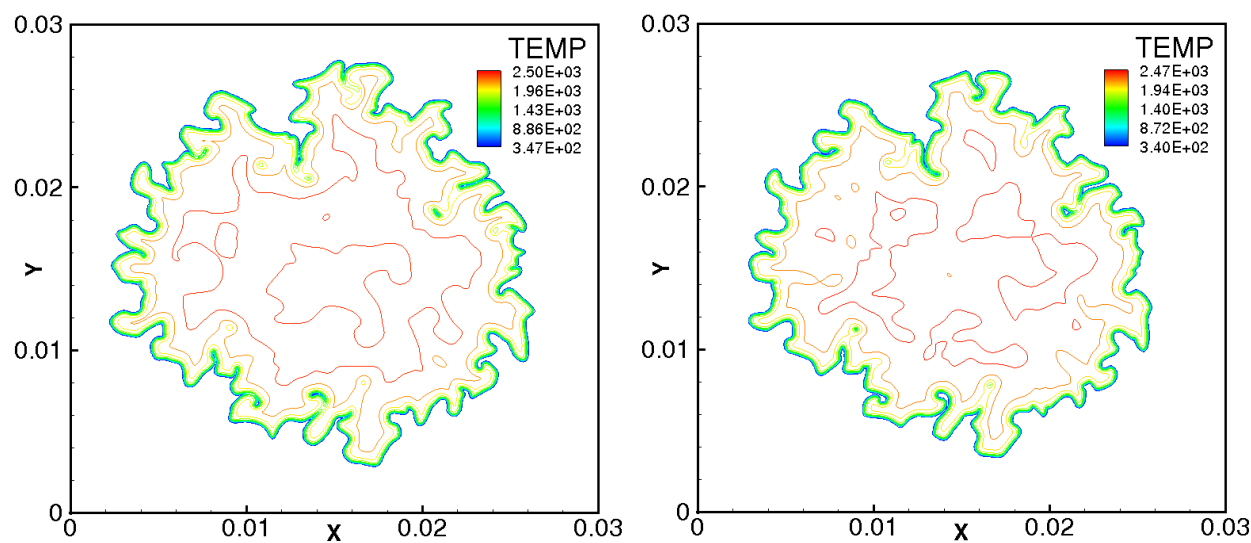
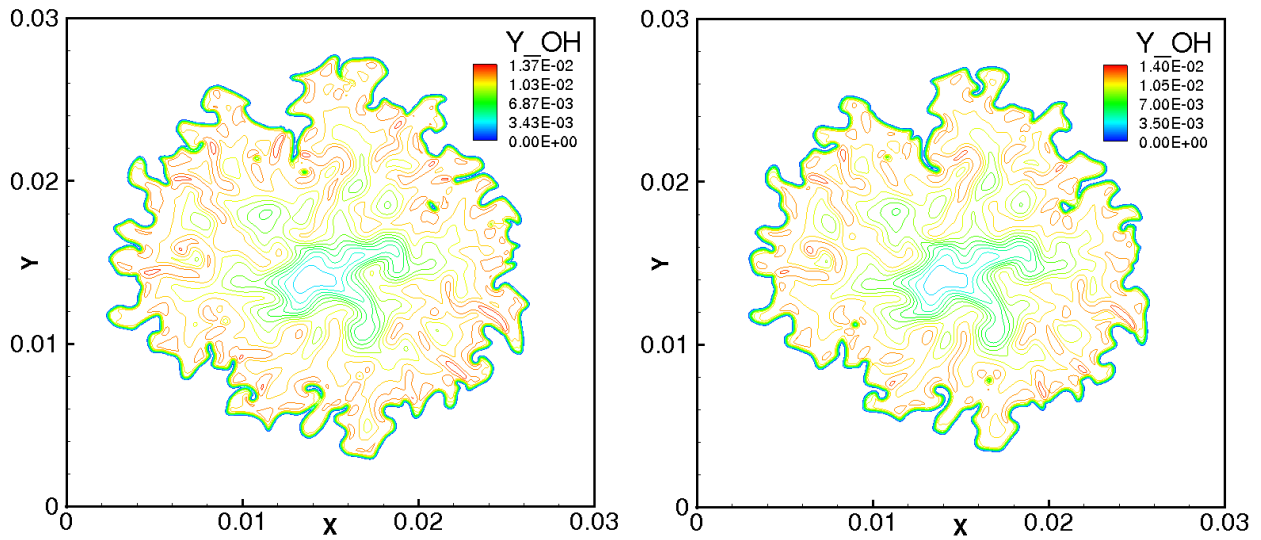
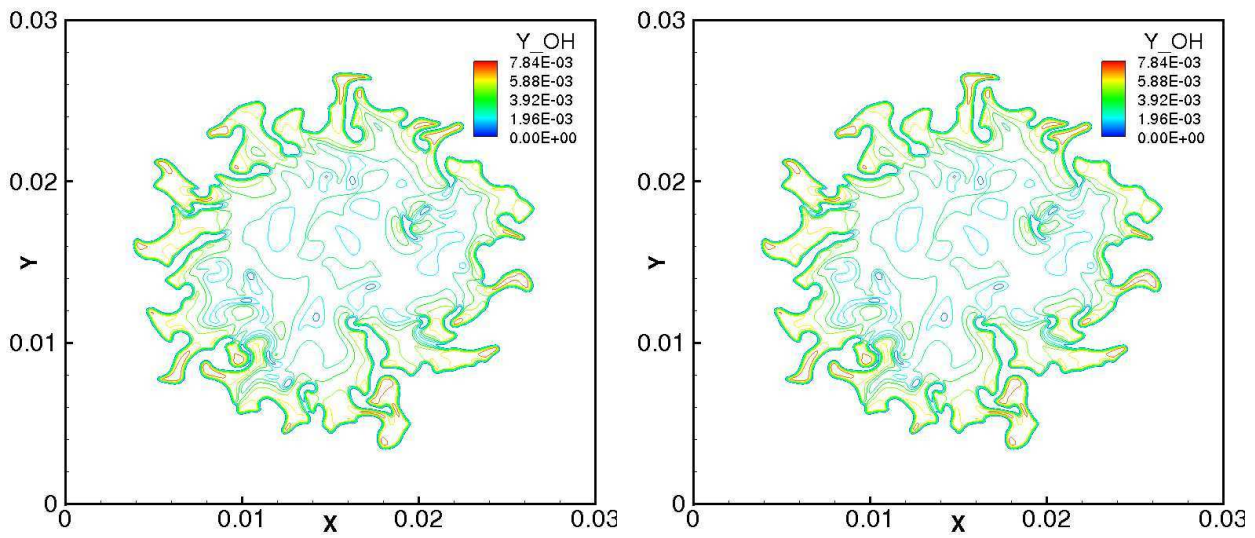
(a) $t = 0.25\tau$ (b) $t = 1.0\tau$ (c) $t = 1.5\tau$

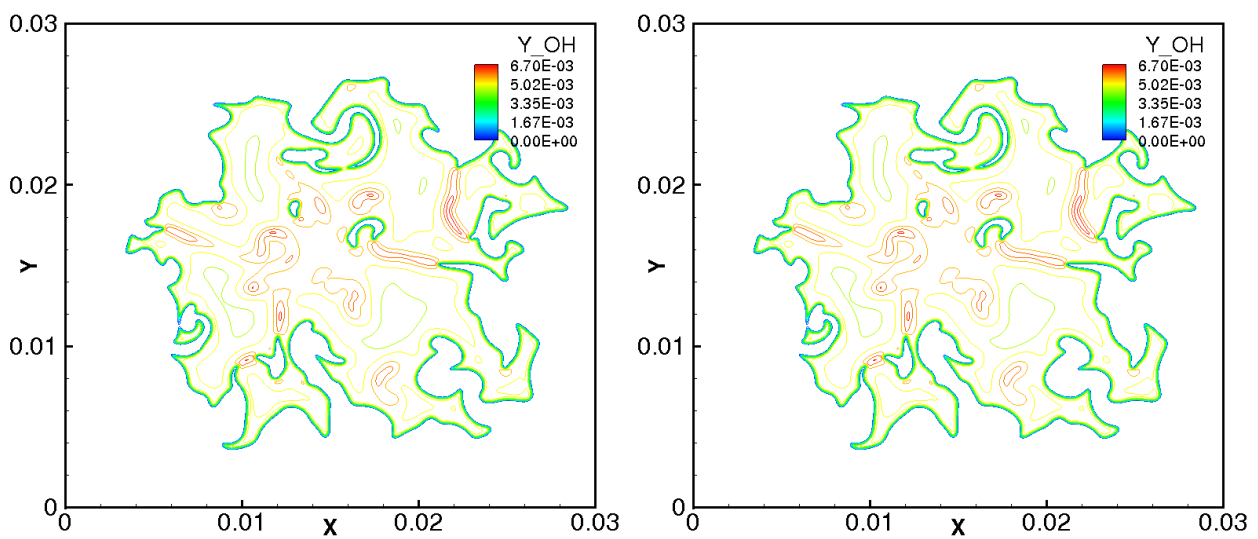
Figure 5.42: case *E2d*: Instantaneous contours of temperature for the hydrogen flame with (left) and without (right) volume viscosity effects at different times



(a) Hydrogen



(b) Syngas



(c) Methane

Figure 5.43: *case E*: Instantaneous contours of the mass fraction of OH with (left) and without (right) volume viscosity for *case E2d* (hydrogen), *case E3* (syngas) and *case E4* (methane) at $t = 1.5\tau$

5.3.4.3 Turbulent flame properties

To this effect, important integral properties of turbulent flames have been computed and compared when taking into account or disregarding volume viscosity. In particular, the fuel consumption rate S_c and the volume integrated heat release rate H_r are considered in what follows, together with a conditional or PDF analysis of selected flame variables.

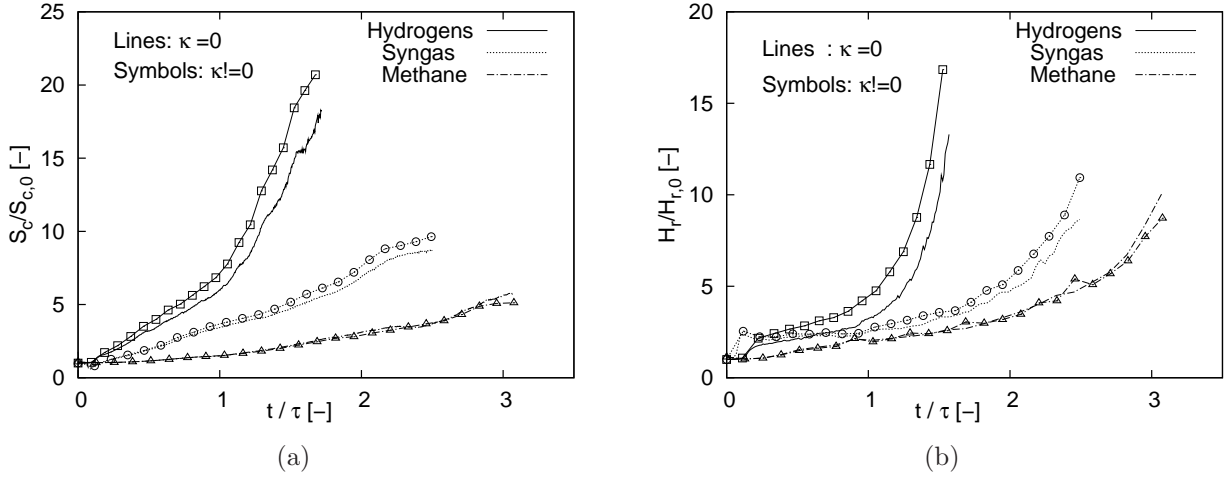


Figure 5.44: *Case E*: Temporal evolution of the scaled (a) fuel consumption and (b) integrated heat release rates at the same turbulence intensity for *Case E2d* (hydrogen), *Case E3* (syngas) and *Case E4* (methane) with (symbols) and without (lines) volume viscosity effects

For *Cases E2d*, *E3* & *E4*, the scaled temporal evolutions of S_c and H_r are shown in Fig. 5.44 at the same turbulence intensity, with and without volume viscosity effects. Considering the fuel consumption rate in Fig. 5.44(a), it is obvious that volume viscosity indeed leads to considerable modifications of this global quantity for *Case E2d* involving pure hydrogen as fuel. As expected, the difference is at first negligible, with noticeable deviations starting for $t \simeq 0.25\tau$. Differences in the profile for *Case E3* involving syngas fuel are much smaller compared to hydrogen, and first become noticeable at a later time ($t \approx 0.75\tau$). The profile associated with the flame burning pure methane fuel shows almost no differences with or without volume viscosity. Comparing the three profiles, the increase rate grows from *Case E4* to *Case E2d*. This is as expected theoretically, since hydrogen flames burn and propagate much faster. The same observations and conclusions hold for the volume integrated heat release profiles in Fig. 5.44(b).

Many turbulent combustion models rely on conditional values, very often based on the reaction progress variable. It is therefore interesting to check as well such quantities in order to quantify a possible impact of volume viscosity. For instance, the instantaneous profile of the heat release rate, the magnitude of the mean progress variable gradient $|\nabla C|$ and the mass fractions of $Y_{H_2O_2}$ and Y_{HO_2} conditioned on the progress variable C are shown in Fig. 5.45 at $t = 1.35\tau$ for *Case 2d*, *3* & *4* with and without volume viscosity effects. All profiles reveal a noticeable impact of volume viscosity for conditional values when burning hydrogen fuel. For instance, the conditional value of the heat release rate shows a relative peak difference of more than 10%. The conditioned species profiles lead to peak modifications between 10 and 15% depending on the considered variable. On the other hand, the same profiles for the flames burning syngas (*Case E3*) and methane (*Case E4*) show a relative difference in peak conditional values of less than 2% and 0.25%, respectively. For all flame variables, neglecting volume viscosity systematically results in an underestimation of the peaks of conditional profiles. Since such results, averaged over time or over several realizations support further model testing and improvement, working with realistic transport models accounting for volume viscosity effects appears to be important for hydrogen-containing fuels. Additionally, neglecting volume viscosity in turbulent

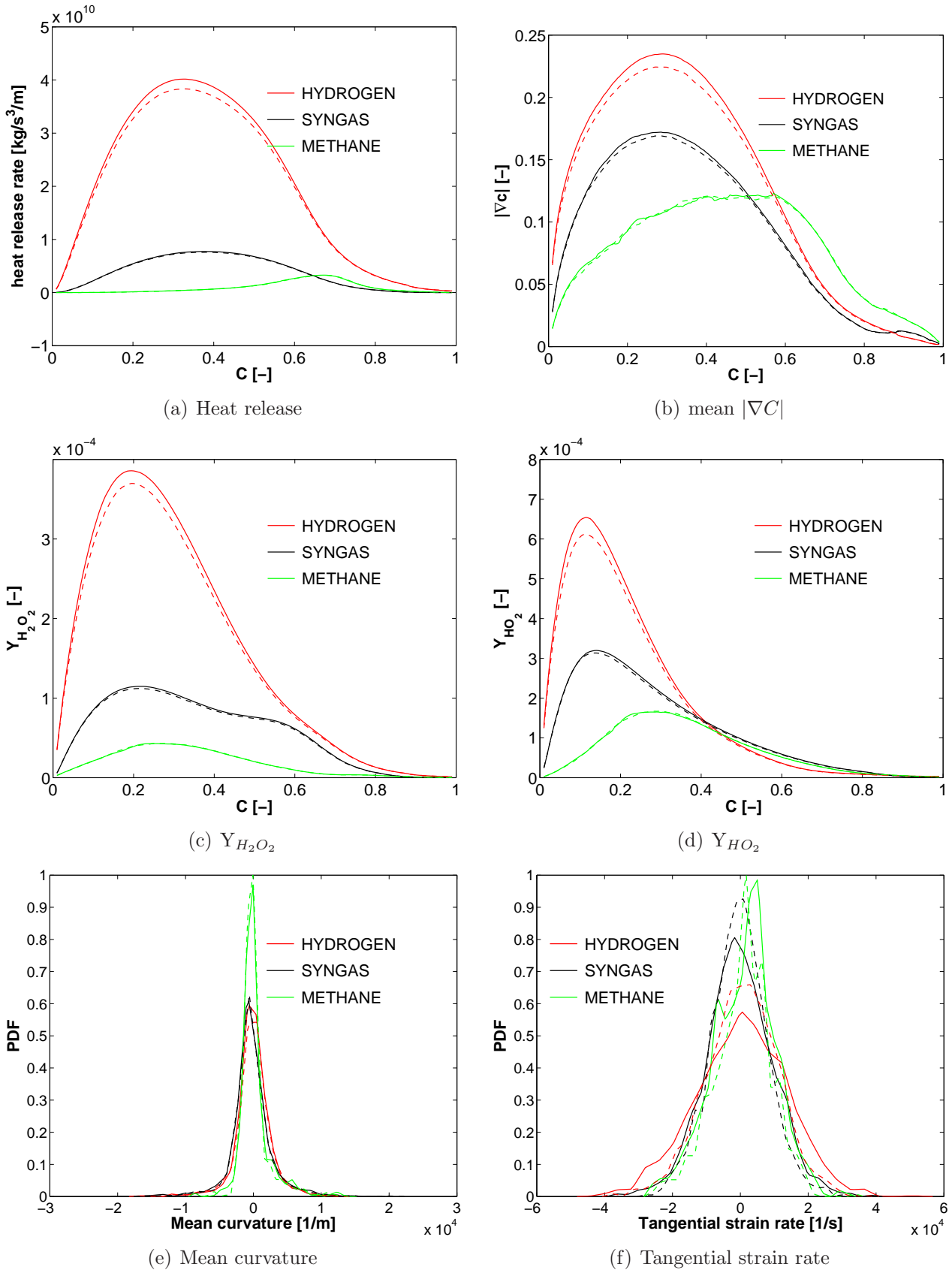


Figure 5.45: *Case E*: Comparison of the instantaneous conditional profiles of (a) heat release rate, (b) mean progress variable gradient, mass fractions of (c) $Y_{H_2O_2}$, (d) Y_{HO_2} conditioned on the reaction progress variable C and PDFs (divided by the methane peak value) of (e) the mean curvature and (f) tangential strain rate for *Case E2d*, *E3* & *E4* at $t = 1.35\tau$ with (solid lines) and without (dashed lines) volume viscosity

flames burning hydrogen will result in thicker flames, as shown by the conditional $|\nabla C|$ profiles in Fig. 5.45(b), since its reciprocal gives a measure of the flame thickness [138, 156].

PDFs of the local mean curvature and local tangential strain rate extracted along the flame front at $t = 1.5\tau$ are shown in Fig. 5.45(e) and Fig. 5.45(f). These properties control in particular extinction and are therefore vital for modeling purposes. When plotted along the flame surface, they show large differences with and without volume viscosity. The peak pdfs for both curvature and strain rates are overestimated in the absence of volume viscosity effects for both the hydrogen and syngas pre-mixtures, leading eventually to associated modifications of the local burning rates.

From a theoretical point of view, the effect of volume viscosity is expected to be maximum for hydrogen flames, since the volume viscosity of hydrogen is highest (see Table 2.1). This is confirmed by the present simulations, since *Case E3* (syngas flame) leads to much lower variations compared with *Case E2d* (hydrogen flame) at the same turbulence level and global mixture ratio for all the above flame variables. On the other hand, considering the flames burning methane fuel, all the profiles and statistics of the variables examined here show a negligible impact of volume viscosity on the resulting turbulent flame structure. This is indeed an interesting result and shows that for direct simulations of turbulent premixed flames burning higher hydrocarbons, the impact of volume viscosity is expected to be negligible and can be ignored.

5.3.4.4 Influence of turbulent intensity

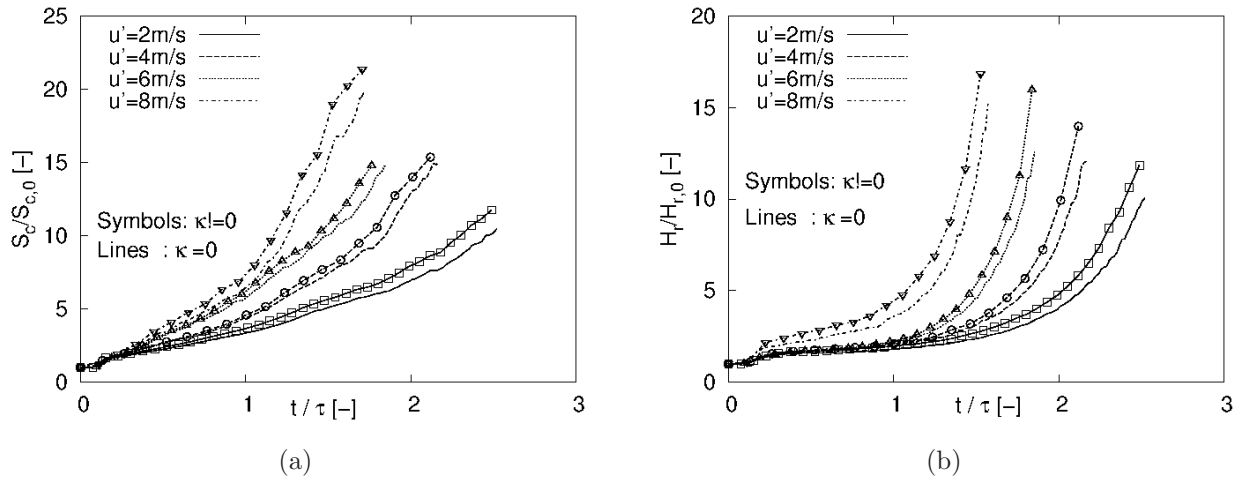


Figure 5.46: *Case E2*: Temporal evolution of the scaled (a) fuel consumption and (b) integrated heat release rates at different turbulence intensities

Varying turbulent intensity could modify the findings. On one hand, a higher Reynolds number should lead to larger differences if the chaotic nature of turbulence explains the findings presented up to now. On the other hand, many authors assume that laminar transport processes become negligible for highly turbulent conditions. In the latter case, differences could become smaller for increasing Re_t . As can be seen in Fig. 5.46, by comparing the time evolutions of S_c and H_r for *Cases 2a-d*, which are identical apart from turbulence intensities (and hence Re_t), the observed differences do not change considerably when increasing the Reynolds number. Hence, it appears that volume viscosity still leads to considerable flame modifications for highly turbulent conditions when burning hydrogen.

The influence of turbulence on the flame structure can be further quantified by probability density functions. For instance, the local curvature and tangential strain rates extracted along the flame front for different turbulence intensities are shown in Fig. 5.47. The peak PDF of the

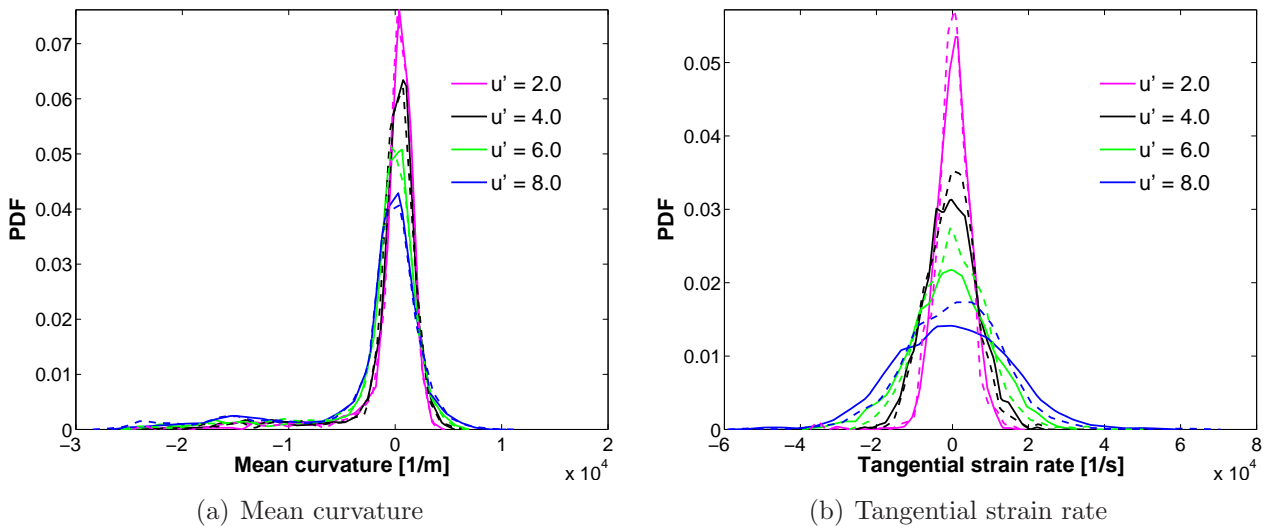


Figure 5.47: *Case E2:* Comparison of the instantaneous PDFs of (a) mean curvature and (b) local tangential strain rate at $t = 1.5\tau$ with (solid lines) and without (dashed lines) volume viscosity

local tangential strain rate is highly flattened when increasing turbulence intensity and reveal structural changes associated with volume viscosity (lowered peaks of almost the same proportion when $\kappa \neq 0$ for all u'). On the other hand, large modifications are also observed in the PDF of the mean flame curvature with increased turbulent stirring but volume viscosity appears to be irrelevant for this quantity.

As a whole, these computations do not show a considerable impact of the turbulence intensity on the effect of volume viscosity. It is therefore impossible to decide if laminar transport processes might become negligible under highly turbulent conditions. Even higher values of Re_t would be needed in the DNS to check this point.

5.3.4.5 Statistical significance

From the above analysis, it is obvious that even global flame properties are noticeably modified when taking into account volume viscosity, at least for the flames burning hydrogen-containing fuels. In turbulent reacting flows at low-Mach number, the instantaneous local impact of volume viscosity might be very small, but it will nevertheless lead to completely different evolutions due to the chaotic nature of turbulence. Of course, it is well understood that any kind of perturbation (initial and/or boundary conditions, numerics, etc.) in a turbulent flow should lead to different realizations. Therefore, in order to check if the observed differences are indeed induced by volume viscosity, additional DNS were carried out for *cases E2b* and *E2c*.

Scaled volume viscosity

For *case E2b*, the computations where the volume viscosity is accounted for were repeated three times, in which the computed values of the volume viscosities were systematically substituted by $\kappa^* = \kappa/2$, $\kappa^* = \kappa/4$ and $\kappa^* = \kappa/8$, as observable in Fig. 5.48, where the temporal evolution of the maximum value of the volume-to-shear viscosity ratio κ/η and the normalized fuel consumption rate are plotted. The temporal profiles of S_c for these scaled-down simulations are shown together with the corresponding solution for $\kappa = 0$ and $\kappa \neq 0$. Clearly, the various profiles are clearly distinct, even more so with the zoom around $t = 1.5\tau$. A closer look reveals S_c profiles which are steadily and progressively tending towards the $\kappa = 0$ solution, as expected. It is equally clear that in the presence of volume viscosity, hydrogen burns faster and with a higher heat release rate than for $\kappa = 0$. Switching to global flame structure, the heat release rate

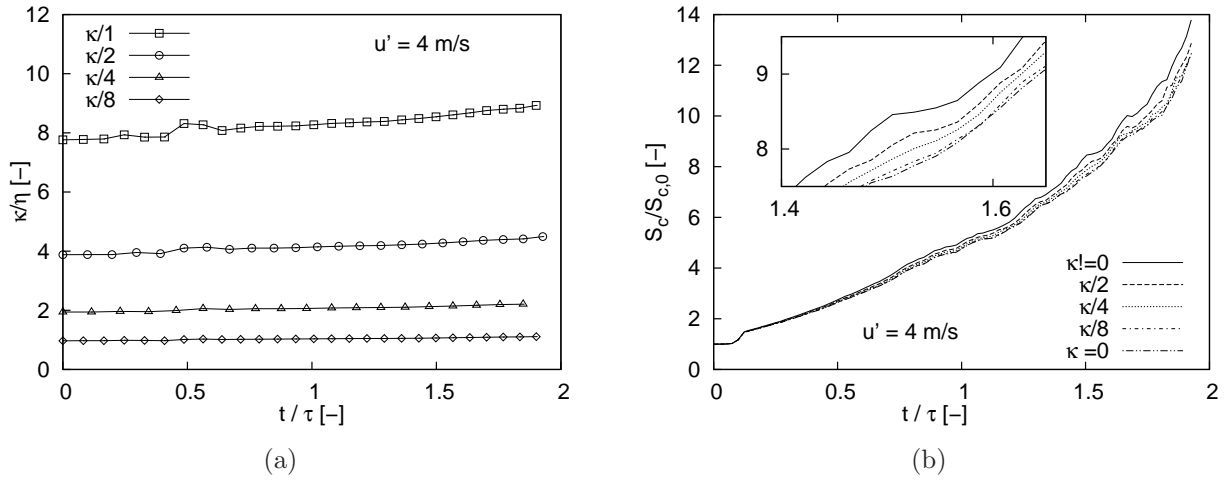


Figure 5.48: Further computations for case E2b ($u' = 4 \text{ m/s}$; $\kappa \neq 0$): Temporal evolution of (a) maximum value of the volume-to-shear viscosity ratio κ/η and (b) fuel consumption rate for which the computed κ values have been scaled by 1/2, 1/4 and 1/8 of its actual value

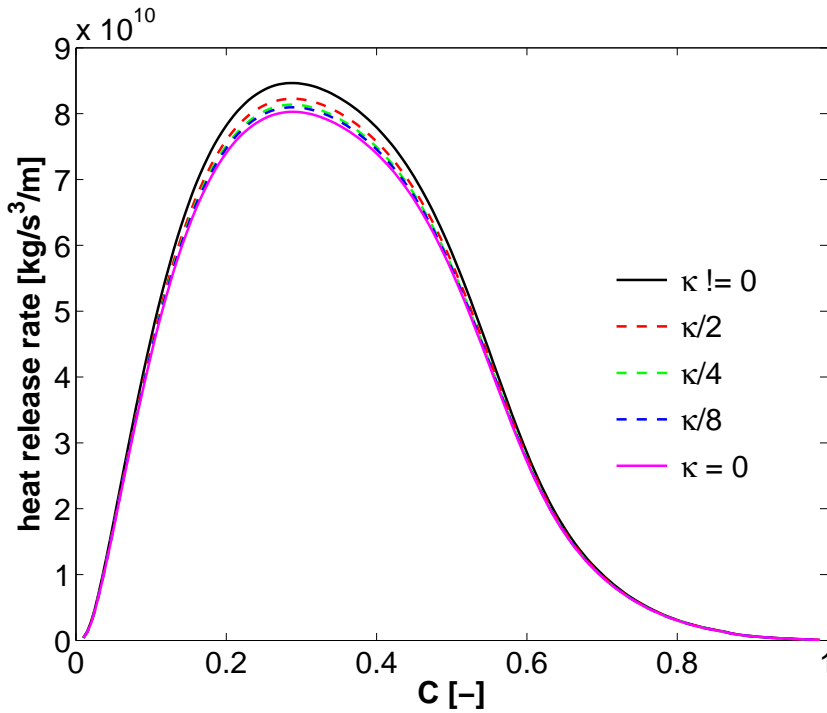


Figure 5.49: Further computations for case E2b ($u' = 4 \text{ m/s}$; $\kappa \neq 0$): instantaneous conditional profiles of the heat release rate conditioned on the reaction progress variable C for which the computed κ values have been scaled by 1/2, 1/4 and 1/8 of its actual value

is shown in Fig. 5.49. All other variables (not shown) behave in a similar manner. Neglecting volume viscosity results in peak profiles being underestimated. Once more, the $\kappa \neq 0$ profiles gradually collapse onto the $\kappa = 0$ profile when scaling down κ by 1/2, 1/4 and 1/8.

All these results prove that the previously discussed observations are indeed directly induced by the volume viscosity term and are not the result of any modeling or numerical artifact.

Ensemble averaging

To establish the statistical significance of the results reported here, the experiment for *case E2c* have been finally repeated four times with different turbulence fields initialized with different random seeds but having the same turbulent intensity ($u' = 6.0$ m/s) for both $\kappa \neq 0$ and $\kappa = 0$. The instantaneous structure of the expanding flame kernel in the turbulent flow at $t = 1.5\tau$ are shown for four of the five realizations in Fig. 5.50 where the iso-contours of the heat release rate for $\kappa = 0$ are plotted along $z = 0$. Even if the statistical properties of the turbulent fields are identical, considerable variations are observed at first, justifying the importance of ensemble averaging.

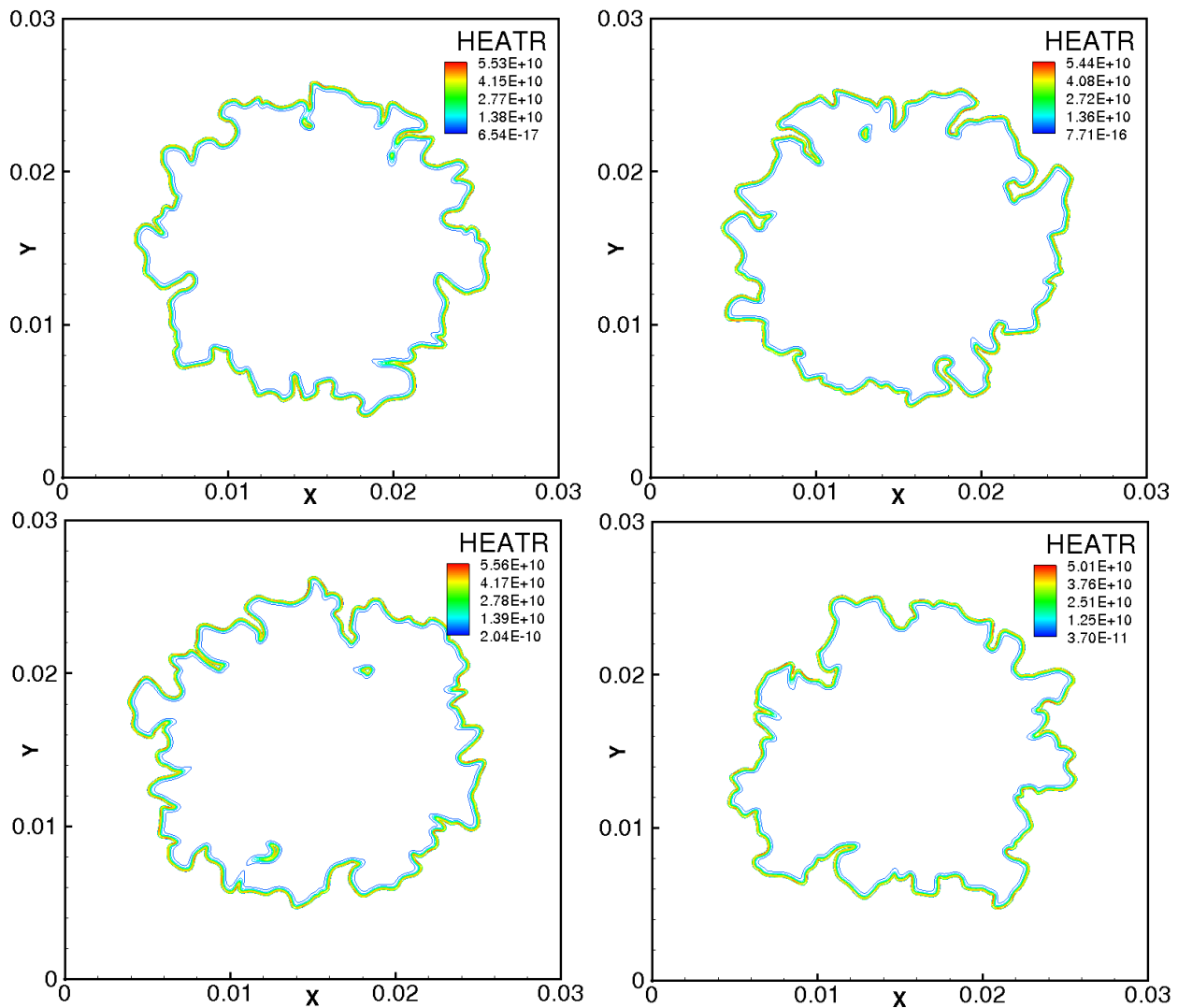


Figure 5.50: *case E2c* ($u' = 6.0$ m/s; $\kappa = 0$): Instantaneous contours of the heat release rate (on the $z = 0$ cm plane). All four statistically-identical realizations are shown at the same time, $t = 1.5\tau$

The time evolution of H_r and S_c are shown in Fig. 5.51. The $\kappa = 0$ and $\kappa \neq 0$ groups are all plotted with solid and dashed lines, with their averages in bold, respectively. A zoom starting at $t = 1.2\tau$ reveals substantial differences in the temporal evolution of both H_r and S_c with

and without volume viscosity. Once more, the flames involving volume viscosity burn faster and release more energy, as proved by a comparison of the mean curves.

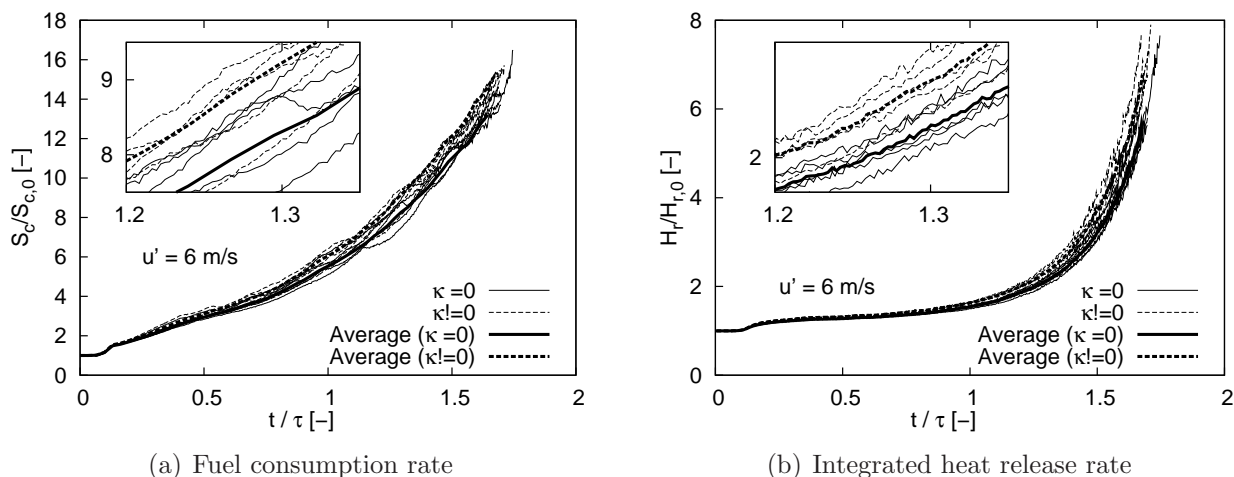


Figure 5.51: *case E2c*: Statistical significant results – Temporal evolution of (a) the fuel consumption rate and (b) integrated heat release rate with (dashed lines) and without (solid lines) volume viscosity effects. The bold line is the respective average of the five realizations

In the absence of volume viscosity, the peak profiles of the considered conditional flame variables for all five realizations are noticeably underestimated, as exemplified in Fig. 5.52 for the heat release rate conditioned on C at $t = 1.5\tau$.

5.3.5 Summary

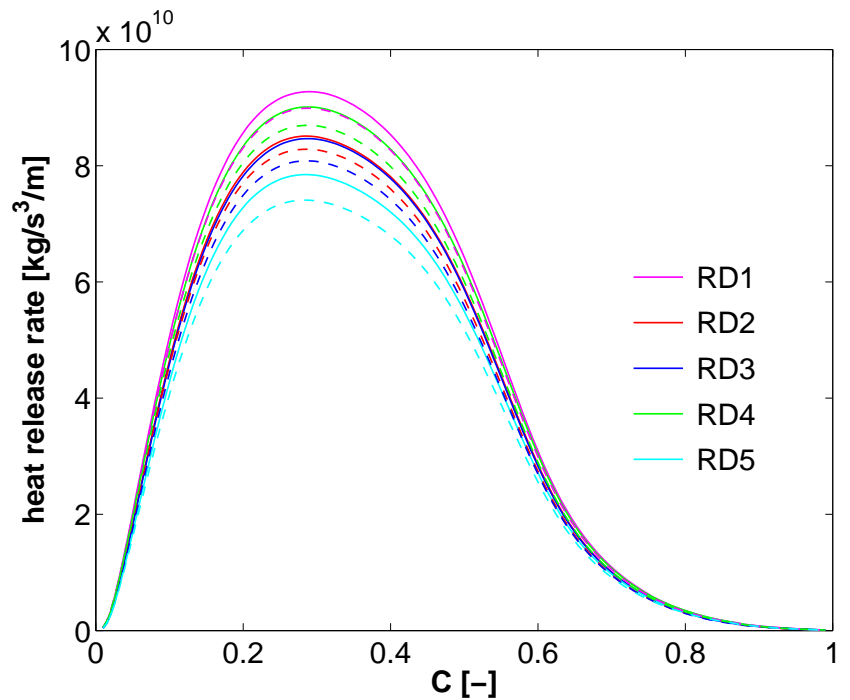
For realistic cases, where Re_t exceeds considerably 1000, considerable structural modifications such as flame–flame interactions, pinch off and local re-ignition fronts become prominent for premixed burning. On average, the flame responds to the increasing turbulence intensity by getting thicker. The flame speed is found to rapidly increase with increasing turbulence stirring. Simultaneously, peak conditional profiles of heat release, major and minor species mass fractions are systematically lowered with increasing turbulence intensity. All the observations point to the fact that analyzing DNS results at high Reynolds numbers is essential to obtain realistic information for modeling purposes.

Three different premixtures – hydrogen-air, syngas-air and methane-air have been considered in order to quantify the impact of volume viscosity and turbulence intensity on the flame properties. It has been shown that no differences are found in laminar computations due to volume viscosity, confirming theoretical findings for such low-Mach number conditions.

On the other hand, the chaotic nature of turbulence amplifies small instantaneous differences with time, eventually leading to completely different evolutions for the turbulent flames burning hydrogen-containing fuels. As a consequence, taking into account volume viscosity leads to noticeable differences even before reaching the characteristic turbulent time τ . This effect is clearly visible locally, changing for instance the local flame structure. But it is also observed with a considerable magnitude on all global flame properties and increases with time. These observations are more intense for the pure hydrogen flames compared to when using syngas (CO/H_2) as a fuel. For these hydrogen-containing fuels, the influence of volume viscosity appears to be independent of the turbulent Reynolds number even though the peak value of κ/η increases timidly. The inclusion of volume viscosity effects in multi-component multi-dimensional turbulent premixed flame computations is therefore recommended for all hydrogen-containing fuels.

On the other hand, in all considered cases, premixed methane flames show a negligible impact of volume viscosity. No differences at all are found in laminar computations, confirming

Figure 5.52: *Case E2c:* Statistical significant results – Comparison of the instantaneous conditional profiles of heat release rate at $t = 1.5\tau$ with (solid lines) and without (dashed lines) volume viscosity



theoretical findings for low-Mach number conditions. To save computing resources, the inclusion of volume viscosity effects in multi-component multi-dimensional turbulent flame computations burning methane, and probably higher hydrocarbons as well is therefore discouraged, as long as low-Mach numbers are considered.

This study demonstrates also the importance of repeating DNS realizations in order to obtain statistically significant data. Single realizations might lead to spurious discrepancies, rapidly smoothed out when averaging over several results, as observed here when comparing the findings for several and single DNS realizations.

5.4 Conclusions

From the few figures given on the computational cost associated with fully resolved DNS computations using detailed transport and chemistry models, there is an obvious need for reduced yet predictive models despite the emergence of extremely powerful scientific calculators. This is particularly important to be able to access even higher Reynolds numbers in more complex geometries. In order to go further, the next and last chapter will present our first contributions in this direction. First, the implementation of reduced models (low-Mach number, tabulated chemistry) in flame DNS will be tested. Then, first DNS involving a more realistic geometry will be attempted.

Present challenges

6.1 Introduction

In this chapter, direct computations with reduced but realistic models, aimed at reducing further the user waiting time and general computational cost for full-scale three-dimensional turbulent flame calculations are presented (Sect. 6.2). In particular, a direct combination of the FPI complex chemistry tabulation and of the low-Mach number formulation (see Chapter 3) are employed to simulate laminar and turbulent premixed flames burning various fuels in air. Results obtained with both the classical and advanced FPI chemistry tables are compared and contrasted, bringing out in particular the gain in computing time as a result of the structured grid on which the advanced table is built. The effects of the use of a detailed transport chemistry database on the resulting flame structure is also examined.

In Sect. 6.3, we consider a much more complex configuration: a spatially developing premixed methane-air slot-burner Bunsen flame in the TRZ regime, simulated with a 2-step methane-air chemical mechanism using *AVBP*. The reaction zone structure, curvature, flame thickness, etc. are studied by a direct comparison and contrasting with detailed chemistry results from the literature.

6.2 Tabulated chemistry results

In this section, direct simulations of laminar and turbulent flames using both the classical (Sect. 6.2.2 and 6.2.3) and advanced (Sect. 6.2.4) FPI tabulated chemistry are presented. These test cases will be used to check the proper coupling of the look-up table with the low Mach number DNS solver described in Sect. 4.4.2. Results from DNS computations using the two FPI variants will be compared and contrasted. Typical computing times are reported.

6.2.1 Problem and initialization

Three validation test cases for the generated FPI tables have been considered – a spherical expanding (2-/3-dimensional) and double (2-dimensional) premixed flame configurations under laminar and turbulent conditions. Three different fuels are considered: a fully premixed methane/air flame at $Y_z = 0.72$, a hydrogen/air flame diluted in nitrogen at $Y_z = 0.84$; and a syngas/air at $Y_z = 0.64$. All cases are carried out at atmospheric pressure and the fresh gas temperature is $T_u = 298$ K. Periodicity is assumed on all the boundaries. The range of turbulent Reynolds numbers Re_t , domain sizes L , fuels, dimensions and grid resolution for the various cases is summarized in Table 6.1.

Cases	Fuel	L (cm)	Dimension	Re_t	Resolution (μm)
1a	CH_4	0.8	2D	laminar	53
1b	CH_4	0.8	2D	90	40
2	CO-H_2	2.0	2D	970	26
3	CH_4	0.5	3D	183	50
4	H_2	0.5	3D	190	99

Table 6.1: Simulation parameters for the FPI validation test cases

Case 1:

A perfectly spherical and fully premixed laminar (*Case 1a*) CH_4 -air flame kernel is initialized at zero velocity in a 2D box of side 8 mm. The number of grid points on each coordinate direction is 151, yielding a resolution of 53 μm . The same flame subject to the same initialization is now superposed with a field of synthetic homogeneous isotropic turbulence corresponding to a von Kármán spectrum with Pao correction for near dissipation scale (*Case 1b*). The number of grid points on each coordinate direction is 201, yielding a resolution of 40 μm . The unburned mixture viscosity $\nu = 1.57 \times 10^{-5} \text{ m}^2\text{s}^{-1}$. The generated turbulence as resolved on the grid corresponds to a turbulent integral scale $l_t = 0.97 \text{ mm}$, a velocity fluctuation $u' = 1.46 \text{ m/s}$, leading to a turbulent Reynolds number $Re_t = 90.1$ and to an eddy turn-over time $\tau = l_t/u' = 0.66 \text{ ms}$.

Case 2:

The second test case is a two-dimensional double premixed CO-H_2 -air flame setup at a relatively higher value of $Re_t = 970$. The number of grid points on each coordinate direction is 768, yielding a resolution of 26 μm . The turbulence initialization is done with the technique described in Sect. 4.5, and corresponds to $l_t = 3.2 \text{ mm}$ and $u' = 5.0 \text{ m/s}$.

Case 3:

The third case is a full three-dimensional DNS computation of a turbulent spherical premixed methane-air flame in a cube of side 1.0 cm, with 200 grid points on each coordinate direction. The grid resolution is 50 μm and the unburned mixture viscosity is same as for *Case 1*. The generated turbulence as resolved on the grid corresponds to a turbulent integral scale $l_t = 1.77 \text{ mm}$, a velocity fluctuation $u' = 1.62 \text{ m/s}$, leading to $Re_t = 183$ and $\tau = 1.09 \text{ ms}$.

Case 4:

Similar to the premixed methane-air flames, a perfectly spherical laminar H_2 -air flame kernel is initialized at zero velocity in a cube of sides 0.5 cm and superposed with synthetic homogeneous isotropic turbulence. It is resolved on a mesh with 101 grid points on each coordinate direction, yielding a resolution of 99 μm (which is extremely coarse and only possible with FPI!) and an unburned mixture viscosity $\nu = 1.71 \times 10^{-5} \text{ m}^2\text{s}^{-1}$. The generated turbulence as resolved on the grid corresponds to $l_t = 1.4 \text{ mm}$, $u' = 2.31 \text{ m/s}$, leading to $Re_t = 189.8$ and $\tau = 0.61 \text{ ms}$.

All the laminar and low Reynolds number computations have been realized on a single Pentium 2.6 GHz PC with 2 GB of memory, illustrating the numerical efficiency of this approach. The Linux cluster *karman* is only needed for *case 2*.

6.2.2 Laminar flame structure

The instantaneous fields of the mass fraction of HO_2 for *Case 1a* at two different time instances is shown in Fig. 6.1, while instantaneous fields of temperature and CH_4 , CH_2 and CH_3O mass fractions are displayed in Fig. 6.2. It is interesting to see that both the major and stiff radicals appear to be properly resolved, although only the table coordinates are really computed. The structure and expansion of the laminar flame proceed as expected.

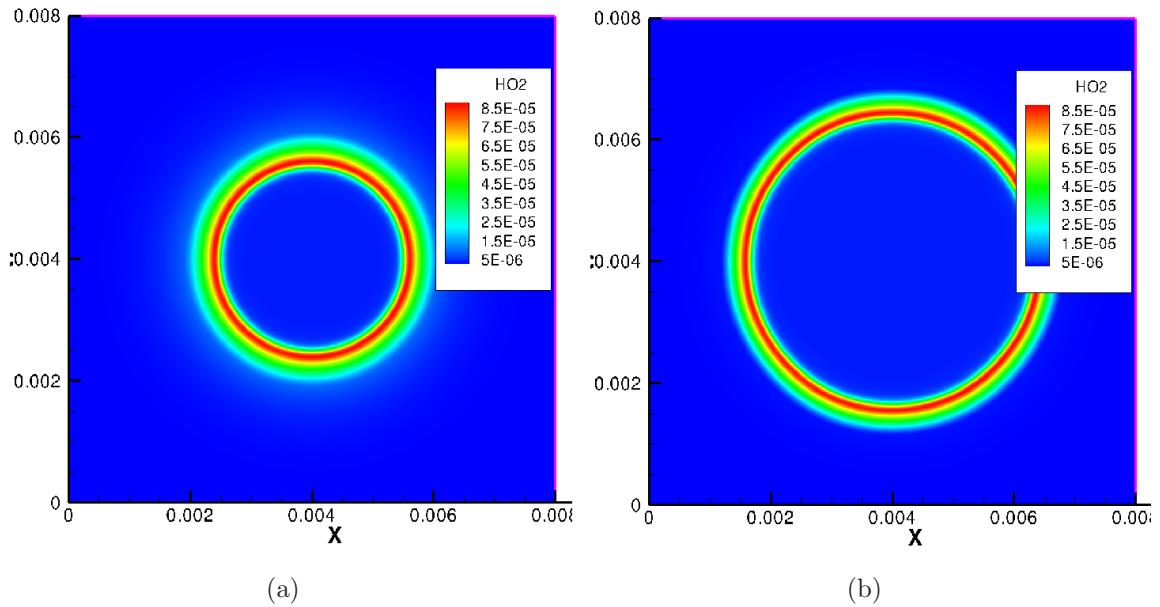


Figure 6.1: *Case 1a:* Instantaneous field of the mass fraction of HO_2 in a spherical laminar premixed CH_4 -air flame at (a) $t = 1.0$ and (b) 1.5 ms

6.2.3 Turbulent flame structure

The mass fraction of HCO is displayed in Fig. 6.3 at two different time instances. The computations are carried out up till $t = 2.3\tau$. The initially spherical flame is observed to become wrinkled by the mild turbulence. HCO , which is a stiff radical, is well resolved.

Plots of the reaction progress variable are displayed in Fig. 6.4 for *case 2*. Again, the detailed turbulent flame structure is well captured on the grid and the evolutions are qualitatively correct.

The time evolution of the expanding turbulent flame for *case 3* is shown in Fig. 6.5, where the flame position is defined as the isosurface of $Y_c = 0.03$. The initially perfect spherical flame is seen to evolve, heavily wrinkled and deformed due to the strong interaction with the turbulent field. Plots of the mass fractions of OH and H_2O_2 are displayed in Fig. 6.6 at $t = 1.6\tau$ for *case 4*. Indeed, the overall flame structure as well as all major and minor species profiles appear to be captured, even when using a relatively coarse grid as large as $99 \mu\text{m}$!

6.2.4 Advanced versus classical FPI tables

In Sect. 3.4.3, a novel variant of the FPI chemistry tabulation was proposed allowing the direct inclusion of not only complex chemistry effects in the generation stage but also detailed transport. The construction of one such table with the incorporation of the recommended modifications was realized and tested. The obtained results are compared to those from the classical FPI table. The improved FPI procedure has been validated in two steps. First, an a priori test in Sect. 3.4.4.3 has proved that the new mapping does not lead to any loss of accuracy, even for minor radicals. Fig. 3.8 shows a comparison between the results obtained by solving directly the exact flame structure using the complete reaction scheme (symbols) and the FPI result obtained with the interpolated (rectangular) look-up table for the mass fractions of CH_2O , HCO and HO_2 radicals in a freely propagating laminar premixed methane/air flame. The agreement is as expected perfect.

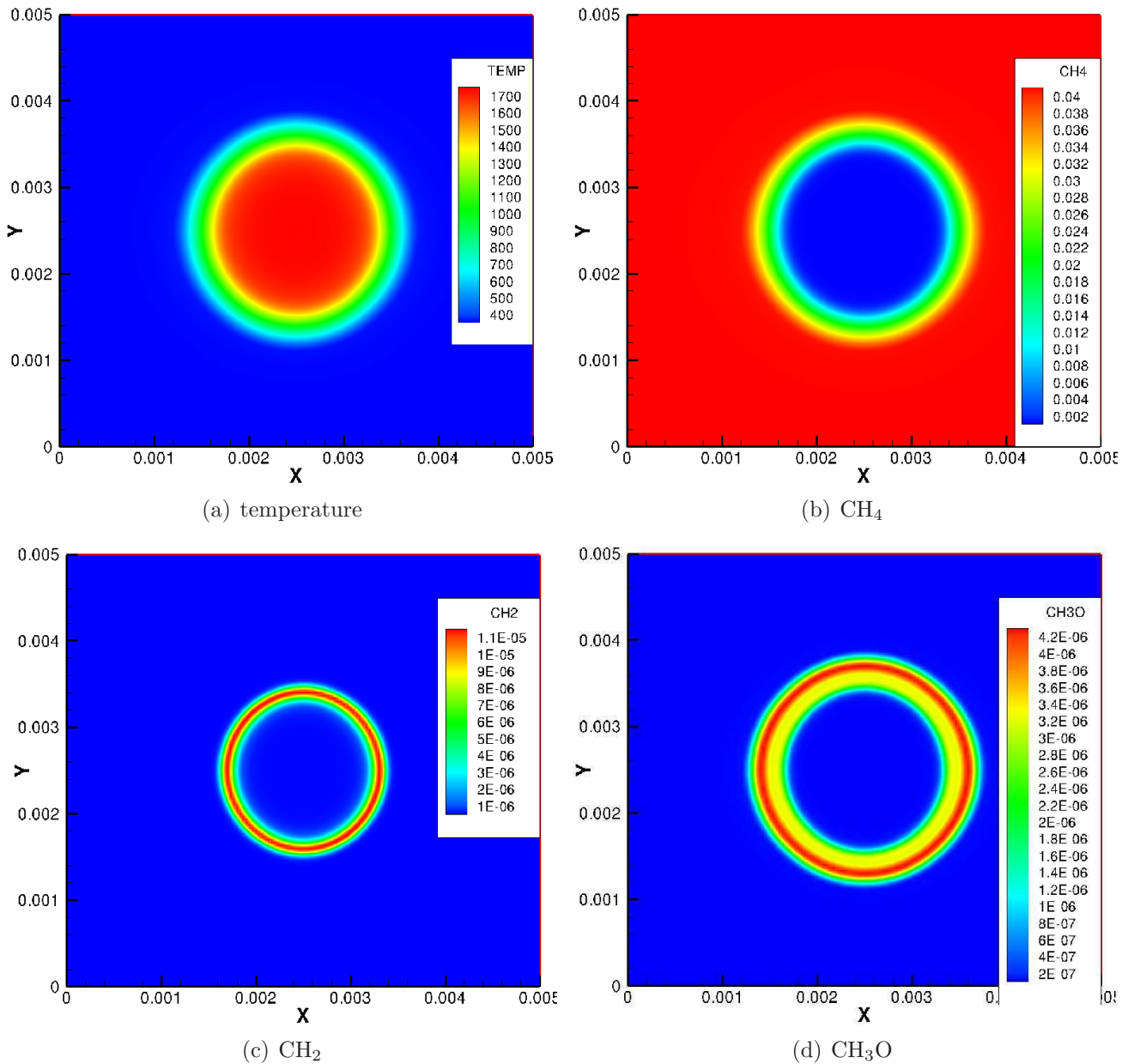


Figure 6.2: *Case 1a:* Snap-shots of a spherical premixed CH₄-air flame at $t = 0.95$ ms

6.2.4.1 Time evolution profiles

In addition, a direct comparison has been carried out for an expanding premixed CO/H₂-air flame configuration under the influence of turbulence [139]. Results obtained with detailed physicochemical models are directly compared to the results obtained with the corresponding (advanced) FPI formulation. Three different time instants are shown for such an expanding turbulent flame in two dimensions in Fig. 6.7, where the iso-surface of the HCO radical is displayed. A good agreement is obtained, demonstrating the accuracy of the extended FPI approach. However, slight discrepancies are still visible. Corresponding modifications are presently being implemented to correct those.

6.2.4.2 Flame propagation speed

One essential property is the propagation speed. The advanced FPI approach described previously has been employed to compare the time-dependent growth of the flame surface area for an initially spherical flame expanding in a turbulent flow field (Fig. 6.8). For stoichiometric con-

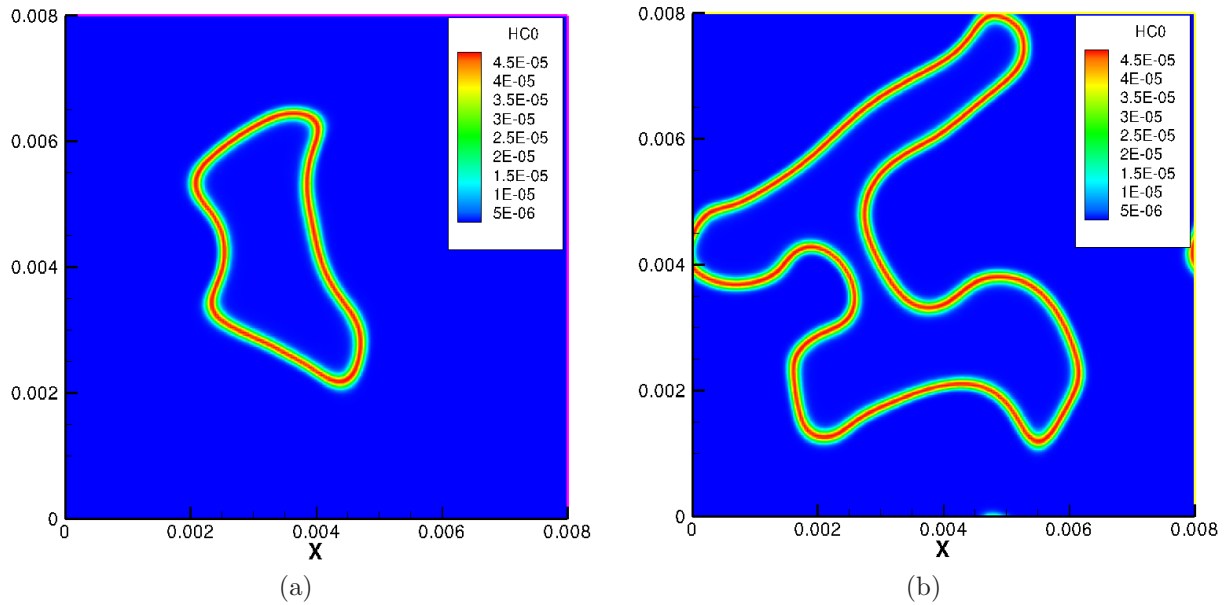


Figure 6.3: *Case 1b:* Instantaneous field of the mass fraction of HCO in a 2D spherical turbulent ($Re_t = 90$) premixed CH_4 -air flame at (a) $t = 0.5$ and (b) 1.25 ms

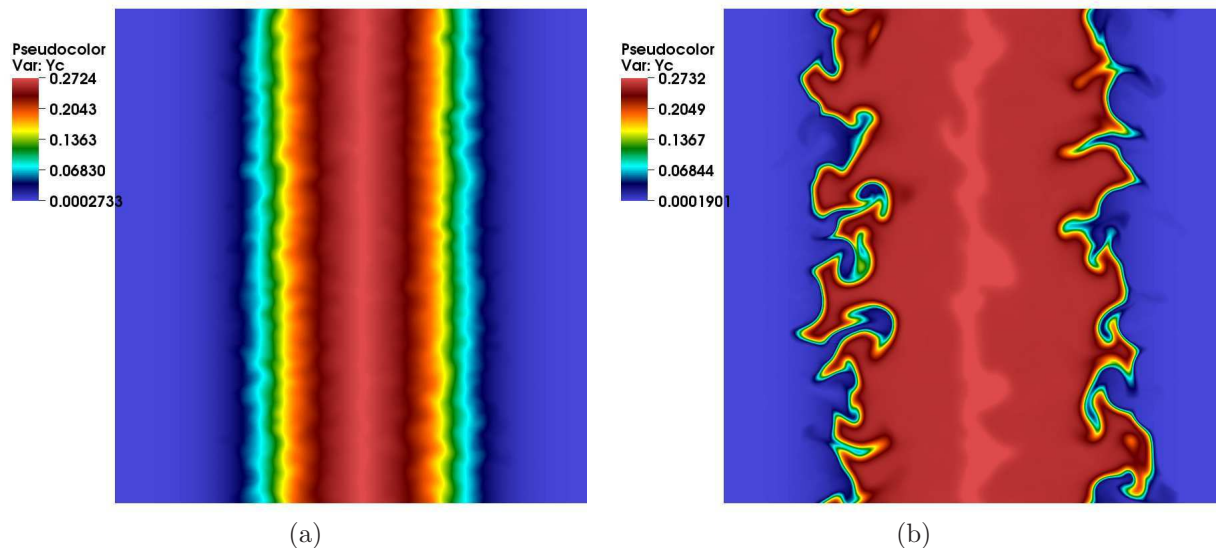


Figure 6.4: *Case 2:* Snap-shots of a 2D turbulent ($Re_t = 970$) double premixed CO/H_2 -air flame showing the reaction progress variable Y_c at (a) $t = 0.05\tau$ and (b) $t = 0.7\tau$

ditions, major differences appear between the computation relying on differential diffusion and that associated with $Le = 1$. The divergence of the two profiles soon after ignition shows that the location of the flame front (defined as the isosurface $Y_c = 0.03$) for the two computations are different, implying that the equivalent flame radius grows at a slower rate for the $Le = 1$ case, as expected (see Fig. 6.9).

From these observations, we can conclude that, for methane flames, the unity Lewis number hypothesis which is adopted in the construction of classical FPI look-up tables is a reasonable assumption when one is interested only in major species and global trends of a flame. This assertion is not necessarily accurate for minor species profiles and flame speed. Moreover, flame position and extinction limits will be affected, depending on the transport model with which the FPI table is generated. For computations of flames with large differential diffusivities, such as hydrogen/air flames, a table with mixture-averaged transport properties is highly recommended.

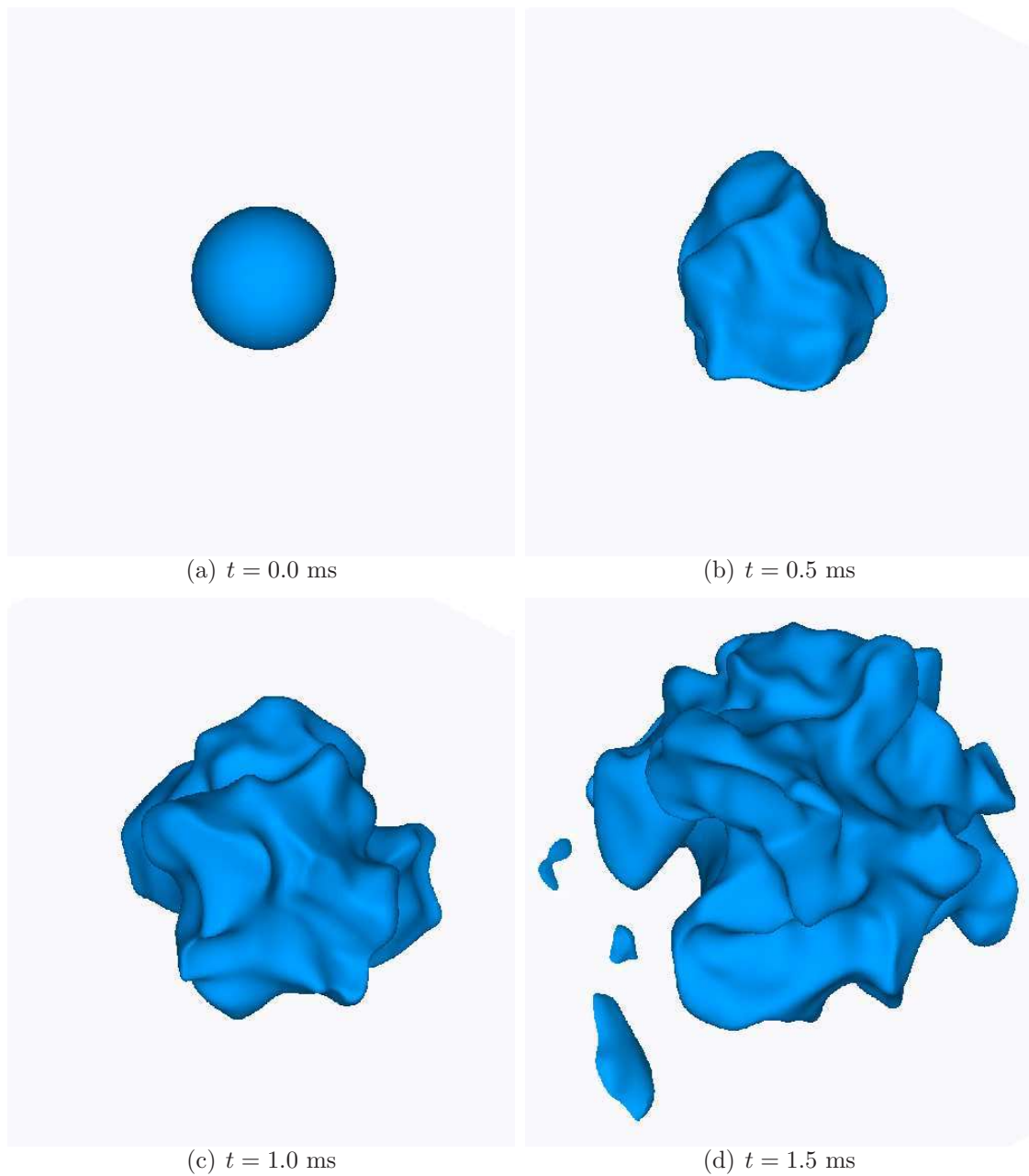


Figure 6.5: *Case 3:* Time evolution of a turbulent flame structure computed with FPI, showing successive isosurfaces of the progress variable, Y_c for an initially 3D spherical turbulent premixed methane/air flame, expanding under the influence of an initially homogeneous isotropic turbulence field

6.2.5 Trade-off in computing time

As mentioned in section 3.4.5, we observe a speed up in computing time for the above DNS computations using the new FPI database. The speed-up factor is defined as

$$S_p = \frac{T_{old}}{T_{new}},$$

where T_{old} and T_{new} are the observed elapsed times when using the classical and new FPI tables, respectively. The speed-up factor is plotted in Fig. 6.10 with increasing number of grid points for a series of 1D and 2D laminar premixed methane-air flames computations. As can be observed, the new FPI table offers a speed-up in computing time of up to 4.71 (1D) and 3.95 (2D) for a

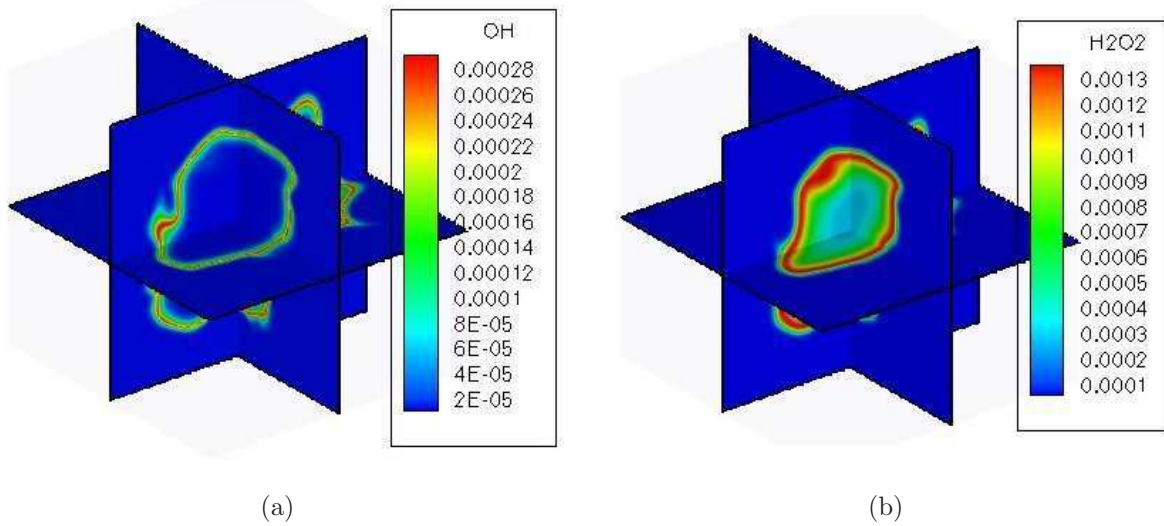


Figure 6.6: *Case 4:* Snap-shots of a three-dimensional spherical turbulent ($Re_t = 190$) premixed H_2 -air flame showing the mass fractions of (a) OH and (b) H_2O_2 at $t = 1.6\tau$

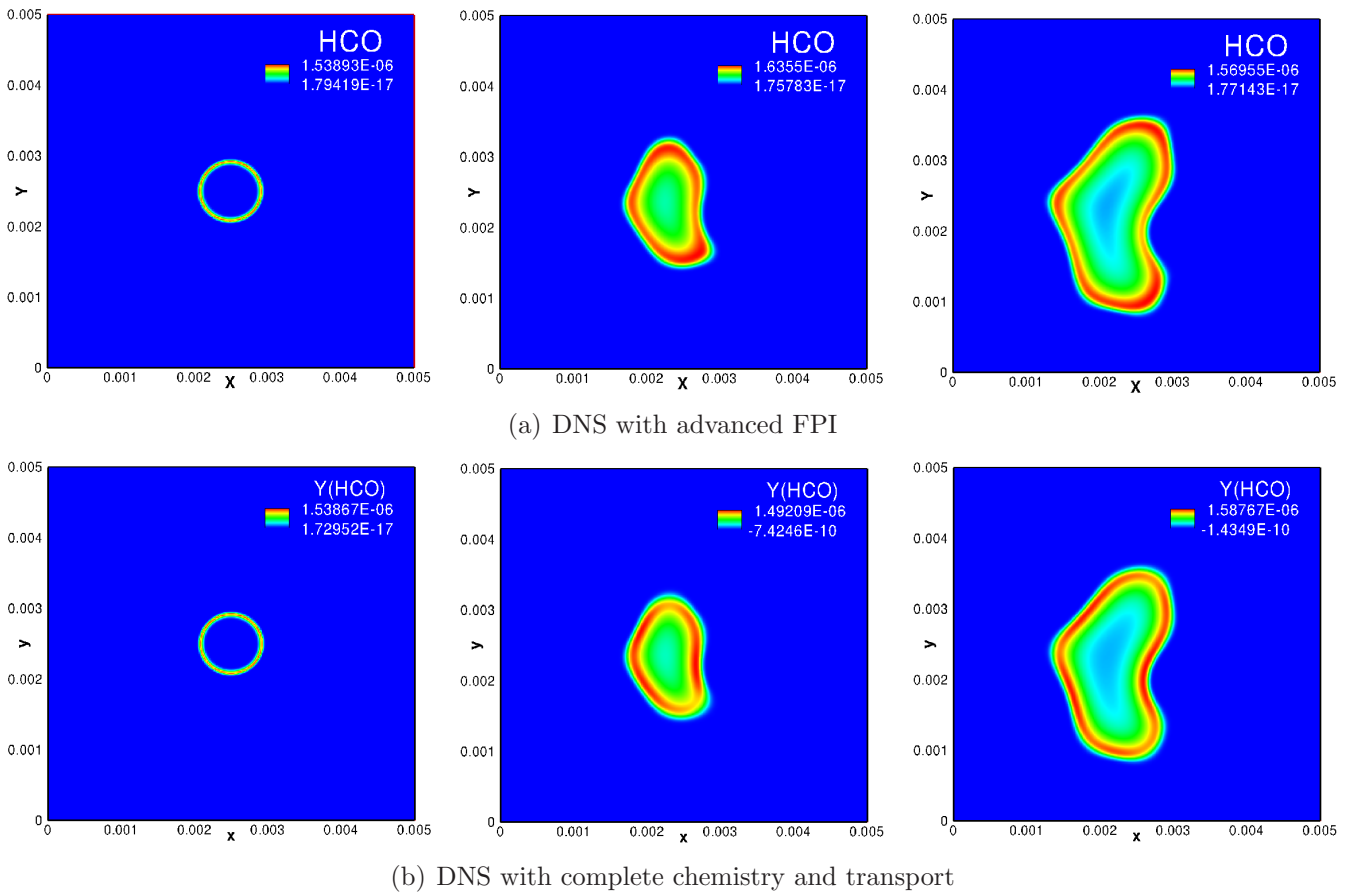


Figure 6.7: Validation of the advanced FPI procedure showing the iso-levels of HCO mass fraction at three times (from left to right 0.0, 0.25 and 0.5 ms): (a) advanced FPI results; (b) complex chemistry and transport models.

double premixed flame configuration. It should be pointed out that the new FPI routines are not yet fully optimized, so the relative speed up might be even higher. The same figure also reveals that there exist a number of grid points with which to obtain a maximum speed up. On a High Performance Computing system, if this number is known for a given flame configuration, the number of processors can be wisely chosen in such a way that each CPU solves approximately this

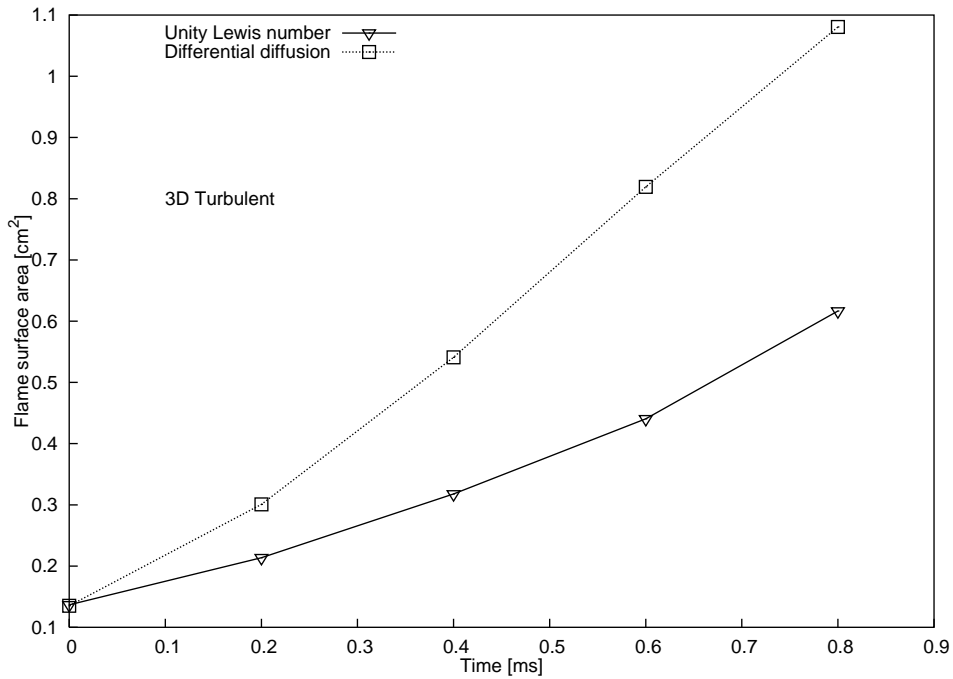


Figure 6.8: Time evolution of the surface area for a premixed stoichiometric methane/air flame computed using differential diffusion and unity Lewis number FPI tables

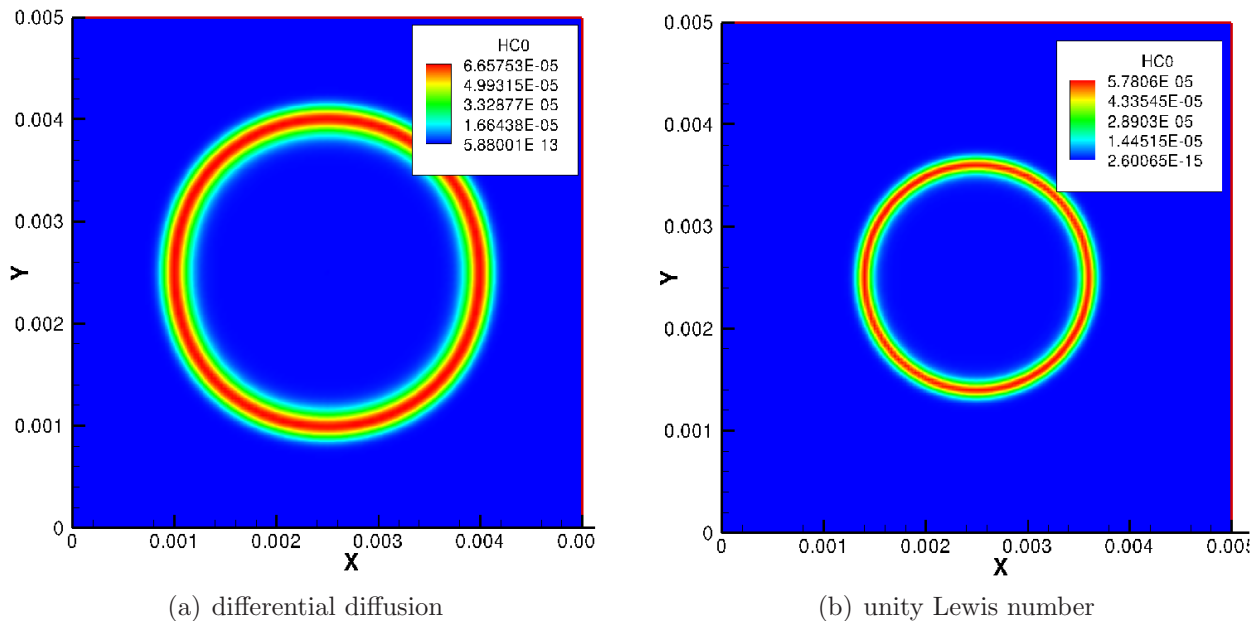


Figure 6.9: Instantaneous isosurface of the mass fraction of HCO from a 2D spherical laminar premixed CH_4 -air flame computed with (a) advanced and (b) classical FPI tables at $t = 0.5\text{ms}$

optimal number of grid points. As such, maximum speed up in computing time is guaranteed, as far as the FPI database is concerned.

6.2.6 Summary

Tools for the automatic generation of FPI look-up tables are now available in Magdeburg. In the development process, 2D FPI chemistry databases have been generated and successfully incorporated into a 3D low-Mach number DNS code. Preliminary results from this coupling confirm, not only its proper implementation but also its good functionality. The database has

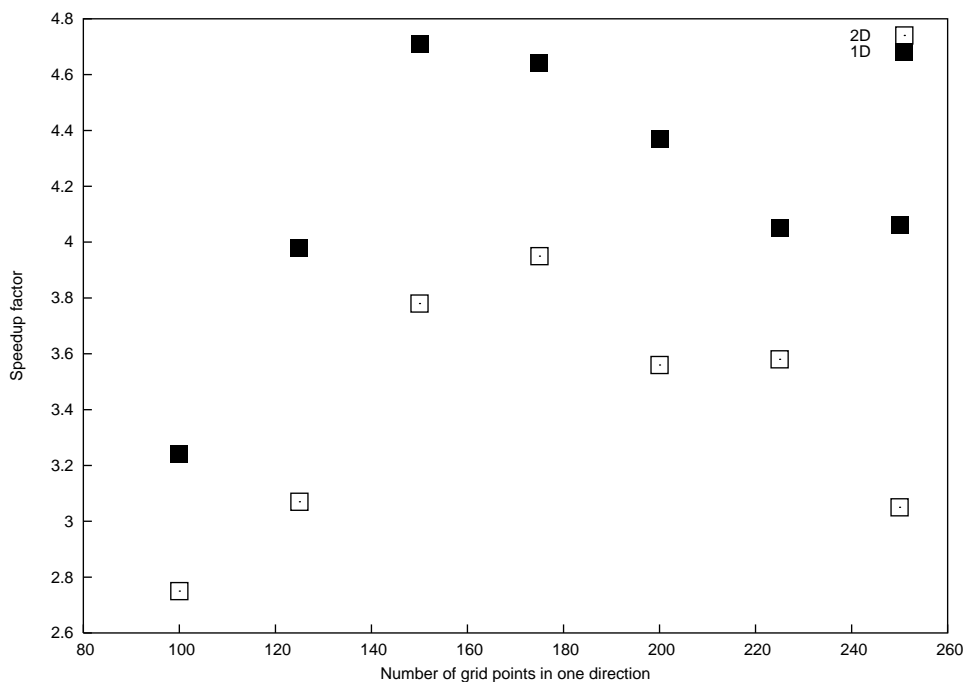


Figure 6.10: Speed up factor against number of grid points (one direction only) when using the new FPI table, for a series of 1D and 2D laminar premixed methane-air flames computations

been tested successfully for both laminar and turbulent methane and hydrogen premixed flames, for a number of turbulent Reynolds numbers and grid resolution. From these first validation test cases, the flame structure as well as the major and minor species profiles are well captured, even when using a coarse grid.

This version of the FPI look-up table has been built on a rectangular grid, unlike the triangular grid on which its predecessors are tabulated. Such a regular grid results in a computational speed-up since a search procedure is no longer needed [139].

The unity Lewis number assumption on which the classical FPI tables have been computed has been checked. Using the new FPI strategy, a database taking into account differential diffusion (mixture-averaged transport properties) has been constructed. The effects and impact of FPI tables built with these transport models on the flame structure has been quantified. For computations of flames with large differential diffusivities, a table taking into account differential diffusion is highly recommended.

More validation computations are now needed before extending the database by adding a third coordinate (enthalpy) to account for heat losses.

The size of the database is still an issue. We hope to build a master database containing all possible thermo-chemical and transport quantities, from where only a strictly necessary number of tabulated parameters will be loaded for a given simulation. This should reduce further memory constraints.

6.3 Towards realistic geometries in DNS

In a collaboration with CERFACS (Toulouse, France, B. Cuenot), we decided to test if a fully resolved three-dimensional DNS of turbulent premixed combustion in the thin reaction zone regime can be performed for a realistic geometry: a spatially developing slot-burner Bunsen flame configuration computed with a 2-step methane-air chemical mechanism. The same problem (initial flow conditions, grid resolution and turbulent parameters) has been the subject of thorough studies by the combustion group at SANDIA [156, 173, 174] using the high order *S3D*

parallel flame solver with detailed chemistry. The simulation is repeated here in an attempt to reproduce the original results using the compressible turbulent flame solver *AVBP* together with reduced (2-step) chemistry. Details of the problem and numerical configuration as extracted from [173, 174], together with first results are presented in what follows. Since *AVBP* is able to consider very complex real geometries, a success would open the door for DNS of realistic problems, unlike *parcomb*, π^3 and *S3D*, which can only handle academic configurations.

6.3.1 Problem and initialization

The slot-burner Bunsen configuration is especially interesting due to the presence of mean shear in the flow and is similar to burners used in experimental studies, for example by Filatyev *et al.* [175]. Figure 6.11 shows the configuration which consists of a central jet through which premixed reactants are supplied. This central jet is surrounded on both sides by a heated co-flow, whose

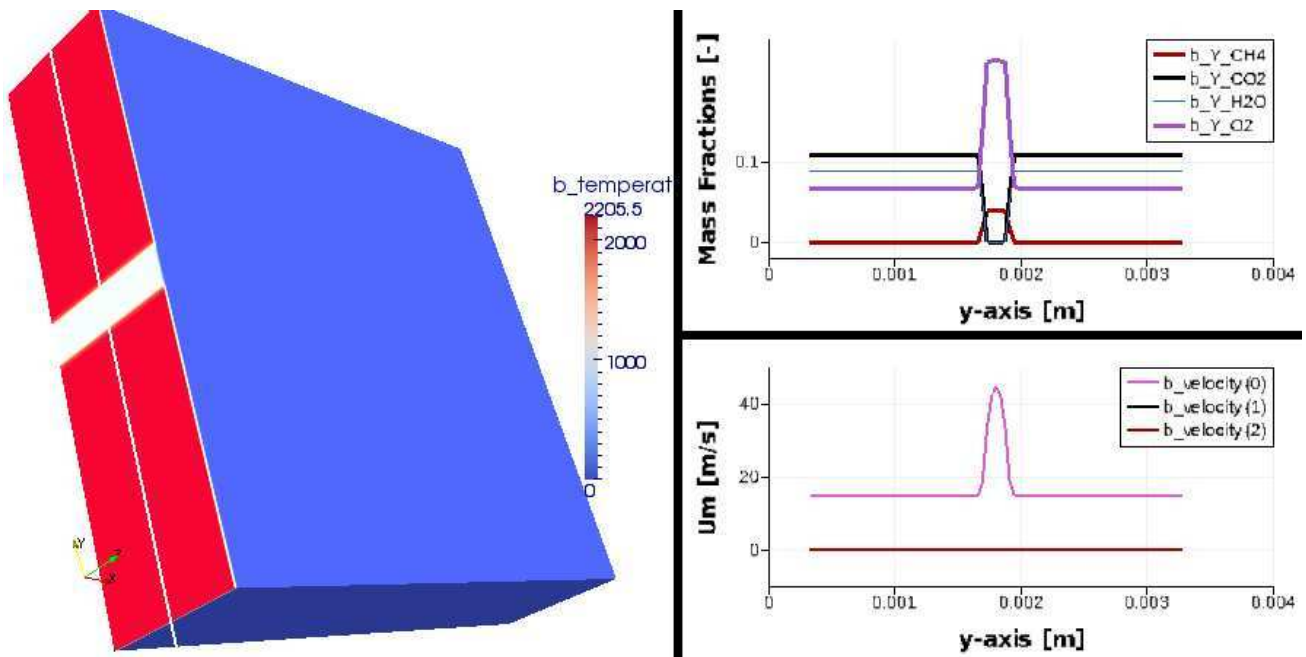


Figure 6.11: The slot-burner Bunsen configuration consists of a central jet through which premixed reactants are supplied. This central jet is surrounded on both sides by a heated co-flow, whose composition and temperature are those of the complete combustion products of the reactant jet

composition and temperature are those of the complete combustion products of the reactant jet. This arrangement is similar to the pilot flame surrounding slot burners commonly used in experiments [175]. The reactant jet was chosen to be a premixed methane-air jet at 800 K and mixture equivalence ratio, $\Phi = 0.7$. The unstrained laminar flame properties at these conditions computed using PREMIX [60] are as follows:

- flame speed, $S_L = 1.8$ m/s,
- thermal thickness based on maximum temperature gradient, $\delta_L = 0.3$ mm,
- full-width at half-maximum (FWHM) of heat release rate, $\delta_H = 0.14$ mm, and
- flame time-scale, $\tau_f = \delta_L/S_L = 0.17$ ms.

One of the reasons for choosing a preheated inflow condition is that the cost of computation is inversely proportional to the Mach number at the inflow. Preheating the reactants leads to a higher flame speed and allows a higher inflow velocity without blowing out the flame. Also, many practical devices such as internal combustion engines, gas turbines and recirculating furnaces

operate at highly preheated conditions. One important consequence of preheating is that the reaction zone is broadened at 800 K ($\delta_L/\delta_H = 2$) compared to 300 K ($\delta_L/\delta_H = 3$). However, the preheat temperature chosen here is low enough so that flameless combustion does not occur.

The domain size in the stream-wise (x), crosswise (y) and span-wise (z) directions, in terms of the slot width ($h = 1.2$ mm) is $L_x \times L_y \times L_z = 12h \times 12h \times 3h$. A uniform grid spacing of $20 \mu\text{m}$ was used in the x and z directions, whereas an algebraically stretched mesh was used in the y direction, such that $y(s) = f(s) \times s$, where s is the equi-spaced computational grid and $0 \leq s \leq 1$. The stretching function is given by

$$f(s) = \beta s + \frac{1}{2} \left[1 + \tanh \left(\frac{s - s^*}{\sigma} \right) \right] (\exp^{k(s-1)} - \beta s) \quad (6.1)$$

where $k = \ln(\beta s^*)/(s^* - 1)$, $\beta = 0.55$, $s^* = 0.75$ and $\sigma = 1/16$. This choice of constants yield a mesh that has a uniform spacing of $20 \mu\text{m}$ in a $5h$ wide region in the center and stretches outward. Although the uniform grid spacing at the center of the jet ensures numerical fidelity and flexibility in post-processing, the boundaries are pushed farther away to reduce their influence on the flame. The resultant mesh size is $N_x \times N_y \times N_z = 720 \times 400 \times 180 = 52$ million. The simulation parameters are as follows [156, 173, 174]:

Turbulent jet velocity	$\tilde{U} = 60$ m/s
Laminar co-flow velocity	15 m/s
Jet Reynolds number	$\text{Re}_{jet} = \tilde{U}h/\nu = 840$
Turbulence intensity	$u'/S_L = 3$
Turbulence length scale	$l_{33} = 0.7\delta_L$
Integral length scale	$l_t = 2\delta_L$
Turbulence Reynolds number	$\text{Re}_t = u'l_t/\delta_L = 40$
Karlovitz number	$\delta_L/l_k = 100$
Damköhler number	$S_L L_t/u'L = 0.23$

The kinematic viscosity at the inflow conditions, $\nu = 8.5 \times 10^{-5} \text{ m}^2/\text{s}$, is used to compute the Reynolds number. The turbulence length scale l_{33} is estimated as $l_{33} = u'^3/\tilde{\epsilon}$, where $\tilde{\epsilon}$ is the average turbulent kinetic energy dissipation rate. Integral length scale l_t is defined as the integral of the auto-correlation of the span-wise component of velocity in the span-wise direction. The turbulence scales evolve from the synthetic turbulence specified at the inflow. The u' , l_t and l_{33} values reported here are measured at the 1/4th stream-wise location along the jet centerline.

6.3.2 Laminar flame structure

The initial mixture composition consists of $Y_{CH_4} = 0.0$, $Y_{O_2} = 6.7 \cdot 10^{-2}$, $Y_{N_2} = 0.74$, $Y_{CO_2} = 0.107$, $Y_{H_2O} = 8.8 \cdot 10^{-2}$, $Y_{CO} = 0.0$ at $T_b = 2205.5$ K on the burnt gas side and $Y_{CH_4} = 3.9 \cdot 10^{-2}$, $Y_{O_2} = 0.223$ and $Y_{N_2} = 0.74$ at $T_u = 800$ K on the fresh gas side (central jet). These values are smoothed out using hyperbolic tangent functions at the fresh/burnt gas interface, as illustrated in Fig. 6.11 (right). The initial axial velocity is imposed as an exponential profile:

$$U(y) = \begin{cases} 105.0 - 45.0 \exp\left(\frac{y^2}{0.71 \cdot 10^{-6}}\right) & -h/2 \leq y \leq h/2 \\ 15.0 & \text{otherwise} \end{cases}$$

The other two velocity components are zero everywhere. These profiles are imposed on the left (x) boundary. Non-reflecting outlet boundaries are imposed on the right (x) boundary and along the y direction, while periodicity is applied along z .

The laminar flame results are exemplified in Fig. 6.12 where two-dimensional slices through $z = 0$ of the instantaneous fields of the heat release and O_2 mass fraction are displayed at $t = 4.3$ ms. Everything looks as expected and fluctuating velocities can now be switched on.

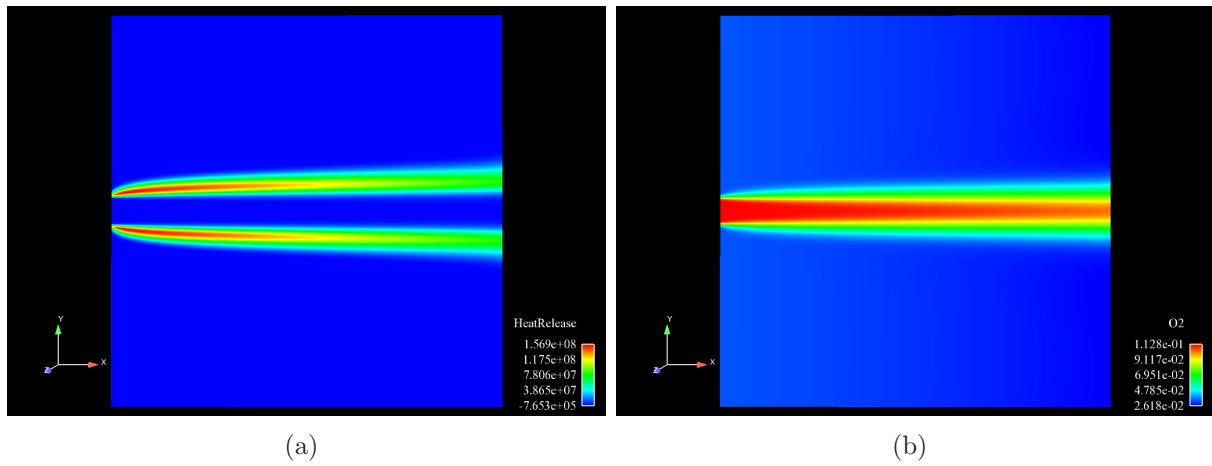


Figure 6.12: Two dimensional slice through $z = 0$ of a laminar lean premixed methane-air flame showing (a) heat release and (b) O_2 mass fraction fields at $t = 4.3$ ms

6.3.3 Turbulent flame structure

For the turbulent case, a fluctuating velocity field damped with a similar exponential root-mean-square profile is injected from the left side on top of the mean velocity:

$$U_{rms}(y) = \begin{cases} 30.0 - 15.0 \exp\left(\frac{y^2}{0.71 \cdot 10^{-6}}\right) & -h/2 \leq y \leq h/2 \\ 0.0 & \text{otherwise} \end{cases}$$

Using 128 computing cores on the *SGI ALTIX ICE* parallel scalar calculator (JADE) at the Centre Informatique National de l'Enseignement Supérieur (CINES) in Montpellier, France, the solution could be advanced up to 340 000 iterations.

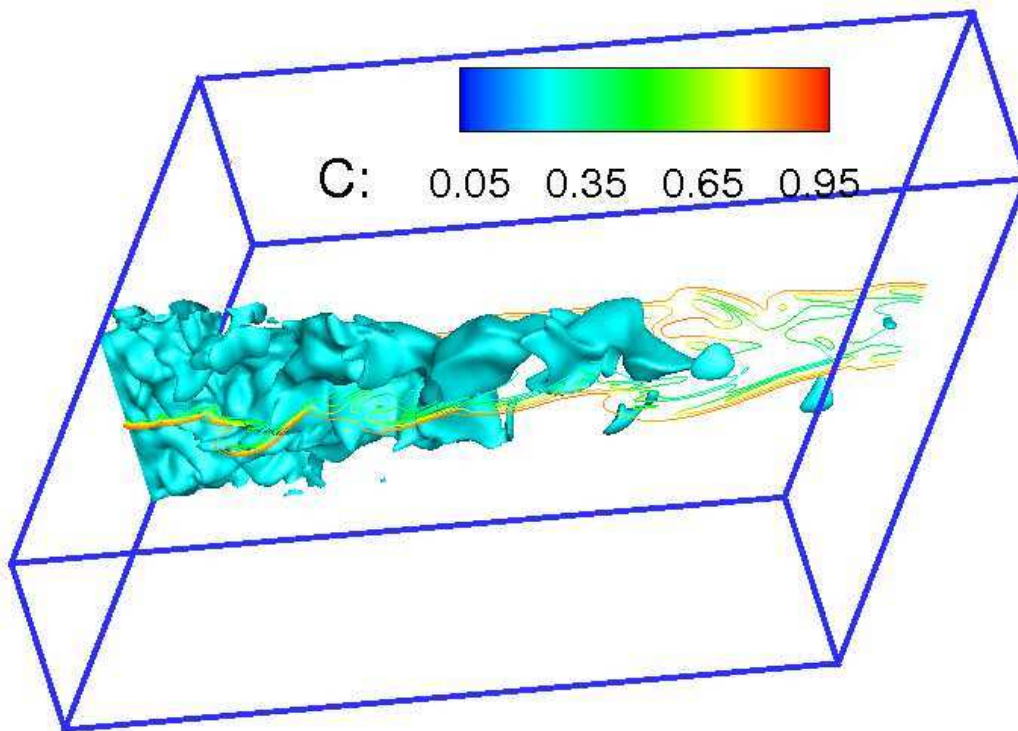


Figure 6.13: Instantaneous iso-surface of the progress variable with iso-levels of the magnitude of its mean gradient along the plane $z = 0$ at $t = 10.5$ ms

The three-dimensional turbulent flame structure is exemplified in Fig. 6.13 where the instantaneous iso-surface of the progress variable and the iso-levels of the magnitude of its mean

gradient along the plane $z = 0$ at $t = 10.5$ ms are shown. The flame is initially planar at the inlet. Wrinkled structures develop further downstream by interaction with the spatially developing turbulent field. With increasing turbulent straining downstream, flame pinch off events appear.

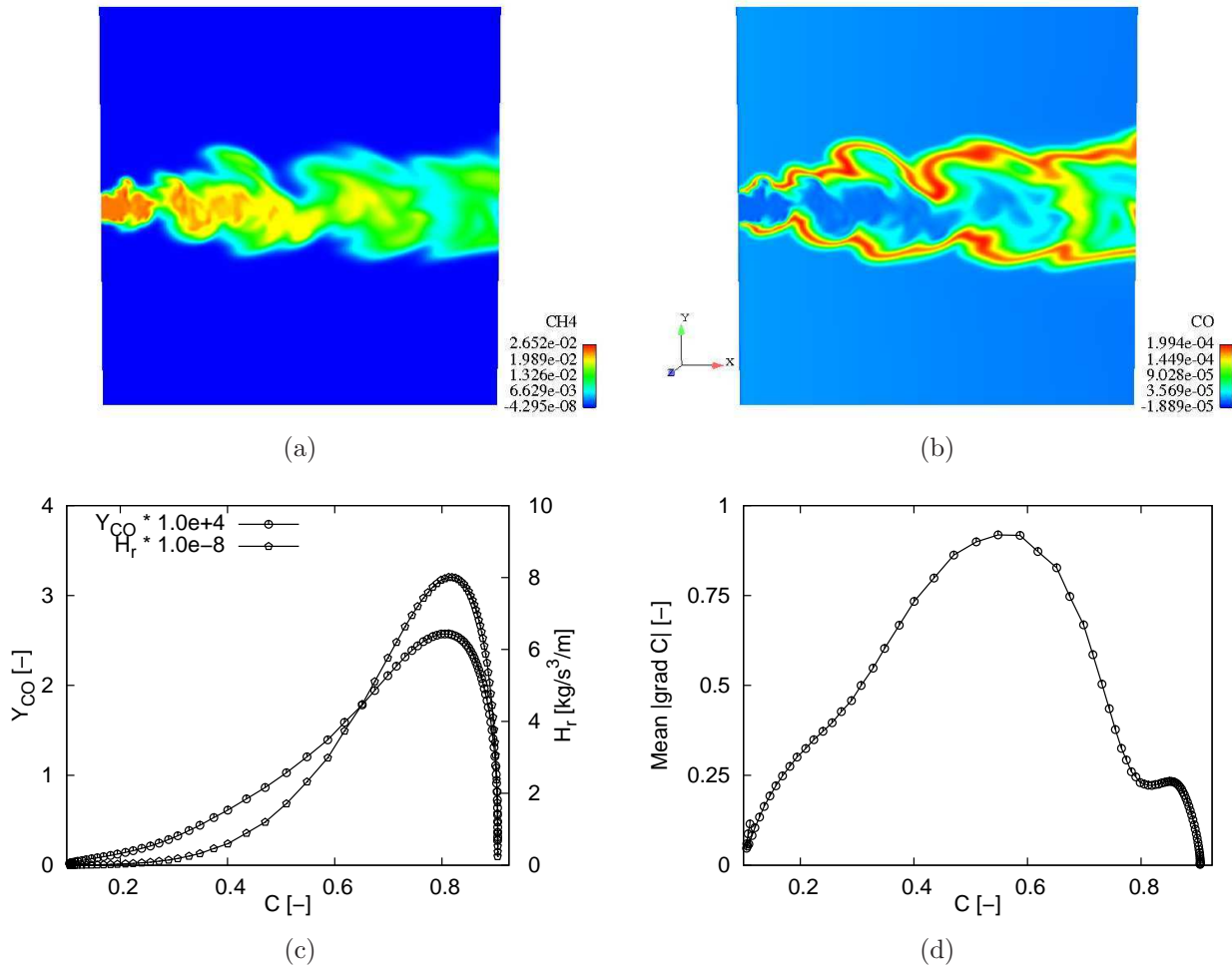


Figure 6.14: Two dimensional slice through $z = 0$ showing instantaneous fields of (a) CH₄ mass fraction, (b) CO mass fraction and profiles of (c) CO mass fraction and heat release and (d) magnitude of the mean gradient of the progress variable along the axis ($x = 0$) at $t = 10.5$ ms.

Two dimensional slices at $z = 0$ have been extracted and are shown in Fig. 6.14, where the instantaneous fields of the mass fractions of CH₄ and CO are displayed at $t = 10.5$ ms. On the same figure are profiles of CO mass fraction, heat release and magnitude of mean progress variable gradient in the progress variable space

6.3.4 Summary

Mindful of the type of problems usually handled by *AVBP* (LES-like grids with SGS and/or thickened flame models), the above configuration was non-trivial.

The code's capabilities were stretched to its limits through several modifications (hard coded variable arrays) in order to accommodate a large mesh of up to 52 million grid points on a relatively small number of computing cores. In addition to the numerous test cases, the overall computations were extremely data intensive and very expensive in terms of computing times. It should be pointed out that the above results are not yet statistically converged.

To the best of my knowledge, it was the first time that the boundary condition combination outlined above were being applied in *AVBP*. The computations could not therefore go beyond

the stated number of iterations, since numerical instabilities appeared at the y boundaries.

As of now, Direct Numerical Simulations of real applications (complex geometries, large dimensions) remain extremely challenging.

Conclusions and outlook

The tremendous progress in numerical techniques as well as computational power witnessed over the recent decades now allow quantitative investigations of turbulent reacting flows including detailed physicochemical models. The increasing importance of Computational Fluid Dynamics in the design and construction of efficient, low emission burners requires that turbulent combustion computations must be realized under realistic conditions. Combustion DNS in a highly turbulent medium is particularly important for this purpose. The most powerful existing super-computers must be employed in an efficient manner to carry out corresponding DNS simulations.

In order to access high values of Re_t on fine-grain parallel systems, a turbulence generator based on random noise diffusion was derived, implemented and parallelized on massively parallel computers. With this simple, flexible and accurate approach, the restriction on problem size imposed by the previously implemented generator based on inverse FFT has been removed, paving the way for simulations of larger domains at considerably higher turbulent Reynolds numbers. The second major issue that needed attention towards fine-grain parallelism was that of efficient, fully parallel data I/O. With this implemented I/O strategy, the code performance was boosted by a noticeable speedup in computing time and parallel performance.

After solving these algorithmic issues, a wide range of parametric studies for turbulent flames mostly in the TRZ regime have been considered in this thesis for lean to stoichiometric conditions. Very high turbulent Reynolds numbers Re_t up to 4 500 have been explored by accessing high-end parallel computers at European level using the massively parallel, finite-difference, three-dimensional DNS flame solver *parcomb*, which solves the compressible reactive Navier-Stokes equations for multicomponent flows with accurate physicochemical models. A detailed post processing has been performed using the dedicated Matlab-based library *AnaFlame*. Structural modifications such as flame-flame interactions and pinch off have been observed, becoming prominent for realistic turbulence conditions for which Re_t exceeds considerably 1 000. The statistical significance of the results has been increased by repeating the simulations and using ensemble averaging.

Using the flame index, non-premixed flame data has been analyzed and the coexistence of different burning regimes has been quantified. Two thirds of the heat release are shown to take place in the diffusion mode, as expected for this globally non-premixed configuration. Typical correlation values above 0.9 are obtained for a β -function PDF reconstruction of Z for 90% of the cases. The γ -function leads to a much poorer approximation.

The controversial volume viscosity transport term for both premixed and diffusion flames has been investigated and its impact on the resulting flame structure and properties quantified. It has been demonstrated that no differences are found in laminar computations, confirming theoretical findings for low Mach number conditions for all fuels. On the other hand, the chaotic nature of turbulence amplifies small instantaneous differences with time, eventually leading to

completely different evolutions for the turbulent flames burning hydrogen-containing fuels. This effect is clearly visible locally, changing for instance the local flame structure. But it is also observed with a considerable magnitude on all global flame properties and increases with time. These observations are more intense for the pure hydrogen flames compared to when using syngas as a fuel. For these hydrogen-containing fuels, the influence of volume viscosity appears to be independent of the turbulent Reynolds number. The inclusion of volume viscosity effects in multi-component multi-dimensional turbulent premixed flame computations is therefore recommended for all hydrogen-containing fuels. In direct contrast to the above results, methane flames show no convincing modifications in the presence of volume viscosity at all Reynolds numbers considered in the study. To save computing resources, the inclusion of volume viscosity effects in detailed DNS turbulent flame computations burning methane, and probably higher hydrocarbons as well is therefore discouraged, as long as low Mach numbers are considered.

In a separate parametric study, the response of turbulent velocity described by the fuel consumption rate was investigated for premixed methane–air combustion. Five different mixture equivalence ratios Φ have been considered. Quenching effects appear earlier with the leaner mixtures, as expected. Qualitative theoretical and experimental findings regarding the correlation between rms velocity u' and turbulent flame speed have been numerically confirmed. Intense turbulence stirring usually results in flames that burn and/or propagate faster and release higher amounts of energy in the form of heat. However, the obtained results demonstrate that optimum conditions exist, depending on mixture stoichiometry, above which the resulting flames will be weakened by a further increase in turbulent stirring.

This study demonstrates also the importance of repeating DNS realizations in order to obtain statistically significant data. Single realizations might lead to spurious discrepancies, rapidly smoothed out when averaging over several results. Moreover, all the observations point to the fact that analyzing DNS results at high Reynolds numbers is essential to obtain realistic information for modeling purposes.

There is still much to be done regarding combustion DNS. Concerning numerical models, there has been recent theoretical developments suggesting an extension/modification of the Navier-Stokes equations. First studies concerning such extensions have been carried out in our group [176]. The results obtained are still preliminary, since multi-dimensional cases were not tested. Nevertheless, first one-dimensional results show significant differences, for example, 10% in the peak values of temperature for non-premixed hydrogen flames. We will extend the implementation to the two remaining coordinate directions and then use detailed turbulent combustion DNS (like those presented in this report) to check and confirm if these extensions lead to realistic results and how large the resulting modifications are.

On the combustion side, the verification of the influence of diffusion models and of reaction schemes for computations at such high turbulence intensities could be a possible objective for further research work. A more detailed analysis and exploration of the generated DNS data, for instance to check any deviation from flamelet and presumed PDF models is also important. Further DNS simulations at even higher Reynolds numbers would be essential, highlighting the need for Peta-scale and exascale computing capabilities.

Talking about ultrascale computing, the future equally reserves a lot of surprises as HPC is pushing the frontiers of science and technology. Computing power has increased by a factor of 1 000 since 1997 and the top 2 machines today are each more powerful than the combined power of the top 500 machines in 2004 [177]. As demonstrated in this report, we can now access length scales, time scales, and integral turbulent Reynolds numbers relevant to support further breakthrough in energy science and such a trend will continue, since we expect another factor of 1 000 in computational capability before 2020 [178].

Extreme scale computing is key to accelerating progress on some of our most challenging science and technology problems. The challenges to exploiting such ultrascale computing are

eminent: (1) potential applications will be required to scale to millions of (possibly heterogeneous) cores; (2) sophisticated mathematical algorithms will be essential to support the exascale impact (another factor of 1 000) and (3) massive collaboration across communities (e.g. between combustion and computer scientist or visualization experts) will be an absolute necessity to tackle software and application challenges. Power consumption concerns, reliability and budget constraints will definitely go hand-in-hand with such billion computing core machines.

One more HPC's fundamental road block towards increased performance at extreme scale is data formatting and I/O issues [179]. The access speed of disk drives is several orders of magnitude smaller than that of CPU-to-memory accesses. The writing of results to disk files is already a major bottleneck and this situation will only worsen with the coming of the exascale era [180]. There is therefore a growing need to bypass I/O to disk in favor of in-situ visualization, whereby an application code is instrumented with a set of visualization representations selected on-the-fly at a given time-step, instructing the visualization server to save images and processed results to disk while the simulation iterates. We are thus replacing a possible enormous 3D transient archiving of results of raw data, with a sequence of well defined visualization images and final data. With apparent need in view, visualization libraries in open-source form with support of in-situ visualization capabilities are already available [181, 182].

APPENDIX

A

Reaction mechanisms

The chemical oxidation mechanism of hydrogen (H_2), syngas (CO/H_2) and methane (CH_4) in air used in the computations presented in Chapter 5 are hereby listed. The rate coefficients are in the form $k_f = \mathcal{A}T^\beta \exp(-E_a/RT)$. Except otherwise stated, the units are moles, cubic centimeters, seconds, degrees Kelvins and calories/mole. All other third body efficiencies are unity. Instructions regarding the generation of the corresponding physical chemistry input file is presented elsewhere [112].

A.1 Hydrogen oxidation mechanism

The oxidation of hydrogen in air is described by two different reaction mechanisms listed in table A.1 [40] and A.2 [41].

Table A.1: Hydrogen-Oxygen reaction mechanism [40]

No.	Reaction	\mathcal{A}	β	E_a
R ₁	$\text{O}_2 + \text{H} \rightleftharpoons \text{OH} + \text{O}$	2.000E+14	0.0	16818.2
R ₂	$\text{H}_2 + \text{O} \rightleftharpoons \text{OH} + \text{H}$	5.060E+04	2.670	6291.87
R ₃	$\text{H}_2 + \text{OH} \rightleftharpoons \text{H}_2\text{O} + \text{H}$	1.000E+08	1.600	3301.44
R ₄	$\text{OH} + \text{OH} \rightleftharpoons \text{H}_2\text{O} + \text{O}$	1.500E+09	1.140	100.478
R ₅	$\text{H} + \text{H} + \text{M} \rightleftharpoons \text{H}_2 + \text{M}$	1.800E+18	-1.000	0
R ₆	$\text{H} + \text{OH} + \text{M} \rightleftharpoons \text{H}_2\text{O} + \text{M}$	2.200E+22	-2.000	0
R ₇	$\text{O} + \text{O} + \text{M} \rightleftharpoons \text{O}_2 + \text{M}$	2.900E+17	-1.000	0
R ₈	$\text{H} + \text{O}_2 + \text{M} \rightleftharpoons \text{HO}_2 + \text{M}$	2.300E+18	-0.800	0
R ₉	$\text{HO}_2 + \text{H} \rightleftharpoons \text{OH} + \text{OH}$	1.500E+14	0.0	1004.78
R ₁₀	$\text{HO}_2 + \text{H} \rightleftharpoons \text{H}_2 + \text{O}_2$	2.500E+13	0.0	693.78
R ₁₁	$\text{HO}_2 + \text{H} \rightleftharpoons \text{H}_2\text{O} + \text{O}$	3.000E+13	0.0	1722.49
R ₁₂	$\text{HO}_2 + \text{O} \rightleftharpoons \text{OH} + \text{O}_2$	1.800E+13	0.0	-406.699
R ₁₃	$\text{HO}_2 + \text{OH} \rightleftharpoons \text{H}_2\text{O} + \text{O}_2$	6.000E+13	0.0	0
R ₁₄	$\text{HO}_2 + \text{HO}_2 \rightarrow \text{H}_2\text{O}_2 + \text{O}_2$	2.500E+11	0.0	-1244.02
R ₁₅	$\text{OH} + \text{OH} + \text{M} \rightleftharpoons \text{H}_2\text{O}_2 + \text{M}$	3.250E+22	-2.000	0
R ₁₆	$\text{H}_2\text{O}_2 + \text{H} \rightleftharpoons \text{H}_2 + \text{HO}_2$	1.700E+12	0.0	3755.98
R ₁₇	$\text{H}_2\text{O}_2 + \text{H} \rightleftharpoons \text{H}_2\text{O} + \text{OH}$	1.000E+13	0.0	3588.52
R ₁₈	$\text{H}_2\text{O}_2 + \text{O} \rightleftharpoons \text{OH} + \text{HO}_2$	2.800E+13	0.0	6411.48
R ₁₉	$\text{H}_2\text{O}_2 + \text{OH} \rightleftharpoons \text{H}_2\text{O} + \text{HO}_2$	5.400E+12	0.0	1004.78

Third body efficiency: $\text{H}_2 = 1.0$, $\text{O}_2 = 0.35$, $\text{H}_2\text{O} = 6.5$, $\text{N}_2 = 0.5$

Table A.2: Hydrogen-Oxygen reaction mechanism [41], with E_a in kJ/mol

No.	Reaction	\mathcal{A}	β	E_a
R ₁	O ₂ + H → OH + O	2.00E+14	0.00	70.30
R ₂	OH + O → O ₂ + H	1.46E+13	0.00	2.08
R ₃	H ₂ + O → OH + H	5.06E+4	2.67	26.30
R ₄	OH + H → H ₂ + O	2.24E+4	2.67	18.40
R ₅	H ₂ + OH → H ₂ O + H	1.00E+8	1.60	13.80
R ₆	H ₂ O + H → H ₂ + OH	4.45E+8	1.60	77.13
R ₇	OH + OH → H ₂ O + O	1.50E+9	1.14	0.42
R ₈	H ₂ O + O → OH + OH	1.51E+10	1.14	71.64
R ₉	H + H + M → H ₂ + M	1.80E+18	-1.00	0.00
R ₁₀	H ₂ + M → H + H + M	6.99E+18	-1.00	436.08
R ₁₁	H + OH + M → H ₂ O + M	2.20E+22	-2.00	0.00
R ₁₂	H ₂ O + M → H + OH + M	3.80E+23	-2.00	499.41
R ₁₃	O + O + M → O ₂ + M	2.90E+17	-1.00	0.00
R ₁₄	O ₂ + M → O + O + M	6.81E+18	-1.00	496.41
R ₁₅	H + O ₂ + M → HO ₂ + M	2.30E+18	-0.80	0.00
R ₁₆	HO ₂ + M → H + O ₂ + M	3.26E+18	-0.80	195.88
R ₁₇	HO ₂ + H → OH + OH	1.50E+14	0.00	4.20
R ₁₈	OH + OH → HO ₂ + H	1.33E+13	0.00	168.30
R ₁₉	HO ₂ + H → H ₂ + O ₂	2.50E+13	0.00	2.90
R ₂₀	H ₂ + O ₂ → HO ₂ + H	6.84E+13	0.00	243.10
R ₂₁	HO ₂ + H → H ₂ O + O	3.00E+13	0.00	7.20
R ₂₂	H ₂ O + O → HO ₂ + H	2.67E+13	0.00	242.52
R ₂₃	HO ₂ + O → OH + O ₂	1.80E+13	0.00	-1.70
R ₂₄	OH + O ₂ → HO ₂ + O	2.18E+13	0.00	230.61
R ₂₅	HO ₂ + OH → H ₂ O + O ₂	6.00E+13	0.00	0.00
R ₂₆	H ₂ O + O ₂ → HO ₂ + OH	7.31E+14	0.00	303.53
R ₂₇	HO ₂ + HO ₂ → H ₂ O ₂ + O ₂	2.50E+11	0.00	-5.20
R ₂₈	OH + OH + M → H ₂ O ₂ + M	3.25E+22	-2.00	0.00
R ₂₉	H ₂ O ₂ + M → OH + OH + M	2.10E+24	-2.00	206.80
R ₃₀	H ₂ O ₂ + H → H ₂ + HO ₂	1.70E+12	0.00	15.70
R ₃₁	H ₂ + HO ₂ → H ₂ O ₂ + H	1.15E+12	0.00	80.88
R ₃₂	H ₂ O + H → H ₂ O + OH	1.00E+13	0.00	15.00
R ₃₃	H ₂ O + OH → H ₂ O ₂ + H	2.67E+12	0.00	307.51
R ₃₄	H ₂ O ₂ + O → OH + HO ₂	2.80E+13	0.00	26.80
R ₃₅	OH + HO ₂ → H ₂ O ₂ + O	8.40E+12	0.00	84.09
R ₃₆	H ₂ O ₂ + OH → H ₂ O + HO ₂	5.40E+12	0.00	4.20
R ₃₇	H ₂ O + HO ₂ → H ₂ O ₂ + OH	1.63E+13	0.00	132.71

Third body efficiency: H₂ = 1.00; O₂ = 0.35; H₂O = 6.50; N₂ = 0.50

A.2 Syngas oxidation mechanism

The oxidation of syngas (CO-H₂) in air is described by the reaction mechanism from [42] listed in table A.3.

Table A.3: Syngas oxidation mechanism [42]

No.	Reaction	\mathcal{A}	β	E_a
R _{1f}	O ₂ + H → OH + O	2.000E+14	0.0	16820.
R _{1b}	OH + O → O ₂ + H	1.470E+13	0.0	502.
R _{2f}	H ₂ + O → OH + H	5.060E+04	2.67	6290.
R _{2b}	OH + H → H ₂ + O	2.240E+04	2.67	4402.
R _{3f}	H ₂ + OH → H ₂ O + H	1.000E+08	1.6	3301.

Continued on Next Page...

Table A.3 – Continued

No.	Reaction	\mathcal{A}	β	E_a
R _{3b}	H ₂ O + H \rightarrow H ₂ + OH	4.460E+08	1.6	18445.
R _{4f}	OH + OH \rightarrow H ₂ O + O	1.500E+09	1.14	96.
R _{4b}	H ₂ O + O \rightarrow OH + OH	1.510E+10	1.14	17129.
R _{5f}	H + H + M \rightarrow H ₂ + M	1.800E+18	-1.0	0.
R _{5b}	H ₂ + M \rightarrow H + H + M	6.980E+18	-1.0	104306.
R _{6f}	H + OH + M \rightarrow H ₂ O + M	2.200E+22	-2.0	0.
R _{6b}	H ₂ O + M \rightarrow H + OH + M	3.800E+23	-2.0	119475.
R _{7f}	O + O + M \rightarrow O ₂ + M	2.900E+17	-1.0	0.
R _{7b}	O ₂ + M \rightarrow O + O + M	6.780E+18	-1.0	118756.
R _{8f}	H + O ₂ + M \rightarrow HO ₂ + M	2.300E+18	-0.8	0.
R _{8b}	HO ₂ + M \rightarrow H + O ₂ + M	2.660E+18	-0.8	49330.
R _{9f}	HO ₂ + H \rightarrow OH + OH	1.500E+14	0.0	1005.
R _{9b}	OH + OH \rightarrow HO ₂ + H	1.630E+13	0.0	37800.
R _{10f}	HO ₂ + H \rightarrow H ₂ + O ₂	2.500E+13	0.0	694.
R _{10b}	H ₂ + O ₂ \rightarrow HO ₂ + H	8.390E+13	0.0	55694.
R _{11f}	HO ₂ + H \rightarrow H ₂ O + O	3.000E+13	0.0	1722.
R _{11b}	H ₂ O + O \rightarrow HO ₂ + H	3.290E+13	0.0	55550.
R _{12f}	HO ₂ + O \rightarrow OH + O ₂	1.800E+13	0.0	-407.
R _{12b}	OH + O ₂ \rightarrow HO ₂ + O	2.670E+13	0.0	52703.
R _{13f}	HO ₂ + OH \rightarrow H ₂ O + O ₂	6.000E+13	0.0	0.
R _{13b}	H ₂ O + O ₂ \rightarrow HO ₂ + OH	8.970E+14	0.0	70144.
R _{14f}	HO ₂ + HO ₂ \rightarrow H ₂ O ₂ + O ₂	2.500E+11	0.0	-1244.
R _{14b}	OH + OH + M \rightarrow H ₂ O ₂ + M	3.250E+22	-2.0	0.
R _{15f}	H ₂ O ₂ + M \rightarrow OH + OH + M	2.110E+24	-2.0	49474.
R _{15b}	H ₂ O ₂ + H \rightarrow H ₂ + HO ₂	1.700E+12	0.0	3756.
R _{16f}	H ₂ + HO ₂ \rightarrow H ₂ O ₂ + H	9.350E+11	0.0	21818.
R _{16b}	H ₂ O ₂ + H \rightarrow H ₂ O + OH	1.000E+13	0.0	3589.
R _{17f}	H ₂ O + OH \rightarrow H ₂ O ₂ + H	2.660E+12	0.0	73589.
R _{17b}	H ₂ O ₂ + O \rightarrow OH + HO ₂	2.800E+13	0.0	6411.
R _{18f}	OH + HO ₂ \rightarrow H ₂ O ₂ + O	6.800E+12	0.0	22584.
R _{18b}	H ₂ O ₂ + OH \rightarrow H ₂ O + HO ₂	5.400E+12	0.0	1005.
R _{19f}	H ₂ O + HO ₂ \rightarrow H ₂ O ₂ + OH	1.320E+13	0.0	34211.
R _{19b}	CO + OH \rightarrow CO ₂ + H	4.400E+06	1.5	-742.
R _{20f}	CO ₂ + H \rightarrow CO + OH	6.120E+08	1.5	22512.
R _{20b}	CO + HO ₂ \rightarrow CO ₂ + OH	1.500E+14	0.0	23612.
R _{21f}	CO ₂ + OH \rightarrow CO + HO ₂	2.270E+15	0.0	83660.
R _{21b}	CO + O + M \rightarrow CO ₂ + M	7.100E+13	0.0	-4545.
R _{22f}	CO ₂ + M \rightarrow CO + O + M	1.690E+16	0.0	121148.
R _{22b}	CO + O ₂ \rightarrow CO ₂ + O	2.500E+12	0.0	47847.
R _{23f}	CO ₂ + O \rightarrow CO + O ₂	2.550E+13	0.0	54785.
R _{23b}	HCO + M \rightarrow CO + H + M	7.100E+14	0.0	16818.
R _{24f}	CO + H + M \rightarrow HCO + M	1.070E+15	0.0	2057.
R _{24b}	HCO + H \rightarrow CO + H ₂	2.000E+14	0.0	0.
R _{25f}	CO + H ₂ \rightarrow HCO + H	1.170E+15	0.0	89569.
R _{25b}	HCO + O \rightarrow CO + OH	3.000E+13	0.0	0.
R _{26f}	CO + OH \rightarrow HCO + O	7.720E+13	0.0	87679.
R _{26b}	HCO + O \rightarrow CO ₂ + H	3.000E+13	0.0	0.
R _{27f}	CO ₂ + H \rightarrow HCO + O	1.070E+16	0.0	110933.
R _{27b}	HCO + OH \rightarrow CO + H ₂ O	1.000E+14	0.0	0.
R _{28f}	CO + H ₂ O \rightarrow HCO + OH	2.600E+15	0.0	104713.
R _{28b}	HCO + O ₂ \rightarrow CO + HO ₂	3.000E+12	0.0	0.
R _{29f}	CO + HO ₂ \rightarrow HCO + O ₂	5.210E+12	0.0	34569.
R _{29b}	CH ₂ O + M \rightarrow HCO + H + M	1.400E+17	0.0	76555.
R _{30f}	HCO + H + M \rightarrow CH ₂ O + M	2.620E+15	0.0	-13589.
R _{30b}	CH ₂ O + H \rightarrow HCO + H ₂	2.500E+13	0.0	3995.
R _{31f}	HCO + H ₂ \rightarrow CH ₂ O + H	1.820E+12	0.0	18182.
R _{31b}	CH ₂ O + O \rightarrow HCO + OH	3.500E+13	0.0	3493.
R _{32f}	HCO + OH \rightarrow CH ₂ O + O	1.120E+12	0.0	15789.
R _{32b}	CH ₂ O + OH \rightarrow HCO + H ₂ O	3.000E+13	0.0	1196.
R _{33f}	HCO + H ₂ O \rightarrow CH ₂ O + OH	9.710E+12	0.0	30526.
R _{33b}	CH ₂ O + HO ₂ \rightarrow HCO + H ₂ O ₂	1.000E+12	0.0	8014.
R ₃₄	HCO + H ₂ O ₂ \rightarrow CH ₂ O + HO ₂	1.320E+11	0.0	4139.

Third body efficiency: H₂ = 1.0, O₂ = 0.35, N₂ = 0.5, CO = 1.5
CO₂ = 1.5, H₂O = 6.5, O = 0, H = 0 and OH = 0

A.3 Methane oxidation mechanism

The oxidation of methane in air is described by the skeletal combustion reaction mechanism from [43, 153] listed in Table A.4.

Table A.4: Skeletal methane-air reaction mechanism [43, 153]

No.	Reaction	\mathcal{A}	β	E_a
R _{1f}	H+O ₂ ⇌ OH+O	2.000E+14	0.0	16800.0
R _{1b}	OH+O ⇌ H+O ₂	1.575E+13	0.0	690.0
R _{2f}	O+H ₂ ⇌ OH+H	1.800E+10	1.0	8826.0
R _{2b}	OH+H ⇌ O+H ₂	8.000E+09	1.0	6760.0
R _{3f}	H ₂ +OH ⇌ H ₂ O+H	1.170E+09	1.3	3626.0
R _{3b}	H ₂ O+H ⇌ H ₂ +OH	5.090E+09	1.3	18588.0
R _{4f}	OH+OH ⇌ O+H ₂ O	6.000E+08	1.3	0.0
R _{4b}	O+H ₂ O ⇌ OH+OH	5.900E+09	1.3	17029.0
R ₅	H+O ₂ +M → HO ₂ +M ¹	2.300E+18	-0.8	0.0
R ₆	H+HO ₂ → OH+OH	1.500E+14	0.0	1004.0
R ₇	H+HO ₂ → H ₂ +O ₂	2.500E+13	0.0	0700.0
R ₈	OH+HO ₂ → H ₂ O+O ₂	2.000E+13	0.0	1000.0
R _{9f}	CO+OH ⇌ CO ₂ +H	1.510E+07	1.3	-0758.0
R _{9b}	CO ₂ +H ⇌ CO+OH	1.570E+09	1.3	22337.0
R _{10f}	CH ₄ +(M) ⇌ CH ₃ +H+(M) ²	2.300E+14	-7.0	104000.0
R _{10b}	CH ₃ +H+(M) ⇌ CH ₄ +(M) ²	5.200E+12	-7.0	-1310.0
R _{11f}	CH ₄ +H ⇌ CH ₃ +H ₂	2.200E+04	3.0	8750.0
R _{11b}	CH ₃ +H ₂ ⇌ CH ₄ +H	9.570E+02	3.0	8750.0
R _{12f}	CH ₄ +OH ⇌ CH ₃ +H ₂ O	1.600E+06	2.1	2460.0
R _{12b}	CH ₃ +H ₂ O ⇌ CH ₄ +OH	3.020E+05	2.1	17422.0
R ₁₃	CH ₃ +O → CH ₂ O+H	6.800E+13	0.0	0.0
R ₁₄	CH ₂ O+H → HCO+H ₂	2.500E+13	0.0	3991.0
R ₁₅	CH ₂ O+OH → HCO+H ₂ O	3.000E+13	0.0	1195.0
R ₁₆	HCO+H → CO+H ₂	4.000E+13	0.0	0.0
R ₁₇	HCO+M → CO+H+M	1.600E+14	0.0	14700.0
R ₁₈	CH ₃ +O ₂ → CH ₃ O+O	7.000E+12	0.0	25652.0
R ₁₉	CH ₃ O+H → CH ₂ O+H ₂	2.000E+13	0.0	0.0
R ₂₀	CH ₃ O+M → CH ₂ O+H+M	2.400E+13	0.0	28812.0
R ₂₁	HO ₂ +HO ₂ → H ₂ O ₂ +O ₂	2.000E+12	0.0	0.0
R _{22f}	H ₂ O ₂ +M ⇌ OH+OH+M	1.300E+17	0.0	45500.0
R _{22b}	OH+OH+M ⇌ H ₂ O ₂ +M	9.860E+14	0.0	-5070.0
R _{23f}	H ₂ O ₂ +OH ⇌ H ₂ O+HO ₂	1.000E+13	0.0	1800.0
R _{23b}	H ₂ O+HO ₂ ⇌ H ₂ O ₂ +OH	2.860E+13	0.0	32790.0
R ₂₄	OH+H+M → H ₂ O+M ¹	2.200E+22	-2.0	0.0
R ₂₅	H+H+M → H ₂ +M ¹	1.800E+18	-1.0	0.0

Third body efficiency:

¹ CH₄ = 6.5, H₂O = 6.5, CO₂ = 1.5, H₂ = 1.0, CO = 0.75, O₂ = 0.4,

O₂ = 0.4, N₂ = 0.4, All other species = 1.0

² Lindemann form, $k = k_\infty / (1 + \alpha/[M])$ where $\alpha = 0.0063 \exp(-18000/RT)$

REFERENCES

- [1] D. Veynante. Large eddy simulation of turbulent combustion. In *Conference on Turbulence and Interactions TI2006*, Porquerolles, France, 2006. **1, 45**
- [2] S. Pope. *Turbulent Flows*. Cambridge Univ. Press, 2005. **1, 46, 66**
- [3] D. Veynante and T. Poinso. Reynolds average and Large Eddy Simulation modeling for turbulent combustion. In O. Métais and J. Ferziger, editors, *New tools in turbulence modeling*, Les Editions de Physique, pages 105–140. Springer, Berlin, 1997. **46**
- [4] H. Pitsch. Large-eddy simulations of turbulent combustion. *Annu. Rev. Fluid Mech.*, 38:453–482, 2006. **1, 46**
- [5] T. Poinso and D. Veynante. *Theoretical and Numerical Combustion*. R. T. Edwards, 2nd edition, 2005. **1, 8, 9, 41, 43, 45, 46, 47, 79, 115, 117**
- [6] N. Peters. *Turbulent combustion*. Cambridge University Press, 2nd edition, 2000. **43, 44, 82, 83, 93, 94, 95, 96, 99**
- [7] D. Veynante and L. Vervisch. Turbulent combustion modeling. *Prog. Energy Combust. Sci.*, 28(3):193–266, 2002. **44, 46, 47, 75, 79**
- [8] J. Warnatz, U. Maas, and R. W. Dibble. *Combustion: Physical and chemical fundamentals, modeling and simulations, experiments, pollutant formation*. Springer, 3rd edition, 2001. **10, 14, 15, 115**
- [9] R. Fox. *Computational models for turbulent reacting flows*. Cambridge University Press, 2003. **1**
- [10] O. Gicquel, N. Darabiha, and D. Thévenin. Laminar premixed hydrogen/air counterflow flame simulations using flame prolongation of ILDM with differential diffusion. *Proc. Combust. Inst.*, 28:1901–1908, 2000. **3, 17, 19, 20, 21, 22, 23, 25, 32**
- [11] J. de Charentenay, D. Thévenin, and B. Zamuner. Comparison of direct numerical simulations of turbulent flames using compressible or low-mach number formulation. *Int. J. Numer. Meth. Fluids*, 39:497–515, 2002. **3, 40, 47, 55, 56, 97**
- [12] H. Shalaby and D. Thévenin. Statistically significant results for the propagation of a turbulent flame kernel using direct numerical simulation. *Flow Turb. Comb.*, 84(3):357–367, 2010. **3, 77, 90, 97, 104**
- [13] F. Williams. *Combustion Theory*. Addison-Wesley, 2nd edition, 1985. **7, 14**
- [14] K. Kuo. *Principles of Combustion*. John Wiley & Sons, Inc., 2nd edition, 2005.
- [15] V. Giovangigli. *Multicomponent flow modeling*. Birkhäuser, Boston, 1999. **7, 11, 12, 13, 14, 39**
- [16] R. D. Stull and H. Prophet. Janaf thermodynamical tables, 2nd edition. Technical Report NSRDS-NBS 37, US National Bureau of Standard, 1971. **9**
- [17] A. Burcat. Third millenium ideal gas and condensed phase thermodynamical database for combustion. Technical Report (TAE) Report #867, Technion Aerospace Engineering, 2001. URL <ftp://ftp.technion.ac.il/pub/supported/aeldd/thermodynamics>. **9**

- [18] A. Ern and V. Giovangigli. *Multicomponent Transport Algorithms*. Lecture Notes in Physics. New series Monographs m24, 1994. 9, 12, 13, 14
- [19] A. Ern and V. Giovangigli. Thermal conduction and thermal diffusion in dilute polyatomic gas mixtures. *Physica A*, 214: 526–546, 1995. 9
- [20] A. Ern and V. Giovangigli. Thermal diffusion effects in hydrogen-air and methane-air flames. *Combust. Theory Modeling*, 2:345–372, 1998. 9
- [21] C. R. Wilke. A viscosity equation for gas mixture. *J. Chem. Phys.*, 18:517, 1950. 9
- [22] R. B. Bird, W. E. Stewart, and E. N. Lightfoot. *Transport phenomena*. J. Wiley & Sons, 1960. 9, 12
- [23] G. Billet, V. Giovangigli, and G. de Gasowski. Impact of volume viscosity on a shock-hydrogen-bubble interaction. *Combust. Theory Modeling*, 12(2):221–248, 2008. 10, 11, 12, 84, 86, 106, 120
- [24] G. Prangma, A. Alberga, and J. Beenakker. Ultrasonic determination of the volume viscosity of N₂, CO, CH₄ and CD₄ between 77 and 300 K. *Physica*, 64:278–288, 1973. 10, 11
- [25] P.W. Hermans, L.F.J. Hermans, and J.J.M. Beenakker. A survey of experimental data related to the non-spherical interaction for the hydrogen isotopes and their mixture with noble gases. *Physica A*, 122:173–211, 1983.
- [26] A. Ern and V. Giovangigli. Volume viscosity of dilute polyatomic gas mixtures. *European J. Mech., B/Fluids*, 14:653–669, 1995. 10, 12, 13
- [27] G. Emanuel. Bulk viscosity of a dilute polyatomic gas. *Phys. Fluids*, 2:2252–2254, 1990. 10
- [28] G. Fru, G. Janiga, and D. Thévenin. Direct numerical simulation of turbulent methane flames with and without volume viscosity. In *8th Euromech Fluid Mechanics Conference (EFMC-8)*, pages MS2–9, Bad Reichenhall, Germany, 2010. 10, 71, 99, 117
- [29] R.E. Graves and B. Argrow. Bulk viscosity: past to present. *J. Thermophys and Heat Transf.*, 13(3):337–342, 1999. 11
- [30] A. Ern and V. Giovangigli. Impact of detailed multicomponent transport on planar and counterflow hydrogen/air and methane/air flames. *Combust. Sci. Tech.*, 149(1-6):157–181, 1999. 11
- [31] R. Hilbert, F. Tap, H. El-Rabii, and D. Thévenin. Impact of detailed chemistry and transport models on turbulent combustion simulations. *Prog. Energy Combust. Sci.*, 30:165–193, 2004. 11, 12, 13, 19, 47, 48, 82
- [32] A. Ern and V. Giovangigli. Optimized transport algorithms for flame codes. *Combust. Sci. Tech.*, 118(4-6):387–395, 1996. 11, 13
- [33] S. Chapman and T.G. Cowling. *The Mathematical Theory of Non-Uniform Gases*. Cambridge Univ. Press, 1970. 12
- [34] A. Ern and V. Giovangigli. *eglib* server and user’s manual, 2009. URL <http://www.cmap.polytechnique.fr/www/eglib>. 12
- [35] J. Hirschfelder, C. Curtiss, and R. Bird. *Molecular theory of gases and liquids*. New York: Wiley, 1954. 12, 13
- [36] D. E. Rosner. *Transport Processes in Chemically reacting Flow Systems*. New York: Dover, 2000. 13
- [37] K. Jenkins and R. Cant. Curvature effects on flame kernels in a turbulent environment. *Proc. Combust. Inst.*, 29:2023–2029, 2002. 15, 47, 98
- [38] K. Deshmukh, D. Haworth, and M. Modest. Direct Numerical Simulation of turbulence-radiation interactions in homogeneous nonpremixed combustion systems. *Proc. Combust. Inst.*, 31:1641–1648, 2007. 15, 47

- [39] R. Kee, J. Warnatz, and J. Miller. A fortran computer code package for the evaluation of gas-phase viscosities, conductivities and diffusion coefficients. Technical Report SAND83-8209, Sandia National Lab., 1983. [16](#), [22](#), [49](#)
- [40] R. Yetter, F. Dryer, and H.J. Rabitz. A comprehensive reaction mechanism for carbon monoxide/hydrogen/oxygen kinetics. *Combust. Sci. Tech.*, 79:91–128, 1991. [16](#), [49](#), [76](#), [77](#), [149](#)
- [41] U. Maas and J. Warnatz. Ignition processes in carbon-monoxide-hydrogen-oxygen mixtures. *Proc. Combust. Inst.*, 22:1695–1704, 1988. [16](#), [149](#), [150](#)
- [42] U. Maas and S. Pope. Simplifying chemical kinetics: Intrinsic low-dimensional manifolds in composition space. *Combust. Flame*, 88:239–264, 1992. [16](#), [17](#), [20](#), [49](#), [77](#), [150](#)
- [43] M. D. Smooke and V. Giovangigli. Formulation of the premixed and non-premixed test problems. In M. D. Smooke, editor, *Reduced Kinetic mechanism and Asymptotic Approximations for Methane-Air Flames*, volume 384 of *Lecture Notes in Physics*, pages 1–47. Springer-Verlag, 1991. [16](#), [49](#), [99](#), [152](#)
- [44] S. Pope. Computationally efficient implementation of combustion chemistry using in-situ adaptive tabulation. *Combust. Theory Modeling*, 1:41–63, 1997. [17](#), [20](#)
- [45] J. van Oijen, F. Lammers, and L. de Goey. Modelling of complex premixed burner systems by using flamelet generated manifolds. *Combust. Flame*, 127:2124–2134, 2001. [17](#)
- [46] E. Hawkes, R. Sankaran, J.C. Sutherland, and J.H. Chen. Direct numerical simulation of turbulent combustion: fundamental insight towards predictive models. *J. Phys. Conf. Series*, 16:65–79, 2005. [19](#), [47](#)
- [47] E. Hawkes, R. Sankaran, J.C. Sutherland, and J.H. Chen. Scalar mixing in direct numerical simulations of temporally-evolving plane jet flames with detailed CO/H₂ kinetics. *Proc. Combust. Inst.*, 31:1633–1640, 2007. [19](#)
- [48] J. Bell, M. Day, J. Grcar, M. Lijewski, J. Driscoll, and S. Filatyev. Numerical simulation of a laboratory-scale turbulent slot flame. *Proc. Combust. Inst.*, 31:1299–1307, 2007. [19](#), [47](#)
- [49] D. Thévenin, E. van Kalmthout, and S. Candel. Two-dimensional direct numerical simulations of turbulent diffusion flames using detailed chemistry. In J. Chollet, P. Voke, and L. Kleiser, editors, *Direct and Large Eddy Simulation II*, pages 343–354. Kluwer Academic Publishers, 1997. [19](#), [48](#), [60](#), [71](#)
- [50] D. Thévenin. Three-dimensional direct simulations and structure of expanding turbulent methane flames. *Proc. Combust. Inst.*, 30:629–637, 2005. [19](#), [47](#), [54](#)
- [51] S. Lam and D. Goussis. Understanding complex chemical kinetics with computational singular perturbation. *Proc. Combust. Inst.*, (22):931–341, 1988. [20](#)
- [52] O. Gicquel. *Développement d’une nouvelle méthode de réduction des schémas cinétiques: Application au méthane*. PhD thesis, École Centrale de Paris, Laboratoire EM2C, 1999. [21](#)
- [53] B. Fiorina, R. Baron, O. Gicquel, D. Thévenin, S. Carpentier, and N. Darabiha. Modelling non-adiabatic partially premixed flames using flame-prolongation of ILDM. *Combust. Theory Modeling*, 7:449–470, 2003. [21](#), [23](#), [25](#), [32](#)
- [54] G. Ribert, M. Champion, O. Gicquel, N. Darabiha, and D. Veynante. Modeling non adiabatic turbulent premixed reactive flows including tabulated chemistry. *Combust. Flame*, 141:271–280, 2005. [21](#)

- [55] P. Domingo, L. Vervisch, S. Payet, and R. Hauguel. DNS of a premixed turbulent V-flame and LES of a ducted-flame using a FSD-PDF subgrid scale closure with FPI tabulated chemistry. *Combust. Flame*, 143:566–586, 2005. 21
- [56] B. Fiorina, O. Gicquel, L. Vervisch, S. Carpentier, and N. Darabiha. Premixed turbulent combustion modelling using tabulated chemistry and PDF. *Proc. Combust. Inst.*, 30:867–874, 2005. 21
- [57] J. van Oijen and L. de Goey. Modelling of premixed counterflow flames using the flamelet generated manifold method. *Combust. Theory Modeling*, 6:463–478, 2002. 21
- [58] J. Keck and D. Gillespie. Rate-controlled partial-equilibrium method for treating reacting gas mixtures. *Combust. Flame*, 17:237–241, 1971. 21
- [59] R. Kee, J. Miller, and T. Jefferson. Chemkin, a general purpose problem-independent transportable FORTRAN chemical kinetics code package. Technical Report SAND80-8003, Sandia National Lab., 1980. 22, 49
- [60] R. Kee, J. Grcar, M. Smooke, and J. Miller. A Fortran program for modeling steady laminar one-dimensional premixed flames. Technical Report SAND85-8240, Sandia National Laboratories, 1985. 22, 140
- [61] G. Fru. FPI chemistry tabulation and Direct Numerical Simulation of turbulent flames. Technical Report TR/LSS/GF-1/08, LSS/ISUT, Univ. of Magdeburg, 2008. 22
- [62] C. Bowman, R. Hanson, W. Gardiner, V. Lissianski, M. Frenklach, M. Goldenberg, G. Smith, D. Crosley, and D. Golden. An optimized detailed chemistry reaction mechanism for methane combustion and NO formation and re-burning. Technical Report GRI-97/0020, Gas Research Institute, Chicago, IL, 1997. 22, 29, 39
- [63] P. Lindstedt. Modelling of the chemical complexities of flames. *Proc. Combust. Inst.*, 27:269–285, 1998. 22
- [64] Tecplot 360, 2010. URL <http://www.tecplot.com>. 22
- [65] J. Miller, R. Mitchell, M. Smooke, and R. Kee. Toward a comprehensive chemical kinetic mechanism for the oxidation of acetylene: Comparison of model predictions with results from flame and shock tube experiments. *Proc. Combust. Inst.*, 19:181–196, 1982. 29
- [66] N. Marinov, C. Westbrook, and W. Pitz. *Detailed and Global Chemical Kinetics Model for Hydrogen in Transport Phenomena in Combustion*, volume 1. Taylor and Francis, Washington, DC, 1996. 29
- [67] G. Ribert, O. Gicquel, N. Darabiha, and D. Veynante. Tabulation of complex chemistry based on self-similar behaviour of laminar premixed flames. *Combust. Flame*, 146:649–664, 2006. 30
- [68] D. Veynante, B. Fiorina, P. Domingo, and L. Vervisch. Using self-similar properties of turbulent premixed flames to downsize chemical tables in high-performance numerical simulations. *Combust. Theory Modeling*, 12:1055–1088, 2008. 30
- [69] B. Fiorina, O. Gicquel, and D. Veynante. Turbulent flame simulation taking advantage of tabulated chemistry self-similar properties. *Proc. Combust. Inst.*, 32:1687–169, 2009. 30
- [70] G. Volpe. On the use and accuracy of compressible flow codes at low Mach numbers. *AIAAJ*, 91:1662, 1991. 39
- [71] R. H. Pletcher and K-H Chen. On solving the compressible Navier-Stokes equations for unsteady flows at very low Mach numbers. *AIAAJ*, 93:3368, 1993. 39

- [72] A. Majda and J. Sethian. The derivation and numerical solution of the equation for zero Mach number combustion. *Combust. Sci. Tech.*, 42:185–205, 1985. [39](#), [40](#), [55](#)
- [73] A. J. Chorin. A numerical method for solving incompressible viscous flow problems. *J. Comput. Phys.*, 2:12–26, 1967.
- [74] P. A. McMurtry, W-H Jou, J. J. Riley, and R. W. Metcalfe. Direct numerical simulations of reacting mixing layer with chemical heat release. *AIAAJ.*, 24:962–970, 1986. [40](#)
- [75] F. F. Grinstein. Introduction: boundary conditions for large eddy simulation. *AIAA J.*, 42(3):437, 2004. [41](#)
- [76] T. Poinso and S. Lele. Boundary conditions for direct simulation of compressible viscous reacting flows. *J. Comput. Phys.*, 101(1):104–129, 1992. [41](#), [49](#), [56](#)
- [77] R. Bilger. The structure of turbulent nonpremixed flames. *Proc. Combust. Inst.*, 22:475–488, 1988. [44](#), [83](#)
- [78] Bei Jin. *Conditional sources-term estimation methods for turbulent reacting flows*. PhD thesis, University of British Columbia, December 2007. [46](#)
- [79] D. C. Wilcox. *Turbulence modeling for CFD*. DCW Industries, La Canada, 1998. [46](#)
- [80] J. Smagorinsky. General circulation experiments with the primitive equations I: The basic experiment. *Monthly Weather Review*, 91(3):99–164, 1963. [46](#)
- [81] M. Germano, U. Piomelli, P. Moin, and W. H. Cabot. A dynamic subgrid-scale eddy viscosity model. *Phys. Fluids*, 3:1760–1765, 1991. [46](#)
- [82] P. Moin, K. Squires, W. Cabot, and S. Lee. A dynamic subgrid-scale model for compressible turbulence and scalar transport. *Phys. Fluids*, 3:2746–2757, 1991.
- [83] A. E. Tejada-Martínez and K. E. Jansen. A dynamic Smagorinsky model with dynamic determination of the filter width ratio. *Phys. Fluids*, 16:2514–2528, 2004. [46](#)
- [84] P. Moin and K. Mahesh. Direct Numerical Simulation: a tool in turbulence research. *Annu. Rev. Fluid Mech.*, 30:539–578, 1998. [47](#)
- [85] V. Eswaran and S. B. Pope. An examination of forcing in direct numerical simulations. *Comput. Fluids*, 16:257–278, 1988. [47](#)
- [86] J. Kim, P. Moin, and R. Moser. Turbulence statistics in fully developed channel flow. *J. Fluid Mech.*, 177:133–166, 1987.
- [87] P. R. Spalart. Direct numerical study of leading-edge contamination. In *Fluid Dynamics of Three-Dimensional Turbulent Shear Flows and Transition*, page 438. AGARD CP, 1989. [47](#)
- [88] L. Vervisch. Using numerics to help the understanding of non-premixed turbulent flames. *Proc. Combust. Inst.*, 28:11–24, 2000. [47](#)
- [89] P. Domingo, L. Vervisch, and J. Réveillon. DNS analysis of partially premixed combustion in spray and gaseous turbulent flame bases stabilized in hot air. *Combust. Flame*, 140:172–195, 2005.
- [90] L. Vervisch and T. Poinso. Direct numerical simulation of non-premixed turbulent flame. *Annu. Rev. Fluid Mech.*, 30:655–692, 1998.
- [91] R. Bilger, S. Stårner, and R. Kee. On reduced mechanisms for methane-air combustion in nonpremixed flames. *Combust. Flame*, 80:135–149, 1990.
- [92] S. Mahalingham, J.H. Chen, and L. Vervisch. Finite rate chemistry and transient effects in direct numerical simulations of turbulent nonpremixed flames. *Combust. Flame*, 102:285–297, 1995.

- [93] B. Cuenot and T. Poinso. Asymptotic and numerical study of diffusion flames with variable lewis number and finite rate chemistry. *Combust. Flame*, 104(1-2):111–137, 1996.
- [94] C.F. Kaminski, J. Hult, M. Alden, S. Lindenmaier, A. Dreitzler, U. Maas, and M. Baum. Spark ignition of turbulent methane/air mixtures revealed by time-resolved planar laser-induced fluorescence and direct numerical simulations. *Proc. Combust. Inst.*, 28:399–405, 2000.
- [95] D. Thévenin, O. Gicquel, J. de Charentenay, R. Hilbert, and D. Veynante. Two-versus three-dimensional direct simulations of turbulent methane flame kernels using realistic chemistry. *Proc. Combust. Inst.*, 29:2031–2039, 2002. 54, 82
- [96] S. Sreedhara and K.N. Lakshmisha. Autoignition in a non-premixed medium: DNS studies on the effects of three-dimensional turbulence. *Proc. Combust. Inst.*, 29:2051–2059, 2002. 47
- [97] E. Richardson, N. Chakraborty, and E. Mastorakos. Analysis of direct numerical simulations of ignition fronts in turbulent non-premixed flames in the context of conditional moment closure. *Proc. Combust. Inst.*, 31:1683–1690, 2007.
- [98] Y. Wu, D. Haworth, M. Modest, and B. Cuenot. Direct numerical simulation of turbulence/radiation interaction in premixed combustion systems. *Proc. Combust. Inst.*, 30:639–646, 2005.
- [99] M. Tanahashi, M. Fujimura, and T. Miyauchi. Coherent fine-scale eddies in turbulent premixed flames. *Proc. Combust. Inst.*, 28:529–535, 2000.
- [100] M. Tanahashi, Y. Nada, Y. Ito, and T. Miyauchi. Local flame structure in the well stirred reactor regime. *Proc. Combust. Inst.*, 29:2041–2049, 2002.
- [101] Y. Mizobuchi, S. Tachibana, J. Shinjo, S. Ogawa, and T. Takeno. A numerical analysis of the structure of a turbulent hydrogen jet lifted flame. *Proc. Combust. Inst.*, 29(2):2009–2015, 2002. 78
- [102] Y. Mizobuchi, J. Shinjo, S. Ogawa, and T. Takeno. A numerical study on the formation of diffusion flame islands in a turbulent hydrogen jet lifted flame. *Proc. Combust. Inst.*, 30:611–619, 2005. 78
- [103] T. Takeno and Y. Mizobuchi. Significance of DNS in combustion science. *C. R. Mécanique*, 334(8/9):517–522, 2006.
- [104] V. Favier and L. Vervisch. Edge flames and partially premixed combustion in diffusion flame quenching. *Combust. Flame*, 125:788–803, 2006. 78
- [105] J. Bell, M. Day, and J. Grcar. Numerical simulation of premixed turbulent methane combustion. *Proc. Combust. Inst.*, 29:1987–1993, 2002.
- [106] J. van Oijen, G. Groot, R. Bastiaans, and L.P. de Goey. A flamelet analysis of the burning velocity of premixed turbulent expanding flames. *Proc. Combust. Inst.*, 30:657–664, 2005.
- [107] J. van Oijen, R. Bastiaans, and L. de Goey. Low-dimensional manifolds in direct numerical simulations of premixed turbulent flames. *Proc. Combust. Inst.*, 31:1377–1384, 2007. 47
- [108] D. Thévenin, F. Behrendt, U. Maas, B. Przywara, and J. Warnatz. Development of a parallel direct simulation code to investigate reactive flows. *Comput. Fluids*, 25(5):485–496, 1996. 48
- [109] M. Lange, U. Riedel, and J. Warnatz. Parallel DNS of turbulent flames with detailed reaction schemes. In *29th AIAA Fluid Dynamics Conference*, Albuquerque, NM, USA, AIAA Paper 98-2979, 1998.
- [110] R. Hilbert and D. Thévenin. Autoignition of turbulent non-premixed flames investigated using direct numerical simulations. *Combust. Flame*, 128(1-2):22–37, 2002. 48, 71, 76, 82

- [111] R. Hilbert and D. Thévenin. Influence of differential diffusion on maximum flame temperature in turbulent nonpremixed hydrogen/air flames. *Combust. Flame*, 138:175–187, 2004. 48, 70, 75
- [112] A. Laverdant. Notice d'utilisation du programme SIDER (PARCOMB3D). Technical Report RT 2/13635 DEFA, The French Aerospace Lab., ONERA, 2008. 48, 149
- [113] U. Maas and D. Thévenin. Correlation analysis of direct numerical simulation data of turbulent non-premixed flames. *Proc. Combust. Inst.*, pages 1183–1189, 1998. 48
- [114] A. Honein and P. Moin. Higher entropy conservation and numerical stability of compressible turbulence simulations. *J. Comput. Phys.*, 201:531–545, 2004. 49
- [115] H. Choi and P. Moin. Effects of the computational time-step on numerical solutions of turbulent flows. *J. Comput. Phys.*, 113:1–4, 1994. 49
- [116] M. Baum, T. Poinsot, and D. Thévenin. Accurate boundary conditions for multicomponent reactive flows. *J. Comput. Phys.*, 116:247–261, 1995. 49, 76
- [117] J. de Charentenay, D. Thévenin, and B. Zamuner. Comparison of direct numerical simulations of turbulent flames using compressible or low-Mach number formulations. In B.J. Geurts, R. Friedrich, and O. Métais, editors, *Direct and Large Eddy Simulation IV*, pages 129–136. Kluwer Academic Publishers, 2001. 54
- [118] J. de Charentenay and A. Ern. Multicomponent transport impact on premixed turbulent H_2/O_2 flames. *Combust. Theory Modeling*, 6(3):439–462, 2002. 54
- [119] F. Nicoud. Conservative high-order finite-difference schemes for low Mach flows. *J. Comput. Phys.*, 158:71–97, 2000. 55
- [120] C.J. Rutland, J. Ferziger, and S. El-Thary. Full numerical simulations and modeling of turbulent premixed flames. *Proc. Combust. Inst.*, 23:621–627, 1990. 55, 71, 78, 95, 99
- [121] S. Cant. Direct numerical simulation of premixed turbulent flames. *Phil. Trans. R. Soc. Lond.*, 357(1764):3583–3604, 1999.
- [122] S. Zhang and C.J. Rutland. Premixed flame effects on turbulence and pressure related terms. *Combust. Flame*, 102:447–461, 1995.
- [123] V. R. Katta and M W. Roquemore. On the structure of stretched/compressed laminar flamelet—influence of preferential diffusion. *Combust. Flame*, 100:61–70, 1995.
- [124] H. N. Najm, P. S. Wyckoff, and O. M. Knio. A semi-implicit numerical scheme for reacting flow. *J. Comput. Phys.*, 143:381–402, 1998.
- [125] O. M. Knio, H. N. Najm, and P. S. Wyckoff. A semi-implicit numerical scheme for reacting flow ii: stiff, operator-split formulation. *J. Comput. Phys.*, 154:428–467, 1999.
- [126] R. Ben Dakhli and V. Giovangigli. Multiradii modeling of counterflow spray diffusion flames. *Proc. Combust. Inst.*, 28:1039–1045, 2000. 55
- [127] Swarztrauber P. N. In G. Rodrigue, editor, *Parallel Computations*, pages 51–83. Academic Press: New York, 1982. 56
- [128] Message Passing Interface Forum. A message-passing interface standard [special issue]. *Int. J. Supercomputer Applications and High Performance Computing*, 8(3/4), 1994. 57
- [129] L. Giraud, R. Guivarch, and J. Stein. Parallel distribution FFT-based solvers for 3D Poisson problems in meso-scale atmospheric simulations. *Int. J. High Perf. Comput. Appl.*, 15(1):36–46, 2001. 58

- [130] The AVBP code. A parallel CFD code for reactive unsteady flow simulations on hybrid grids, August 2010. URL <http://www.cerfacs.fr/4-26334-The-AVBP-code.php>. 59
- [131] D. Thévenin and G. Fru. *parcomb* user's guide. Technical Report TR/LSS/GF-5/10, LSS/ISUT, Univ. of Magdeburg, 2010. 60
- [132] M. Klein, A. Sadiki, and J. Janicka. A digital filter based generation of inflow data for spatially developing direct numerical or large eddy simulations. *J. Comput. Phys.*, 186(2):652–665, 2003. 60, 71
- [133] A. Kempf, M. Klein, and J. Janicka. Efficient generation of initial and inflow-conditions for transient flows in arbitrary geometries. *Flow Turb. Comb.*, 74:67–84, 2005. 60, 63, 71
- [134] C. Zistl, R. Hilbert, G. Janiga, and D. Thévenin. Increasing the efficiency of post-processing for turbulent reacting flows. *Comput. Vis. Sci.*, 12(8):383–395, 2009. 64, 71, 75, 104, 115, 117
- [135] C. Zistl, G. Fru, G. Janiga, and D. Thévenin. *AnaFlame* postprocessing toolbox server and user's manual, March 2011. URL <http://www.ovgu.de/isut/LSS/anaflame>. 64, 75, 104, 117
- [136] Bracco A. and J.C. McWilliams. Reynolds-number dependency in homogeneous, stationary two-dimensional turbulence. *J. Fluid Mech.*, 646:517–526, 2010. 66
- [137] J. O. Hinze. *Turbulence*. McGraw-Hill, new York, 2nd edition, 1975. 71
- [138] G. Fru, G. Janiga, and D. Thévenin. Direct Numerical Simulation of highly turbulent premixed flames burning methane. In H. Kuerten et. al, editor, *Direct and Large-Eddy Simulation VIII*, volume 15 of *ERCOFTAC Series*, pages 327–332. Springer Netherlands, 2011. ISBN 978-94-007-2482-2. doi: 10.1007/978-94-007-2482-2_52. URL http://dx.doi.org/10.1007/978-94-007-2482-2_52. 71, 99, 100, 120, 125
- [139] G. Fru, H. Shalaby, A. Laverdant, C. Zistl, G. Janiga, and D. Thévenin. Direct Numerical Simulations of turbulent flames to analyze flame/acoustic interactions. In A. Schwarz and J. Janicka, editors, *Combustion Noise*, pages 239–268. Springer-Verlag, 2009. 75, 117, 134, 139
- [140] G. Fru, G. Janiga, and D. Thévenin. Probability of successful ignition events in turbulent flows using direct numerical simulation. In P. Kourdis and M. Agathou, editors, *13th International Conference on Numerical Combustion (ICNC-13)*, page CP150, Corfu, Greece, 2011. 76
- [141] G. Fru, D. Thévenin, C. Zistl, G. Janiga, L. Gouarin, and A. Laverdant. 3D direct simulation of a nonpremixed hydrogen flame with detailed models. In V. Armenio, B. Geurts, and J. Fröhlich, editors, *Direct and Large-Eddy Simulation VII*, ERCOFTAC Series, pages 421–425, Trieste, 2010. Springer-Verlag. doi: 10.1007/978-90-481-3652-0. 78
- [142] G. Fru, L. Gouarin, A. Laverdant, D. Thévenin, C. Zistl, and G. Janiga. Three-dimensional direct simulation of a nonpremixed hydrogen/air flame using detailed models. In *32nd International Symposium on Combustion*, Montreal, Canada, 2008. The Combustion Institute. Poster presentation. 78
- [143] H. Yamashita, M. Shimada, and T. Takeno. A numerical study on flame stability at transition point of jet diffusion flames. *Proc. Combust. Inst.*, 26:27–34, 1996. 78
- [144] N. Peters. The turbulent burning velocity for large-scale and small-scale turbulence. *J. Fluid Mech.*, 384:107–132, 1999. 94, 95, 96, 99

- [145] R. Abdel-Gayed and D. Bradley. Dependence of turbulent burning velocity on turbulent Reynolds number and ratio of laminar burning velocity to rms turbulent velocity. *Proc. Combust. Inst.*, 16(1):1725–1735, 1977. [98](#)
- [146] R. Abdel-Gayed, D. Bradley, M. Lawes, and F. Lung. Premixed turbulent burning during explosions. *Proc. Combust. Inst.*, 21(1):497–504, 1986.
- [147] R. Abdel-Gayed, D. Bradley, and M. Lawes. Turbulent burning velocities: A general correlation in terms of straining rates. *Proc. R. Soc. Lond.*, A414:389–413, 1987. [98](#), [114](#)
- [148] L. Kozachenko and I. Kuznetsov. Burning velocity in a turbulent stream of a homogeneous mixture. *Combust. Explos. Shock Waves*, 1(1):22–30, 1965.
- [149] R. Abdel-Gayed and D. Bradley. A two-eddy theory of premixed turbulent flame propagation. *Phil. Trans. Roy. Soc.*, 1(A301):1–25, 1981. [98](#)
- [150] R. Abdel-Gayed and D. Bradley. The influence of turbulence upon the rate of burning. In J. Lee, C. Guirao, and D. Grierson, editors, *Proceedings of the international conference on fuel-air explosions*, number 16 in Studies series, pages 51–68, McGill University, 1982. University of Waterloo press.
- [151] R. Abdel-Gayed, K. Al-khishali, and D. Bradley. Turbulent burning velocities and flame straining in explosions. *Proc. R. Soc. Lond.*, A391:393–414, 1984. [98](#), [114](#)
- [152] D. Bradley. How fast can we burn? *Proc. Combust. Inst.*, 24:247, 1993. [98](#), [117](#)
- [153] R. Bilger, M. Esler, and S. Stårner. On reduced mechanisms for methane-air combustion. In M. D. Smooke, editor, *Reduced Kinetic Mechanisms and Asymptotic Approximations for Methane-Air Flames*, volume 384 of *Lecture Notes in Physics*, pages 86–110. Springer-Verlag, 1991. [99](#), [152](#)
- [154] S. James and F.A. Jaber. Large scale simulations of two-dimensional nonpremixed methane jet flames. *Combust. Flame*, 123:465–487, 2000. [99](#)
- [155] T. Echekki, J.H. Chen, and I.R. Gran. The mechanism of mutual flame annihilation of stoichiometric premixed methane-air flames. *Proc. Combust. Inst.*, 26:855–864, 1996. [100](#)
- [156] J. H. Chen, A. Choudhary, B. de Supinski, M. DeVries, E. R. Hawkes, S. Klasky, W. K. Liao, K. L. Ma, J. Mellor-Crummey, N. Podhorszki, R. Sankaran, S. Shende, and C. S. Yoo. Terascale direct numerical simulations of turbulent combustion using S3D. *Comput. Sci. Discov.*, 2:31, 2009. [102](#), [111](#), [125](#), [139](#), [141](#)
- [157] G. Fru, G. Janiga, and D. Thévenin. Direct numerical simulation of the impact of high turbulence intensities and volume viscosity on premixed methane flames. *J. of Combustion*, (Article ID 746719):1–12, 2011. ISSN 2090-1976. URL <http://dx.doi.org/10.1155/2011/746719>. [104](#), [117](#)
- [158] B. Bédard, F. Egolfopoulos, and T. Poinsot. Direct numerical simulation of heat release and NOx formation in turbulent non premixed flames. *Combust. Flame*, 119:69–83, 1999. [107](#), [112](#)
- [159] J.E. Rehm and N.T. Clemens. The turbulent burning velocity for large-scale and small-scale turbulence. *Proc. Combust. Inst.*, 27:1113–1120, 1998. [107](#), [120](#)
- [160] S. Candel, D. Durox, and T. Schuller. Flame interactions as a source of noise and combustion instabilities. In *Collection of Technical Papers – 10th AIAA/CEAS Aeroacoustics Conference*, pages 1444–1454. May 2004. [107](#)
- [161] A. Schwarz and J. Janicka. *Combustion noise*. Springer, Berlin Heidelberg, 2009. [107](#)

- [162] J.F. Driscoll. Turbulent premixed combustion: flamelet structure and its effects on turbulent burning velocities. *Prog. Energy Combust. Sci.*, 34:91–134, 2008. 109, 114
- [163] T. Poinsot, T. Echehki, and M. Mungal. A study of the laminar flame tip and implications for premixed turbulent combustion. *Combust. Sci. Tech.*, 81:45–73, 1992. 109, 114
- [164] H.G. Im and J.H. Chen. Effects of flow transients on the burning velocity of laminar hydrogen/air premixed flames. *Proc. Combust. Inst.*, 28:1833–1840, 2000. 109
- [165] R. Sankaran and H. Im. Effect of hydrogen addition on the flammability limit of stretched methane/air premixed flames. In *Proceedings of the Third joint meeting of the U.S. section of the Combust. Inst.*, pages 1–6, Chicago, March 2003. 109, 114
- [166] G. Fru, D. Thévenin, and G. Janiga. Impact of turbulence intensity and equivalence ratio on the burning rate of premixed methane–air flames. *Energies*, 4(6):878–893, 2011. ISSN 1996-1073. URL <http://dx.doi.org/10.3390/en4060878>. 111
- [167] R. Abdel-Gayed, D. Bradley, N. Hamid, and M. Lawes. Lewis number effects on turbulent burning velocity. *Proc. Combust. Inst.*, 20:505, 1985. 117
- [168] S. Shy, W. Lin, and J. Wei. An experimental correlation of turbulent burning velocities for premixed turbulent methane–air combustion. *Proc. R. Soc. Lond.*, 456:1997–2019, 2000. 117
- [169] I. Shepherd and R. Cheng. The burning rate of premixed flames in moderate and intense turbulence. *Combust. Flame*, 127:2066–2075, 2001. 117
- [170] G. Janiga, G. Fru, and D. Thévenin. Direct numerical simulations of turbulent flames at high reynolds numbers. In *DEISA PRACE Symposium*, Barcelona, Spain, 2010. Poster presentation. 117
- [171] G. Fru, G. Janiga, and D. Thévenin. Impact of volume viscosity on the structure of turbulent premixed flames in the Thin Reaction Zone Regime. *Flow Turb. Comb.*, pages 1–28, 2011. ISSN 1386-6184. doi: 10.1007/s10494-011-9360-1. URL <http://dx.doi.org/10.1007/s10494-011-9360-1>. 117
- [172] G. Fru, G. Janiga, and D. Thévenin. *Simulation of turbulent combustion processes under realistic conditions*, pages 20–22. Extreme Computing in Europe. DEISA Media, 2011. ISBN 978-952-5520-40-8. URL http://www.deisa.eu/news_press/media. 117
- [173] R. Sankaran, E. Hawkes, and J. Chen. Structure of a spatially developing turbulent lean methane-air Bunsen flame. *Proc. Combust. Inst.*, 31:1291–8, 2006. 139, 140, 141
- [174] R. Sankaran, E. Hawkes, H. Chen, T. Lu, and C Law. Structure of a spatially developing turbulent lean methane-air bunsen flame. *Proc. Combust. Inst.*, 31:1291–1298, 2007. 139, 140, 141
- [175] S. A. Filatyev, J. F. Driscoll, C. D. Carter, and J. M. Donbar. Measured properties of turbulent premixed flames for model assessment, including burning velocities, stretch rates, and surface densities. *Combust. Flame*, 141:1–21, 2005. 140
- [176] B. Linseisen. Direct numerical simulation of flames on parallel supercomputers: Corrections to the navier-stokes equations. Master’s thesis, LSS-M03/09, Lehrstuhl für Strömungsmechanik und Strömungstechnik, Univ. of Magdeburg “Otto von Guericke”, 2009. 146
- [177] J. B. Roberto. Extreme scale computing: Transformational opportunities in science, March 2011. URL <http://extremecomputing.labworks.org>. 146

- [178] Top 500 Supercomputer Site. Performance projection, March 2011. URL <http://top500.org>. 146
- [179] J.M. Favre. Simulations go live, a.k.a. *in-situ* visualization, March 2011. URL <http://www.kcse.kth.se/archive/Favre-inSituVisualization.pdf>. 147
- [180] Brutal facts of high-performance computing, March 2011. URL <http://www.hp2c.ch/background/hpcfacts/>. 147
- [181] Paraview visualization toolkit, March 2011. URL http://www.paraview.org/Wiki/SC10_Coprocessing_Tutorial. 147
- [182] VisIt visualization toolkit, March 2011. URL <http://visitusers.org/index.php?title=VisIt-tutorial-in-situ>. 147

G. Fru: Curriculum Vitae and Own scientific production

CONTACT

INFORMATION

Laboratory of Fluid Dynamics and Technical Flows
 University of Magdeburg
 Universitätsplatz 2,
 39106 Magdeburg, GERMANY
E-mail: gordon.fru@ovgu.de
www.ovgu.de/isut/LSS



PERSONAL

DATA

Birthdate and place : 1977 in Mbatu
 Citizenship : Cameroonian
 Family Status : Married

RESEARCH

INTERESTS

Computational physics, with affinity for

- (Applied) Computational Fluid Dynamics (CFD)
- Direct Numerical Simulation (DNS) of (complex) turbulent (reacting) flows
- High Performance Computing (HPC) and Parallel algorithms for turbulent flows
- General Numerical Analysis

EDUCATION

University of Magdeburg, Magdeburg, Germany

Ph.D., **Chemical Engineering**, **2007 – 2011**

- Thesis Topic: *DNS of Turbulent Flames on Parallel Computers*
- Advisor: [Professor Dominique Thévenin](#)
- Area of Study: Chemical Engineering, CFD

Lund Institute of Technology, Lund, Sweden

Advanced course in **Turbulence, Theory and Modeling**, **Aug. – Dec. 2006**

Umea University, Umea, Sweden

M.Sc., **Computational Physics**, **2004 – 2006**

- Thesis Topic: *Flame acceleration in tubes*
- Advisor: [Professor Vitaly Bychkov](#)
- Area of Study: Physics

University of Buea, Buea, Cameroon

B.Sc., **Physics**, **1998 – 2002**

- Minor in **Computer science**

GBHS-Essos, Yaounde, Cameroon

GCE Advanced Level, **Sciences**, **1996 – 1998**

- Passed in 5/5 papers

GCE Ordinary Level, **Sciences**, **1991 – 1996**

- Passed in 10/10 papers

ACADEMIC

TRAINING

EU-US Summer School (TeraGrid/XD/DEISA/PRACE), California, USA

HPC Challenges in Computational Sciences, **August 7–12, 2011**

European Centre for Research and Advanced Training in Scientific Computation (CERFACS), Toulouse, France

Marie-Curie Action, **May – July, 2010**

- Efficient and Clean Combustion Experts Training (ECCOMET)

Jülich Supercomputing Center (JSC), Jülich, GermanyDEISA training course, **January 13–14, 2009**

- Introduction to the DEISA infrastructure and the Blue Gene/P

Leibniz Supercomputing Center (LRZ), Munich, GermanyHigh Performance Computing (HPC) Workshop, **February 7, 2008**

- Performance Analysis of Parallel programmes with VAMPIR

Technische Universität Berlin (TUB), Berlin, GermanyDNS Summer School, **Sept. 2–8, 2007**

- International summer school on DNS of reacting and two-phase flows

Lund Institute of Technology (LTH), Lund, SwedenAdvance course, **Aug. – Dec., 2006**

- Turbulence, Theory and Modelling

Royal Institute of Technology (KTH), Stockholm, SwedenHPC Summer School, **August 14–25, 2006**

- Introduction to High Performance Computing (HPC) with MPI and OpenMP

AWARDS

Marie-Curie Action for Young Researchers Fellowship

- **under the Efficient and Clean Combustion Experts Training (ECCOMET) at CERFACS, Toulouse, France** **May – July, 2010**

First prize in Flow Visualization Gallery: "Virtual Turbulent Flame"

- **Conference on Modeling Fluid Flow, Budapest, Hungary** **12 Sept. 2009**

WORK
EXPERIENCE**University of Magdeburg**, Magdeburg, Germany*PostDoc Fellow (DFG Project – FOR1447)* **August 2010 to present**

- Safety Related Ignition Processes
 - Probability of successful ignition events in turbulent flows using DNS

Teaching Assistant **April 2007 to present**

- Computer Hands-on exercise instructor:
 - CFD course
- Instructor for the Advanced Fluid Dynamics course tutorials

Research Assistant **Jan. 2007 to present**

- Complex Chemistry modeling/reduction with FPI technique
- DNS flame solver development & parallelization for distributed systems

University of Buea, Buea, Cameroon*Computer Lab. Instructor* **April – June, 2002**

- Assisting students in the computer labs of the department of computer science during lab session

Undergraduate Student **Sept. 1999 – June 2004**

Freelance Instructor, Yaounde, Cameroon

Private high school tutor

June 2002 – 2003

- Preparing GCE advance level candidates in Mathematics, Physics, and Advanced mathematics.

JOURNAL
PUBLICATIONS

G. Fru, G. Janiga, and D. Thévenin. Impact of volume viscosity on the structure of turbulent premixed flames in the Thin Reaction Zone Regime. *Flow, Turbulence and Combustion*, 1–28, **2011**. 10.1007/s10494-011-9360-1.

G. Fru, G. Janiga, and D. Thévenin. Direct numerical simulation of the impact of high turbulence intensities and volume viscosity on premixed methane flames. *Journal of Combustion*, (Article ID 746719), 1–12, **2011**. 10.1155/2011/746719.

G. Fru, D. Thévenin, and G. Janiga. Impact of turbulence intensity and equivalence ratio on the burning rate of premixed methane–air flames. *Energies*, 4(6):878–893, **2011**. 10.3390/en4060878

V. Bychkov, V. Akkerman, **G. Fru**, A. Petchenko and L. Eriksson. Flame acceleration at the early stages of burning in tubes. *Combustion and Flame*, 150:263–276, **2007**.

CONFERENCE
PUBLICATIONS

G. Fru, D. Thévenin, and G. Janiga. Direct numerical simulations of synthetic gas oxidation under realistic conditions. In *First ERCOFTAC Conference on Simulation of Multiphase Flows in Gasification and Combustion (MFGC-1)*, Dresden, Germany, **2011**.

G. Fru, G. Janiga, and D. Thévenin. Probability of successful ignition events in turbulent flows using direct numerical simulation. In *13th International Conference on Numerical Combustion (ICNC-13)* (P. Kourdis and M. Agathou, Eds.), paper CP150, Corfu, Greece, **2011**.

G. Fru, G. Janiga, and D. Thévenin. Direct Numerical Simulation of highly turbulent premixed flames burning methane. In *Direct and Large-Eddy Simulation VIII* (J.G.M. Kuerten, B. Geurts, V. Armenio, and J. Fröhlich, Eds.), ERCOFTAC Series, Springer, 327–332, Eindhoven, **2011**.

G. Fru, G. Janiga, and D. Thévenin. Direct numerical simulation of turbulent methane flames with and without volume viscosity. In *8th Euromech Fluid Mechanics Conference (EFMC-8)*, pages MS2–9, Bad Reichenhall, Germany, **2010**.

G. Janiga, **G. Fru**, and D. Thévenin. Direct numerical simulations of turbulent flames at high Reynolds numbers. In *DEISA PRACE Symposium*, Barcelona, Spain, **2010**. Poster presentation.

G. Fru, D. Thévenin, C. Zistl, G. Janiga, L. Gouarin, and A. Laverdant. 3D direct simulation of a nonpremixed hydrogen flame with detailed models. In *Direct and Large-Eddy Simulation VII* (V. Armenio, B. Geurts, and J. Fröhlich, Eds.), ERCOFTAC Series, Springer, 421–425, **2010**.

G. Fru, D. Thévenin, and G. Janiga. Impact of volume viscosity on turbulent non-premixed flames. In *33rd International Symposium on Combustion*, Beijing, China, **2010**. Poster presentation.

G. Fru, L. Gouarin, A. Laverdant, D. Thévenin, C. Zistl, and G. Janiga. Three-dimensional direct simulation of a nonpremixed hydrogen/air flame using detailed models. In *32nd International Symposium on Combustion*, Montreal, Canada, **2008**. Poster presentation.

G. Fru, C. Zistl, G. Janiga, and D. Thévenin. Direct numerical simulation of methane flames using tabulated chemistry. In *DNS and LES of Reacting Flows*, pages 65–66, Maastricht, The Netherlands, **2008**. Poster presentation.

BOOK
CHAPTER
PUBLICATIONS

G. Fru, G. Janiga, and D. Thévenin. Simulation of turbulent combustion processes under realistic conditions. In *DEISA DIGEST 2011* (A. Turunen, H. Lederer, T. Autio, S. Pyysalo, N. Morgan, and P. Rötönen, Eds.), Extreme Computing in Europe Series, DEISA Media (www.deisa.eu/news_press/media), 20–22, **2011**.

G. Fru, H. Shalaby, A. Laverdant, C. Zistl, G. Janiga, and D. Thévenin. Direct Numerical Simulations of turbulent flames to analyze flame/acoustic interactions. In *Combustion Noise, Fluid Mechanics and its Applications* (A. Schwarz and J. Janicka, Eds.), Springer, 239–268, **2009**.

OTHER
PUBLICATIONS

C. Zistl, **G. Fru**, G. Janiga, and D. Thévenin. AnaFlame postprocessing toolbox server and user’s manual, www.ovgu.de/isut/LSS/anaflame, March **2011**.

D. Thévenin and **G. Fru**. parcomb user’s guide. Tech. Report TR/LSS/GF-5/10, LSS/ISUT, Univ. of Magdeburg, **2010**.

G. Fru, G. Janiga, and D. Thévenin. DECI DNS-HiRe project: Volume viscosity and methane DNS. Tech. Report TR/LSS/GF-4/09, LSS/ISUT, Univ. of Magdeburg, **2009**.

G. Fru, G. Janiga, and D. Thévenin. DECI DNS-HiRe project: Improving the performance of parcomb. Tech. Report TR/LSS/GF-3/09, LSS/ISUT, Univ. of Magdeburg, **2009**.

G. Fru. FPI chemistry tabulation and Direct Numerical Simulation of turbulent flames. Tech. Report TR/LSS/GF-1/08, LSS/ISUT, Univ. of Magdeburg, **2008**.

G. Fru. *Flame Acceleration in Pipes*. Master’s thesis, Department of Physics, Umea University, February **2006**.